Dissertation

submitted to the
Combined Faculties for the Natural Sciences and for Mathematics
of the Ruperto-Carola University of Heidelberg, Germany
for the degree of
Doctor of Natural Sciences

presented by
Dipl.-Phys. Alexander Gansen
born in: Koblenz

Oral examination: 16.01.2008

Chromatin at the Nanolevel -
Development of a single molecule FRET experiment
and analysis of the structure and stability
of individual nucleosomes.

Referees:

Prof. Dr. Jörg Langowski

Prof. Dr. Dr. Christoph Cremer

Zusammenfassung

Chromatin auf der nm-Skala - Entwicklung eines Einzelmolekül-FRET Spektrometers zur Untersuchung der Struktur und Stabilität einzelner Nukleosomen

Die Struktur und Stabilität einzelner Nukleosome wird im Rahmen dieser Arbeit auf Einzelmolekülebene untersucht. Beide Aspekte spielen eine entscheidende Rolle in der Chromatinorganisation im Zellkern. Sie steuern zum Beispiel die Zugänglichkeit bestimmter DNA Regionen für Transkriptionsfaktoren. Auf der Ebene einzelner Nukleosome können *in vitro* Experimente wertvolle Informationen über die Prozesse liefern, die dynamische Strukturänderungen innerhalb des Nukleosoms hervorrufen. Dazu wurde eine experimentelle Platform konzipiert und aufgebaut, welche es erlaubt, die Konformation frei diffundierender Nukleosome zu untersuchen. Dazu wird nukleosomale DNA mit Fluoreszenzfarbstoffen markiert, und lokale Änderungen der Nukleosomstruktur durch Fluoreszenz-Resonanzenergietransfer (FRET) im Nanometer-Bereich nachgewiesen. Unter anderem werden Messungen an verschiedenen Remodellierungsfaktoren präsentiert, welche deutliche Unterschiede in der Nukleosomenstruktur hervorriefen. Ein Hauptaugenmerk wird ebenfalls auf die Stabilität einzelner Nukleosomen gelegt. Diese wurde in Abhängigkeit verschiedener Faktoren wie Ionenstärke, Gesamt-Nukleosomkonzentration, Acetylierung von Histonschwänzen, sowie Verwendung verschiedener DNA Sequenzen untersucht. Es wird demonstriert, dass Nukleosomkomplexe unter niedrigen Konzentrationen spontan dissoziieren und dabei sequenzabhängig einer Strukturänderung unterliegen. Die dabei auftretenden Konformationsänderungen weisen eine Dynamik im Millisekunden-Bereich auf und nehmen mit steigender Ionenstärke zu. Die Acetylierung der Histonschwänze wirkt sich ebenfalls destabilisierend auf die Nukleosomstruktur aus. Das erhöhte Dissoziationsverhalten korreliert mit einer Öffnung der Nukleosomstruktur, welche sich hauptsächlich in der Linker DNA Region bemerkbar macht.

Abstract

Chromatin at the Nanolevel -
Development of a single molecule FRET experiment and analysis of the structure and stability of individual nucleosomes

The structure and stability of individual nucleosome complexes is analysed on the single molecule level. Both aspects are important for the organisation of chromatin inside the nucleus, e.g. by controlling the accessibility of DNA to transcription factors. On the level of individual nucleosomes *in vitro* experiments provide valuable information on the processes responsible for dynamic changes in the nucleosome structure. An experimental setup is presented which monitors the conformation of freely diffusing complexes. Nucleosomal DNA is labeled with small fluorophores and Fluorescence Resonance Energy Transfer (FRET) is used to monitor changes in nucleosome structure with nm accuracy. Experiments are presented in which various remodelling factors induce detectable changes in the nucleosome conformation. A major focus is laid on the stability of nucleosomes under the influence of various factors such as ionic strength, total nucleosome concentration, histone tail acetylation and the use of different DNA sequences. Nucleosomes dissociate spontaneously at low sample concentrations and sequence-specific changes in nucleosome structure occur on the ms time scale. Histone tail acetylation also results in a destabilisation of the nucleosome complex. The dissociation at larger ionic strength correlates with an opening of the overall nucleosome structure which predominantly affects the linker DNA region.

Contents

List of Figures

List of Tables

Introduction

Undoubtly, the most important component in any living cell is its DNA. It contains all the information required to build the huge protein machinery that exerts the vital functions of the cell. Arranged in a highly organised complex, the chromatin fulfils two at first glance contradictory functions [6]. On the one hand, it stows the huge amount of DNA into the small cell nucleus which requires a considerable compaction of the DNA. On the other hand, the information encoded in the DNA sequence has to be correctly processed. In response of external stimuli certain regions of DNA have to be made accessible to DNA-processing enzymes such as the transcription machinery or DNA repair proteins. Other parts of the DNA may be rendered inaccessible, if their information is not required (gene silencing). Obviously both requirements can only be met by a highly dynamic chromatin structure which is largely determined by the properties of its elemental unit, the nucleosome.
Stretches of about 200 bp DNA are wrapped almost two-fold around a cylindrical histone core, forming a series of nucleosomes along an extended piece of DNA. The delicate balance between the energy-consuming bending of the DNA and numerous sttractive interactions between histones and DNA renders the nucleosome a slippery yet stable complex [121]. Any process that influences the DNA-octamer interactions results in changes in nucleosome structure which potentially alters the local chromatin morphology. A variety of ATP-dependent enzymes, so called remodeling factors, rearrange nucleosomes to allow access to DNA sites that were previously occluded by the octamer [6, 137]. Other proteins modify the charged residues of the individual components of the nucleosome [126] which potentially destabilises the complex which might facilitate its repositioning.

It is thus not surprising that the nucleosome moved into the focus of modern chromatin research, both *in vivo* and *in vitro*. Suitable model systems can be obtained by extracting nucleosomes out of cells or reconstitution from purified DNA and histones either as mononucleosomes or nucleosome arrays. These can then be used to study the dynamics and mobility of these complexes as a function of various parameters, such as DNA sequence, histone content, histone modification and ionic strength.
In various standard assays it was observed that DNA can partially detach from the nucleosome [91] and slide along the histone core [111, 101, 53]. Both processes can lead to the exposure of previously occluded DNA regions as was shown by accessibility assays. All these processes occur within dimensions of a few nm (the size of the nucleosome) and on time scales between milliseconds and several hours. Methods from classical biology are not able to fully capture this information due to the lack of spatial

and temporal resolution. Consequently new hybrid areas of science were born in which researchers made use of the instrumentation provided by other scientific areas to investigate complex biological processes. With combined forces is now possible to learn much more about the processes responsible for nucleosome dynamics and chromatin organisation.

Structural information on the nm-scale can be obtained with various non-optical methods such as Electron Microscopy or X-ray Crystallography. The recent publication of the nucleosome structure at $1.9\,\mathring{A}$ resolution [29] provided valuable information about the local interactions between DNA and octamer, yet it resembled a static picture only. The exact dynamics is not accesseble. Moreover, these techniques require the fixation of the sample or even its staining to enhance the contrast of the specimen. The energy of the probing particle (electron or photon) has to be very large to resolve structural features in the nm-range and can destroy the specimen.
A considerably less invasive technique is optical microscopy. The combination of two or more lenses arranged in the correct order can be used to magnify structures within the specimen that cannot be resolved by the bare human eye. Since the first observation and identification of bacteria by van Leeuwenhoek in 1676 optical microscopy has become an integral part in modern biology. Its power grew even stronger with the advent of fluorescence microscopy. The fact that the fluorescence signal can be separated from the excitation light provides a greatly enhanced contrast compared to conventional optical microscopy which relied on differences in the refractive index as the contrast-defining property. The subsequent invention of the confocal microscope by Minsky in 1957 and the use of modern laser sources confined the volume from which fluorescence is detected to about $1\,\mu m$ in each dimension. In form of a Confocal Laser Scanning Microscope (CLSM) [26] sectional images can now be obtained from complex biological specimen. The resolution that is provided by light microscopy, however, is limited to about half the wavelength, which for visible light is just above 200 nm. This is still more than one order of magnitude larger than the size of the nucleosome and distance changes will not be resolved. The confocal microscope has been recently refined in a variety of ways to achieve a spatial resolution well above this theoretical limit [69, 68, 2] but still below the size of the nucleosome yet.
Although fluorescence microscopy cannot *directly* resolve the nucleosome structure it can be used to obtain detailed information in an *indirect* way, via the process of Fluorescence Resonance Energy Transfer (FRET). In the early 1930's Perrin discovered that two chromophores can interact over distances much greater than their diameter. A quantitative formulation of this non-radiative energy transfer was later provided by Theodor Förster. Since its first application in biology by Stryer and Haugland in 1967 [128] FRET has become the most commonly applied technique to determine distances between biomolecules in solution [23]. Its sensitivity range matches the dimensions of the nucleosome and thus provides an ideal tool to monitor conformational changes within the complex.
Two fluorophores, a donor and an acceptor, are either attached to the nucleosomal DNA or to the histone proteins. The amount of energy transfer between both dye molecules strongly depends on their mutual distance. Variations in the fluorescence

signals from both dye molecules report on potential conformational changes within the sample. In fact the first FRET experiments on nucleosomes helped to understand their structure long before a detailed crystal structure was resolved [44]. Nowadays FRET is widely used to study the conformation and dynamics of an emsemble of nucleosomes under a variety of different conditions [91, 71, 14, 134, 135, 146]. These experiments were successful in determining overall structural features of nucleosomes but did not provide detailed information on the heterogeneity within the ensemble. This problem is inherent to all ensemble-based techniques, since the information obtained is averaged out over many molecules.

The analysis of the conformational heterogeneity, however, is important to understand the details of the processes that lead to nucleosome mobilisation. The identification of transient intermediates enables scientists to refine existing models on nucleosome dynamics or to postulate new ones. Information about the heterogeneity in the system can be obtained if the FRET efficiency is analysed for individual members of the ensemble one-by-one [63, 141]. The distribution of measured FRET values then displays the underlying heterogeneity in the ensemble.
The ability to detect single molecules was demonstrated by Hirschfeld who detected individual antibodies that were labeled with more than 100 fluorophores each [70]. The single fluorophore sensitivity was reached in the early 90's, first for molecules embedded in a host matrix [103] than for freely diffusing molecules [124]. The technique was later refined to enable the first single molecule FRET experiments on immobilised molecules by Ha et al. [64] and the detection of subpopulations in a freely diffusing ensemble shortly after [30]. Nowadays the analysis of single molecules has matured into a precise method to determine the conformational heterogeneity within an ensemble of proteins [123, 122, 31, 99, 34] or nucleic acids [100, 129, 72, 93].
These experiments laid the groundwork to apply single molecule FRET spectroscopy to individual nucleosomes. One class of experiments concentrated on the local dynamics of the entry-exit region of the nucleosomes. In previous FCS experiments Li et al. showed that the ends of the nucleosome are subject to transient unpeeling and subsequent rewrapping of the DNA [91]. This facilitates the exposure of occluded DNA sites for time periods of about 50 ms which would be slow enough to provide access to the DNA for nuclear proteins. Subsequent single molecule FRET experiments analysed conformational changes within surface-tethered nucleosomes and determined a time scale of 50-150 ms for the unpeeling of DNA [133, 80]. However, the presence of the surface and the fixation of one part of the nucleosome might change the intrinsic behavior of the complex and introduce unwanted artefacts.

The purpose of this thesis is to analyse the structure and dynamics of nucleosomes in free diffusion. In contrast to immobilized molecules this defines an environment free from perturbations. An experimental platform was designed and built which detemined the FRET efficiency for nucleosomes which successively diffuse through the laser focus of a confocal microscope. One aspect of this work was to optimise the conditions at which nuclesome dynamics can be studied. When working at the pM concentration range which is usually required for single molecule experiments in diffusion the stability

of the nucleosome has to be considered [61, 22]. An elegant way to prevent nucleosome dissociation while maintaining single molecule detection capabilities is the addition of unlabeled nucleosome complexes. On the one hand this allows to stabilise or destabilise nucleosomes in a controlled way, on the other hand it allowed to better compare the single molecule data with previous bulk experiments.
Recently Lohr and collegues demonstrated that the DNA sequence has a considerable impact on the nucleosome structure and stability [79] by monitoring internally labeled nucleosomes reconstituted with different DNA sequences. The studies presented in this thesis expand their findings in such that different DNA sites within the nucleosome were analysed. For the first time single molecule FRET data were obtained from the linker DNA region of nucleosomes. The combination of data from different DNA loci offers a more complete picture of nucleosome dynamics. This strategy is then applied to investigate how the acetylation of the histone tail regions or the ATP-hydrolysing activity of nucleosome remodeling factors alter the structure and stability of nucleosomes.

Chapter 1

Chromatin - structure and function

1.1 Introduction

The carrier molecule of the information that is required to synthesize the cellular material of an organism is the desoxiribonucleic acid (DNA) [144, 113]. It forms a linear semiflexible polymer, which is composed of 4 different nucleotides, adenine (T), cytosine (C), guanosine (G) and thymine (T). The sequence of these monomers encodes the structure of the proteins in form of three nucleotides for each amino acid, the so called codons. The codons are not uniformly distributed along the DNA but are clustered in genes, which contain between 5000 and 100000 nucleotides each. The genes, of which a human cell contains between 20000-25000, only represent 5 % of the total DNA content. The remaining 95 % are non-coding and partially contain other functional sites including the replication foci, the centromeres and the telomeres.

In its native form two strands of the polymer form a left-handed double helix with a diameter of about $2\,nm$. Exclusive base-pairing between A and T and C and G significantly stabilise the helix and keep the DNA structure in precise register.
Given the variety in function and protein content between different cells a huge amount of DNA is required to store all relevant information. In total each diploid human cell contains the same genetic information in form of approximately 6.6 billion nucleotide pairs. If they were arranged in a single piece of DNA, a double helix of more than 2m length would have to be stored inside each nucleus. In solution this would form a coiled structure with a radius around $400\,\mu m$. It is evident that DNA has to be rigorously compacted to make it fit into a cell nucleus of less than $10\,\mu m$ diameter. This requires a more than 10000-fold compaction of the DNA.
At the same time, the information on the DNA has to be correctly processed. Some genes have to be activated in response to external stimuli, while others have to be temporarily silenced. This implies a highly dynamic packaging strategy, which regulates the genetic processes by modulation of the accessibility of the DNA to nuclear factors. These two contradictory aspects are accomplished by the organisation of DNA into chromatin.

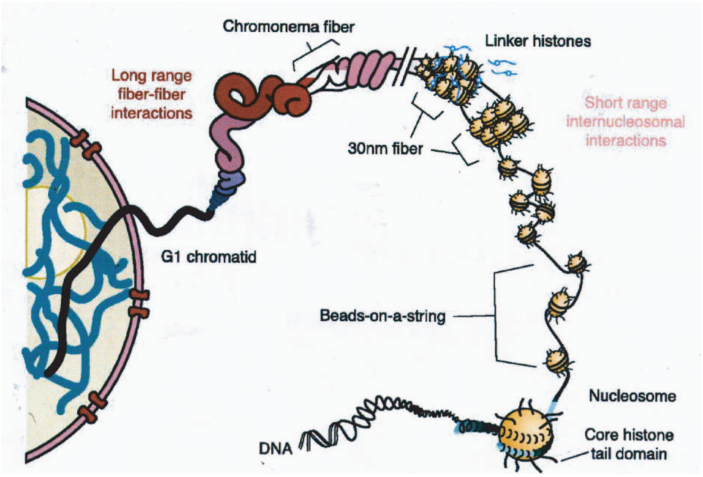

Figure 1.1: Schematic illustration of the multiple levels of chromatin folding that lead to compaction of DNA inside the cell nucleus. Adapted from Horn and Peterson, Science 297, 2002.

1.2 From DNA to chromatin

DNA compaction is facilitated by a hierarchical organised DNA-protein-complex called chromatin [144]. The various levels of packaging, that lead to an overall compaction of more than a factor of 10000 are illustrated in Figure 1.2 .

In the first step stretches of 160-230 bp DNA are wrapped around protein cores build up of 8 histone proteins. These complexes are called nucleosomes and provide a net compaction of a factor of 7. At low salt concentrations nucleosomes arrange themselves in an extended beads-on-a-string like structure [82, 83]. At larger ionic strength this structure progressively folds into a fiber of 30 nm diameter which compacts the DNA by an additional factor of 40.
The 30 nm fiber folds itself into more complex loop structures of 100 - 300 nm diameter [47], which in turn are arranged into 46 distinct chromosomes. These have a linear extension of $3 - 6\ \mu m$ and contain between 50 and 250 million base pairs. The observations, that chromosomes are not randomly distributed within the cell nucleus but occupy distinct territories, lead to the postulation of structural models such as the inter-chromosomal domain model [28, 27]. Active genes are arranged at the periphery of the chromosomal domains and are accessible to regulatory proteins that are mobile within the space between the territories.

1.3 The structure of the nucleosome

The nucleosome is the essential unit of chromatin organisation. Its first experimental observation dates from electron microscopic studies in 1973 [106] and its individual components were resolved one year later by Roger Kornberg [82]. A subsequent series of crystallographic studies [96] provided structural information which culminated in an atomic resolution of 1.9 Angström [29].

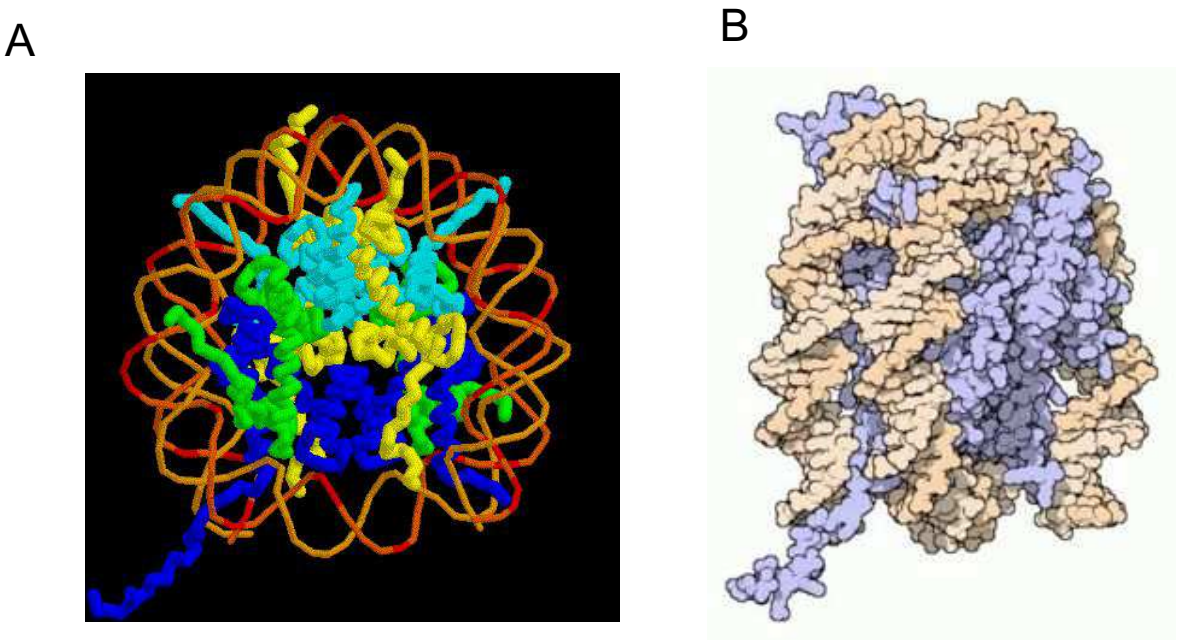

Figure 1.2: Structure of the nucleosome **A**: Top view **B**: Side view.

In its minimal form the nucleosome consists of 146-147 bp DNA which are wrapped around a cylindrical wedge of eight histone proteins in about 1.7 left-handed superhelical turns. This is referred to as the nucleosome core particle (NCP). The octamer is composed of two histones of H2A, H2B, H3 and H4 each. Upon assembly the central portion of DNA associates with a $(H3)_2(H4)_2$ tetramer. The NCP is then completed by addition of two H2A/H2B dimers on either side of the tetramer which organise the remaining $25-26\,bp$ of DNA each [67]. The NCP has an overall cylindrical shape with a length of 5.5 nm and a diameter of $11\,nm$ [48].
The tetramer itself is already capable of wrapping DNA around it, leading to sub-nucleosomal complexes such as the tetrasomes [65]. Similar structures, so called hexasomes, where one H2A/H2B is removed from the octamer, are expected to form intermediate states in the assembly and disassembly of nucleosomes [148].
The stretch of DNA within the NCP is of the order of the persistence length of free DNA ($\approx 150\,bp \equiv 50\,nm$). Wrapped around the octamer almost two-fold this requires a high cost of bending energy[1], which is compensated by numerous interactions between DNA and histone octamer. More than 116 direct and 358 water-bridged interactions are clustered around 14 distinct points, where the minor groove of the DNA faces the octamer [96, 29]. Each contact point contributes about $6\,k_BT$ to the total adsorption energy [120], which results in a net stabilisation of the complex.
Despite the numerous interactions, the nucleosome is far from being a rigid entity. The interaction strength is not uniformly distributed across the contact points but increases from the linker DNA sites towards the dyad axis. The neighboring DNA strands in the

[1]Pictorally spoken the bending energy in the nucleosome reflect a hypothetical wrapping of a $2\,cm$ thick plexiglass cylinder around a coffee mug [49]

nucleosome repell each other and a partial dissociation of the first $30 - 35\,bp$ DNA on either side can occur with relatively low energy cost [11, 89]. The ends of the nucleosome are thus loci of frequent spontaneous DNA detachment rewrapping which exposes a significant portion of DNA for time scales of the order of $50 - 250\,ms$ [133, 80, 91]. The confinement of the DNA to the nucleosome surface generates a distortion of the DNA. The average torsion of DNA wrapped around the nucleosome (10.2 bp per revolution) deviates from that observed for free DNA in solution (10.5 bp per revolution), and is not uniformly distributed along the superhelical path [117]. Owing to this large distortion naturally bent or bendable DNA sequences appear be preferred in their stability to the octamer as shown by Anderson and Widom [3]. Apparently, the bending energy to wrap these sequences around the octamer is lower, since the DNA is less resistant against the distortion. Despite the different affinities observed, the organisation of DNA into nucleosomes *per se* is probably not sequence-specific. About 80 % of all genomic DNA is bound to octamers and the histones are amongst the most conserved proteins found in nature.

About 15 % of the histone polypeptide constitute flexible extensions that protrude out of the octamer core. These N-terminal histone tails are enriched in positively charged lysines and arginines, which can form additional interactions with the negative phosphate backbone of the DNA. These further stabilize the nucleosome, as has been shown in digestion experiments for the N-terminal tails of histone H3 [92]. Within a nucleosome array the H4 tails can form attractive water bridge interactions with a H2A/H2B dimer of the next histone (tail-bridging effect), which mediate a progressive folding of the array into a compact conformation [98]. Digestion of these tails by trypsin disabled nucleosome arrays to fold into a compact regular form [54, 58], which shows the relevance of tail in the organisation of the higher-order chromatin structure.

Besides the nucleosome core particle, micrococcal digestion of native chromatin yielded another stable fragment consisting of 166 base pairs of undigested DNA [8]. This results from complexation of the NCP with a linker histone H1, which binds another 10 bp on each side of the protruding linker DNA. This complex is referred to as the chromatosome [125].
Its exact structure is still unresolved, although electron microscopy studies indicate, that the H1 forms an asymmetrically positioned stem-like motiv. Fluorescence studies showed that addition of linker histone H1 caused a compaction of the linker DNA path [135] and incorporation of H1 generated considerable more compact fiber structures of nucleosomal arrays [8]. This is probably linked to its effect in reducing the opening angle between the two linker DNA arms.

1.4 Nucleosome remodeling

Beside the maintenance of DNA packaging a major task of chromatin is to regulate the activity of specific genes. Genes, that have to be expressed, need to be made accessible to nuclear proteins, while genes, which have to be silenced, have to be rendered inac-

cessible. The local (de-)compaction of chromatin is determined by the condensation of the nucleosomes into the higher-order structure, which then controls the accessibility of gene loci to the nuclear transcription machinery.
It is assumed that this packaging is largerly controlled at the level of individual nucleosomes. The processes that alter the structure of the histone-DNA interaction are commonly referred to as nucleosome remodeling. These include modifications of the DNA and the histone proteins, the incorporation of histone variants and the translocation of the octamer along the DNA [51, 6]. A controlled alteration of nucleosome structure is vital for the cell's proliferation and differentiation program. Uncontrolled perturbations lead to severe malfunction and diseases [37, 16].

1.4.1 ATP-dependent chromatin remodeling

Generally all activities that alter the DNA-histone interactions within a nucleosome are commonly referred to as nucleosome remodeling. These can include repositioning of the octamer along DNA (sliding), removal or exchange of histone components and the modification of DNA and octamer [17, 51]. Upon octamer sliding DNA sites previously occluded by the octamer are transferred into the accessible linker DNA region. Nucleosomes were found to be mobile per se, where sliding of the octamer was observed at elevated temperatures [53, 111]. Factors that modulated transcription activity *in vivo* such as binding of H1 were found to alter the intrinsic nucleosome mobility [112], which indicates a close interplay between nucleosome mobility and transcription activation. From then on a variety of different enzyme complexes was found that catalyse these transitions in the nucleosome structure *in vivo* [7, 108, 89, 138]. Fueled by the hydrolysis of ATP, these factors can rearrange nucleosomes along the DNA. They mediate folding of the chromatin fiber by rearranging nucleosomes which were randomly deposited along newly synthesized DNA [146, 73]. Another example is the displacement of nucleosomes at promoters during gene activation (reviewed in [145]). Depending on the structure for their ATPase subunit these factors are classified into different groups [138, 6]. BRG1 and ISWI, the factors used in this study, are the core ATPases of the human SWI/SNF complex and the ISWI complex. Of special interest for this work is the observation that these core ATPases can exert nucleosome remodeling activity *in vitro* without being complexed to additional factors *in vivo*. These enzymes are expected to differ in the mechanism by which octamer translocation ic achieved [45] and have recently be reviewed with special focus on single molecule force experiments that aim to unravel the underlying processes [17].

Mechanism of remodeling

All ATPase subunits show a structural homology with the helicase SF2 protein family [52]. This suggests a common basis for their function, namely the generation of superhelical torsion in DNA [137]. This induces a stress on the DNA and triggers a sliding mechanism, the details of which are still under discussion.
A simple rolling of the DNA off the nucleosome is energetically not favorable, since it would imply a simultaneuous breakage of all contact points. Such a process would also

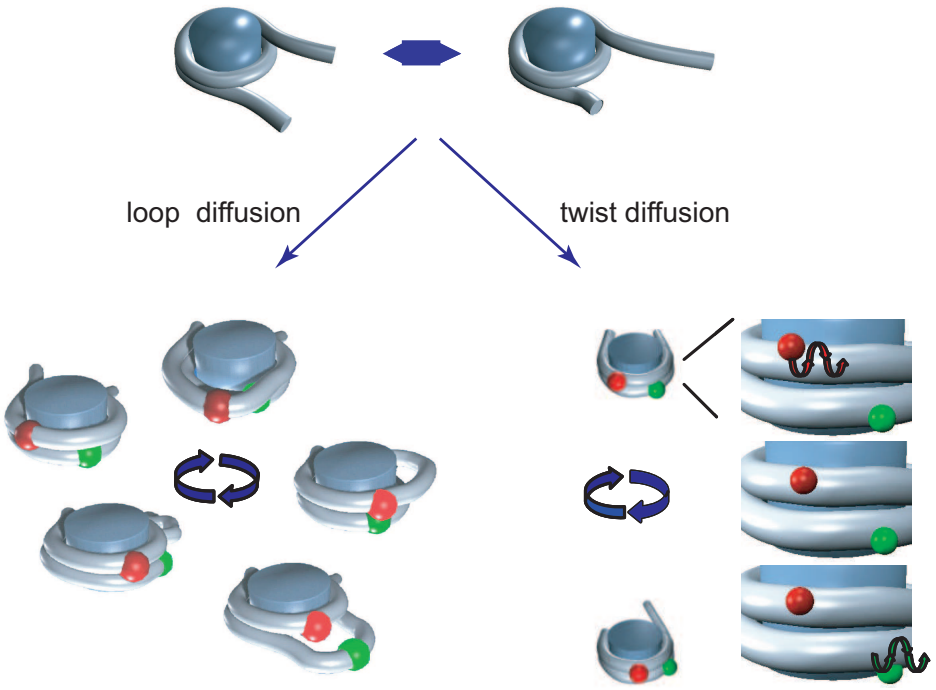

Figure 1.3: Illustration of different models that account for an octamer repositioning along the DNA. Left side: Loop propagation around the octamer. Right side: Twist diffusion of the DNA. Courtesy of F. Hauger.

rotate the octamer out of the plane of the DNA. Over the last decade various models have thus been proposed that describe the mobilisation of nucleosomes by a distortion of only a few DNA-histone interactions at a time. The two most frequently discussed models are summarized briefly and sketched in Figure 1.3.

Diffusion of a DNA bulge around the octamer

Spontaneous unwrapping of a short DNA stretch at the nucleosome ends is followed by a subsequent rebinding of more distal DNA stretches, forming a bulge of DNA in between. This bulge formation can either result from thermal fluctuations in the linker DNA or from an enzyme pushing more DNA towards the nucleosome as proposed by Längst et al. [89]. In a series of successive unbinding/rebinding events the loop migrates along the octamer surface until it is released on the other end of the nucleosome. By this multiples of 10 base pairs are translocated into the linker DNA. Various calculations were presented that predict the occurence of loop sizes between 40-60 base pairs to be most probable for larger DNA fragments [86, 51], which has also been supported by several experiments [46]. A recent study on the activity of the RSC remodeling factor from the SWI/SNF family showed that the octamer can be relocated along even shorter DNA fragments (of the order of 170 *bp*) [119]. This aspect will be important for the studies of BRG1, which is the catalytic subunit of the human SWI/SNF complex. The loop model has gained recent support by the observation of discrete step sizes

during octamer translocation [78, 5, 127] and the maintenance of remodeling ability of nicked DNA [88]. In recent AFM experiments loop intermediates were observed in nucleosomes formed on long superhelical DNA where the sample was fixed on a surface [13].

Twist defect propagation

The octamer translocation is described as the migration of a local twist defect around the nucleosome. From the crystallographic data the nucleosome was found to easily incorporate an over-/undertwist of 1 additional base pair [116]. These defects are likely to develop on the entry site of the DNA. They propagate along the octamer surface and emerge at the opposite end of the nucleosome effectively displacing 1 bp of DNA [85], [49, 7]. Experiments which showed that smaller step sizes ($< 10\,bp$) occured upon remodeling [53] were considered an indication for a twist diffusion process.

Whether or not both mechanisms occur exclusively during remodeling has not been satisfactorily answered. Recent calculations determined the energy barriers involved in both mechanisms to be of the same order of magnitude [121], so both mechanisms could coexist. An experiment that would discriminate between the discrete step sizes predicted in the loop mechanism and the 1 bp steps characteristic for a twist motion could provide direct evidence for one or the other model.

1.4.2 Posttranslational modifications of histones

In the early years histone proteins were merely considered as simple packaging material to organize the chromatin folding. Recent findings, however, discovered that octamers were much more than just static entities and put the octamer into the focus of reseach. It was shown, that histone proteins can exchange between nucleosomes [12] and that incorporation of variant histones is a frequent mean to alter the nucleosome stability (e.g. reviewed in [52].

The N-terminal tail domains found widespread notification as target sites for post-translational modifications, which emerged as important epigenetic markers for gene regulation. More than 30 positively charged residues can be modified in specific ways, like acetylation, methylation, phosphorylation or ubiquitination. Upto now more than 150 different modifications are known which mediate various regulatory signals. By changing the charge of the tails these modifications alter DNA-histone interactions and trigger structural changes by (de-)stabilising the nucleosome. In this way they influence the nucleosome-nucleosome interactions within chromatin fibers [126] and control the accessibility of chromatin during transcription.
A well studied example is the effect of histone acetylation [Wade1997a]. *In vivo*, a variety of enzymes were identified, which attach acetyl groups to specific lysine residues (HAT's: histone acetyl transferases), whereas other enzymes removed these functional groups (HDAC's: histone de-acetylases). Neutralisation of the positive tail charges causes a decondensation of the chromatin fiber and increased the accessibility of the

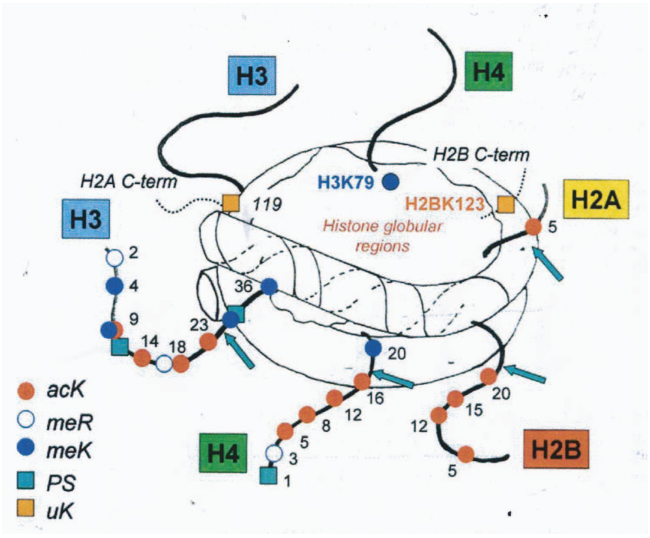

Figure 1.4: Modification of the histone tails as a mediator of various regulatory functions. The notation od the different sites is: acK: acetyl lysine, meR methyl arginine, meK methyl lysine, PS phosphoryl serine, uK ubiquitinated lysine. Adapted from [Turner2002].

chromatin to small nuclear proteins [60]. It generally correlates with gene activation and was found to be essential for the formation of transcriptionally active chromatin. The total picture of histone modification is much more complex though, since apparently the exact position of the modification along the tails determine whether the effect will be gene activating or repressive. Almost all chemical modifications can exert both functions and it is subject of current research to identify this "histone code" [126].
In recent years a close relationship has been established between ATP-dependent chromatin remodeling and histone modifications. Histone modification was found to be essential for various ISWI containing factors to remodel the nucleosome substrate [137]. These enzymes recognize modified tails via specific peptide domains such as the bromodomain. The complex interplay between these different aspects of remodeling is still far from being completely understood.

A lot has been learned about the structure of chromatin and its interactions with various nuclear proteins, but its intrinsic dynamics is still unresolved. The details of the mechanisms that lead to nucleosome repositioning or the change in conformation upon histone modification are subject of current research.
The extensions of the nucleosome confine the spatial dimensions, at which these processes occur, to a few nm. Conformational changes in this range are best monitored by using Fluorescence Resonance Energy Transfer (FRET). A substantial amount of FRET data is available that obtained valuable information from the whole ensemble of nucleosomes [91, 71, 14, 134, 135, 146]. This is now to be taken one step further, i.e. into the single molecule regime. The analysis of individual nucleosomes provides new insight into the mechanisms involved in nucleosome remodeling and will be subject of this thesis.

Chapter 2

Theory of single molecule detection

2.1 Molecular photophysics

2.1.1 Introduction

Fluorescence based detection of biomolecules generally requires labeling with specific reporter molecules. Although proteins contain several autofluorescent amino acids (tyrosine, tryptophane and phenyl alanine), their intrinsic fluorescence is essentially too weak to be useful for single molecule identification. Typical fluorescent dyes on the other hand are specifically designed to have a high excitation probability and a large quantum yield of fluorescence. These properties allow for efficient detection of the labeled biomolecule, even in the background of an excess of unlabeled species or background. The wavelength range at which the dye is excited and emits fluorescence depends on its electronic structure and the properties of the local environment. The basic processes involved in the photophysics of a fluorophore are described in terms of a Jablonski diagram as shown in Figure 2.1.

Depending on the total spin of all electrons Σ the electronic states are classified into triplet states T_i, where $\Sigma = 1$ and singulet states S_i, where $\Sigma = 0$. The index i denotes the i-th excited state of the molecule. Optical transitions by absorption or emission of photons are only allowed between states of equal spin coupling. A transition between T_i and S_j requires a flip of the total spin and is thus forbidden by the laws of quantum mechanics[1]. These processes are termed intersystem crossing (ISC) and occur at considerably lower rates compared to fast radiative transitions. The corresponding probability is very low due to the coupling of spin and angular momentum. For the T_1 triplet state a radiative decay can only occur by a spin-flip, and T_1 thus has a prolonged lifetime (few μs).
The inherent vibronic and rotational motion of the molecule in each electronic state gives rise to a series of discrete substates which due to the thermal broadening smear out to form a band structure. Optical transitions can occur in a wide range of wave-

[1]In quantum mechanics only probabilities for a given process to occur can be calculated. For a forbidden transition the probability is very low which results in low transition rates. The initial state from which the transition occurs has a considerably longer lifetime

lengths determined by the absorption spectrum. In fluorescence spectroscopy only the transition from the electronic ground state S_0 into the first excited singulet state S_1 is of relevance. The absorption of a photon levels the molecule into a higher vibronic substate of S_1. Within $10^{-13}\,s$ the molecule relaxes into the vibronic ground state of S_1 via internal conversion of energy. S_1 is energetically higher than S_0 and therefore instable. It will deexcite by one of the following processes:

1. Transition into a lower vibronic state of S_0 by emission of a fluorescence photon.

2. Non-radiative transition into a higher vibronic state of S_0, followed by fast internal conversion into the vibronic ground state of S_0.

3. Symmetry forbidden transition into T_1, which has a much longer lifetime compared to S_1. A transition back into S_0 occur either by collisions (non-radiatively) or by emission of a delayed photon (phosphorescence).

4. At high irradiance an occupation of higher excited states (S_n, T_n) is possible by absorption of a second photon from S_1 or T_1. Those states have very short lifetimes and do not contribute to the fluorescence process. They are involved in irreversible reactions which lead to a decomposition of the fluorophore.

5. Chemical reactions of the excited state with its environment. The reaction products generally have different photophysical properties. These processes strongly depend on the excitation intensity since they start from any excited state and are proportional to its occupation density.

Photoreactions constitute a serious problem in single molecule spectroscopy. They limit the time a molecule can be observed to a few seconds and restrict the total number of emitted photons to $10^5 - 10^6$. In Fluorescence Correlation Spectroscopy (FCS) systematic deviations in the autocorrelation curve are introduced by photobleaching. The premature termination of fluorescence emission leads to apparently smaller diffusion times and a change in the correlation amplitude. Furthermore it limits the signal-to-noise ratio by reducing the total fluorescence output. Suitable dyes for single molecule spectroscopy should have a low probability of photodestruction in order to survive as many excitation cycles as possible.

2.1.2 Kinetic description of photophysical processes

The photophysical properties of a dye molecule, e.g. its photobleaching probability and saturation behavior, are described using a term scheme as shown in Figure 2.1. Most theoretical work include 5 energy levels which are [41]:

- electronic ground state S_0
- first excited singulet state S_1
- first excited triplet state T_1

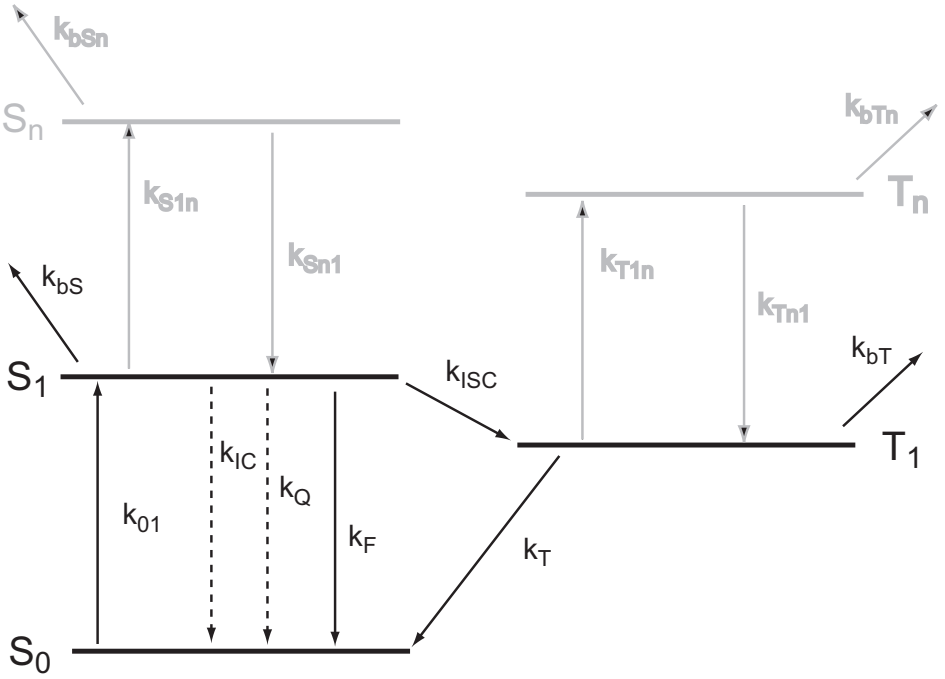

Figure 2.1: Jablonski diagram showing the electronic ground state (S_0) and the first excited singulet and triplet states (S_1 and T_1). Higher order states, (S_n and T_n), only contribute at larger intensities and are shown in light grey. For simplicity the vibronic and rotational substates are omitted. Arrows indicate the transition between state i anf f which can occur within the fluorophore. The corresponding kinetic rates are defined as k_{if}. We have: $k_{10} \equiv k_F$: rate of fluorescence from S_1, k_{bX}: bleaching events from state X, k_{ISC}: intersystem crossing, k_{IC}: internal conversion, k_Q: quenching processes (the latter two were not considered in the context of photokinetics). The index n denotes any higher state in the triplet (T) or singulet (S) system.

- higher-order singulet states S_n
- higher-order triplet states T_n.

Light absorption that causes a transition from an initial state i to a final state f is described by transition rates $k_{(T)if}$. The index T is added if the process occurs between triplet states. The parameters $k_{(T)if}$ depend on the irradiance and the corresponding absorption cross sections: $k_{(T)if} = I_0(\lambda/hc)\sigma_{(T)if}$. c and h denote the velocity of light and the Planck constant, while λ is the wavelength of the incident light.
The kinetic rates for deactivation by internal conversion (IC), k_{IC}, intersystem crossing (ISC), k_{ISC}, and fluorescence (F), k_F, determine the lifetime of the excited state S_1, according to

$$\tau_0 = \frac{1}{k_0} = \frac{1}{k_{IC} + k_{ISC} + k_F}, \tag{2.1}$$

if no additional quenching processes are involved. The lifetime τ_0 characterises the temporal decay in fluorescence.

For each process a quantum yield describes its relative strength which is defined as the ratio of the corresponding kinetic rates. For fluorescence emission we have

$$\Phi_F = \frac{k_F}{k_0} = k_F \tau_0 \tag{2.2}$$

while for the population of the triplet state

$$\Phi_{ISC} = \frac{k_{ISC}}{k_0} = k_{ISC} \tau_0. \tag{2.3}$$

Similar rates are defined for the remaining processes shown in Figure 2.1 : k_T : transition from T_1 to S_0; k_{Tn1} : transition from T_n to T_1 and k_{Sn1} : transition from S_n to S_1. The rates k_{bS}, k_{bT}, k_{bSn}, k_{bTn} describe irreversible photoreactions from the corresponding states.

An additional source for depletion of the excited states are quenching processes. For example the S_1 state is efficiently quenched by photoinduced electron transfer reactions while triplet states can undergo bimolecular reactions with dissolved oxygen in the buffer ([41] and references within).
All quenching processes depend on the concentration of the quencher molecule and reduce the fluorescence quantum yield and lifetime of S_1 according to $1/\tau' = k'_0 = k_0 + k_{Q_S}[Q]$ and $k'_T = k_T + k_{Q_T}[Q]$.

The photophysical parameters are quantified by occupation probabilities $S_i(t)$ and $T_i(t)$ under steady state conditions. For each state a rate equation is defined under quasi constant illumination and negligible bleaching, i.e. $k_{bX} \ll k_0$, k_{IC}, k_{ISC}:

$$\begin{aligned}
\dot{S}_0(t) &= -k_{01} S_0(t) + k_0 S_1(t) + k_T T_1(t) \\
\dot{S}_1(t) &= k_{01} S_0(t) - (k_0 + k_{1n}) S_1(t) + k_{Sn1} S_n(t) \\
\dot{T}_1(t) &= k_{ISC} S_1(t) - (k_T + k_{T1n}) T_1(t) + k_{Tn1} T_n(t) \\
\dot{S}_n(t) &= k_{1n} S_1(t) - k_{n1} S_n(t) \\
\dot{T}_n(t) &= k_{T1n} T_1(t) - k_{Tn1} T_n(t)
\end{aligned} \tag{2.4}$$

where $S_0(t) + S_1(t) + T_1(t) + S_n(t) + T_n(t) = 1$.
$\dot{X}$ denotes the first derivative of X w.r.t. time. At moderate laser intensities the occupation of higher excited states T_n und S_n can be neglected, since they can only be accessed from S_1 and T_1 by absorption of another photon during the lifetime of these states. The 5-level scheme therefore reduces to a more convenient 3-level scheme with only the first excited states and S_0 contributing.
The effect of high irradiances and the influence of the higher electronic states is considered in the literature, e.g. in [15]. Depending on the fluorophore used variations from the 3-level system occur at intensities of a few $100\,kW/cm^2$. In this work the laser intensity was considerably lower.

3-level scheme

Under steady state conditions the occupation probabilities are constant, i.e. all temporal derivatives vanish, $\dot{S}_i = 0$.

$$\begin{pmatrix} 0 \\ 0 \\ 0 \end{pmatrix} = \begin{pmatrix} -k_{01} & +k_0 & +k_T \\ +k_{01} & -k_0 & 0 \\ 0 & +k_{ISC} & -k_T \end{pmatrix} \cdot \begin{pmatrix} S_0(t) \\ S_1(t) \\ T_1(t) \end{pmatrix} \tag{2.5}$$

Using the tools of matrix algebra this equation system is readily solved and we obtain [41]:

$$S_0^{eg} = \frac{k_0 k_T}{k_{01}(k_{ISC} + k_T) + k_0 k_T} \tag{2.6a}$$

$$S_1^{eg} = \frac{k_{01} k_T}{k_{01}(k_{ISC} + k_T) + k_0 k_T} = \frac{k_{01}}{k_0} \cdot S_0^{eg} \tag{2.6b}$$

$$T_1^{eg} = \frac{k_{01} k_{ISC}}{k_{01}(k_{ISC} + k_T) + k_0 k_T} = \frac{k_{ISC} k_{01}}{k_T k_0} \cdot S_0^{eg} \tag{2.6c}$$

2.1.3 Photodestruction and survival probability

Irreversible photoreactions damage the fluorophore and cause a termination of photon emission. Analogous to equation 2.2 a quantum yield of photobleaching can be defined as

$$\Phi_b = \frac{\text{number of bleached molecules}}{\text{total number of absorbed photons}}$$

All absorbed photons are to be considered, including those that might populate the higher excited states. A different quantity which is more appropriate is the probability for photodestruction, p_b, defined as

$$p_b = \frac{\text{number of bleached molecules}}{\text{average number of molecules in } S_1}$$

For a 3-level system and one photon excitation p_b and Φ_b are identical [38].
Bleaching of the molecule occurs from T_1 and S_1 only and leads to a monoexponential decay of the concentration of intact fluorophores, $C(t) = C(0) \cdot \exp(-k_z t)$. The probability for bleaching depends on the steady state population of S_1 and T_1, where

$$\frac{dC(t)}{dt} = -k_{bS} S_1^{eg} C(t) - k_{bT} T_1^{eg} C(t) \tag{2.7}$$

with the kinetic rate constants of bleaching, k_{bT} and k_{bS} (see Figure 2.1). The macroscopic decay constant k_z is thus related to k_{bS} und k_{bT} according to $k_z = -k_{bS} S_1^{eg} - k_{bT} T_1^{eg}$. With equation 2.6 we obtain

$$k_z = \left(k_{bS} + k_{bT} \cdot \frac{k_{ISC}}{k_T} \right) S_1^{eg} \tag{2.8}$$

In the limit of low irradiance (3-level system) the probability of photobleaching is independent on the laser intensity. Only at high irradiances an explicite dependence on the laser intensity has to be taken into account.

Survival probability

The probability $P(n)$ to survive n absorption steps and being bleached after the $(n+1)^{st}$ absorption is given by a geometric distribution $P(n) = (1 - p_b)^n \cdot p_b$ with expectation value

$$m = \frac{1 - p_b}{p_b} \approx \frac{1}{p_b} \tag{2.9}$$

, since $p_b \ll 1$. The average number of survived cycles is roughly given by the inverse of the bleaching probability. For typical fluorophores p_b is of the order of 10^{-5}.
The time span during which a molecule remains intact under quasi continuous excitation determines the net photon yield. The probability that a molecule is bleached after a time t is given by $P(t) = k_z \cdot exp(-k_z t)$, with the macroscopic decay constant k_z defined in 2.8 . The probability for a fluorophore to bleach within a time interval T is calculated as the integral sum

$$P_{dec}(T) = \int_0^T P(t')dt' = 1 - exp(-k_z T). \tag{2.10}$$

It follows that the probability of surviving the time span T is

$$P_{intact}(T) = 1 - P_{dec}(T) = exp(-k_z T) \tag{2.11}$$

P_{intact} decays exponentially with time, and the probability to photobleach is highest for the first excitation cycle.

2.1.4 Total fluorescence signal under continuous excitation

The number of emitted photons will be proportional to the steady state population S_1^{eg} and the fluorescence quantum yield of the fluorophore. The emission is limited by saturation processes, photobleaching reactions and the finite observation time t_0.

Finite observation times

In the case of a finite observation time t_m and negligible photobleaching we obtain

$$N_\gamma = k_F S_1^{eg} t_m = \Phi_F k_0 S_1^{eg} t_0 \tag{2.12}$$

If photobleaching has to be considered the emission is reduced by the probability to survive the observation period t_0. In this case equation 2.11 yields

$$\begin{aligned} N_\gamma &= \Phi_F k_0 S_1^{eg} t_0 \left(\frac{1}{t_0} \int_0^{t_0} P_{intact}(t')dt' \right) \\ &= \frac{\Phi_F}{p_b} \left(1 - exp(-k_z t_0)\right). \end{aligned} \tag{2.13}$$

The number of emitted photons strongly depends on the laser intensity, since the intensity dependent absorption rate k_{01} determines the occupation probability S_1^{eg}.

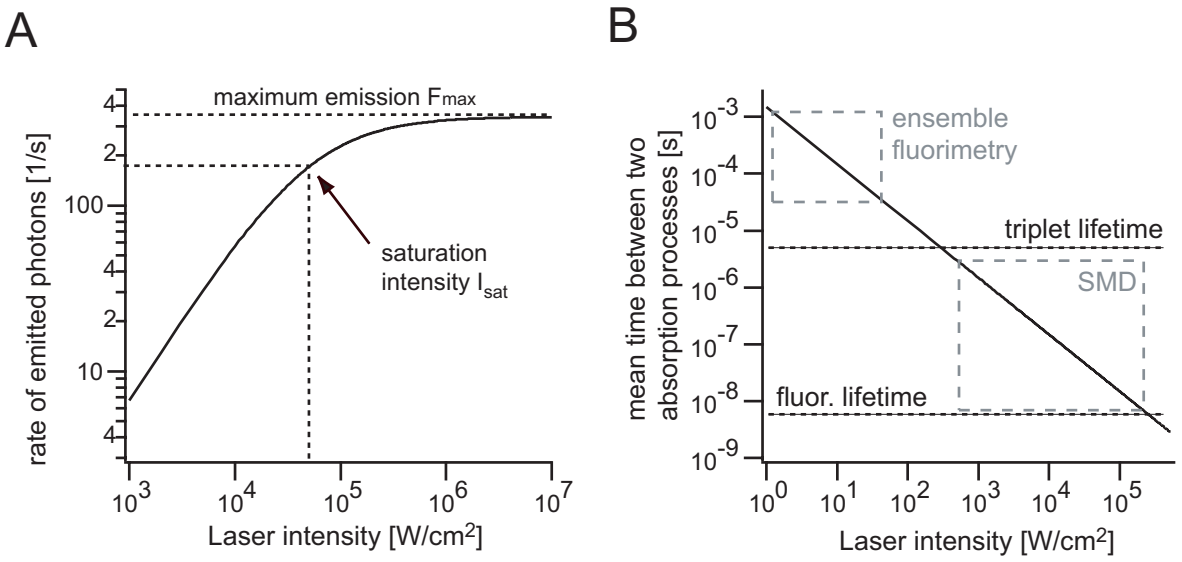

Figure 2.2: **A**: Emission rate of a typical fluorophhore as a function of applied laser intensity as calculated from equation 2.12. The following photokinetic parameters were used: $\sigma_{01} = 2.71 \cdot 10^{-16}\, cm^2$; $k_{ISC} = 1.2 \cdot 10^6\, s^{-1}$, $k_T = 1.8 \cdot 10^5\, s^{-1}$ and $\tau = 3.8\, ns$. **B**: Average time interval between two successive photon absorption processes as a function of laser intensity. At intensities used for bulk fluorimetry the mean time between two absorption processes exceeds the average triplet state lifetime and triplet effects need not to be considered. At intensities typical for SMD experiments the time between two successive absorption processes is considerably lower then the triplet state lifetime, and T_1 starts to accumulate.

The dependence of N_γ/t_0 on I_0 for a typical fluorophore like Alexa488 is plotted in Figure 2.2A . For low irradiance the number of emitted photons increases linearly with laser intensity. Deviations occur at intensities at which saturation of the fluorophore sets in. The laser intensity at which the rate of absorption equals the rate of de-excitation is called the saturation intensity, I_{sat}, which relates to the photokinetic rates by

$$I_{sat} = \frac{k_0 k_T}{k_{ISC} + k_T} \frac{h\nu}{\sigma_{01}}. \tag{2.14}$$

The corresponding emission rate $F_\gamma(I_{sat})$ equals half the maximum emission rate (F_{max}). Typical values for I_{sat} are of the order of a few ten kW/cm^2.
Panel B depicts the average time between two successive absorption processes as a function of the laser intensity. At intensities used for bulk fluorimetry, the mean time between two absorption processes exceeds the average triplet state lifetime and no triplet effects have to be considered. At intensities typical for SMD experiments, however, photons are absorbed faster than the the triplet state lifetime and T_1 starts to accumulate. At intensities above $200\, kW/cm^2$ the time between successive absorption processes is comparable to the lifetime of the S_1 state. Saturation due to triplet state accumulation will occur at considerably lower intensities.

Infinite observation times

In the limit of infinitely long observation times, e.g. for immobilised molecules, the photon yield is ultimately limited by photodestruction. N_γ equals the number of survived absorption cycles times the probability to emit a photon per each absorption step.

$$N_\gamma = \frac{\Phi_F}{m} = \frac{\Phi_F}{p_b} = \frac{k_F}{k_b}, \tag{2.15}$$

Apparently N_γ is independent of the quantum yield. A reduction in Φ_F, for example caused by quenching of the fluorophore, leads to lower emission rates, but also reduces the probability for photobleaching and increases the survival time. This is often observed when stabilising agents are used to prevent premature photobleaching of the fluorophore. Although the photostability is enhanced no net gain in photon emission is observed [70, 41]. It is important to find stabilising agents that do not quench the fluorophore but prevent accelerated photobleaching as discussed in section 4.2.

2.2 Confocal single molecule spectroscopy

Single molecule experiments in diffusion often utilize a confocal microscope setup like the one described in section 3.2. In the focus of a laser beam the fluorophore is continuously excited and cycles between S_1, T_1 and S_0. The fluorescence emission is imaged onto the detector, where it generates an electronic output signal. The detected signal can no longer be described by equations 2.12 and 2.13. The finite size of the pinhole and transmission losses in the optical system significantly reduce the number of detected photons and the conditions of constant excitation do not hold for several reasons:

1. The inhomogeneous excitation profile results in a position-dependent laser intensity.
2. The various diffusion trajectories for individual molecules result in a distribution of observation times and burst sizes. Most molecules will diffuse in the peripheral region of low intensity yielding low burst sizes only.
3. Raman- and Rayleigh scattering, as well as background from impurities, limit the signal-to-noise level.

2.2.1 Excitation profile and fluorescence generation

In the ideal case, the excitation profile is defined by the spatial extent of a diffraction limited focus of a Gaussian shaped laser beam (TEM_{00} mode). The radial intensity distribution is described by a two-dimensional Gaussian profile, while the axial intensity follows a Lorentzian distribution [114]:

$$I(x,y,z) = I_0 \cdot W_{gl}(x,y,z) = I_0 \cdot \frac{w_0^2}{w(z)^2} \cdot exp\left(-2\frac{x^2+y^2}{w^2(z)}\right) \tag{2.16}$$

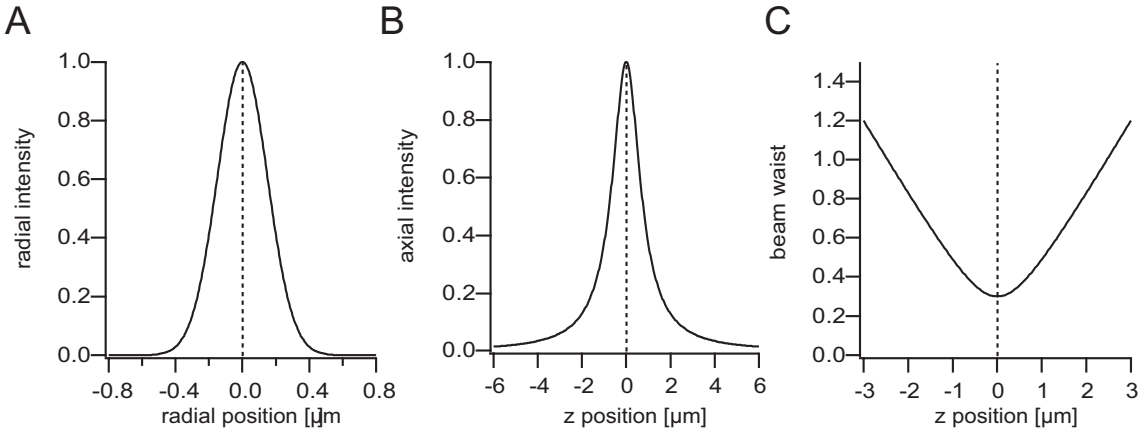

Figure 2.3: Schematic illustration of the intensity profile of the laser focus in radial (**A**) and axial (**B**) distance from the focus center (0,0,0). Panel **C** shows the beam waist w(z) as a function of axial distance.

$W_{gl}(x, y, z)$ is the normalised 3D Gau"s-Lorentz profile, with $w^2(z) = w_0^2 + (\lambda/n\pi w_0)^2 z^2$ and $I_0 = P_{laser}/A_{focus} = 2P_{laser}/(\pi w_0^2)$. The cross section area is calculated as $A_{focus} = \int_{-\infty}^{\infty}\int_{-\infty}^{\infty}(exp(-2(x^2+y^2)/w_0^2))\,dxdy$. λ is the wavelength of the laser light and $w(z)$ denotes the beam waist at axial position z. Figure 2.3 shows the intensity distribution in axial and radial direction, as well as the dependence on the beam waist from the axial position.

For large values of z $w(z)$ is linearly proportional to z, as expected from geometric ray optics. In the vicinity of the focal spot, where $z \approx \lambda$ (which is referred to as the Rayleigh zone), a minimal beam waist $w_0 = 0.61\lambda/\mathrm{NA}$ is generated. The numerical aperture $NA = n \cdot sin(\alpha_{obj}/2)$ defines the extent of the laser spot in the focal plane, where n is the refractive index of the medium and α_{obj} the opening angle of the objective lens (see Figure 2.4).

2.2.2 Fluorescence detection and intermediate optics

Geometric collection efficiency of the objective lens

Fluorescence photons are emitted isotropically in all directions. Due to its finite aperture the objective lens only collects part of these photons. Its geometric collection efficiency is given by the solid angle from which photons can be collected, Ω_{obj}. This quantity depends on the numerical aperture of the objective and is given by

$$\Psi_{obj} = \frac{\Omega_{obj}}{\Omega_{total}} = \frac{\Omega(\alpha_{obj})}{\Omega(\alpha = 180)} = \frac{1}{2}\,(1 - cos(\alpha_{obj})) \tag{2.17}$$

The objective lens used in this work (UPLANAPO, $60x/1.2W$ from Olympus) has a numerical aperture of $NA = 1.2$. For aqeuous solvents with $n = 1.33$ the opening angle is given as $\alpha_{obj} = 64.5$ and $\Psi_{obj} = 0.25$. Only 25 % of all emitted photons will be transmitted by the objective.

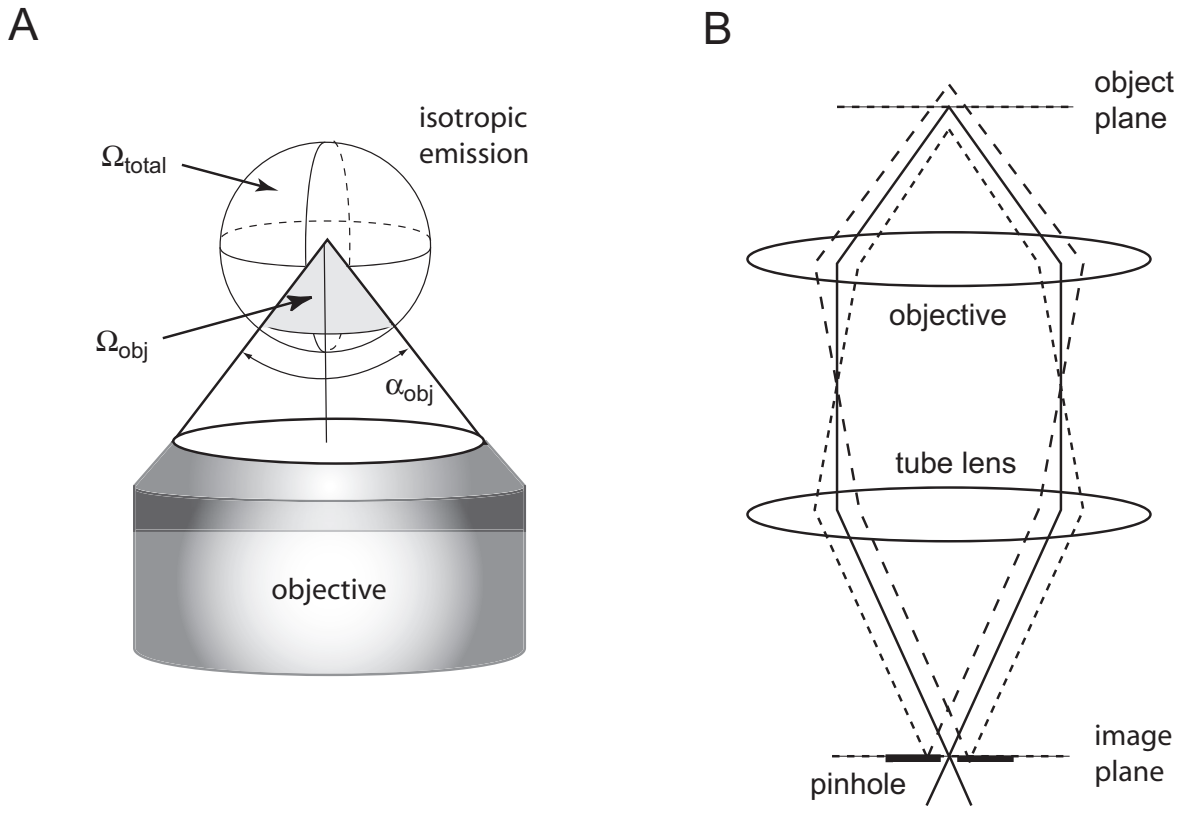

Figure 2.4: **A**: Definition of the geometric collection efficiency Ω_{obj} of the objective lens. α_{obj} is the opening angle of the objective lens. **B**: The confocal principle: Insertion of a pinhole in the conjugated image plane of the microscope (objective + tube lens) efficiently rejects out-of-focus light (dotted and dashed lines), while light emerging from the focal plane is transmitted through the aperture.

Spatial imaging properties, Point Spread Function (PSF)

The intermediate optics image the transmitted photons onto the pinhole aperture located in a conjugated image plane. The corresponding radial intensity distribution is determined by the *point spread function* PSF. The PSF describes the intensity distribution $I(\mathbf{r}')$ in the image plane which arises from a point source located at point $(\mathbf{r}, z)$ in object space.

$$PSF(\mathbf{r}, \mathbf{r}', z) = \frac{circ(|(\mathbf{r} - \mathbf{r}')|/R(z))}{\pi R(z)^2} \tag{2.18}$$

with $circ(x) = 1$ for $x \leq 1$ and $circ(x) = 0$ elsewhere.
The radius of the spot in the image plane, $R(z)$, is a function of the axial distance of the point emitter from the object plane, z, and is given by $R(z) = R_0^2 + z^2 tan(\alpha_{obj})$, with $R_0 = 1.22\lambda/NA$. A point emitter in the object plane is imaged into a circular area whose extent depends on the axial position z. The smallest image size is obtained for objects located in the focal plane.

Collection Efficiency Function (CEF)

The pinhole has a finite diameter and only those photons will be transmitted which are imaged within its aperture. Its transmission function T_{ph} is defined as

$$T_{ph}(\mathbf{r}') = \frac{circ(|\mathbf{r} - \mathbf{r}'|)}{s_0}, \tag{2.19}$$

where s_0 denotes the projection of the pinhole radius into the object plane, $s_0 = d_{ph}/2M$. M is the magnification of the intermediate optics. It is noted that for the UPLANAPO objective the value $(60x)$ is standardized for a tube lens of $f = 180\,mm$. The tube lens used in the IX70 microscope has a focal length of $f = 190\,mm$ and the effective magnification[2] is enlarged to $M = 60x \cdot 190/180 = 63.3x$.
PSF and pinhole transmission function are combined into the collection efficiency function $CEF(\mathbf{r}, z)$ [81]. This quantity describes the fraction of photons emitted from point (**r**,z) that are transmitted through the pinhole.

$$CEF(\mathbf{r}, z) = \frac{1}{\Delta} \int\int T(\mathbf{r}') \cdot PSF(\mathbf{r}, \mathbf{r}', z) d^2\mathbf{r}' \tag{2.20}$$

Δ is a normalisation factor with $\Delta = |min(s_0, R_0)|^2/R_0^2$. In single molecule experiments the pinhole diameter is usually chosen larger than the corresponding size of the laser focus. In the image plane, i.e. $s_0 > R_0$ and $\Delta = 1$.

Molecular Detection Function (MDE)

To describe the photon flux on the detector the probability that a photon, which is emitted at point $(\mathbf{r}, z)$, is transmitted by the pinhole, i.e. $CEF(\mathbf{r}, z)$, has to be combined with the probability of the photon being emitted itself.
The position dependence of the fluorescence flux is determined by the inhomogeneous excitation profile of the laser and the steady state occupancy S_1^{eg}. The molecular detection efficiency $MDE(\mathbf{r}, z, I_0)$ describes the probability with which a photon is generated at point $(\mathbf{r}, z)$ and then imaged into the open aperture of the pinhole.

$$MDE(\mathbf{r}, z, I_0) = CEF(\mathbf{r}, z) \cdot S_1^{eq}(I(\mathbf{r}, z)) \tag{2.21}$$

For the 3-level system $S_1^{eq}(I(\mathbf{r}, z))$ is given by equation 2.6. For intensities below the saturation limit the rate of absorption is smaller than the inverse lifetime $(\sigma_{01}(\lambda/hc)I_0 \ll k_0 = 1/\tau_0)$ and the MDE can be approximated by

$$MDE(\mathbf{r}.z) = \frac{\sigma_{01}(\lambda/hc)}{k_0} \cdot [I_0 \cdot CEF(\mathbf{r}, z) \cdot W_{gl}(\mathbf{r}, z)]\,, \tag{2.22}$$

where $W_{gl}(\mathbf{r}, z)$ denotes the three dimensional laser focus, equation 2.16. A convenient approximation for the MDE is a three dimensional Gaussian volume, which is often used

[2] We have $M' = f_{TL}/f_{obj} = (f_{TL}/180) \cdot (180/f_{obj}) = M_{nominal} \cdot f_{TL}/180$

for FCS experiments as described below. $CEF(\mathbf{r}, z)$ and excitation profile $W_{gl}(\mathbf{r}, z)$ are combined to an effective volume $W_g(\mathbf{r}, z)$ given by

$$W_g(\mathbf{r}, z) = CEF(\mathbf{r}, z) \cdot W_{gl}(\mathbf{r}, z) = exp\left(-\frac{2\mathbf{r}^2}{w_0^2}\right) \cdot exp\left(-\frac{2z^2}{z_0^2}\right). \tag{2.23}$$

Here, w_0 and z_0 denote the semiaxes of the ellipsoidal observation volume. Both quantities are linked by the structure parameter, $\kappa = z_0/w_0$, that describes the geometric shape of the volume. The size of this effective volume is given as

$$V_{eff} = \pi^{3/2} w_0^2 z_0 \tag{2.24}$$

which emerges from the FCS theory[3] [102]. The precise value of the focal volume agrees within a factor of 1.3 with the volume of a rotational ellipsoid with semiaxes (w_0, w_0, z_0).
Under high intensities a decrease in the central part of the MDE is observed due to saturation of the fluorophore. In the focal spot the laser intensity is highest and saturation effect are strongest. At the periphery fluorophores do not saturate and still contribute to the fluorescence. Thus a distortion of the MDE changes the effective volume altering both diffusion time and mean particle number in the focus [62].

Influence of the pinhole aperture

Differences between $W_g(\mathbf{r}, z)$ and the true volume are mainly observed in the axial component where the Lorentzian shape of the excitation focus is not matched by the Gaussian approximation. Largest deviations are obtained at very large and very small pinhole diameters [114]. To validate a 3D Gaussian approximation the pinhole size has to be chosen carefully. As discussed in [38, 114], an optimal pinhole size for single molecule applications is of the order of $1.5\, w_0 < s_0 < 2\, w_0$. For a beam waist of $w_0 = 0.25\ \mu m$ and a magnification of $M = 63.3x$ we have $47\, \mu m < d_{ph} < 63\, \mu m$. If the pinhole diameter is chosen too large the background level is unneccessarily increased. For a pinhole much smaller than the optimum value diffraction effects limit the useful fluorescence signal.

2.2.3 Analytical description of the fluorescence signal and burst size distribution of single molecules

With the above definitions equation 2.12 can be modified to be valid for a confocal experiment. For brevity only the final results are presented. For a detailed description the reader is referred to [56].

[3]The amplitude of the autocorrelation function at time 0, G(0), is inversely proportional to the mean particle number in the focus, $G(0) =< F^2 > / < F >^2 \propto 1/N = 1/cV_{eff}$. This implies that $V_{eff} \propto < F >^2 / < F^2 > \propto < W >^2 / < W^2 >$.

Effective excitation intensity

If photodestruction is neglected the rate of fluorescence emission is given by

$$F = \Phi_F k_0 \frac{N}{V_g} \Psi_F \int\int\int MDE(\mathbf{r}, z, I_0)\, d^2\mathbf{r}dz. \tag{2.25}$$

N/V_g denotes the particle concentration in the focus. For a single molecule obviously N = 1. Equation 2.25 has no analytical solution and a simplified model has to be used for a quantitative description. An often used approximation is a cylindrical volume of constant intensity I_0, radius $R = b \cdot w_0$ and height h [15]. This profile has a cross section $A_{focus} = \pi b^2 w_0^2$ and a mean intensity $I = I_0/2b^2$.
The parameter b has to be chosen properly to correctly simulate the real conditions. Under single molecule conditions the approximation $b = 1$ and $I = I_0/2$ appeared to be the best choice [143, 38].

Mean number of emitted photons

The mean number of emitted photons can be calculated similar to equation 2.12 or 2.13. The observation time t_0 is replaced by the mean residence time in the focal volume, $t_0 \rightarrow \tau_0 = w^2/4D$. Without photobleaching we obtain

$$N(I_0/2) = \Psi_D \Phi_F k_0 S_1^{eg}(I_0/2)\tau_0 \tag{2.26}$$

while in the case of photobleaching

$$N(I_0/2) = \Psi_D \frac{\Phi_F}{p_b(I_0/2)} \left[1 - exp\left(-p_b \sigma_{01} \frac{I_0}{2} \tau_0\right)\right] \tag{2.27}$$

The factor Ψ_D describes the detection efficiency of the optical system. It combines the transmission properties of the objective and the various filters and the detection sensitivity of the photodiodes. For a confocal setup this quantity is generally below 5 % [9]. The corresponding emission rates are calculated as $F = N_\gamma/\tau_0$.

Burst size distribution

Beside a mean photon yield the actual distribution of burst sizes is important in a single molecule experiment.
The total detected signal comprises of a background signal and the fluorescence from the particle. The background follows a Poissonian distribution[4], whereas the fluorescence emission shows no-Poissonian character. For the calculation of the single molecule burst distribution the spatial variation of the MDE and the distribution of diffusion trajectories have to be considered. A molecule diffusing in the periphery of the focus will emit fewer photons than a molecule passing through the center of the focus. An

[4]The major contribution of background arises from Raman scattering by water molecules. In a 1 fl volume there are about $1.7 \cdot 10^{10}$ water molecules in the focus. At the typical scattering cross sections being $\sigma_{Raman} \approx 10^{-28}\, cm^2$ and the large amount of molecules involved the conditions for Poissonian statistics are fulfilled.

exact treatment involves the use of a path integral formalism [43]. A mathematical less involved approximation was presented by Fries et al. [56], where the focus was dissected into small volume shells of constant intensity. A molecule within a given volume shell k will emit N_k photons per second. The probability for a particle to emit N photons equals the probability with which the particle is found in that corresponding volume shell, which is given by the respective volume size. The BSD shows a steep increase towards low burst sizes and a quasi monoexponential decay for intermediate burst sizes, compare also to Figure 3.10

Signal-to-background ratio

While the fluorophore saturates at high irradiance the background level scales linearly with intensity. Moreover, the background rate is proportional to the size of the excitation volume, so $B \propto I_0 w^3$. The ratio of the fluorescence to background defines the quality of the experiment:

$$\frac{F}{B} \propto \frac{N_F(I_0/2)/\tau_0}{I_0 w_0^3)} \propto \frac{1}{w_0^5} \tag{2.28}$$

A large F/B ratio is essential to ensure a good discrimination of the fluorescence bursts from the background. Owing to the strong increase of background with focal volume size an increase in effective volume (and in diffusion time) is only reasonable if the gain in photons $N_F \propto \tau_0 \propto w_0^2$ is not on the expense of a too large background level $N_B \propto B\tau_0 \propto w_0^5$.

2.2.4 Multiparticle events

In a confocal experiment we cannot exclude the simultaneous presence of more than one particle in the focus. For a mean number of N particles in the focus the probability of simultaneously observing n molecules is determined by Poissonian statistics:

$$P_n(N) = \frac{N^n}{n!} \cdot exp(-N). \tag{2.29}$$

So $P(0) = exp(-N)$, $P(1) = N \cdot exp(-N)$, $P(2) = 0.5 \cdot N^2 \cdot exp(-N)$ and so forth. To reduce the probability of multiparticle events a small value of N is favorable which implies a highly diluted sample. If N becomes too small the probability of observing any fluorescence signal is considerably reduced. This prolongs the time required to acquire enough events for a reasonable analysis.
Those events, where n molecules diffuse through the volume consecutively are also undesired and should be minimised.
The probability of finding n molecules in the focus within a time period T depends on the mean diffusion time of the particles,

$$P_n(T, N, \tau_0) = \frac{(N(T/\tau_0))^n}{n!} \cdot exp(-(N(T/\tau_0)) \tag{2.30}$$

The probabilty is significantly enhanced if $T \gg \tau_0$. This proves to be problematic for the burst selection process of single molecule events. If the effective event duration

becomes too large these consecutive events might become considered a one particle event.
At low particle concentrations the probability for a second particle to enter the focus after the previous molecule diffused out is lower than the probability for the same particle to re-enter the focus. A time T_m can be defined, during which the detected signal can be considered to arise from the same molecule [55]. T_m is related to the mean diffusion time τ_0, the volume size, V, and the particle concentration,, C_m by

$$T_m = \frac{\tau_0}{C_m N_A \Delta V \cdot exp(-C_m N_A \Delta V)} \equiv \frac{\tau_0}{\langle N \rangle \cdot exp(\langle N \rangle)}, \tag{2.31}$$

where the product $C_m N_A \Delta V$ equals the mean particle number in the focus (N_A is the Avogadro constant). Experimental conditions have to be chosen such that the mean event duration is lower than T_m. Otherwise the presence of multiparticle events cannot be excluded (see section 4.4).

2.3 Theory of Resonance Energy Transfer

Resonance energy transfer is an additional pathway by which the S_1 state of a fluorphore is depleted. In the presence of a second fluorophore an induced dipole-dipole interaction leads to transfer of excitation energy from the donor to the acceptor. The amount of energy transferred depends on the distance between donor and acceptor, which rendered FRET a suitable molecular ruler for distances between $2 - 10\,nm$.
In the classical work of Perrin the fluorophores were described as classical dipoles where the acceptor interacts via the electromagnetic field of the donor and vice versa. Perrin's theory was based on the assumption that both dipoles have exactly the same resonance frequency. This had to be modified in the later work of Theodor Förster. For brevity only the quantum mechanical treatment is presented.

2.3.1 Theoretical description

In the classical picture the donor dipole, $\mathbf{p}_D$, is excited by absorption of energy from the light field and starts to oscillate. Its dipole radiation field excites the acceptor molecule which is a distance d_{DA} away from the donor. In the near field region, where $d_{DA} \ll \lambda$ the electric field generated by the donor is given by [74]

$$\mathbf{E}_D = -\nabla \frac{\mathbf{p}_D \cdot \mathbf{R}}{R} = \frac{\mathbf{p}_D - 3\mathbf{n}(\mathbf{n} \cdot \mathbf{p}_D)}{R^3} \tag{2.32}$$

Here $\mathbf{n}$ denotes the unit vector of the mutual distance between the dipoles. The energy of the acceptor dipole in the local field of the donor is given by $V = -\mathbf{p}_A \cdot \mathbf{E}_D$. We have

$$\begin{aligned} W_{DA} &= \frac{\mathbf{p}_A \cdot \mathbf{p}_D - 3(\mathbf{p}_A \cdot \mathbf{n}) \cdot (\mathbf{p}_D \cdot \mathbf{n})}{R^3} \\ &= \frac{\kappa^2 |\mathbf{p}_A||\mathbf{p}_D|}{n^2 R^3} \end{aligned} \tag{2.33}$$

In the second step all scalar product contributions were summed into an orientation factor κ^2. The rate of energy transfer is calculated by Fermi's golden rule

$$k_{ET} = \frac{2\pi}{\hbar^2}|\langle\Psi_{D^*}\Psi_A|\hat{W}_{DA}|\Psi_D\Psi_{A^*}\rangle|^2 \tag{2.34}$$

Ψ_D and Ψ_A denote the wavefunctions of donor and acceptor fluorophore respectively. The asterics marks the excited state. The interaction operator $\hat{W}_{DA}$ is the quantum mechanical analogue of equation 2.33, where the classical dipoles $\mathbf{p}_A$ and $\mathbf{p}_D$ are replaced by the dipole matrix elements $\hat{\mu}_A$ and $\hat{\mu}_D$. $\hat{\mu}_D$ depends only on the donor coordinates while $\hat{\mu}_A$ is described by acceptor coordinates only. Expression 2.34 can be factorised to yield

$$k_{ET} = \frac{2\pi}{\hbar^2}\cdot\frac{\kappa^2}{n^2R^6}(|\langle\Psi_D^*|\hat{\mu}_D|\Psi_D\rangle|^2\cdot|\langle\Psi_A|\hat{\mu}_A|\Psi_A^*\rangle|^2) \tag{2.35}$$

The squared matrix elements define the corresponding dipole strength, the probability with which the donor returns into the ground state while the acceptor becomes excited. The acceptor term is determined by the absorption profile, $\epsilon_A(\lambda)$, while the donor dipole strength depends on its emission profile, $\epsilon_D(\lambda)$, and the quantum yield Φ_F:

$$|\langle\Psi_D^*|\hat{\mu}_D|\Psi_D\rangle|^2 \propto \int\frac{f_D(\nu)}{\nu^3}d\nu\cdot\frac{\Phi_D}{\tau_D} \tag{2.36a}$$

$$|\langle\Psi_A|\hat{\mu}_A|\Psi_A^*\rangle|^2 \propto \int\frac{\epsilon_A(\nu)}{\nu}d\nu. \tag{2.36b}$$

Putting all together we finally obtain

$$k_{ET} \propto \frac{1}{R^6}\cdot\frac{\kappa^2\Phi_D J}{n^2\tau_D} \equiv \frac{1}{\tau_D}\left(\frac{R_0}{R}\right)^6, \tag{2.37}$$

where J denotes the spectral overlap integral, $J = \int\nu^{-4}\epsilon_A(\nu)f_D(\nu)d\nu$. Equation 2.37 can be rewritten to a transfer efficiency E according to $E = k_{ET}/(k_{ET}+k_0)$.

$$E = \frac{1}{1+(R/R_0)^6}, \tag{2.38}$$

with

$$R_0 = \left(8.79\cdot10^{-28}mol\frac{\kappa^2\Phi_D J}{n^4}\right)^{1/6}. \tag{2.39}$$

R_0 denotes the Förster radius of the dye pair, which equals the distance at which 50 % energy transfer is observed. It is composed of different factors including

1. the quantum yield of the donor in the absense of the acceptor, Φ_D
2. the refractive index of the medium, n

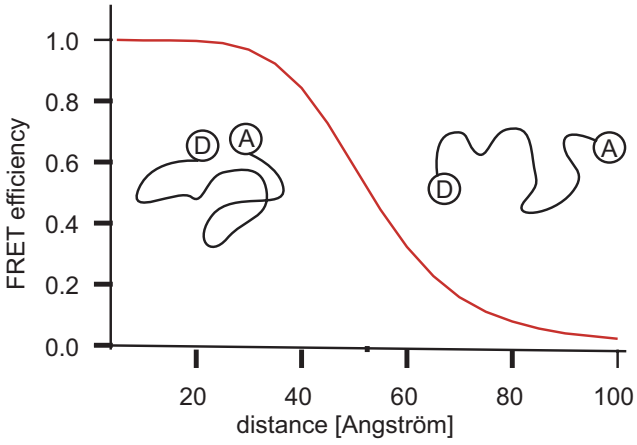

Figure 2.5: Distance dependence of the energy transfer for a fluorophore pair with $R_0 = 55\,\mathring{A}$. The two sketches illustrate the corresponding conformations of a biomolecule in the low- and high-FRET regime.

3. the overlap integral J of the excitation spectrum of the acceptor and the normalised emission spectrum of the donor.

4. an orientation factor κ^2, which includes the relative orientation of the dipole moments. In general κ^2 is assumed to be $2/3$ for freely rotating fluorophores. This is the most crucial factor in R_0 and the assumption of freely rotating fluorophores is not always valid.

To calculate R_0 the quantum yield of the donor, as well as the overlap integral need to be determined experimentally. This is done by evaluation of the absorption and emission spectra. Fluorescence anisotropy is used to determine the freedom of rotational motion and whether the assumption $\kappa^2 = 2/3$ is justified. Figure 2.3.1 shows the distance dependence of energy transfer for a given dye pair with a Förster radius of $55\,\mathring{A}$. The efficiency scales with the inverse sixth power of the ratio R/R_0 and a strong variation of transfer efficiency is observed around distances close to R_0. Within $0.5\,R_0 < R < 1.5R_0$ the efficiency decreases from 98 % to less than 10 %. For most fluorophores the Förster radius ranges between $50 - 60\,\mathring{A}$ and distances between 2.5 and $10\,nm$ can be measured.

Electron transfer reactions

Quantum theory predicts an additional mechanism for energy transfer between two molecules which are in very close proximity to each other.
In the case of FRET the donor transfers its energy onto the acceptor by means of a virtual photon. This process is called weak coupling and the interaction is mediated by a long range dipole-dipole interaction [33].
Once the fluorophores are so close that their electronic orbitals partially overlap, a strong coupling is obtained. In this limit a short range electron exchange dominates to mediate the energy transfer, whose efficiency rapidly decays with distance. It has been suggested that electron transfer is the basis for fluorophore quenching processes caused by specific nucleotides, e.g. guanosine. Recently, electron transfer processes have

found some notification as a method to measure energy transfer at very small interdye distances ($R < 2\ nm$). Rapid small-distance changes, which arise from fluctuations in the local protein structure could be unraveled by a correlation analysis of the electron transfer efficiencies(PET-FCS) [36].

2.3.2 Calculation of the single molecule FRET efficiencies

For a single molecule, the FRET efficiency is calculated from the number of photons detected in the donor and acceptor channel. The raw photon numbers are composed of various contributions that have to be corrected for, like crosstalk, direct acceptor excitation and background. The long-wavelength tail in the donor emission spectrum results in a donor crosstalk into into the acceptor detection channel. The background is usually not negligible under single molecule conditions, where only a fraction of all detected photons originate from fluorescence. If the fluorophores are spectrally not well resolved also the direct excitation of the acceptor by the laser has to be considered. The corrections are performed by a set of parameters, which is determined in separate measurements as described in section 3.4.
Below saturation the single burst signal in both channels is given by:

1. **donor channel**:
   rest donor emission + background + crosstalk of acceptor into donor channel
   $$I_D^{det} = \eta_D \sigma_D \Phi_D I_0 (1 - E) + B_D + \eta_{AD} \Phi_A \sigma_A I_0 \tag{2.40}$$

2. **acceptor channel**:
   FRET based acceptor emission + emission due to direct excitation + background + crosstalk from donor into acceptor channel
   $$I_A^{det} = \eta_A \sigma_D \Phi_A I_0 E + \eta_A \Phi_A \sigma_A I_0 + B_A + \eta_{DA} \sigma_D \Phi_D I_0 (1 - E) \tag{2.41}$$

$\eta_{D/A}$ denote the efficiencies of donor and acceptor detection in their respective detection channels. η_{DA} and η_{AD} are the efficiencies for the corresponding crosstalk into the other channel. $\Phi_{D/A}$ are the quantum yields of fluorescence and $\sigma_{D/A}$ describe the corresponding absorption cross sections. It is assumed that the contribution from direct acceptor excitation is negligible ($\sigma_A = 0$), a valid approximation if the fluorophores are spectrally well separated. The crosstalk from acceptor emission into the donor channel is neglected ($\eta_{AD} = 0$). and the remaining contributions yield:

$$I_D^{det} - B_D = \eta_D \sigma_D \Phi_D I_0 (1 - E) \tag{2.42a}$$
$$I_A^{det} - B_A = \sigma_D I_0 (\eta_A \Phi_A E + \eta_{DA} \Phi_D (1 - E)). \tag{2.42b}$$

The first equation is solved w.r.t. $\sigma_D I_0$ and then inserted into the second equation to yield

$$\begin{aligned} \frac{I_D^{det} - B_D}{I_A^{det} - B_A} &= \frac{\eta_D \Phi_D (1 - E)}{\eta_A \Phi_A E + \eta_{DA} \Phi_D (1 - E)} \\ &= \frac{1}{\gamma \frac{E}{1-E} + \frac{\eta_{DA}}{\eta_D}}. \end{aligned} \tag{2.43}$$

$\gamma = \eta_A \Phi_A / \eta_D \Phi_D$ is the detection factor of the system. It is composed of the detection efficiencies of both channels, η_D and η_A, and the quantum yields of the fluorophores, Φ_D and Φ_A. Equation 2.43 can be solved w.r.t. the energy transfer E:

$$E = \frac{N_A}{N_A + \gamma N_D}, \tag{2.44}$$

with the background and crosstalk corrected photon numbers

$$N_A = (I_A^{det} - B_A) - \frac{\eta_{DA}}{\eta_D} \cdot (I_D^{det} - B_D) \tag{2.45a}$$

$$N_D = (I_D^{det} - B_D). \tag{2.45b}$$

η_{DA}/η_D denotes the crosstalk of the donor emission into the acceptor channel. It is determined by a separate measurement of a donor-only sample.

Proximity ratio vs. FRET efficiency

If $\gamma = 1$ equation 2.44 simplifies to the so called proximity ratio P

$$E_{\gamma=1} = \frac{N_A}{N_A + N_D} \equiv P. \tag{2.46}$$

In contrast to the energy transfer, P does not explicitly contain the information on detection efficiencies and quantum yields and only states the ratio of acceptor to total signal. Both quantities are related to each other by

$$E = \frac{1}{1 + \gamma \frac{1-P}{P}}, \tag{2.47}$$

which follows from equation 2.46, since $N_D = N_A \cdot (1 - P)/P$. This expression can be rewritten to

$$P = \frac{\gamma}{\gamma - 1 + 1/E}. \tag{2.48}$$

Figure 2.3.2 shows the mutual relation between the proximity ratio and the energy transfer for various values of γ.

1. For values $\gamma < 1$ a given interval of low FRET efficiencies translates into a smaller proximity ratio interval. Two populations of low FRET efficiency will be less separated in their proximity ratios. High FRET states will show more separated P values than their FRET efficiencies ($P_2 - P_1 > E_2 - E_1$).

2. At values $\gamma > 1$ two low FRET states become more separated in their proximity ratios. At high FRET values the opposite is observed.

3. For $\gamma = 1$ we have $E = P$ and obtain a straight line with slope unity.

Apparently, the experimental setup can be "tuned" sensitive to a specific FRET regime by varying the detection conditions. This will be dealt with in detail in section 5.3.

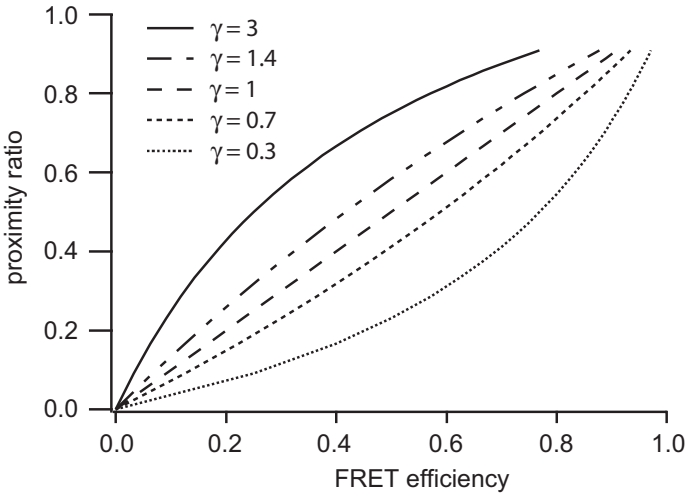

Figure 2.6: Mutual relation between FRET efficiency and proximity ratio for different values of γ. Depending on the value of the detection factor significant differences are observed between both quantities. Further details are given in the text.

Distribution width and shot noise limit

Even a point-like energy transfer distribution generates a broadened peak in the measured histogram. This minimum width is caused by the shot noise in the photon counting statistics and is a function of the mean energy transfer m_E and the detection factor γ.
Let S be the number of detected photons[5] and m_E the mean energy transfer of a population, then the number of detected acceptor and donor photons, N_A and N_D, are related by $N_D = N_A(1 - m_E)/\gamma m_E$. With $N_D + N_A = S$ we have

$$N_A = S \cdot \left(1 + \frac{1 - m_E}{\gamma m_E}\right)^{-1}. \tag{2.49}$$

An upper limit of the shot noise, ΔE, is given by the sum of the variances of donor and acceptor counts. Contrary to previous reports in the literature, where mostly the case $\gamma = 1$ was considered [32] we explicitly account for values $\gamma \neq 1$.

$$(\Delta E)^2 = \left(\frac{\partial E}{\partial N_A}\right)^2 (\Delta N_A)^2 + \left(\frac{\partial E}{\partial N_D}\right)^2 (\Delta N_D)^2. \tag{2.50}$$

In the following γ is assumed to be constant and only values of $N_A > 0$ are considered for mathematical reasons. For $N_A = 0$ we have $E = 0$ by definition. The standard deviations of the Poissonian distributed photon numbers correspond to their square root, $\Delta N_{A/D} = (N_{A/D})^{1/2}$. The partial derivatives w.r.t. N_A and N_D are straightforward to calculate. We have:

$$\Delta E = \left[\frac{\gamma}{(1 + \gamma N_D/N_A)^2}\right] \cdot \sqrt{\left(\frac{N_D}{N_A^2}\right)\left(\frac{N_D}{N_A}\right) + 1}. \tag{2.51}$$

[5]For simplicity the value of S is set to the burst selection threshold setting N_{min}.

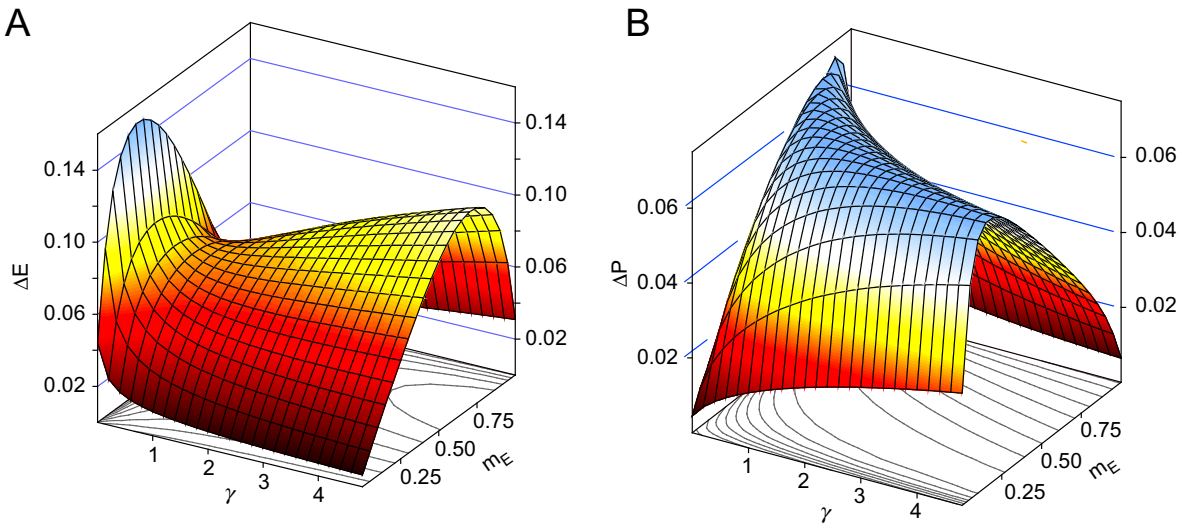

Figure 2.7: Calculated shot noise for the FRET efficiency (**A**) and proximity ratio (**B**) as a function of mean energy transfer m_E and detection factor γ. While the maximum value of ΔP remains constant and only varies in its position in the (m_E,γ)-space, stronger variation in both position and absolute value are observed for ΔE. Further details are given in the text.

With equation 2.49, N_A and N_D can be replaced by m_E and S, and we obtain as the final result:

$$\Delta E = m_E(1 + m_E(\gamma - 1))\sqrt{\left(\frac{1 - m_E}{\gamma m_E}\right)\frac{1}{S}}. \tag{2.52}$$

For $\gamma = 1$ this gives the familiar expression from the literature [32] where:

$$(\Delta E)_{\gamma=1} = \sqrt{\left(\frac{m_E(1 - m_E)}{S}\right)}. \tag{2.53}$$

The corresponding calculation for the proximity ratio differs in such that γ enters the calculation only intrinsical, namely by its effect on N_A and N_D. The final result obtained is

$$\Delta P = \frac{\gamma}{(\gamma - 1) + 1/m_E}\sqrt{\left(\frac{1 - m_E}{\gamma m_E}\right)\frac{1}{S}}. \tag{2.54}$$

If we consider the case $\gamma = 1$, equation 2.54 yields the same result than equation 2.53 as expected, since $E_{\gamma=1} = P$. The dependence of $\Delta E(\gamma, S, m_E)$ and $\Delta P(\gamma, S, m_E)$ on the parameters γ and m_E is shown in Figure 2.7 for an exemplary threshold of $S = 50$.

The combination of γ and m_E determines which of the both widths is larger. The ratio $\Delta E/\Delta P$ is calculated as

$$\frac{\Delta E}{\Delta P} = \frac{(1 + m_E(\gamma - 1))^2}{\gamma}., \tag{2.55}$$

and reduces for unity, if $\gamma = 1$. As the detection factor is increased ΔP significantly exceeds the value of ΔE for small energy transfers m_E. This aspect has to be considered if the detection system is sensitized towards the low FRET regime. Although the separation of two FRET states is increased in their proximity ratio, the shot noise widths in P increases as well. In how far these two contradictory effects compensate each other will be discussed in section 5.3.

2.4 Fluorescence fluctuation analysis

Complementary to the analysis of individual events a global analysis of the fluorescence trace yields valuable information on the system under study. Dynamic processes which affect the emission of the particle or the amount of energy transfer lead to fluctuations in the fluorescence properties which can be analysed by appropriate methods. Fluctuations comprise local deviations from the average value of a quantity. They can be analysed with respect to their time course or their amplitude distribution. By a time-domain correlation analysis the characteristic time scales of the underlying dynamics and the particle concentration can be determined. The analysis of the fluorescence intensity distribution yields additional information on the emissivity of the molecule [20, 77]. Both aspects yield complementary information and are essential to fully describe the fluctuation process.

2.4.1 Fluctuations

In general a given fluorescence signal can be written as

$$F(t) = \langle F \rangle + \delta F(t). \tag{2.56}$$

The change in signal is determined by the time-dependent fluctuation $\delta F(t)$ around the average value $\langle F \rangle$. Equation 2.56 implies that the time average of the fluctuations vanishes[6], i.e. $\langle \delta F(t) \rangle = 0$. The time scale and magnitude of $\delta F(t)$ is determined by the underlying process that generates the fluctuations. They can arise from the diffusion process of individual molecules, chemical reactions, photophysical dynamics of the fluorophore and variations in the laser intensity. In a confocal system the fluctuations in intensity result in a fluctuation of the number of detected photons. These are governed by Poissonian statistics[7] where the variation in the number of detected photons is given by its square root $\delta N = \sqrt{N}$. The relative fluctuations $\Delta N/N$ are thus proportional to $1/\sqrt{N}$ and increase in size as the number of photons (and of emitting molecules) decreases.
Fluctuation analysis is thus an ideal tool to investigate dynamical processes under low particle concentrations, where classical ensemble methods do not reach the necessary sensitivity. If the temporal dynamics of the fluctuations is of interest, Fluorescence

[6] We can write: $\langle F(t) \rangle = \langle \langle F \rangle + \delta F(t) \rangle = \langle F \rangle + \langle \delta F(t) \rangle$. Since $\langle F(t) \rangle \equiv \langle F \rangle$ we immediately obtain $\langle \delta F(t) \rangle = 0$.

[7] The two major condition for poissonian statistics are: A low probability for the detection of a photon (low detection probability $< 5\%$) and a large number of participating molecules.

Correlation Spectroscopy (FCS) proved to be the method of choice. The more recently developed technique of the photon counting histogram offers information on the brightness of the molecule. Both methods will be described in the following paragraph.

2.4.2 Analysis of temporal dynamics by fluorescence correlation spectroscopy

Fluorescence correlation spectroscopy is a prototype of a single molecule technique although it yields best results if applied under few-molecule conditions, where $N \approx 5-10$ [9]. Since its invention in the early 1970's [97], FCS gained enormous importance in biospectroscopy to extract time scales of fluctuations. The correlation function of a fluorescence signal $F(t)$ is defined as

$$G(\tau) = \frac{\langle F(t)F(t+\tau)\rangle}{\langle F(t)\rangle^2} \tag{2.57}$$

Using definition 2.56 and denoting $\langle F(t)\rangle = \langle F(t+\tau)\rangle = \langle F\rangle$ we can reformulate equation 2.57:

$$\begin{aligned} G(\tau) &= \frac{\langle(\langle F\rangle + \delta F(t))(\langle F\rangle + \delta F(t+\tau))\rangle}{\langle(\langle F\rangle + \delta F(t))\rangle^2} \\ &= \frac{\langle\langle F\rangle^2 + \langle F\rangle\delta F(t+\tau) + \langle F\rangle\delta F(t) + \delta F(t)\delta F(t+\tau))\rangle}{\langle F\rangle^2} \\ &= 1 + \frac{\langle\delta F(t)\delta F(t+\tau)\rangle}{\langle F\rangle^2}, \end{aligned} \tag{2.58a}$$

where we used the fact that the time average of the fluctuations vanishes, $\langle\delta F(t) = 0\rangle$. The normalised correlation function is thus given by the correlation of the fluctuations plus an additional offset of 1. Dynamic and photophysical processes result in statistical variations in the fluorescence signal. In the confocal microscope fluctuations in the fluorescence signal can be written as

$$\delta F(t) = \delta\left(\Phi_D\eta_D\sigma_0\int W_g(\mathbf{r})C(\mathbf{r},t)d^3\mathbf{r}\right) \tag{2.59}$$

Each parameter in equation 2.59 can be subject to fluctuations. These will show up as different components in the correlation function. Of particular interest are changes in particle concentration $\delta C(\mathbf{r},t)$ caused by the diffusion motion or kinetic reactions. These fluctuations are directly linked to structural properties of the biomolecule.
Fluctuations in photophysical parameters usually occur at lower time scales (μs) and are caused by transitions into the triplet state (changes in σ_0) or changes in Φ_D.

Free diffusion of one species in 3D

In the simplest case only the free diffusion of one species contributes to the fluctuations in the signal. The intensity profile $W_g(\mathbf{r})$ is described by equation 2.23 and it is assumed that only changes in the particle concentration $\delta C(\mathbf{r},t)$ contribute to the fluctuations. Under these conditions equation 2.58 reads

$$\begin{aligned} G(\tau) &= 1 + \frac{\langle \delta(\int W_g(\mathbf{r}) C(\mathbf{r},t)\, d^3\mathbf{r}) \delta(\int W_g(\mathbf{r}') C(\mathbf{r}', t+\tau)\, d^3\mathbf{r}') \rangle}{\langle \int W_g(\mathbf{r}) C(\mathbf{r},t) d^3\mathbf{r} \rangle^2} \\ &= 1 + \frac{\int W_g(\mathbf{r}) \int W_g(\mathbf{r}') \langle \delta C(\mathbf{r},t) \delta C(\mathbf{r}', t+\tau) \rangle d^3\mathbf{r} d^3\mathbf{r}'}{\langle \int W_g(\mathbf{r}) C(\mathbf{r},t) d^3\mathbf{r} \rangle^2}. \end{aligned} \tag{2.60}$$

The change in concentration $\delta C(\mathbf{r},t)$ is determined by the laws of diffusion. The concentration profiles $C(\mathbf{r},t)$ and $C(\mathbf{r}',t')$ are linked by the diffusion propagator P_{diff}. This quantity describes the conditional probability of finding a molecule at time t' and spatial coordinate $\mathbf{r}'$ when it has been at point $\mathbf{r}$ at time t:

$$\delta C(\mathbf{r}', t') = P_{diff}(\mathbf{r}, \mathbf{r}', t, t') \delta C(\mathbf{r}, t). \tag{2.61}$$

In case of pure diffusion P_{diff} is the solution of the second law of diffusion, $\dot{C}(\mathbf{r},t) = -D\nabla^2 C(\mathbf{r},t)$.

$$P_{diff}(\mathbf{r}, \mathbf{r}', t, t') = \frac{1}{(4\pi D\tau)^{3/2}} exp\left(-\frac{(\mathbf{r}' - \mathbf{r})^2}{4D(t'-t)} \right). \tag{2.62}$$

With equation 2.62 the final form of the autocorrelation function is given by

$$G(\tau)^{diff} = 1 + \frac{1}{cV_{eff}} \left(1 + \frac{4D\tau}{w_0^2} \right)^{-1} \left(1 + \frac{4D\tau}{z_0^2} \right)^{-1/2}. \tag{2.63}$$

Two important parameters that are obtained from the ACF are the number of molecules in the focus, N, which is related to the inverse amplitude G(0), and the diffusion time, τ_0, which depends on the geometry and size of the particle.

$$\tau_0 = \frac{w^2}{4D} \tag{2.64a}$$

$$N = (G(0) - 1)^{-1} \tag{2.64b}$$

Figure 2.8 shows typical autocorrelation functions, to illustrate the influence of molecular size and particle concentration on the ACF amplitude. The left plot compares particles of different sizes while on the right hand side the ACF is shown for different particle concentrations.

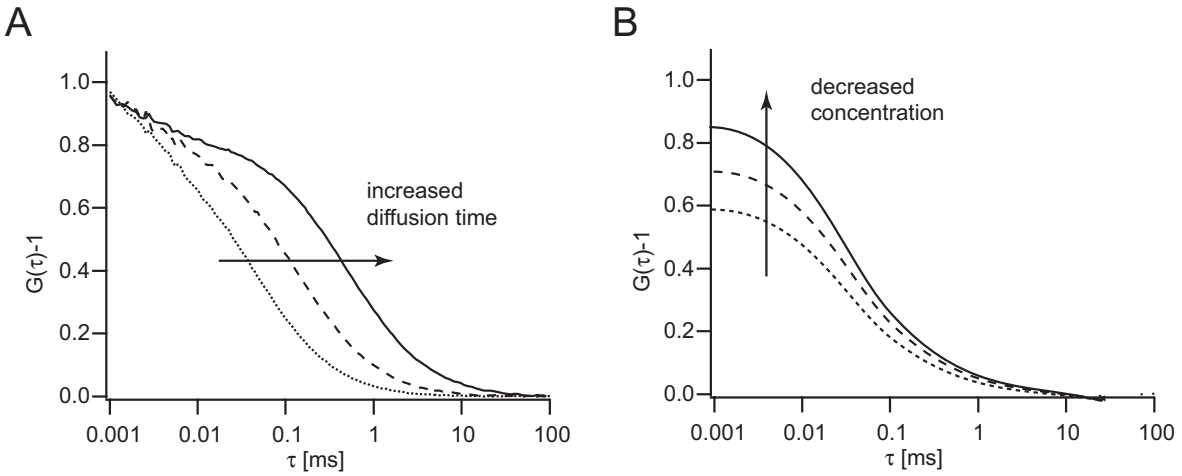

Figure 2.8: Hypothetical autocorrelation curves showing the information obtained from a basic FCS measurement.**A**: Autocorrelation curves for species with different diffusion coefficients yielding a strong difference in observed diffusion time as given by equation 2.64a. **B**: FCS analysis of a species present at different concentrations. The amplitude G(0)-1 scales inversely proportional with the particle number, see equation 2.64.

Additional contributions

To describe the real data equation 2.8 is too simple. Even if only 1 species diffuses in solution there will always be additional fluctuations from its photophysics. If the binding between two molecules is to be studied multiple components need to be considered, i.e. the unbound species and the bound complex. And under very dilute concentrations the effect of uncorrelating background further modifies the correlation amplitude. The more complex the system becomes the more terms have to be included into the autocorrelation function. The most important extensions are briefly summarized.

- **Triplet state correction**
  Even at low intensities there is a certain probability for intersystem crossing into the triplet state. While being in T_1 the emission of the fluorophore is interrupted on the timescale of a few μs. Fluctuations in the fluorescence signal are introduced which decay with the characteristic lifetime of the triplet state.
  In general the triplet fluctuations are much faster than the diffusion process, therefore the dynamics are seperable. The triplet dynamics is then approximated by a monoexponential decay typical for an on/off kinetics [143]. The modified ACF is given by

$$G(\tau)^{tr} = (1 - T + T \cdot exp(-\tau/\tau_{tr})) \cdot G(\tau)^{diff}, \tag{2.65}$$

  where $G(\tau)^{diff}$ is is given in equation 2.63. τ_{tr} is the characteristic triplet state decay time and T denotes the fraction of molecules residing in the triplet state.

Both parameters are related to the photokinetic rates according to

$$T = \frac{k_{01}k_{ISC}}{k_{01}(k_T + k_{ISC}) + k_0 k_T} \tag{2.66a}$$

$$\frac{1}{\tau_{tr}} = k_T + \frac{k_{01}k_{ISC}}{k_{01} + k_0}. \tag{2.66b}$$

- **Multiple components**
  If various species with different diffusion times and quantum yields are present, the autocorrelation function has to be further modified. If the molecules do not interact during the time course of the diffusion the ACF is composed of the weighted correlation functions for each species:

$$G(\tau) = \frac{\sum_1^n N_i Q_i^2 G_i(\tau)^{diff}}{(\sum_1^n N_i Q_i)^2}. \tag{2.67}$$

  Q_i denotes the molecular brightness, i.e. the counts per molecule and second, for species i. The relative contribution of each species is not given by its fraction but scales with the square of its brightness. This renders the interpretation of total particle concentration more difficult, as N_{eff} is no longer given by the sum of the individual particle concentrations. In fact, we have

$$N_{eff} = \frac{\left(\sum_1^n N_i Q_i\right)^2}{\sum_1^n N_i Q_i^2}. \tag{2.68}$$

- **Single molecule concentrations**
  In the low concentration range typical for single molecule spectroscopy, the contribution of non correlating background cannot be neglected. If the average fluorescence signal is comparable to the background level the fluctuations in the background become significant and the effective correlation amplitude is reduced [130, 42]. The corrected correlation function is given by

$$G(\tau) = \frac{NQ^2}{\langle I\rangle^2}\left(1 + \frac{4D\tau}{\omega_0^2}\right)^{-1}\left(1 + \frac{4D\tau}{z_0^2}\right)^{-1/2}. \tag{2.69}$$

  where N denotes the mean number of particles in the volume and Q the molecular brightness. $\langle I\rangle$ is the average total signal which is given by $\langle I\rangle = NQ + I_B$, where I_B denotes the background intensity.
  As a consequence the ACF amplitude depends on the signal-to-background ratio, where

$$G(0) - 1 = \frac{1}{N}\left(1 - \frac{I_b}{\langle I\rangle}\right)^2. \tag{2.70}$$

  For values $NQ \approx I_B$ a strong deviation of $G(0)-1$ from the expected value of $1/N$ is observed. Under SMD conditions ($1/N \approx 30$, $Q \approx 40\,kHz$ and $I_B \approx 2\,kHz$) $G(0) - 1$ is reduced to 4.8 instead of 30 as expected.

2.4.3 Analysis of fluctuation amplitudes - PCH and FIDA

A practical limitation of the FCS analysis is the fact that two species which do not differ significantly in their diffusion properties, are barely resolvable. For example, the difference in diffusion time between a monomer and a dimer scales with the cubic root of the respective molar mass, and only amounts to $\sqrt[3]{2} = 1.26$. The difference in molecular brightness, however, will be a factor of 2, assuming that all monomers are labeled, and that both fluorophores remain active upon dimerisation. In such a case, an analysis method that extracts the intensity information from the ensemble is much more suited to distinguish between both species.
To do so, a variety of methods has been developed, such as the Photon Counting Histogram (PCH) [19] or the Fluorescence Intensity Distribution Analysis (FIDA) [77]. These methods analyse the intensity distribution from the fluctuating signal. They share the common principle, that the fluorescence intensity is binned into equal time intervals which are smaller than the mean diffusion time. The major fluorescence parameterws that are determined from the analysis are the concentration of molecules in the focus and nthe molecular brightness of the molecule. The exact algorithm by which these parameters are extracted differ substantially between PCH and FIDA, however, the underlying principle is the same.
The shape of the intensity distribution depends on three sources of fluctuations. The first contribution arises from the shot noise in the photon detection process. This results in a purely Poissonian distribution of intensities. The two other sources are the variation of the particle number in the focus and fluctuations in the intensity observed from each molecule, caused by the inhomogeneous intensity profile of the laser beam. The latter factor is particularly sensitive to the molecular brightness of the molecule. The intensity distribution can no longer be described by Poissonian statistics, and a complex mathematical expression is required to fit the data.

Noteworthy the shape of the intensity histogram also depends on the bin time itself. As the bin time is successively increased the diffusion process will have an increasing impact on the distribution. Bin times smaller than the diffusion time generate a snap shot of the occupancy in the laser focus and contain the full information on particle number fluctuations. On the contrary, the distribtuion for bin times larger than the diffusion time will contain less fluctuations, since the particle number is averaged over longer time periods.
Recent extensions to the method are able to analyse the histogram shape as a function of bin width and are able to extract additional information on the diffusion process, e.g FIMDA - Fluorescence Intensity Mulitple Distribution Analysis [109].

Chapter 3

Material and methods

3.1 Chemicals and preparation protocols

3.1.1 Buffer solutions and additives

All nucleosome experiments were performed in $1\times TE$ buffer ($10\,mM$ Tris-HCl, $0.1\,mM$ EDTA, pH 7.5) with additional substances as denoted in the text. The chemicals were purchased from the following companies:

	substance	**company**
standard reagents	Tris X	Gerbu
	sodium chloride	Fluka
	glycerol	Fluka
	bovine serum albumine	New England Biolabs
photostabilising agents	ascorbic acid	Sigma-Aldrich
	sodium ascorbate	Sigma-Aldrich
	n-propyl gallate	Fluka
	mercaptoethylamine	Fluka

Table 3.1: Chemical substances that were used for buffer preparation

For the preparation of Tris buffer and stock solutions of the additives ddH_20 (Seralpur, Elga Labwater, Germany) was filtered through $0.02\,\mu m$ syringe filters (Whatman). A $1\,M$ stock solution of sodium chloride was frequently prepared to adjust the salt concentration in the buffer. Stock solutions of $200-400\,mM$ of the photostabilising agents were freshly prepared every day. Glycerol was mixed with ddH_20 and slowly equilibrated to obtain a stock concentration of $75\,\%$ glycerol from which appropriate concentrations were produced by dilution into buffer. Bovine serum albumine was taken from stock solution and diluted prior to buffer use.

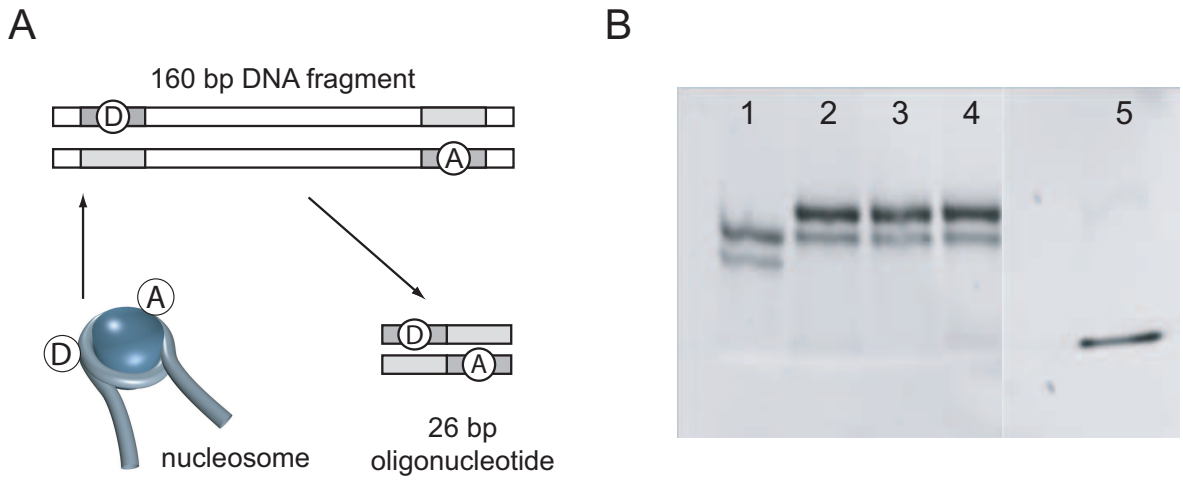

Figure 3.1: **A**: Schematic illustration of the 26 bp FRET standard used thoughout this work and its relation to the 612^{160}_{med} nucleosome construct. **B**: Electrophoretic analysis of hybridised oligonucleotides. Lane 1: donor-only sample, lanes 2-4: double labeled sample. The occurence of the lower lying band indicates a missing fluorophore on one strand, presumably the donor strand. Lane 5: unhybridised single strands

3.1.2 Preparation of oligonucleotide standards

Fluorescently labeled oligonucleotides of 26 and 40 bases in length were purchased from IBA (IBA Naps, Göttingen, Germany). Two different sequences were used as test standards for FRET measurements:

- standard 1 (26 bp):
  $5' - \text{CAA ACT ACC GAG TCT GAT ACA GGC GC} - 3'$

- standard 2 (40 bp):
  $5' - \text{CTC TTC AGT TCA CAG AGG ATC CTA TCA GCC GCT TGC C} - 3'$

In the 40 bp standard the donor fluorophore (Alexa488) was positioned at the DNA end while the acceptor (Rhodamine X) was internally attached 7 bp and 16 bp away from the donor. This sequence was used for the experiments with glycerol.
In the 26 bp sample the fluorophores were attached at a distance 6 bp from the $5'$ end of both strands via aminolink-dT carbon 6 linkers. 5 bp on either side of the fluorophores match the local DNA sequence in the 612^{160}_{med} nucleosome model system as shown in Figure 3.1A. One strand was labeled with various acceptor fluorophores (Rhodamine X, Alexa568, Alexa594), while the same donor fluorophore (Alexa488) was used in all experiments. For the preparation of an additional low-FRET standard Alexa568 was attached at the $5'$ end of the acceptor strand.

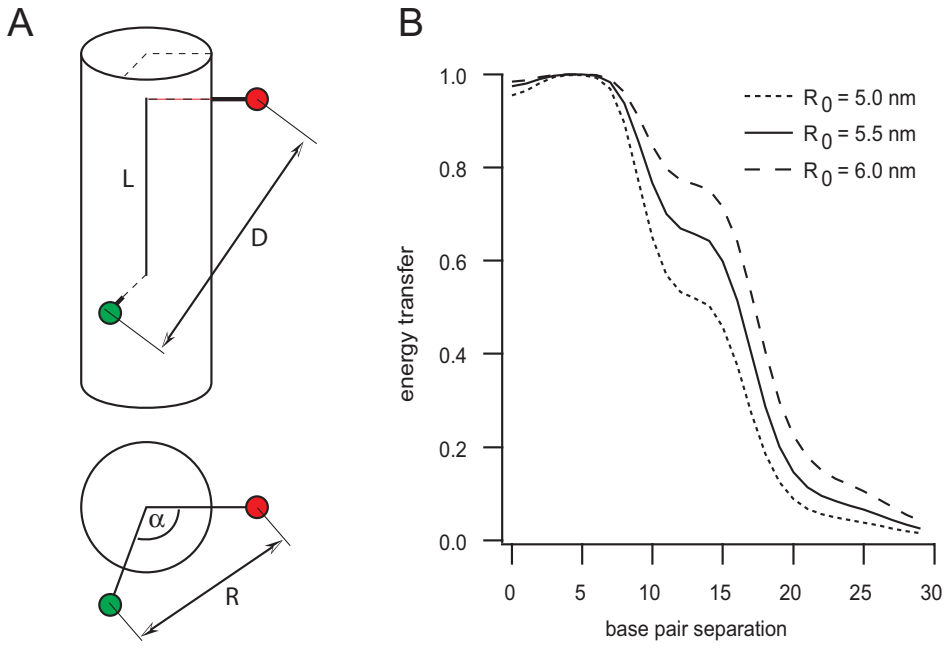

Figure 3.2: Helical DNA model used to estimate the interfluorophore distance. **A**: Geometry of the DNA helix and parameters used for the calculation of the interdye distance R. **B**: Calculated FRET efficiency as a function of base pair separation for three different values of R_0.

Helical DNA model

The interfluorophore distance was estimated from the helical DNA geometry of double stranded DNA as described by Clegg et al. [23].

As shown in Figure 3.2A the interdye distance is calculated as $D^2 = R^2 + L^2$, where R and L are the radial and axial component of the distance vector. The axial component is given by $L = N \cdot 3.4\,\mathring{A} + L_0$, where N is the number of base pairs separating both fluorophores and L_0 describes the axial offset if both dyes are positioned at the same base pair. The radial distance is given as $R = 2(l + r)sin(\alpha/2)$ where α is the angle included by the projected fluorophore positions. r is the radius of the DNA double helix and l the length of the c6-linker. Based on the repeat length of 10.5 bp/turn for free DNA we have $\alpha = 34.1 \cdot N + \pi/2$. A phase factor of $\pi/2$ is introduced since both fluorophores are opposite to eachother if they are located at the same base pair ($N = 0$). Figure 3.2B shows the estimated FRET efficiencies for three representative R_0 values of 50 $\mathring{A}$, 55 $\mathring{A}$ and 60 $\mathring{A}$.

The energy transfer resembles the helical path of the DNA as the fluorophore separation is gradually increased. Noteworthy, a change from 10 to 15 base pair separation only results in a 20 % change in energy transfer.

After inspection of the labeling quality by absorption spectroscopy, donor and acceptor labeled strands were hybridised in $1 \times TE$ and $100\,mM$ NaCl at pH 7.5. DNA was used at concentrations between 1 and 10 μM. Samples were heated to 95 °C to melt any prehybridised strands and slowly cooled down to room temperature for about

$2\,h$. An optimum ratio between donor and acceptor strand was determined by gradual variation of the mixing ratio and inspection on a 20 % polyacrylamide gel (19:1 bisacrylamide:acrylamide, 160 V for 1.5 hours) as shown in Figure 3.1 . An additional band below the upper population is caused by samples that lack one fluorophore.
Only those samples were considered for further experiments, which yield a predominant double strand population. They were kept at 4 °C for several months.

3.1.3 Preparation of mononucleosomes

The preparation of mononucleosomes is described in detail in the dissertation of Florian Hauger [66]. This paragragh briefly summarizes the essential steps involved in the formation of mononucleosomes.
The DNA sequences used in this work were part of the 601 and 612 positioning sequences [95] contained in the templates pgem3z601 and pgem3z612 (kindly provided by Jon Widom, Northwestern University) as well as the *X. borealis* 5S rDNA. The full sequences of the fragments can be found in [66]. The fluorophore position was varied to label different parts of the nucleosomal DNA, either internal DNA sites close to the dyad axis or the linker DNA protruding out of the nucleosome. This set of constructs monitors conformational changes occuring in the different parts of the nucleosome. The different labeling positions are schematically shown in Figure 3.3. For DNA's different from the 601 sequence the notation is changed, e.g $5S^{170}_{med}$.

Preparation of DNA fragments
Fluorescently labeled primers were purchased form IBA GmbH (Göttingen, Germany) and Purimex (Grebenstein, Germany). The DNA was prepared using preparative PCR. Conditions were $40\,pmol$ for each primer, $8\,ng$ of template DNA in $200\,\mu l$ final volume using the PCR Master Kit from Promega (Madison, WI, USA). Ten PCR preparations were usually enough to obtain around $10 - 12\,\mu g$ of DNA. Purity was checked on an 8 % polyacrylamide gel and with absorption spectroscopy as described below. The DNA was precipitated with Isopropanol, purified using the NucleosSpin kit from Macherey-Nagel and gel filtrated with NAP-5 columns (Pharmacia), eluted in $1 \times TE$ and concentrated to $0.1 - 0.5\,mg/ml$ in a vacuum centrifuge. Only DNA generating a sharp single band was used for the experiments.

Nucleosome assembly
Recombinant *X. laevis* histones were separately expressed in E.coli strain BL21 DE3 from Novagen and purified. Recombinant octamers were assembled by unfolding the purified histones and by a subsequent overnight dialysis in refolding buffer as described in [135, 66].
Nucleosomes of the 601 and 612 sequence were reconstituted by mixing the purified labeled DNA with the histone octamer at a ratio of 1:1.3-1.4 in a final volume of $50\,\mu l$ buffer ($1 \times TE$ and $2\,M$ NaCl) [66]. Nucleosomes of the 5S sequence were mixed at a different ratio of 1:1.8 DNA:histone. For the experiments on histone acetylation, 601^{170} nucleosomes were prepared identically to the $5S^{170}$ constructs. Salt step dialysis

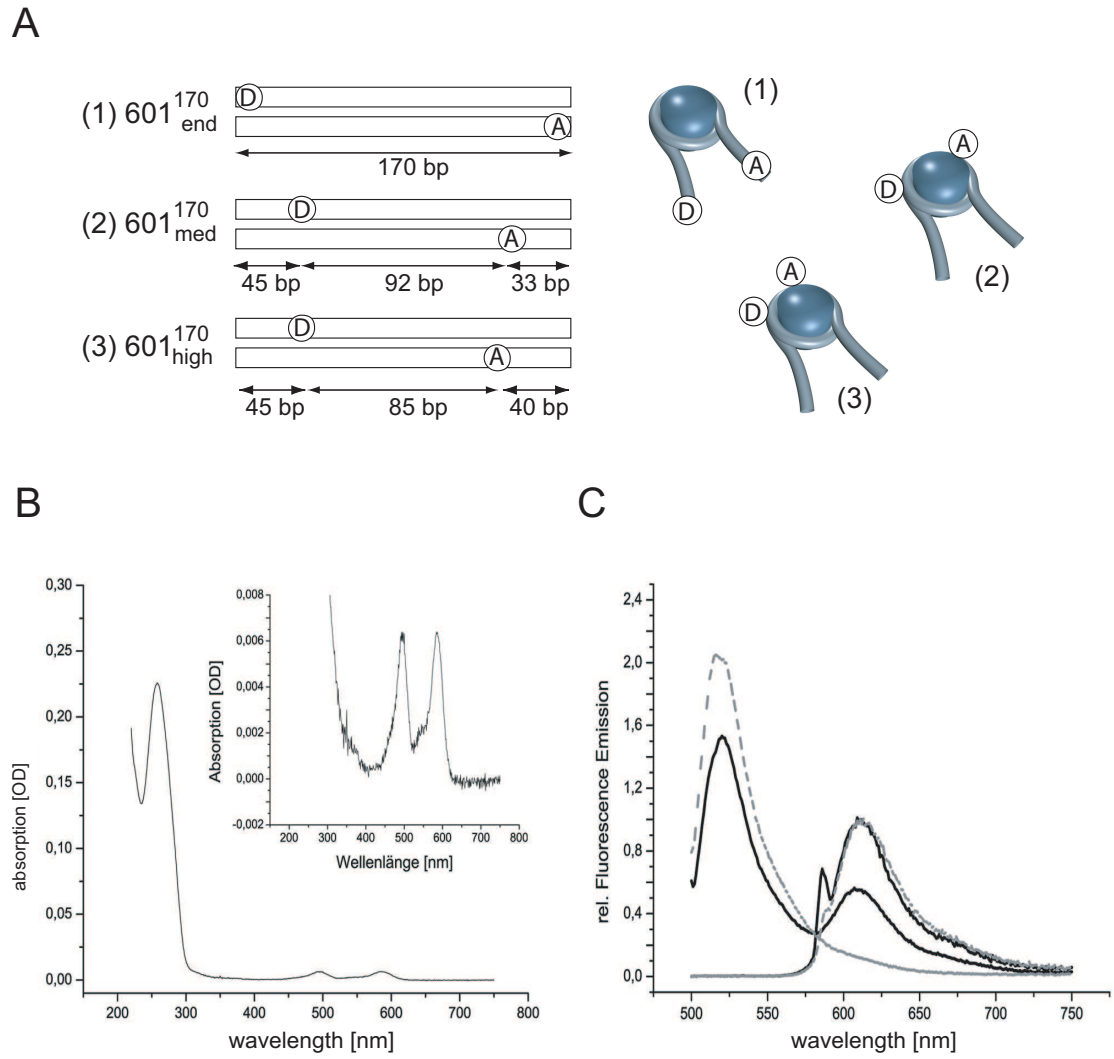

Figure 3.3: **A**: Schematic representation of the different fluorescent nucleosome constructs used in this work. The fluorophore position is determined by their respective position in the primers. **B**: Typical absorption spectrum of mononucleosomes. The labeling quality was assessed from the ratio of the maxima of the DNA at 260 nm and the corresponding fluorophore peak. Inlay sketch: magnified view of the fluorophore emission portion. **C**: Instrument-corrected fluorescence emission scans of 601^{170}_{med} nucleosomes compared to the free DNA fragment. Solid lines: nucleosomes excited at 495 nm and 585 nm, dashed lines: free DNA, excited at 495 nm and 585 nm. The average FRET efficiency was calculated applying the method described in [135].

was carried out at 4 °C with the steps being 1.8 M, 1.4 M, 1 M, 0.8 M, 0.6 M, 0.4 M, 0.2 M, 0.1 M and a final over night incubation at 5 mM NaCl. Linker histone H1 was added in equimolar ratio to the octamer at the 0.4 M step when required.
An alternative assembly protocol replaced the stepwise dialysis by a gradual dialysis from 2 M to 0.1 M for 3 hours followed by an overnight step from 0.1 M to 5 mM NaCl. This was shown to produce a comparable salt gradient within the dialysis tube to that for the stepwise dialysis.

Analysis of reconstituted nucleosomes

- Reconstituted nucleosomes were checked by gel electrophoresis in a 2 % agarose gel to measure the ratio of bound to free DNA. The free DNA was below 10% in the undiluted sample (about 0.3 μM).
  The positioning properties of the nucleosomes were analysed in a polyacrylamide gel. Figure 3.4 shows the typical gel pattern observed for 601^{170} nucleosomes when mixed at a ratio of 1:1.3 (DNA:octamer). Two different positioning bands were observed (lane 2), where symmetrically positioned nuclesomes migrate slower than the conformation, where the octamer is positioned asymmetrically on the DNA. The fastest migrating band is attributed to the free DNA fragment.
  Restriction of the DNA increases the mobility since less DNA is contained in the nucleosome and the mass of the complex is reduced. An additional nucleosome band is observed if the restriction site is accessible to the enzyme (lane 4). On the contrary, only DNA is digested if the restriction site is occluded by the octamer (lane 3). The details of the restriction analysis can be found in [66, 57].

- The ratio between the fluorophores in the nucleosome sample was measured in a dual-beam absorption spectrophotometer (Cary 4E, Varian, Mulgrave, Australia). A typical absorption spectrum is shown in Figure 3.3 B . An excess of donor only labeled samples should be avoided since these samples do not contribute to the FRET species of interest.
  Additionally, the spectrum is checked for aggregated nucleosomes which cause a broad background due to Rayleigh scattering. In the absense of aggregates the baseline in the fluorophore absorption region ($400 - 650\,nm$) is considerably flat. If Rayleigh scattering is present the baseline will be tilted due to the $1/\lambda^4-$dependence of the Rayleigh scattering cross section. Additional centrifugation was applied to remove the aggregates when necessary.

- The bulk FRET efficiency was determined in a commercial fluorimeter (SLM Aminco 8100, Urbana IL, USA), Figure 3.3C . From the spectroscopic data the interfluorophore distance was estimated applying the method of sensitized acceptor emission as described in [135]. A good agreement between the measured distances and those estimated from the crystal structure was found as discussed in [66, 57].

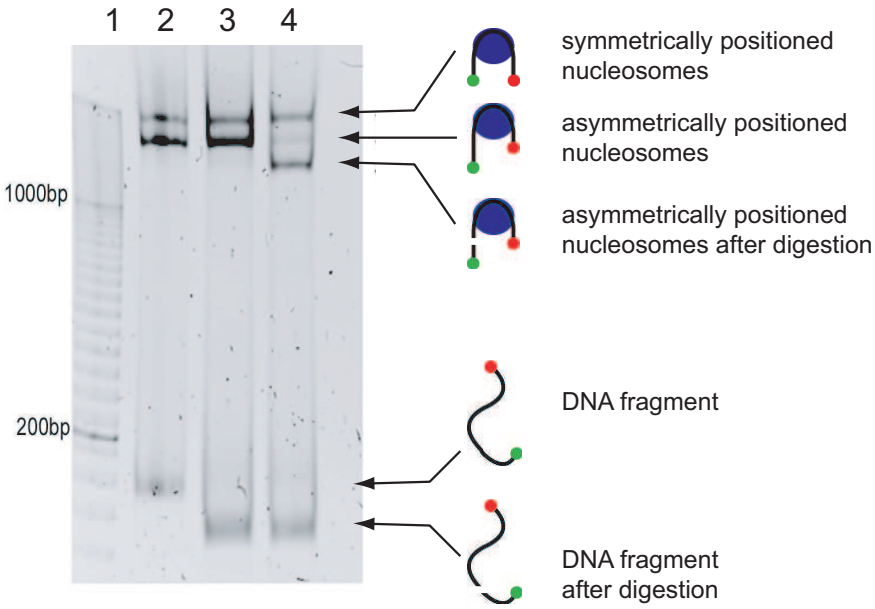

Figure 3.4: Electrophoretic analysis of different nucleosome positioning states in an 8 % polyacrylamide gel. Lane 1: 20 bp DNA ladder (control), lane 2: untrested 601^{170} nucleosomes, lanes 3 and 4: restriction digestions performed with *HinfI* and *PmlI*. Only the restriction site for the latter enzyme was accessible in the nucleosome sample, while both enzymes digested free DNA. The respective conformations are depicted on the right hand side. Further details are given in the text.

3.1.4 Enzymatic remodeling experiments

The remodeling factor BRG1 was purchased from Jena Bioscience. ISWI protein was a generous gift from the group of Peter Becker in munich. NAP1 was purified by Nathalie Brun in our lab.

Bulk experiments

All bulk remodeling experiments were performed by Florian Hauger at conditions detailed in [66]. Mobilisation was done in a volume of $10\,\mu l$ at 37 °C and subsequently analysed on an 8 % polyacrylamide gel.
In all experiments a nucleosome concentration between 100 and $200\,nM$ was used, while the enzyma concentrations varied between the different factors.
For experiments on ISWI $10 - 120\,nM$ enzyme were incubated with the nucleosome substrate. This enzyme-substrate ratio was similar to that reported from other groups ([66] and references within). In the case of BRG1, the enzyme concentration varied between 50 and 100 nM, while experiments on NAP1 were performed with $0.1 - 1.5\,\mu M$ enzyme.

Single molecule experiments

Single pair FRET experiments were conducted in sample volumes between $30-200\,\mu l$, depending on the test chamber used. Most data presented here were measured in $30\,\mu l$ wells (18 well-slide, IBIDI, Germany). For most SMD experiments around $50\,pM$ nucleosomes were incubated with an excess of upto $70\,nM$ enzyme. For details refer to section 6.1.

3.1.5 Preparation of vesicle encapsulated samples

Lipids were purchased from Otto Nordwald GmbH. Lipids were dissolved in glycerol by the manufacturer and stored at $-20\,°C$. The neutral lipids POPC (1,2-Palmityl-oleoyl-phosphatidylcholine) and DOPC (1,2-Dioleoyl-phosphatidylcholine) as well as a natural egg-phosphatidylcholine (egg-PC) extract were used for vesicle preparation. A fluorescent PC-analogue (NBD) was used to label the lipid membrane if required.
Lipid mixtures were prepared from stock solutions of lipids dissolved in glycerol which was subsequently removed under streaming nitrogen. Remnants of glycerol were removed in a low-vacuume exsiccator for about 2 hours. The dried lipids were resuspended in buffer and stored at $-20\,°C$. Prior to vesicle preparation the multilamellar structures that form in aqueous buffer were broken by several freeze-thaw cycles ($n \geq 5$). The lipids were mixed with the labeled oligonucleotides at a ratio of approximately $3\,mg/ml$ lipid to $1.7\,\mu M$ oligonucleotide. Vesicles were formed by extruding the mixture through a $100\,nm$ polycarbonate filter (LipoFast Mini-Extruder, Avestin, Germany). Following the instructions of the manufacturer an uneven number of 17-19 steps was applied to obtain a monodisperse solution of vesicles. The diameter of the vesicles was measured with dynamic light scattering to be $79\,nm$.
Non-encapsulated molecules were separated from vesicles by a size-exclusion column using a matrix of $4\,ml$ Sepharose 4B (Sigma-Aldrich). The eluat was collected in 3-4 drop fractions. The first few fractions contained the encapsulated molecules which were identified by their increased diffusion time measured by fluorescence correlation spectroscopy. For further experiments those fractions were stored at $4\,°C$ for up to 3 days.

3.2 Confocal microscope systems

Parts of the experiments presented in this work were performed on an existing confocal setup, the Fluorescence Fluctuation Microscope (FFM). This setup proved to be useful to detect individual molecules in solution and to optimise a variety of parameters for future experiments, as discussed in chapter 4. In parallel, a new experimental setup was designed to provide a platform which is more adaptable to state-of-the-art single molecule experiments. After a short review on the FFM the new spectrometer is described in detail.

A

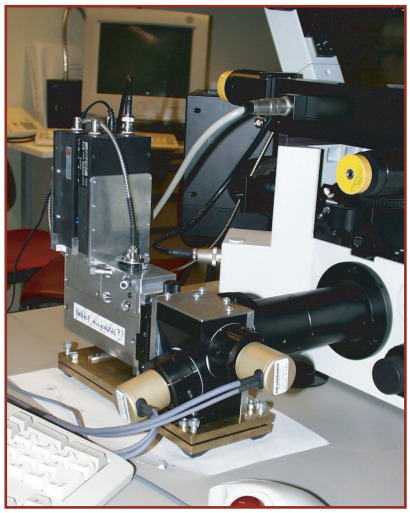

B

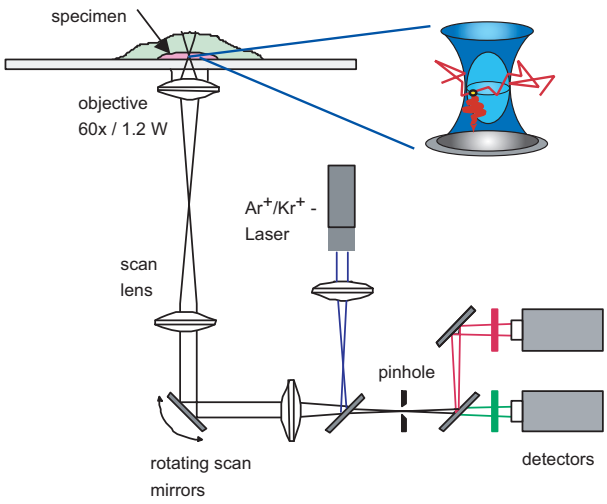

Figure 3.5: **A**: Side view of the FFM with the confocal module and scanning unit attached to the microscope. **B**: Schematic view of the optical layout. Details can be found in the text and references [139, 130, 140].

3.2.1 The Fluorescence Fluctuation Microscope

The FFM combines the optics of a conventional laser scanning microscope with a modular unit for FCS experiments as has been described in detail in the work of Malte Wachsmuth and Michael Tewes [140, 139, 130]. Both, laser scanning and FCS, use the same beam path, which had been a novel feature at the time of construction. This configuration allows to scan the laser beam with a positioning accuracy below $25\,nm$ [140].

A modular FCS unit which houses one excitation path and two detection channels is attached to a pair of galvanometric mirrors (M2, GSI Lumonics, Germany). The assembly is mounted to the video port of an inverted microscope which is equipped with a pupil lens (FVX-IR-PL, Olympus, Germany). This element converts the beam rotation by the scanning mirrors into a proportional change of lateral beam position in the object plane of the microscope ($f\Theta$-lens).

Light from a multiline argon-crypton gas laser (Melles Griot, Germany) is coupled to the module via a singlemode fiber (Schäfter und Kirchhoff, Germany). The laser light passes two achromat lenses which are essential for beam alignment and is deflected into the scanning unit by a dichroic mirror. The scan mirrors stir the beam into the microscope to illuminate the back focal aperture of an objective lens with a high numerical aperture ($60\times$ $1.2W$, UPLANAPO Olympus, Germany).

The fluorescence is detected epifluorescently and imaged onto a pinhole placed in a conjugated image plane. The light passing through the pinhole aperture is split into two spectral regions and detected by two avalanche photodiodes (SPCM-AQ-14, Perkin-Elmer, Canada).

Spectral filters and dichroic mirrors are mounted in replacable filter holders to adapt for various fluorophore combinations. All filters were purchased from Omega Optical (Brattleborn, VT USA). Table 3.2 gives an overview of the filter sets used in this work.

name	excitation	dichroic	emission
A	488DF22	505DRLP	-
D	490-577DBEX	490-575DBDR	-
Q	-	580DRLP	535AF45
E	-	570DRLP02	535DF35
R	-	580DRLP	520DF40
N	-	100 %	OG590/700CSFP
G	-	100 %	635DF55

Table 3.2: Table of filter sets used in this work. The notation resembles that used in the FFM setup.

3.2.2 Acousto-optical intensity modulation

Advanced single molecules applications require a hands-on control of the laser intensity. The dealignment of the fiber coupling and attenuation by a neutral density filter provide a way for a static manipulation of the overall laser intensity, but do not allow to selectively switch between different excitation lines in multicolor experiments.
To control the different emission lines available from the argon-crypton laser the existing laser coupling was expanded by a polychromatic acousto-optical modulator (AOM) (Pegasus Optics, Germany). This element allows to switch between up to 12 individual laser lines on time scales as short as $10-15\,\mu s$. Beside the improvement of current FCS and FCCS experiments, this will be important for the implementation of alternating excitation schemes [76, 90].
A piezoelectric transducer is bonded to a suitable semiconductor crystal and transforms an applied radio frequency into a sound wave, which travels through the crystal medium. The interaction of the sound wave with quasi-free electrons from the crystal generates periodic density fluctuations in the medium. An optical laser beam experiences a periodic change in refractive index and will undergo diffraction if the Bragg condition for constructive interference is fulfilled. The amplitude of the laser beam will be attenuated depending of the power and the frequency of the sound wave, which define the amplitude and spacing of the optical grating. The beam will exit the crystal at twice the angle of incidence. The laser beam is deflected into the entry aperture of the acousto-optical modulator. Two beams exit the AOM, where the modulated beam diverges from an unmodulated beam, which can be easily blocked out of the beam path. A flip mirror behind the AOM is used to select between two fiber coupling units, one which connects to the FFM and one which is coupled to the new spectrometer setup.
In most experiments the laser intensities were adjusted via the remote control. Figure 3.6 shows the variation in output laser power of the $568\,nm$ line as a function of HF frequency and power setting. To quantify the change in laser intensity, the count rate

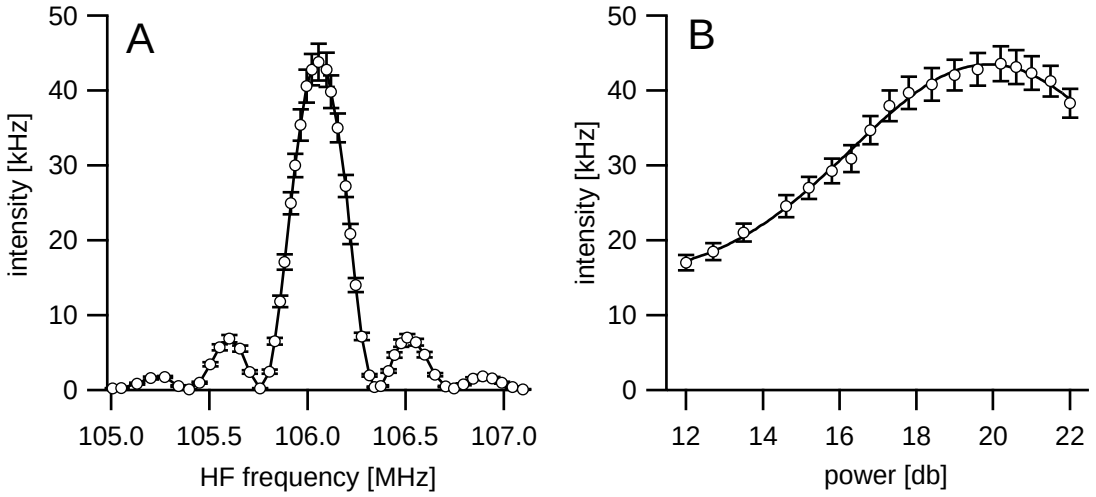

Figure 3.6: Count rate measured from a test solution of $20\,nM$ Alexa568 as a function of frequency (**A**) and power (**B**) of the HF field applied to the AOM. The total laser power was low enough to prevent saturation of the fluorophore. The measured count rate is then directly proportional to the intensity of the modulated laser beam.

wavelength	**power**	**HF frequency**
488 nm	17.2 db	130.275 MHz
568 nm	19.9 db	106.056 MHz
647 nm	20.9 db	90.136 MHz

Table 3.3: Optimum parameter settings for the three different laser lines available from the argon-crypton gas laser.

from a solution of Alexa568 was measured under low laser excitation to prevent fluorophore saturation. The frequency can be modulated in a wide range and a series of smaller side maxima exist. This pattern reflects the Bragg diffraction of the beam in the AOM crystal. The power setting offers a smaller dynamic range and a single maximum is obtained. Table 3.3 lists the conditions at which maximum laser transmission was achieved.

For minor attenuation the power setting is sufficient, which offers a dynamic range of a factor 2-3. Stronger attenuation, i.e. for live cell measurements, is achieved by alteration of the HF frequency and additional neutral density filters, which can be inserted in front of the AOM.

3.2.3 Single molecule spectrometer

Motivation

The FFM was designed to provide a high spatial resolution for live cell imaging by using a diffraction limited laser focus. For single molecule experiments a larger focus is more advantageous, since the photon yield scales linearly with the diffusion time (equation 2.26). The corresponding increase in background signal can be compensated by the burst selection process. The compact and inaccessible layout made it difficult to alter the parameters of the focal volume in the FFM. It prevented a visual control of the beam path within the module, and the alignment was done indirectly via the count rate on the detectors. In cross correlation experiments it was not possible to align both laser lines individually to correct for any chromatic abberations in the beam path. For alternating excitation schemes this would be essential in order to ensure an optimum overlap of the two color foci.
To overcome these limitations a flexible and openly accessible confocal setup was developed. A major focus was laid on an increased functionality in the excitation beam path which allows the use of multiple laser lines and the manipulation of the focal spot size. The modular structure of the detection beam path was preserved though. The new spectrometer was designed to meet the following requirements

1. Flexible and accessible setup which allows to easily exchange the optical components.

2. Capsuled detection module containing the pinhole, avalanche detectors and optical filters.

3. Ability to monitor the laser intensity and the beam path within the optical system.

4. Separated alignment of different laser lines to allow for correction of chromatic abberations in multicolor experiments

5. Capability for multipurpose excitation (pulsed, continuous wave, polarised) to expand the system for multiparameter detection, alternating excitation and lifetime-based methods.

6. Variation of the focal spot size to adapt for single molecule detection while maintaining the potential to perform live-cell FCS experiments.

7. Separation of laser excitation and scanning modality. Future scanning experiments will use a piezo-driven scanner that can be mounted on the microscope stage. For the single molecule analysis of immobilised molecules these systems are genrally preferred over galvanometer-based beam scanners due to an enhanced positioning accuracy.

General layout

A schematic view of the setup is presented in Figure 3.7. A major difference between the FFM and the new spectrometer is the parallel beam path at the dichroic beam splitter DC3. This element is particularly sensitive to small chromatic abberations which cause a misalignment of the two color foci, especially if a divergent beam is used such as in the FFM. As a second difference to the FFM the pinhole is now mounted in a replacable holder but otherwise fixed in position. This reestablishes a fixed reference point for confocal alignment.
In the following the different components of the spectrometer are described.

Multi laser line coupling

All lasers but the pulsed 470 nm diode were coupled to the spectrometer via single-mode fibers. The elliptical beam profile of this laser would limit the efficiency with which it can be coupled into a single-mode fiber to about 50 %. Given its maximum average power of 1 mW, this would result in a significant loss of available laser intensity. To overcome this limitation the 470 nm laser beam directly enters the spectrometer via a set of mirrors.
Various flip mirrors (FM) can be used to combine the different beams into two separate excitation paths. This allows to use any combination of the pulsed diode lasers and the argon-crypton laser without dismounting parts in the optical system. Sufficient spacing is provided for incorporation of a third excitation pathway, e.g. for triple-color alternating experiments [90].

Beam expander

Each excitation beam path contains a pair of lenses (L1a, L1b and L2a, L2b) which is used for beam expansion/reduction and correction of the beam divergence. The achromat lenses with focal lengths f and f' form a telescope with magnification $M = f/f'$. A Galilean style telescope where one of the lenses is replaced by a diverging lens is used for larger expansion/reduction factors since it offers a more compact arrangement. In either configuration the first lens is fixed while the distance between both lenses is varied by moving the second lens in axial direction.

Combination of the beam paths

Two mirrors are placed behind the telescope unit to align the beam path into the microscope. The mirrors are mounted on a wedge which is placed onto miniature translational stages and perform independent motion in x- and y-direction. By this arrangement the laser beam is conveniently positioned downstream without interfering with its passage through the telescope unit. A mirror and the dichroic beam splitter DC2 direct both laser beams onto the dichroic mirror DC3 which reflects the combined beam into the microscope.

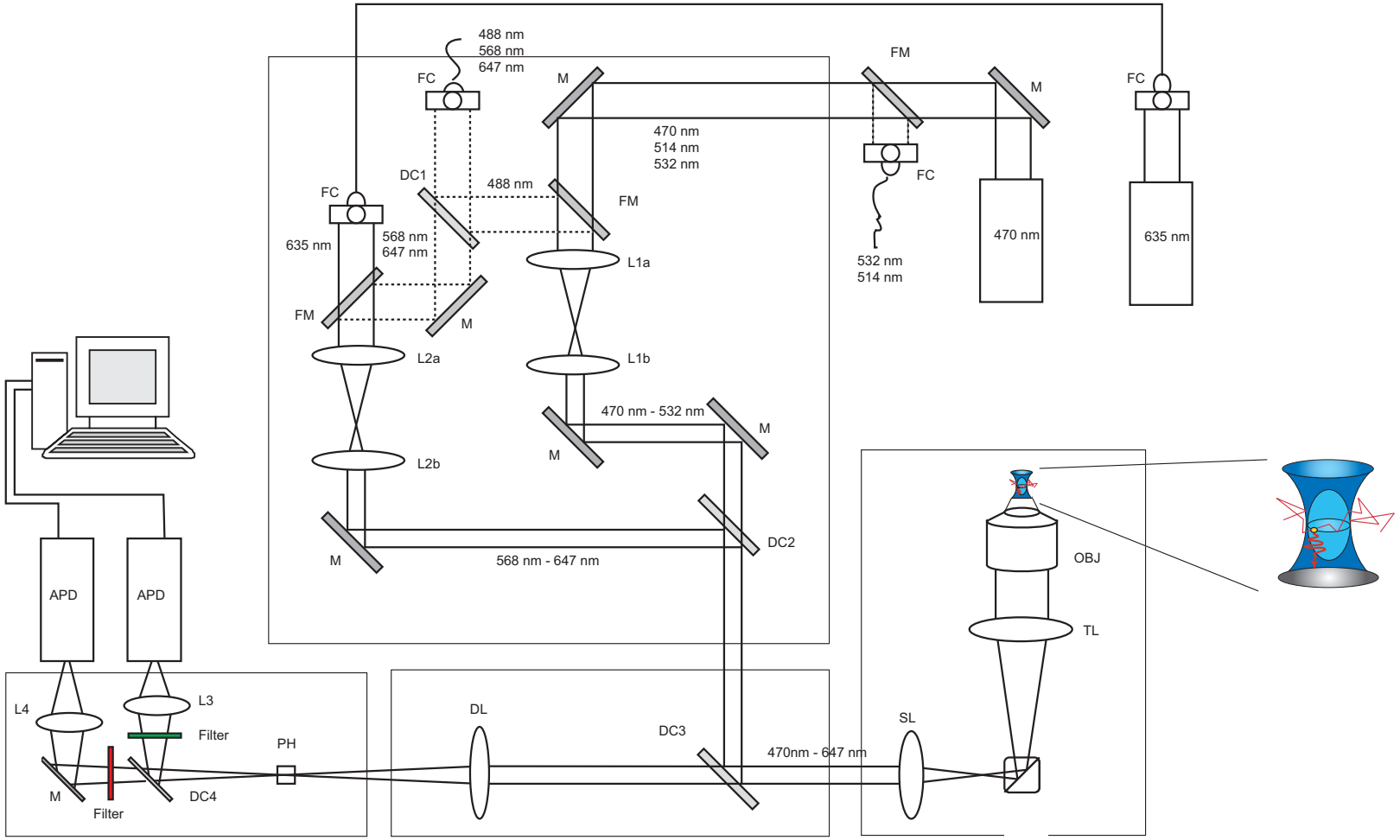

Figure 3.7: Schematic view of the single molecule spectrometer, which was developed in this work. **DCx**: dichroic mirror (x= 1,2,...), **M**: full reflective mirror, **FM**: flip mirror, **FC**: fiber coupler, **LTx**: achromat lens for the telescope unit, **Lx**: converging lens to align detection pathway, **DL**: descan lens, **SL**: scan lens (fΘ-lens), **TL**: tube lens of the microscope, **OBJ**: objective lens, **PH**: pinhole, **APD**: avalanche photodiode. A detailed description is given in the text.

Focus generation and manipulation of spot size

The objective lens focuses the laser beam to a spot whose size depends on the illumination level of its back focal aperture (BFA) and the rest divergence of the beam.
For a non-diverging beam which homogeneously illuminates the BFA we obtain a diffraction limited spot with

$$w_0 = 0.61\frac{\lambda}{NA}, \tag{3.1}$$

where λ is the wavelength of the laser light and NA the numerical aperture of the objective. For a Gaussian laser profile this is realised by overfilling the BFA such that the $1/e^2-$beam diameter is approximately twice the diameter of the back focal aperture. Under-illumination of the back focal aperture results in a reduced effective NA and larger focal volumes. A rest divergence of the beam also causes an increase in focal spot size. Focal spots of variable size were generated by changing the beam diameter entering the objective lens.

Fluorescence detection

The excited fluorophore isotropically emits its fluorescence in all directions. A fraction of these photons which corresponds to the acceptance of the objective lens (about 25 %) is collected and transmitted through the beam splitter DC3. Any photons from residual Rayleigh scattering are efficiently rejected. An achromat lens DL ($f = 120\,mm$) images the fluorescence onto the pinhole aperture located in a conjugated image plane[1]. As shown in Figure 2.4B this arrangement efficiently rejects any out-of-focus light. The fluorescence is split into two spectral regions which are defined by the emission filters and the dichroic mirrors and match the donor and acceptor emission windows.
A collimating lens in front of each detector (L3 and L4) refocuses the fluorescence onto the active area of two avalanche photodiodes which work in the single photon counting mode. The logical output pulses from the detector are further processed by the analysis hard- and software.

3.2.4 Data acquisition

The detector pulses are fed into a router (PRL400) which is coupled to the START gate of a TimeHarp200 time correlated single photon counting (TCSPC) board (both from PicoQuant GmbH, Germany). An additional signal, denoted as SYNC, is provided by a pulse generator (for cw excitation) or the laser source (for pulsed excitation). The detector pulses pass a Constant Fraction Discriminator (CFD), which discards unwanted signals by setting a threshold on the pulse amplitude. Accepted detector pulses trigger a timing circuit that is stopped by the subsequent arrival of a SYNC pulse. In conventional TCSPC systems the timing circuit essentially comprises of a highly linear ramp generator. The voltage which is generated is proportional to the time difference between detector pulse and SYNC signal (TAC - Time to Amplitude

[1]The first conjugated image plane is the common focal plane of the tube lens and the fΘ-lens

parameter	**value**	**max. range**
CFD Discr.	70 mV	0...400 mV
CFD zero Cr.	20 mV	0...40 mV
SYNC level	-60 mV	-1300...+400 mV
SYNC rate	$\approx$ 10 MHz	external device

Table 3.4: Settings of the operation parameters of the TCSPC board that were used throughout this work.

Converter). The voltage signal is then converted into a digital signal by an Analogue to Digital Converter (ADC) for further processing. Modern TCSPC boards combine the function of the TAC and ADC into a Time to Digital Converter (TDC). In these compact ciruits the time difference between two signals is measured by the delay within an array of logical gates. This provides a compact and fast TCSPC system at rather low costs.
The TCSPC board records the arrival time of each photon relative to the start of the experiment (**t**ime **t**agged **t**ime **r**esolved (TTTR-) mode). In this way it captures the full fluorescence information from the high precision ns time scale to the ms range typical for diffusion properties into one output file.
Table 3.4 lists the TCSPC control parameters used throughout all experiments.

Each photon is registered with the following information:

1. A **routing** number which identifies the photodiode in which the photon was detected (i.e. donor or acceptor channel).

2. The macroscopic **time tag** after the start of the experiment is registered with a time resolution of $100\,ns$. This entry describes the photon stream as a function of time and is used for correlation analyses and single molecule identification.

3. The microscopic **arrival time** w.r.t. the reference pulse (TCSPC timing). For pulsed excitation this time index contains the lifetime information.

The time resolution with which the arrival time is recorded can be varied as $\Delta t = 2^N \cdot 39\,ps$, where $N = 0, 1 \ldots 5$, and is stored as a 12 bit number (i.e. 4096 channels). The corresponding time interval which is covered per cycle is given by $4096 \cdot \Delta t$, e.g. $160\,ns$ for the highest resolution of $\Delta t = 39\,ps$. An additional flag marker can be set for synchronization with external devices, e.g. a piezo scanner or acousto-optical modulator.

Operation under pulsed excitation

Under pulsed excitation the SYNC pulse is provided by the laser pulse, where the repetition rate is usually chosen high enough (few $10\,MHz$) to efficiently excite the diffusing fluorophore. The time window in which fluorescence photons are registered is limited by the inverse repetition rate and intrinsic dead time effects of the electronics. Consequently, the relative timing of the START and SYNC pulse has to match the

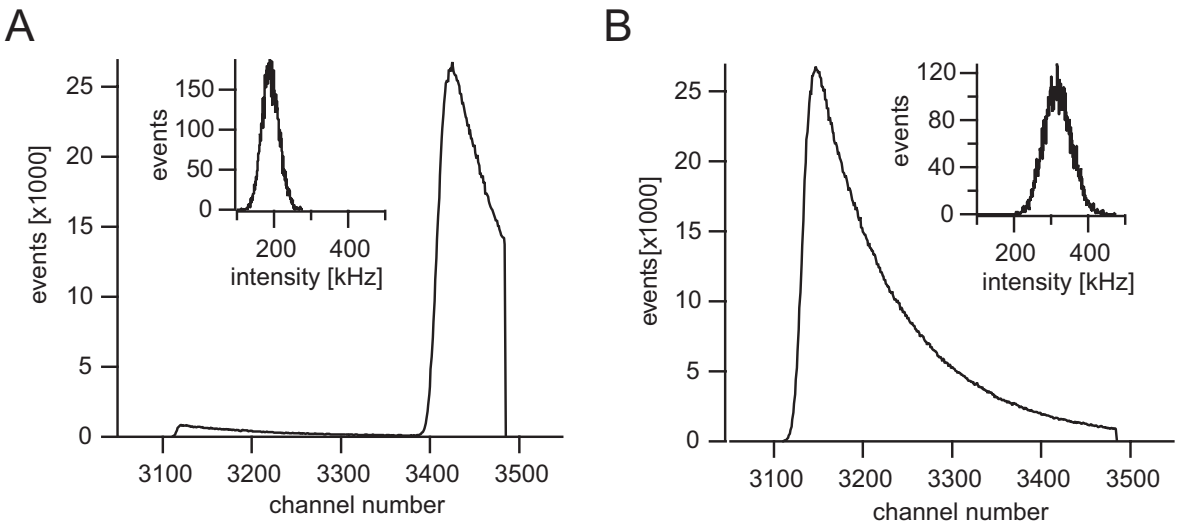

Figure 3.8: Arrival time histogram for a donor-only species under suboptimal (**A**) and optimal (**B**) timing conditions. The inlay sketch depicts the intensity histogram for a bin width of $1\,ms$. Suboptimal timing leads to a significant reduction in the number of detected photons and a distortion of the arrival time histogram.

TCSPC window to optimise the photon yield. A suboptimal timing occurs if the cabel length for both signals is chosen inappropriate as demonstrated in Figure 3.8A .
The time difference between the START and STOP signal does not match the TCSPC window and a truncation of the arrival time histogram was observed. As shown in the inlay histogram this was accompanied by a considerable reduction in count rate compared to optimum timing conditions (panel B). There on average more than 50 % more photons were detected and the arrival time histogram reflected the familiar exponential decay. The lifetime was reproduced more accurately ($\tau_{Al488} = 3.7 - 3.8\,ns$ compared to $\tau_{Al488} = 3.3 - 3.4\,ns$ obtained under suboptimal timing conditions). The timing between START and STOP pulse is adjusted by appropriate cabel lengths. Alternatively a custom built electronic delay unit can be inserted into one of the signal pathways which allows to continuously delay one signal with respect to the other.

3.3 Data analysis

In a typical data file from a single molecule experiment a few million photon records are stored in a binary data format (*.t3r). Most of the entries correspond to background photons and contain no useful information. Consequently, the data has to be reduced to the information on those photons that belong to a single molecule event.
To do so the raw data was smoothed by a LEE filter [42] and single molecule transits were selected by a method presented in [39]. Both tasks were performed by an analysis program (FRETtchen) which was developed during this thesis. The data was further analysed and visualised in a commercial software package (IGOR PRO, WaveMetrics, OR, USA). First, the principle of LEE filtering and subsequent data analysis is outlined, followed by a description of the FRETtchen software.

3.3.1 LEE-filtering of the raw data stream

Ideally, the signature of a single molecule diffusing through the focal volume consists of a gradual rise and fall in fluorescence intensity. The time interval between successive photons decreases and increases back to the background level. The fluctuations in the number of recorded photons result in spurious intermittence of the photon stream. This can be falsely interpreted as the molecule leaving the focus. If already enough photons have been detected a burst with smaller effective size will be registered, otherwise the event might not be registered at all.
To avoid such misclassification the raw data stream was smoothed by a LEE filter [42]. This sliding average filter removes sharp fluctuations from the signal while maintaining the signal strength of the individual bursts. For the interphoton time of the k-th photon, δt_k, a LEE filter of width $2M_L + 1$ determines a sliding average $\overline{\delta t_k}$ and a variance σ_k^2:

$$\begin{aligned} \overline{\delta t_k} &= \frac{1}{2m+1} \sum_{j=-M_L}^{M_L} \delta t_{k+j} \\ \sigma_k^2 &= \frac{1}{2m+1} \sum_{j=-M_L}^{M_L} (\delta t - \overline{\delta t})_{k+j}. \end{aligned} \tag{3.2}$$

The smoothed interphoton time distribution is given by

$$\delta t'_k = \overline{\delta t_k} + (\delta t_k - \overline{\delta t_k}) \frac{\sigma_k^2}{\sigma_k^2 + \sigma_0^2}. \tag{3.3}$$

where σ_0 is a characteristic constant of the filter which was set to 5, if not otherwise stated. As shown in Figure 3.9A , LEE filtering of the raw data efficiently smoothed the background where occasional drops in interphoton time marked true single molecule events. The unfiltered distribution was subject to large background fluctuations and the single molecule bursts were hidden within. It is obvious that reduction of the background fluctuations greatly enhanced the discrimination of true single molecule events.
The consequences of LEE filtering on the proximity ratio distribution is shown in Figure 3.9B . Data was analysed at different thresholds N_{min} with and without prior LEE filtering. While the histograms from the filtered and unfiltered data were similar to eachother for low N_{min} values, (I) and (II), differences were observed at larger values of N_{min}. The double peak structure of the FRET population was correctly reproduced in the filtered data set (IV), whereas the intact FRET distribution was skewed if no LEE filter was applied (III).

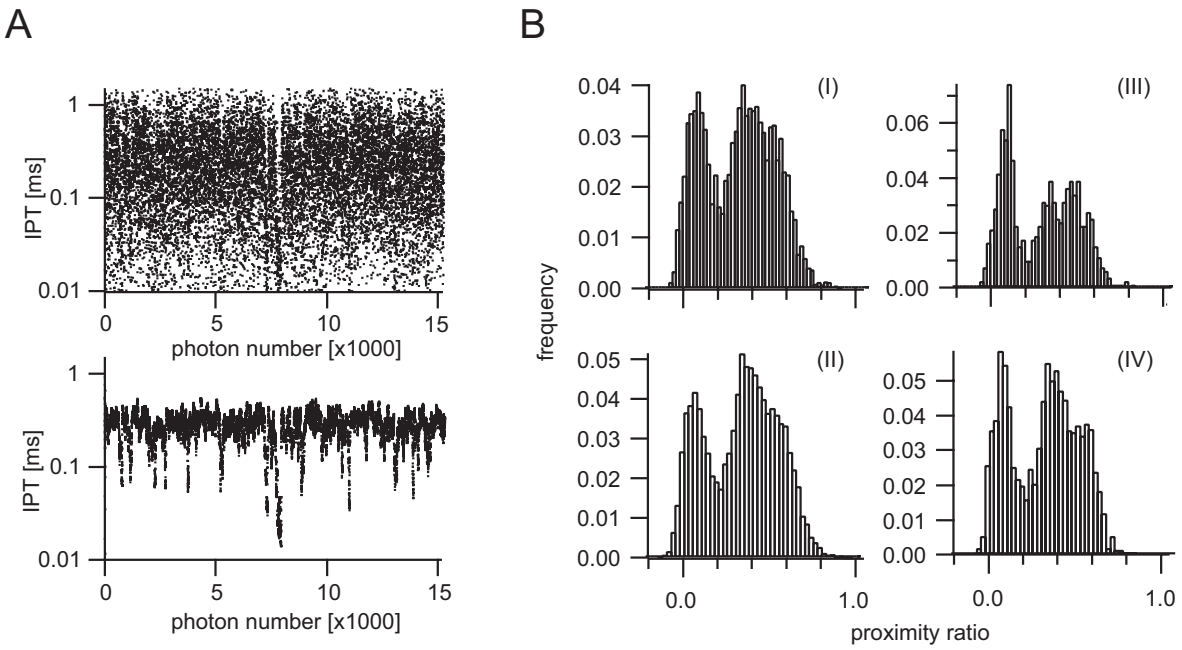

Figure 3.9: **A**: LEE filtering of the raw interphoton time distribution. Top panel: unfiltered data, bottom panel: LEE-filtered data ($M_L = 8$). TSingle molecule transits can be discriminated against the background level. **B**: Single molecule histograms of 601^{170}_{med} nucleosomes with and without prior LEE filtering. Unfiltered data analysed with $N_{min} = 50$ (I) and $N_{min} = 100$ (II). Filtered data analysed with $N_{min} = 50$ (III) and $N_{min} = 150$ (IV).

3.3.2 Single molecule data analysis

A single molecule event is characterized by several parameters. During this thesis mostly the following were analysed:

- The **burst duration** is calculated as the time difference between the first and last photon of the event. It is used to analyse major changes in the diffusion properties. Generally the burst duration is considerably longer than the mean diffusion time of the molecule. The burst selection algorithm prefers long lasting particle transits since only these events produce enough photons to be accepted. The burst duration shows a broad asymmetric distribution and is approximated by a LogNormal function.

- The sum of all detected photons within the burst is the **burst size**. A majority of events has a low number of photons since most molecules transit the focus through the peripheral regions thus emitting less fluorescence. The burst size distribution roughly follows an exponential curve (compare to Figure 3.10).

- An apparent **photon rate** per burst is determined as the burst size divided by the burst duration. This quantity is a measure for the emissivity of the molecule and analogous to the molecular brightness defined in section 2.4. The corresponding distribution follows a LogNormal function.

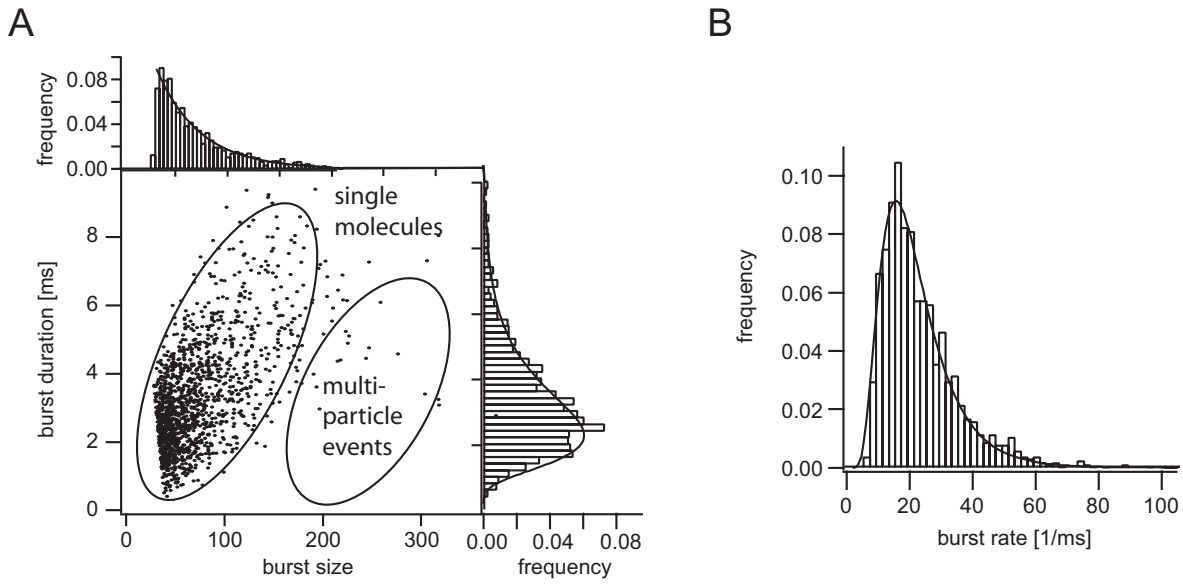

Figure 3.10: **A**: Two-demensional diagram showing the relation between burst size and burst duration. For a single species both parameter are correlated and a larger burst duration generally results in a larger burst size. The distribution of the corresponding parameters are shown as one-dimensional projections. **B**: Distribution of the apparent burst rate, which was calculated as the ratio of burst size and burst duration.

For a single molecule these quantities are correlated to each other as shown in Figure 3.10A . A larger burst duration generally results in an increased burst size. In a two dimensional representation of burst duration versus burst size the majority of molecules are clustered around a straight line, which corresponds to an inverse photon rate per burst. Events of short duration but significantly increased burst size presumably arise from the presence of several molecules in the focus. They show up as an additional distribution in the plot and can be rejected by an appropriate threshold on the apparent burst rate.

Ratiometric histograms

Either the FRET efficiency or the proximity ratio is calculated burstwise to analyse the distribution of interfluorophore distances. Histograms are built for the whole data set (or subsets if required) to reveal the presence of subpopulations in the ensemble. These will cause a heterogeneous distribution of P or E submaxima which are quantified by a series of Gaussian functions[2]. The information which is extracted from the histogram is summarized in Figure 3.11. The relative peak area is a measure of the fractional occupancy of a particular conformation. The center position of a subpopulation relates to its energy transfer. The width contains information about static and dynamic het-

[2]Approximation by a Gaussian function yields accurate results for intermediate transfer efficiencies, where $0.2 < E, P < 0.8$. For the high- and low-FRET regime an asymmetric betafunction was shown to be more appropriate [32]. Due to broadening by background and crosstalk correction, however, a Gaussian function was usually appropriate for those states as well

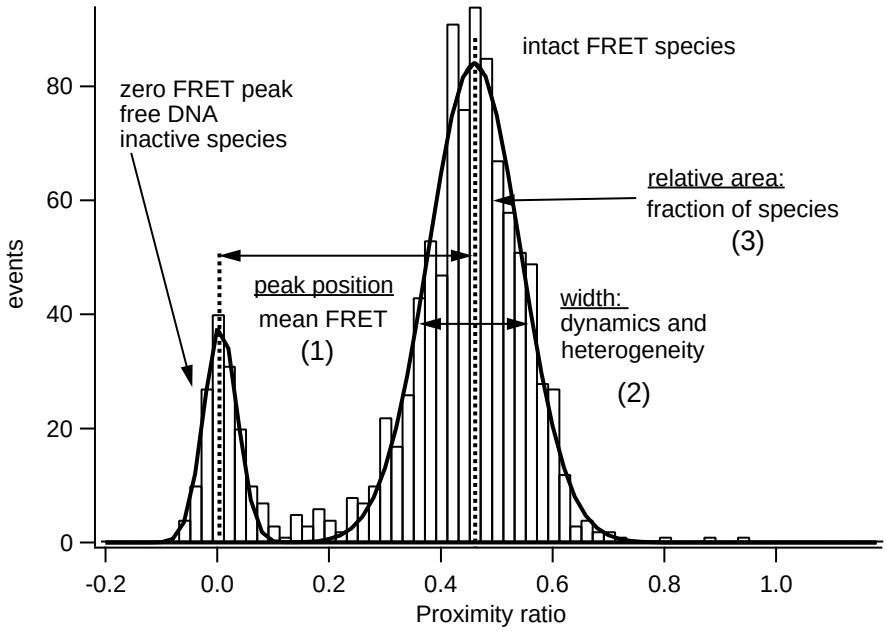

Figure 3.11: Typical proximity ratio distribution of a double labeled 26 bp DNA fragment which shows the various parameters that can be obtained from the populations. Further details are given in the text

erogeneities in the system. Any dynamic processes that occur at time scales faster than the observation time (which usually corresponds to the burst duration) are averaged out and cause further broadening. Quasi-static subpopulations which are below the resolution limit also contribute to the excess width which is considerably larger than the shot noise limit estimated in section 2.3.2. A complete description of this aspect requires a detailed analysis of the underlying photon statistics [4] and will be addressed in section 5.2.

Time trace analysis

To extract dynamic information on a time scale much larger than the diffusion time, the distribution of any burst property can be analysed as a function of time. Figure 3.12 depicts the time course of the detected proximity ratio. The time course is either analysed by binning the property of interest, e.g. the proximity ratio, into sub-histograms for different time intervals. A change in histogram shape directly reflects the presence of conformational transitions in the sample. Alternatively, a particular substate is selected and its occupancy determined over time. In this approach the parameter to be binned is the corresponding time index. In panel B the occupancies of the intact FRET population (a) and the zero-FRET peak (b) are binned over time. The corresponding ratio $b/(a+b)$ is a measure of sample stability and can be used to derive apparent dissociation or assembly rates. This analysis scheme offers a higher

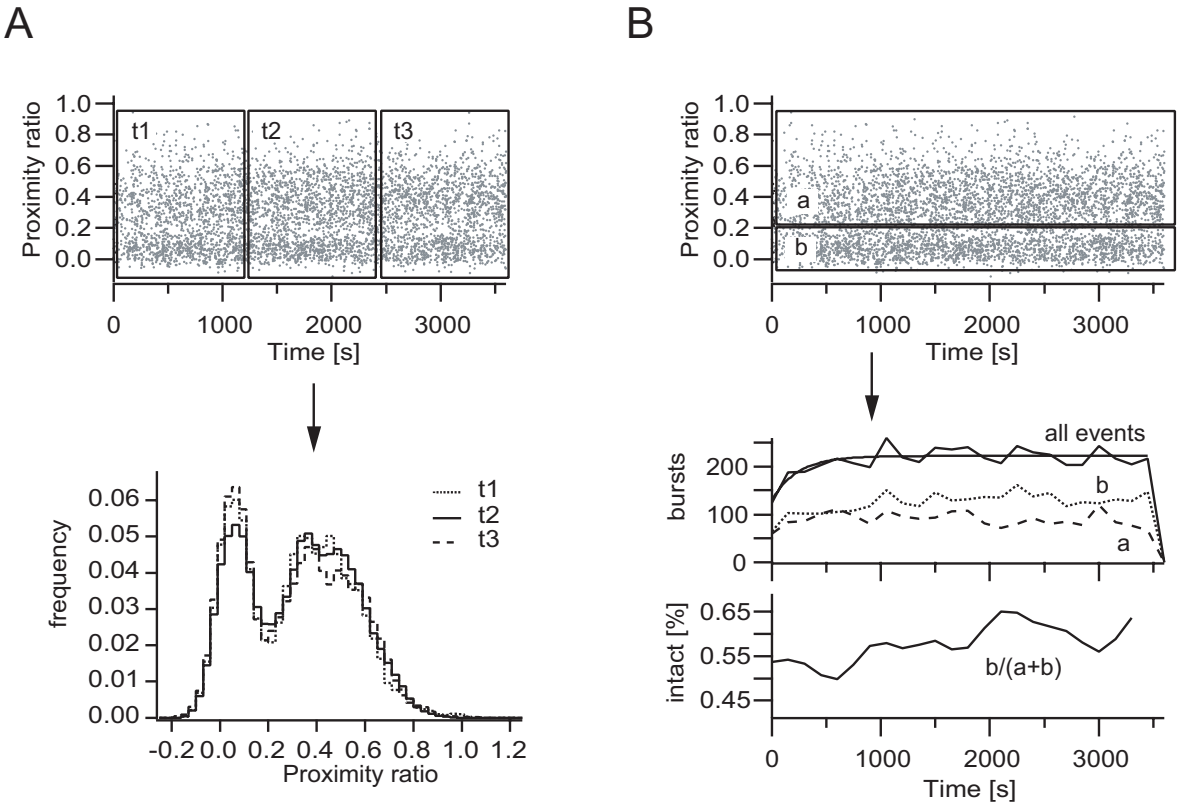

Figure 3.12: Illustration of two methods to analyse the time course of an SMD experiment. **A**: The property of interest (in this example the proximity ratio) is histogrammed for different time intervals t_i. Changes between these subhistograms indicate transitions between different subconformations. **B**: Alternatively, the property itself is grouped into two or more regions, each of which is analysed as a function of time. In this scheme the time of detection is binned for all molecules within the subgroup. This can be used to calculate the temporal change in relative substate occupancy.

time resolution as compared to (A) where a larger time is required to build up the subhistogram. The former method offers a larger discrimination of conformational substates though. Both methods are used in combination with each other and provide complementary information.

3.3.3 Data analysis software - The program "FRETtchen"

The analysis program FRETtchen was developed to perform the data reduction and single burst identification. The functionality of the software is sketched in Figure 3.13. In a first step the photon record is ungrouped and its information (router, timetag and arrival time) is stored into separate arrays. From the time tag information a raw interphoton time (IPT) is calculated which describes the time lag between two successive photons. A LEE filter smoothes the raw interphoton time distribution for further burst selection. The filter parameters M_L and σ_0 can be chosen within the software.

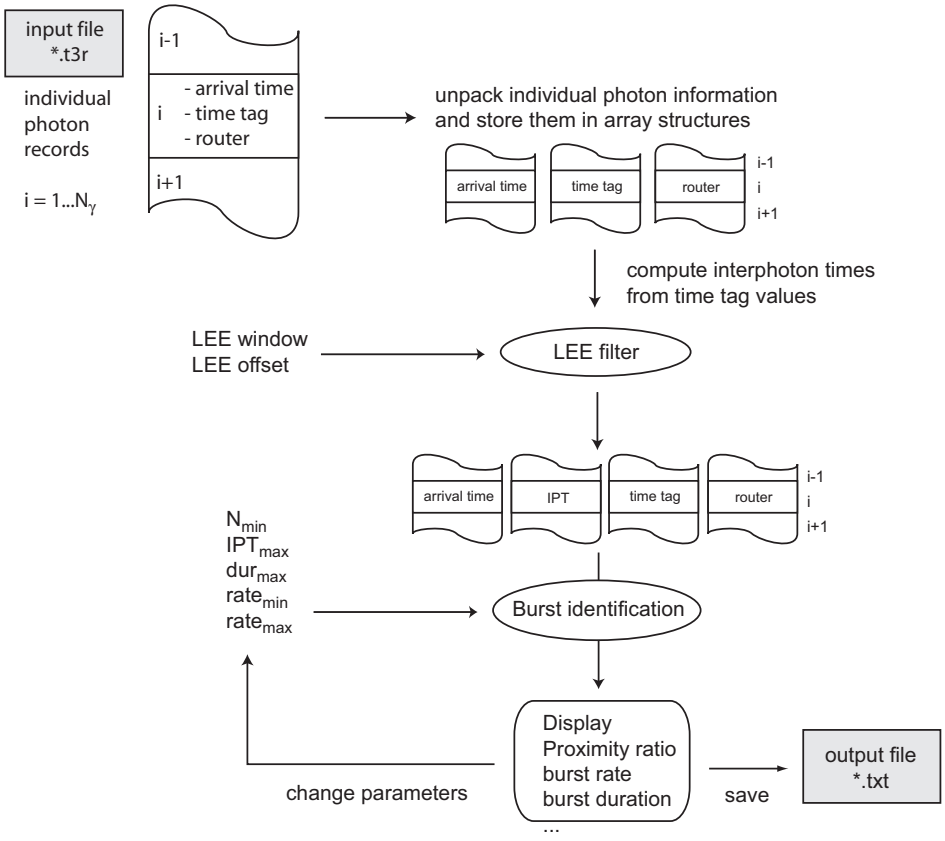

Figure 3.13: Functionality of the FRETtchen software. A detailed description is presented in the text.

A series of consecutive photons defines a single molecule event if the filtered interphoton times of at least N_{min} photons do not exceed an upper threshold IPT_{max}. A suitable value for IPT_{max} is selected by a visual inspection of the interphoton time distribution as shown in Figure 3.14. IPT_{max} should be low enough not to include the background photons. At the same time it cannot be chosen too small since otherwise too many true events are excluded.
After burst selection an apparent burst duration and photon rate per burst are calculated for each event. These parameters are used to discard events that are either too long or too bright, both which are considered as potential multiparticle events.

The distributions of the proximity ratio and the burst duration versus burst photon rate are displayed for further inspection (see Figure 3.14B). The latter distribution should not include any events at large burst rates. The quality of the data is assessed by the number of detected events, a mean proximity ratio and a mean photon rate per burst. Based on those parameters the selection process can either be repeated using a modified set of parameters, or the single molecule data can be stored into an ASCII file. For each event the output file contains the following information:

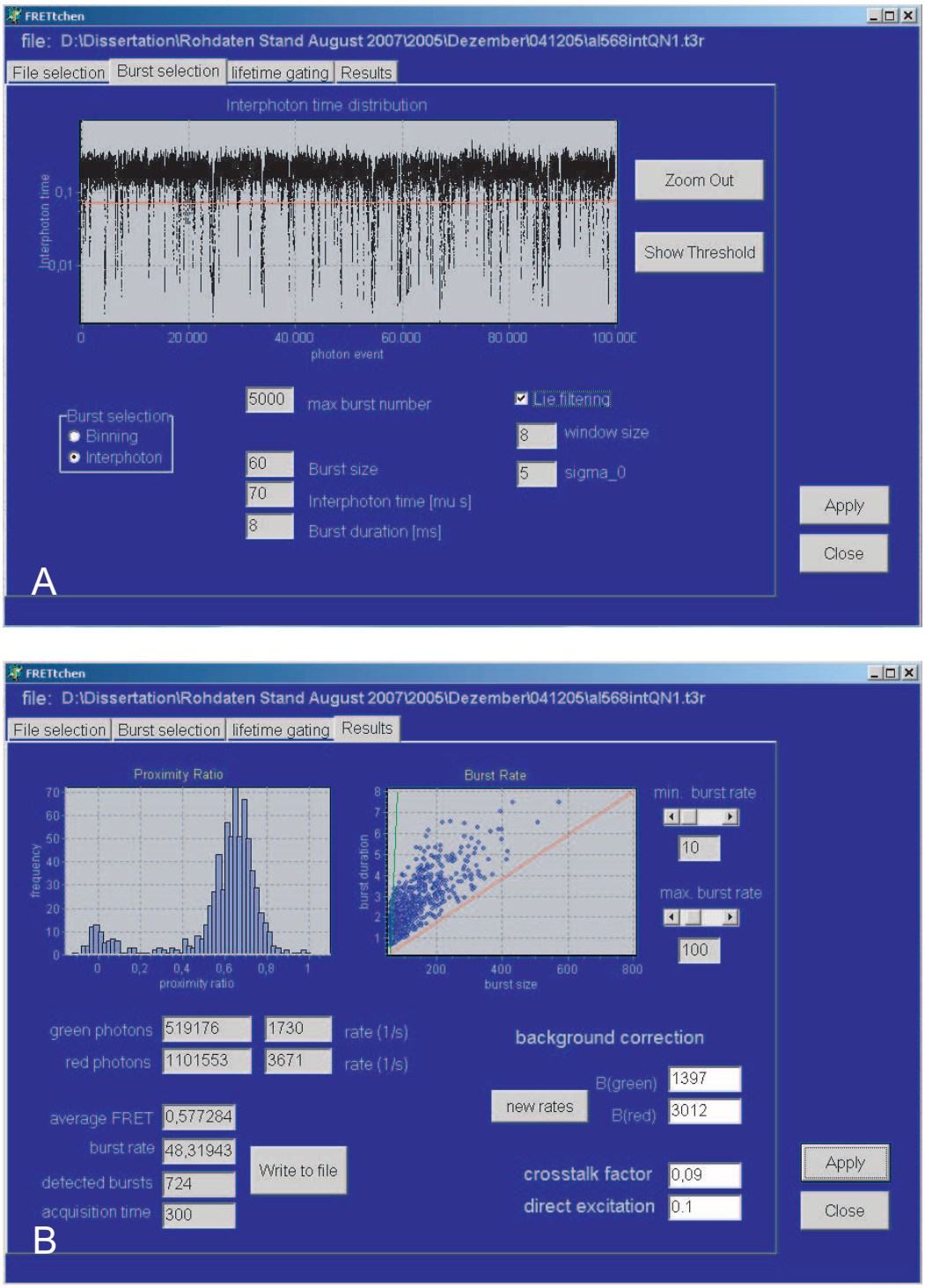

Figure 3.14: User interface of the FRETtchen software. **A**:Setting of burst parameter thresholds and LEE filter window parameters. **B**: Inspection of the analysis results. Preliminary histograms for the proximity ratio, as well as the correlation of burst size and burst duration are shown in the upper part. The lower part depicts a variety of parameters used to assess the quality of the data analysis.

- The time of detection
- The duration of the burst
- The number of photons in both detection channels
- The proximity ratio
- The rate of photons in the burst

Data from various short time runs can be combined to simplify the further analysis (*append* mode).

3.4 Detection parameters and calculation of P

3.4.1 Determination of the detection parameters

To calibrate the system a precise determination of the crosstalk $alpha_{DA}$ and the detection factor γ is required. These parameteres can be determined from the experiment as described in the following.

Crosstalk

A donor-only sample is used to measure the crosstalk factor α_{DA}. Under nM concentrations the crosstalk is calculated as the background-corrected count rate in the acceptor channel, I_A, divided by the corresponding signal in the donor channel, I_D. We have $\alpha_{DA} = I_A/I_D$.
In a single molecule experiment the total count rates are too low to determine a precise crosstalk this way. Instead, the center position of the proximity ratio histogram, $P_{donor-only}$, is used to calculate α_{DA}. According to equations 2.40 and 2.41 the photon signal from a donor-only sample ($E = 0$ and $\eta_A = 0$) is given by

$$N_D = I_D^{det} - B_D = \eta_D \sigma_0 \Phi_D I_0 \tag{3.4a}$$
$$N_A = I_A^{det} - B_A = \eta_{DA} \sigma_D I_0 \Phi_D. \tag{3.4b}$$

$P_{donor-only}$ is then calculated as

$$\begin{aligned} P_{\text{donor-only}} &= \frac{\eta_{DA}\sigma_D\Phi_D I_0}{\eta_{DA}\sigma_D\Phi_D I_0 + \eta_D\sigma_D\Phi_D I_0} \\ &= \frac{1}{1+\eta_D/\eta_{DA}}. \end{aligned} \tag{3.5}$$

The crosstalk factor $\alpha_{DA} \equiv \eta_{DA}/\eta_D$ results as

$$\alpha_{da} \equiv \frac{\eta_{DA}}{\eta_D} = \left(\frac{1}{P_{\text{donor-only}}} - 1\right)^{-1} \tag{3.6}$$

Direct acceptor excitation

Many acceptror fluorophores used for FRET experiments have a non negligible probability to be directly excited at the laser wavelength used to excite the donor. Without correction for the direct excitation the acceptor channel contains additional photons that are falsely attributed to the sensitized emission. Larger proximity ratios are observed and the FRET efficiency is overestimated. Under bulk concentrations the direct excitation, f_{dir} can be estimated as the molecular brightness of a concentrated acceptor-only sample excited at 488 nm:

$$f_{dir} = \frac{\langle F_{acc} \rangle_{488\,nm}}{N}. \tag{3.7}$$

N is the number of molecules in the focus and $\langle F_{acc} \rangle$ the mean count rate in the acceptor channel. f_{dir} depends on the laser intensity which has to be identical to that used in the single molecule experiment.
A different way to determine f_{dir} is to measure it under single molecule conditions. A double labeled species with no FRET, e.g. an end-labeled long DNA fragment, is analysed to obtain an estimate of f_{dir}. After correction for crosstalk and background the center of the proximity ratio peak $P(E = 0)$ is a measure of the rate of direct excitation relative to the emission rate of the donor. With $E = 0$ and $\alpha_{DA} = 0$ equations 2.40 and 2.41 yield

$$N'_D = \eta_D \sigma_0 \Phi_D I_0 \tag{3.8a}$$
$$N'_A = \eta_A \sigma_A \Phi_A I_0 \equiv f_{dir}. \tag{3.8b}$$

The proximity ratio $P(E = 0)$ is given by

$$\begin{aligned} P'(E=0) &= \frac{f_{dir}}{f_{dir} + \eta_D \sigma_D \Phi_D I_0} \\ &= \frac{1}{1 + \eta_D \sigma_D \Phi_D I_0 / f_{dir}}, \end{aligned} \tag{3.9}$$

and we have

$$f_{dir} = \left(\frac{1}{P(E=0)} - 1 \right)^{-1} (\eta_D \sigma_D \Phi_D I_0). \tag{3.10}$$

The signal rate from the donor fluorophore, $\eta_D \sigma_D \Phi_D I_0$, is best determined from an identical construct which carries no acceptor dye.

Detection factor

A bulk experiment of the double labeled no-FRET sample yields an estimate of the detection factor γ. The background corrected count rate in the acceptor channel, I_A, contains the direct excitation as well as the crosstalk:

$$I_A = \alpha_{DA} \cdot I_D + f_{dir}. \tag{3.11}$$

If the extinction coefficients $\epsilon_{D/A}(488\,nm)$ of both fluorophores are known, the detection factor is determined by

$$\gamma = \frac{f_{dir}^{488\,nm}}{I_D^{488\,nm}} \cdot \frac{\epsilon_D(488\,nm)}{\epsilon_A(488\,nm)}. \tag{3.12}$$

3.4.2 Calculation of the proximity ratio

Taken all factors together, the proximity ratio for the $k-$th molecule is calculated as

$$P^{(k)} = \frac{N_A^{(k)} - (b_R + f_{dir})d^{(k)} - \alpha_{DA}(N_D^{(k)} - b_G d^{(k)})}{N_A^{(k)} - (b_R + f_{dir})d^{(k)} - \alpha_{DA}(N_D^{(k)} - b_G d^{(k)}) + (N_D^{(k)} - b_G d^{(k)})}. \tag{3.13}$$

Here b_G and b_R are the background rates determined from the buffer solution. It is noted that the donor-only contribution in the histogram is overcorrected, if P is calculated via equation 3.13. In this case no acceptor fluorophore is present to contribute to the direct excitation. For an exact treatment the proximity ratio of the donor-only fraction has to be calculated with $f_{dir} = 0$. To do so, a donor-only species has to be distinguishable from a double labeled no-FRET species. This requires to probe for the presence of an acceptor while the molecule diffuses through the focus and can be achieved by rapidly alternating between donor and acceptor excitation [76, 104].

Effect of background and crosstalk correction on the distribution width

As stated above the observed distribution width is generally larger than expected from the shot noise. This partially reflects the static and dynamic heterogeneity in the sample but is also due to the crosstalk and background signal.
The correction for background is based on an average rate of background photons multiplied with the burst duration. This only estimates the number of true background photons which vary statistically around the subtracted value. A similar argument holds for the crosstalk correction. As a result additional noise is imposed on the data and the corrected proximity ratio distribution will show a considerable broadening as compared to the histogram from the raw photon counts. These, however, do not contain the correct information as the proximity values are overestimated. Figure 3.15 demonstrates this aspect on a mixture of different FRET standards. The histogram was analysed before and after the correction for background and crosstalk. The corresponding parameters from a Gaussian fit are shown in the table. Crosstalk correction led to a shift of the peak position towards smaller values. The largest effect occurs for the low-FRET population. High-FRET states are less affected by the crosstalk correction since the excess photons contribute less to the detected photons in the acceptor channel.

In summary, the distribution of proximity ratios is considerably broadened, where a $20-25\,\%$ increase was observed for all subspecies. The fractions of the subpopulations in the histogram remained unaffected, indicating that the correction procedure does not affect the apparent occupancy of subconformations within the ensemble.

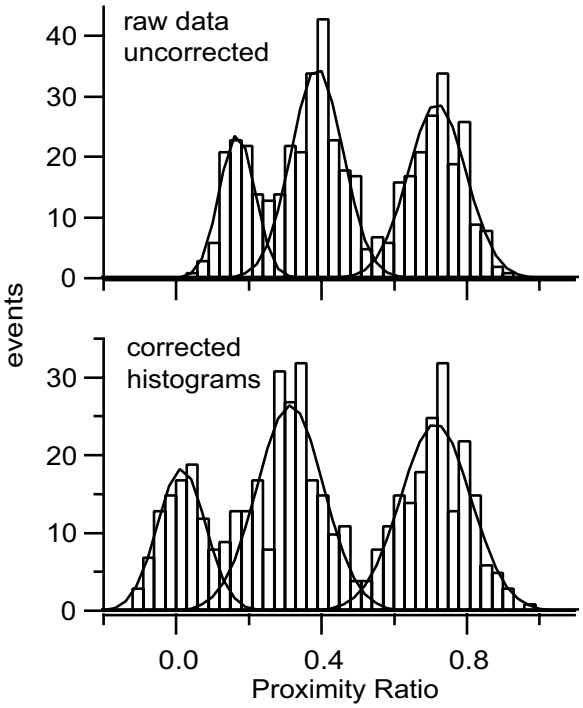

parameter	raw	corr
x_0	0.167	0.012
ω_0	0.069	0.094
A_0	0.194	0.203
x_1	0.387	0.313
ω_1	0.101	0.129
A_1	0.417	0.406
x_2	0.718	0.714
ω_2	0.113	0.137
A_2	0.389	0.391

Figure 3.15: Effect of crosstalk and background correction on the proximity ratio histogram. x_i denote the center peak position, ω_i the distribution width and A_i the relative occupancy if the different peaks. A 20 % increase in the distribution width was observed for all populations. The donor crosstalk results in a FRET-dependent shift of the peak center position.

3.5 Multiparameter fluorescence detection

The fluorescence signal from a single molecule contains a variety of different parameters: the fluorescence intensity, the excited state lifetime, the polarisation and spectral information. The simultaneous analysis of all parameters greatly enhances the ability to discriminate between complex substructures and substates and to can be used to reject potential artefacts from the analysis.
Multiparameter analysis methods have been pioneered by the groups of Claus Seidel [56] and Richard Keller [107] in the late 90's, mainly to reduce the probability of particle misclassification. From then on this approach has been evolved into a powerful concept which recently pushed the distance resolution in FRET experiments down to the Angstöm level [4, 75]. In collaboration with the group of Prof. Seidel for the first time a multiparameter analysis of single nucleosomes was performed in free diffusion. Figure 3.16A shows the confocal setup used to capture all relevant fluorescence parameters.

The sample was excited with a pulsed argon laser at 477 nm. Individual molecules were selected based on the interphoton time distribution as described above. Data was analysed with a complex software package which performed the cleaning and sorting of the raw burst distribution and the further analysis. For each individual burst the following parameters were calculated.

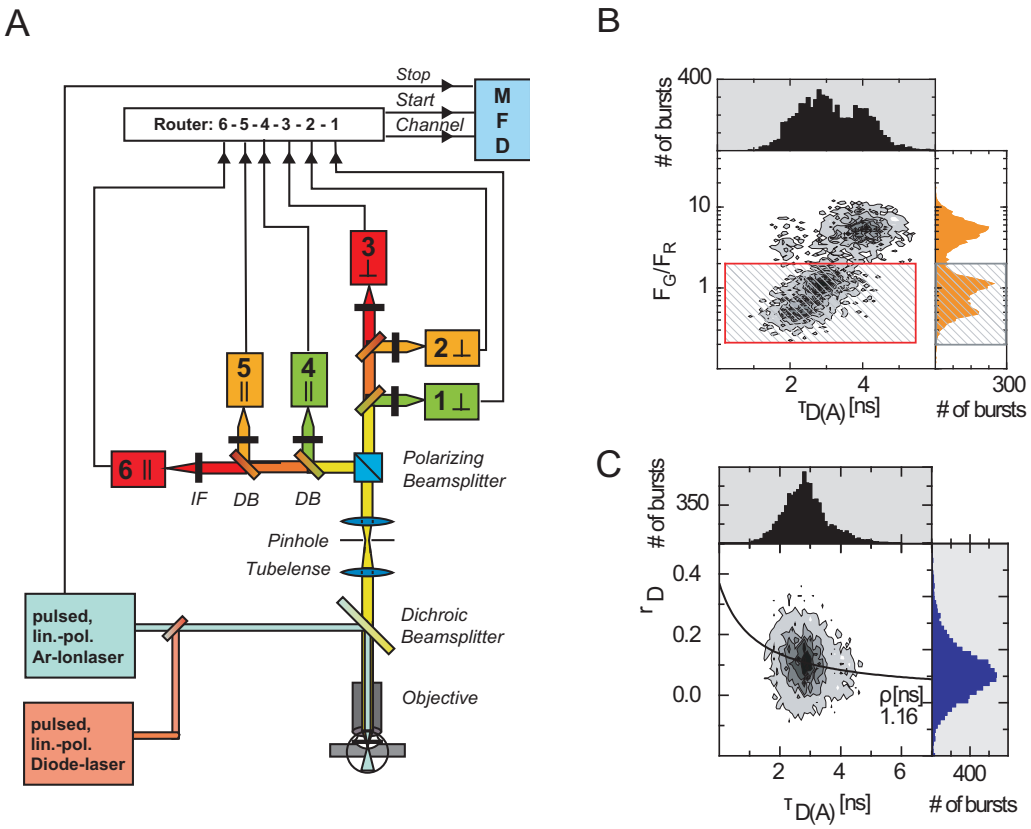

Figure 3.16: **A**: Schematic view of the confocal setup used in the group of Prof.Seidel. Separation of subspecies according to (**B**) their donor lifetime and intensity ratio and (**C**) the donor lifetime versus donor anisotropy (shown for a different sample).

- The **intensity ratio** between donor and acceptor signal, F_D/F_A. In this quantity the FRET effect is amplified since the the nominator and denominator are affected in an opposite way. Using the notation of [56], the intensity ratio is given as

$$\frac{F_D}{F_A} = \frac{g_R}{g_G} \frac{S_G - B_G}{(S_R - B_R) - \alpha_{da}(S_G - B_G)} \tag{3.14}$$

  The equivalent quantities used in this work are: $g_G \equiv \eta_D$, $g_R \equiv \eta_A$, $S_G \equiv I_D^{det}$, $S_R \equiv I_A^{det}$ $F_D \equiv N_D/\eta_D$ and $F_A \equiv N_A/\eta_A$.

- The **lifetime** which is determined from the arrival times of all photons contained in the event. The TCSPC histogram is deconvolved with an instrument response function and approximated by a maximum likelihood estimator to extract a reliable value of τ_F (for details, see [38]).

- The **anisotropy**, which is a measure of the rotational motion of the molecule. This quantity is calculated from the photons with parallel and orthogonal polarisation w.r.t. the excitation light. Corrections have to be applied for polarisation dependent effects in the optical system and the polarisation mixing for high NA objectives.

The total ensemble was represented in a two-dimensional parameter space which classifies the molecules into subpopulations as shown in Figure 3.16B . FRET species were identified as events where the intensity ratio F_G/F_R correlates with the shortening of the donor lifetime (solid line). Molecules where the donor lifetime was reduced, but which did not show a significant acceptor fluorescence, were rejected.
Similarly the anisotropy was analysed to gain further information on the rotational mobility. Again, a correlation between anisotropy and donor lifetime exists for proper FRET species (panel C). Subsequently, regions of interest were defined which were used for further data analysis. Of the various analysis tools developed in the Seidel lab two methods were particularly helpful to uncover dynamic processes within the system.

Time window analysis

A burst-wise analysis in which all photons within the burst are analysed profits from larger photon numbers and reduced shot noise broadening. Any processes which occur on a time scale faster than the diffusion time will be averaged out and result in a dynamic broadening of the distribution beyond the shot noise limit. No information on the time scale of the underlying processes can be obtained.
To gain information on potential intraburst dynamics the photons from all bursts are grouped into fixed time windows which are smaller than the diffusion time. Individual substates are expected to appear in the histogram if there is any dynamics on a time scale comparable to the binning time. A comparison of histograms for different time windows enables to extract the time scale of potential intraburst dynamics that is hidden in the burstwise analysis.

Photon distribution analysis

A thorough analysis of the underlying photon statistics allows to differentiate between static and dynamic heterogeneities and to extract information from a complex FRET efficiency distribution. The width of a distribution comprises of a contribution from intrinsic shot noise and additional broadening from any kind of heterogeneity. If the exact shot noise pattern is known the distribution of conformations that generate the additional broadening can be computed[3].
The exact shot noise limit is calculated from the underlying photon statistics including crosstalk and background correction. From a calculated signal distribution a model histogram is built which includes the shot noise. This is then compared to the experimental distribution. In doing so the minimum number of subspecies required to describe the observed distribution can be deduced [4]. Thie method is expected to provide an ultimated distance resolution of the order of 1 $\mathring{A}$.

[3]This is somewhat analogous to a deconvolution of a signal with an instrument response function, e.g. for image processing

Chapter 4

System optimisation

Efficient detection of a diffusing molecule requires an optimum collection of its emitted photons, in order to discriminate its spurious fluorescence against the background level. This implies optimising the individual processes that influence the number of photons detected from the molecule. These are the excitation of the fluorophore, the conversion of excitation energy into fluorescence and the detection of the emitted photons.
Even if a maximum number of photons is detected, an improper burst selection, which is described in section 3.3, still leads to suboptimal particle identification and potential misinterpretation of the data. Consequently the range of useful selection thresholds has to be defined.

The optimum excitation intensity can be derived from theoretical calculations as well as experimental data. Both aspects are discussed in the first part of this chapter. A significant portion of this chapter then adresses the photostability of the dye molecules. It is important to maintain a high flux of emitted photons and to obtain a correct fluorescence signal according to the interdye distance. A set of stabilising conditions was found which minimised artefacts due to photobleaching and guaranteed a sufficiently high photon flux. The detection effciency was optimised by choosing an appropriate filter combination. Maximising the detection efficiency was found to be not always favorable, in particular if Raman scattering has to be considered. Finally a thorough discussion addresses the question how far the choice of threshold settings influences the outcome of the SMD experiment. The analysis of various burst parameters obtained under different selection conditions led to a range of appropriate threshold settings.

The chapter concludes with a brief discussion of how to further enhance the total photon yield from the diffusing molecule. Two approaches are discussed which aim to increase the diffusion time of the particle. A straightforward method is to enhance the viscosity of the medium, while a more recently developed approach increases the effective hydrodynamic radius of the molecule of interest by embedding it into a lipid vesicle container.

4.1 Optimum fluorophore excitation

Optimising the photon flux from the fluorophore generally requires increasing the absorption rate k_{01}, which is proportional to the laser intensity. At the same time, though, the intensity has to be kept low enough to prevent saturation of the fluorophore. Once the fluorophore saturates, no gain in photons is obtained, while the background is increased unnecessarily. These two contradictory aspects lead to an optimum range of laser intensities, at which the signal-to-background ratio is maximised and which is determined in the following.

Intuitively, it is advisable to increase the intensity until the rate of photon absorption equals the rate of deexcitation. The corresponding intensity is known as the saturation intensity, I_{sat}, and can be determined by measuring the molecular brightness of the fluorophore as a function of applied laser intensity.
Far below saturation the fluorescence output scales linearly with the laser intensity. As the excitation intensity I is of the order of I_{sat} the molecular brightness of the fluorophore is no longer proportional to I and starts to saturate. At intensities $I \gg I_{sat}$ a stagnation of $\eta(I)$ is observed since a further increase of intensity does not result in a gain in emitted photons as shown in Figure 4.1A for a solution of free Alexa488. The data is plotted in terms of the applied laser power rather than the intensity itself. The dependence of the molecular brightness on the laser intensity is described by

$$\eta(I) = \eta_{max} \frac{I/I_{sat}}{1 + I/I_{sat}}, \tag{4.1}$$

For free Alexa488 saturation occured at a power of $P_{sat} = 119 \pm 10\,\mu W$. The corresponding intensity is given as P_{sat} divided by the cross-section area of the laser focus, A_{focus}. If we approximate the detection volume by a rotational ellipsoid with semiaxes (w_0,w_0,z_0), the cross-section area is given by $A_{focus} = \pi w_0^2$. For a measured diffusion time of $59\,\mu s$ and an estimated diffusion coefficient of $D = 3.2 \cdot 10^{-10} m^2/s$ we obtain $w_0 = \sqrt{4D\tau_D} = 275\,nm$, which results in an intensity of $I_{sat} = 50 \pm 5\,kW/cm^2$.
If the photokinetic rates of the fluorophore are known, I_{sat} can be calculated directly from equation 2.14. For Alexa488 the following parameters were taken from the literature: $\sigma_{01} = 2.71 \cdot 10^{-16}\,cm^2$; $k_{ISC} = 1.2 \cdot 10^6\,s^{-1}$, $k_T = 1.8 \cdot 10^5\,s^{-1}$ and $\tau = 3.8\,ns$ [38, 42]. For excitation with $488\,nm$, equation 2.14 then yields $I_{sat} = 51.4\,kW/cm^2$, which is in very good agreement with the results obtained from the experiment.
Panel B shows the signel-to-background ratio (SBR), which was calculated as the molecular brightness $\eta(I)$ divided by the background rate from a buffer solution, $SBR = \eta(I)/F_{back}$. For low irradiance the photon yield increases linearly with laser power. The background from the buffer is still smaller than the electronic noise from the detector and the SBR increases. At moderate laser power both background and fluorescence signal are proportional to the intensity and a plateau is reached where SBR is almost constant. At laser powers above P_{sat} the emission saturates, while the background still increases. Consequently the SBR is reduced. For the above data an optimum SBR was achieved at a laser power of $P_{opt} = 71\,\mu W$, which is significantly lower than P_{sat}.

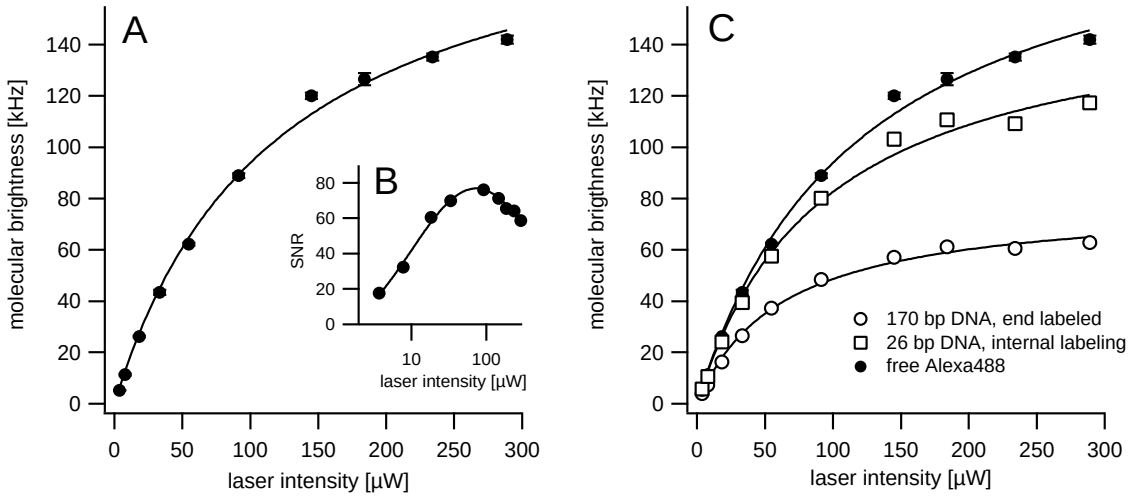

Figure 4.1: Determination of the optimum excitation intensity. **A**: Saturation curve for free Alexa488, **B**: corresponding signal-to-background ratio SBR, calculated as the brigthness divided by the background rate F_{back}. **C**: Saturation behavior of Alexa488 conjugated to DNA as compared to the free fluorophore.

This is not surprising since even below the saturation intensity the incremental increase of the fluorescence emission is already lower than the corresponding increase in background. For practical reasons the laser power was set between P_{opt} and P_{sat} since even at an reduced SBR the burst selection process provides a good discrimination of the fluorescence from the background.

When the fluorophore was conjugated to DNA its photophysical parameters changed and a different saturation behavior was found. This is illustrated in Figure 4.1C , where saturation curves are shown for three different samples, free Alexa488, Alexa488 internally attached to a 26 bp DNA and Alexa488 positioned at the end of a 170 bp DNA fragment. The corresponding fit parameters are listed in table 4.1. Conjugation of the fluorophore at the end of the DNA resulted in a more than twofold reduced emissivity. At the same time saturation was observed at lower laser intensities already. Whether this is caused by interactions of the fluorophore with the particular base, to which it is attached, or is a result of the PCR preparation, remains to be tested.

sample	$\mathbf{P_{sat}}$ $[\mu\mathbf{W}]$	$\mathbf{I_{sat}}$ $[\mathbf{kW/cm^2}]$	$\eta(\mathbf{I_{sat}})$
Al488	119.1 ± 9.9	50.1 ± 4.5	102.8 ± 3.7
Al488-DNA_{int}^{26}	92.8 ± 10.3	39.1 ± 4.3	79.6 ± 3.5
Al488-DNA_{end}^{170}	62.5 ± 5.4	26.3 ± 2.3	39.5 ± 1.2

Table 4.1: Summary of the saturation properties from Figure 4.1C . Listed are the laser power, at which saturation is observed, the corresponding saturation intensity and the molecular brightness at the saturation intensity, $\eta(I_{sat}) = \eta_{max}/2$.

This example points out the necessity to determine the optimum laser intensity for each class of constructs individually. According to Figure 4.1C , a laser intensity, which was optimal for free Alexa488, would be too large for experiments on end-labeled DNA. The conjugated fluorophore is already in saturation and no gain in photon yield would be observed. The signal-to-background level would be considerably reduced due to the increase in background signal.

4.2 Photostability of fluorophores

A major pitfall in single molecule experiments is a premature deactivation of the fluorophore. This leads to a reduction or even termination of the valuable fluorescence emission. Deactivation of the acceptor fluorophore renders the molecule a donor-only species, which might be misinterpreted as a change into a conformation with zero FRET. Inactivation of the donor fluorophore completely prevents detection of the molecule, since the residual direct acceptor excitation is generally too weak to be registered during the burst selection process.
Even more problematic are those events where the deactivation of either fluorophore occurs during the transit through the focus. This may virtually generate all combinations of proximity ratios and severely complicates the subsequent analysis. Only at an optimum photostability does excitation at laser intensities $I \approx I_{sat}$ truely result in an optimised flux of fluorescence photons.

The effect of premature photodestruction is demonstrated in Figure 4.2, where double labeled FRET standards were measured at increasing laser intensities. A significant reduction in the intact FRET species was observed at intensities already far below the saturation intensity. Correspondingly, the zero-FRET population was enhanced, while the number of detected events steadily increased. This indicates a predominant inactivation of the acceptor fluorophore.
Obviously, the photodecomposition can be prevented by lowering the laser intensity. This, however, contradicts to the need for an efficient excitation as discussed in the previous paragraph. It is thus essential to provide a suitable photostabilisation of the fluorophores under conditions of high laser intensities. Care has to be taken, however, that the photostability of the dye does not quench its emission [70]. Otherwise no net gain in fluorescence is achieved. To optimise the photostability of the fluorophore, the molecular basis of photodestruction has to be reviewed briefly.

4.2.1 Molecular basis of photodestruction

A key player involved in photodestruction is molecular oxygen dissolved in solution. Due to its biradical structure with two unpaired electrons it forms a highly reactive triplet ground state, which can react with both singulet and triplet states of a fluorophore [41]. The most efficient reaction is an electron transfer with the triplet state of an excited fluorophore:

$$^3X + ^3O_2 \rightarrow {}^1[X - O_2] \rightleftharpoons X + O_2(^1\Delta_g). \tag{4.2}$$

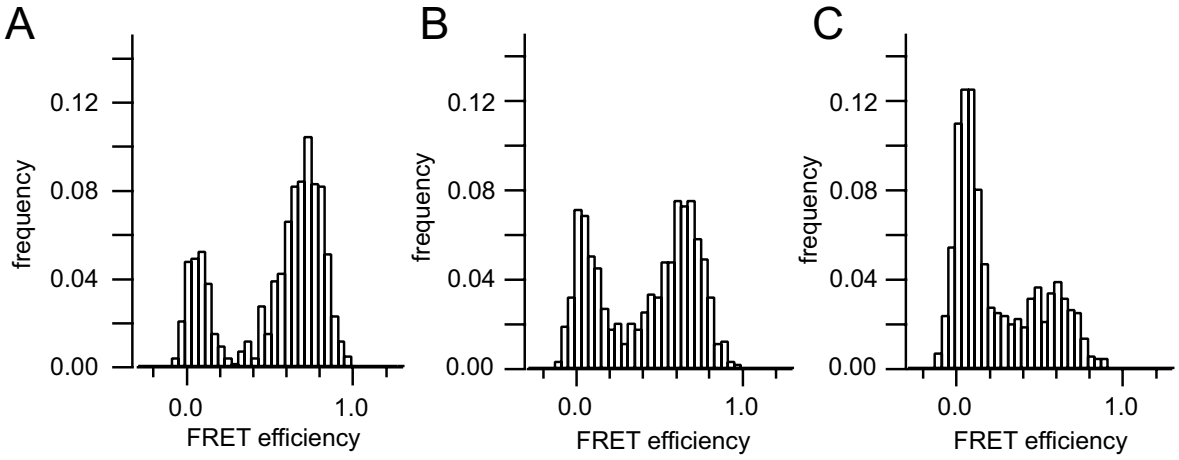

Figure 4.2: Proximity ratio histograms for a FRET standard labeled with Alexa488 and Rhodamine X. Laser power was **A**: $35\,\mu W$, **B**: $75\,\mu W$ and **C**: $110\,\mu W$. The reduction in the high-FREt component is most likely caused ba an premature acceptor deactivation.

This drives molecular oxygen into a highly reactive S_1-level, predominantly the lowest lying $^1\Delta_g$ conformation. Oxygen thus acts as an efficient triplet quencher on the expense of generating a highly reactive species in the vicinity of the fluorophore. The oxygen can either diffuse into solution and react with a different fluorophore during its lifetime of a few μs (in aqueous medium: $\tau(^1\Delta_g) = 3.3 - 7.4\,\mu s$ [41] or undergo an irreverible reaction with the same fluorophore. The latter process is responsible for the photodestruction of the dye molecule.
A reduction in partial oxygen pressure prevents the formation of the $^1\Delta_g$. At the same time it leads to slower quenching of the triplet state of the fluorophore and causes prior saturation and reduced fluorescence emission. Thus, modulation of the oxygen level in solution has to be performed with care.

4.2.2 Comparison of different photostabilizers

Many substances have been described in the literature that can improve the photostability of a fluorophore. They either remove reactive oxygen species from the solution or quench the triplet state of the fluorophore. In the following a few of these substances were tested for their potential to improve the fluorescence signal.
Beside the triplet quencher $\beta-$mercaptoethylamine (MEA, cysteamine) the antioxidants ascorbic acid (vitamine C, VC), sodium ascorbate (ASC), and propyl gallate (PG) were compared. The emission and absorption properties and the quantum yield of the fluorophores were determined by bulk fluorimetry. FCS experiments provided information on the triplet state dynamics and the emissivity under intensities relevant for single molecule spectroscopy. Finally, the photostabilising effect was assessed in single molecule FRET experiments, where both fluorophores were present. 26 bp FRET standards were used to report on the protective effect on different fluorophores attached to DNA.

Quantum yields

The majority of ensemble data was acquired by Anne Hennecke during her practicals. Alexa488 showed a reduction in quantum yield for all additives present at larger concentrations. The strongest effect was observed for cysteamine, with a 15 % reduction in quantum yield at $5\,mM$, and considerably larger quenching at higher [MEA]. Ascorbic acid showed less quenching, about 5 % at $2\,mM$, which was the maximum VC concentration at which the pH value remained sufficiently stable. Sodium ascorbate could be added at higher concentrations without reducing the pH value but quenching was also observed for concentrations above $5\,mM$ ascorbate. Propyl gallate showed a similar tendency to quench Alexa488 at higher concentrations.
None of the acceptor dyes was quenched by MEA and ASC (at about $5\,mM$ additive the change was less than 3 % in either direction). VC did not influence Alexa568 either and even seemed to increase the quantum yield of Rhodamine X. However the effect remained rather small ($3-4$ % at $2\,mM$). Propyl gallate, on the contrary, caused a quenching of all acceptor dyes at higher concentrations, where a reduction of almost 20 % was observed at $5\,mM$ PG.

Spectral properties

The spectral shape and the emission maxima remained stable under all conditions tested here. None of the additives caused a spectral shift at concentrations below $10\,mM$. Only in the case of ascorbic acid a red shift of emission was observed at higher concentrations, which we attribute to the reduced pH value.

Triplet state dynamics

The light intensities applied in bulk fluorimetry are more than 2 orders of magnitude lower than in confocal experiments. The average time between two successive absorption processes is larger than the mean lifetime of the triplet state (few μs), and triplet effects do not influence the signal. These intensities, however, are too weak to produce enough fluorescence photons for an efficient detection of single molecules. FCS experiments were performed to monitor the effect of the protective agents on the triplet state dynamics of the fluorophores at intensities which are relevant to single molecule experiments. Exemplary measurements for Alexa488 and Alexa568 labeled DNA's are shown in Figure 4.3. ASC increases the triplet population and prolongs the triplet lifetime τ_{tr} of both fluorophores. This is the consequence of removing oxygen from the solution. On the contrary, MEA efficiently reduced the triplet population. Similar observations were reported from other research labs as well [35]. For both additives the increase in triplet fraction correlated with a decrease in molecular brightness and vice versa. The reduced quantum yield of Alexa488 (-15 % at $5\,mM$ MEA) was compensated by a decrease of the triplet population (-65 % at $5\,mM$) and caused a net increase in emissivity. The effect of MEA on the triplet state of the acceptor dyes was similar yet less strong. The increased triplet state population resulted in an increased diffusion time if ASC was added into the buffer. This is accompanied by a reduced ACF amplitude (not shown in the normalised plots). Triplet saturation of the fluorophore causes deviations

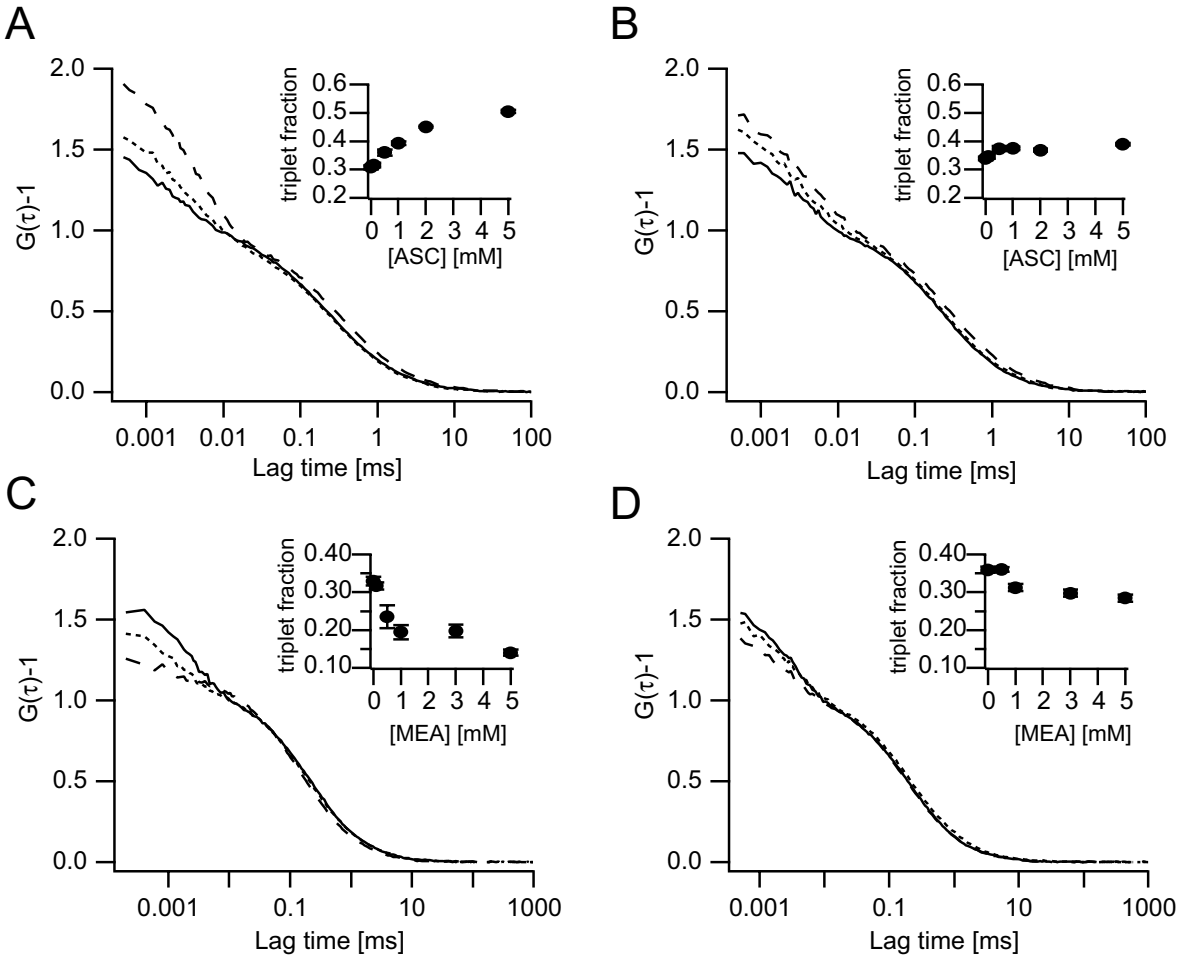

Figure 4.3: Triplet dynamics of DNA-conjugated Alexa488 and Alexa568 for different additives. **A**: Alexa488 and ascorbate, **B**: Alexa568 and ascorbate, **C**: Alexa488 and cysteamine, **D**: Alexa568 and cysteamine. Additive concentrations were $0\,mM$ (solid lines), $1\,mM$ (dotted lines) and $5\,mM$ (dashed lines) in each experiment. The inlay sketches depict the triplet fraction as a function of additive concentration.

in the MDE and an apparent increase in effective volume size [62]. A photobleaching process, on the contrary, reduces the apparent diffusion time and increases the ACF amplitude.

Single molecule FRET experiments under photostabilising conditions

After we quantified the photostabilising effect on the individual fluorophores we now discuss the influence on a complex FRET sample. The protective agents influence the outcome of an spFRET experiment in various ways.

- Changes in the Förster radius might be induced by altering the donor quantum yield, the spectral overlap integral, the refractive index or the orientation factor κ^2. The low bulk anisotropy values observed for additive concentrations $< 5\,mM$ indicated that the orientation factor was $\kappa^2 = 2/3$. The absorption and

emission spectra did not change significantly so the overlap integral should be unaffected.The donor quantum yield was affected only at additive concentrations above $5\,mM$. Potential changes in refractive index should be negligible.

- In a SMD experiment the detection factor γ might be affected, which would cause shifts in the center position of substates in the ratiometric histogram.
  Different $\gamma-$factors result from changes in the quantum yields of the fluorophores or the detection efficiencies. As discussed in the previous paragraph, these factors are only affected by larger additive concentrations.

In summary, the use of a few mM of the additives should neither affect the Förster radius nor the detection factor. It might, however, change the photon rate per burst and alter the relative contribution of the intact molecules and the zero-FRET peak.

Comparison of different acceptor fluorophores
In single molecule FRET, standards labeled with different acceptor fluorophores showed a similar response to the protective agents. Table 4.2 compares the relative change in photon rate and the fraction of intact FRET constructs. Both parameters were determined as described in section 3.3. Data was normalised to the case where no additive was present.

For each acceptor fluorophore the protective agents enhanced the intact FRET population by a comparable amount. Rhodamine X showed the largest variation where ascorbic acid and ascorbate had the strongest effect. The effect on the Alexa fluorophores was slightly lower, but still an increase of $45-50\,\%$ was observed in the intact FRET population. Each of the fluorophores was less stabilized by cysteamine or propyl gallate, with only a $30-35\,\%$ effect.
Larger differences were observed in the photon rate per molecule, where also the emissivity of the donor molecule had to be taken into account. Again, constructs labeled with Rhodamine X showed to be most susceptible to quenching. $1\,mM$ PG already caused a $15\,\%$ reduced emissivity. On the contrary, oligonucleotides labeled with the Alexa fluorophores showed a minor increase in the burst photon rate. Based on these observations the use of ascorbic acid/ascorbate appeared the most promising. We now have to determine the proper concentration range for these protective agents.

	Rhodamine X		**Alexa568**		**Alexa594**	
	intact E	**mean rate**	**intact E**	**mean rate**	**intact E**	**mean rate**
-	1.00	1.00	1.00	1.00	1.00	1.00
VC	1.63	0.91	1.52	1.02	1.44	1.07
ASC	1.59	0.89	1.48	1.04	1.48	1.03
PG	1.37	0.85	1.41	1.04	-	-
MEA	1.33	1.06	1.28	1.08	1.24	1.07

Table 4.2: Comparison of the relative effect of $1\,mM$ additive on short FRET standards labeled with Alexa488 and the different acceptor fluorophores. Data are normalised to the case of pure TE buffer. The laser power was set to 100 μW in each experiment.

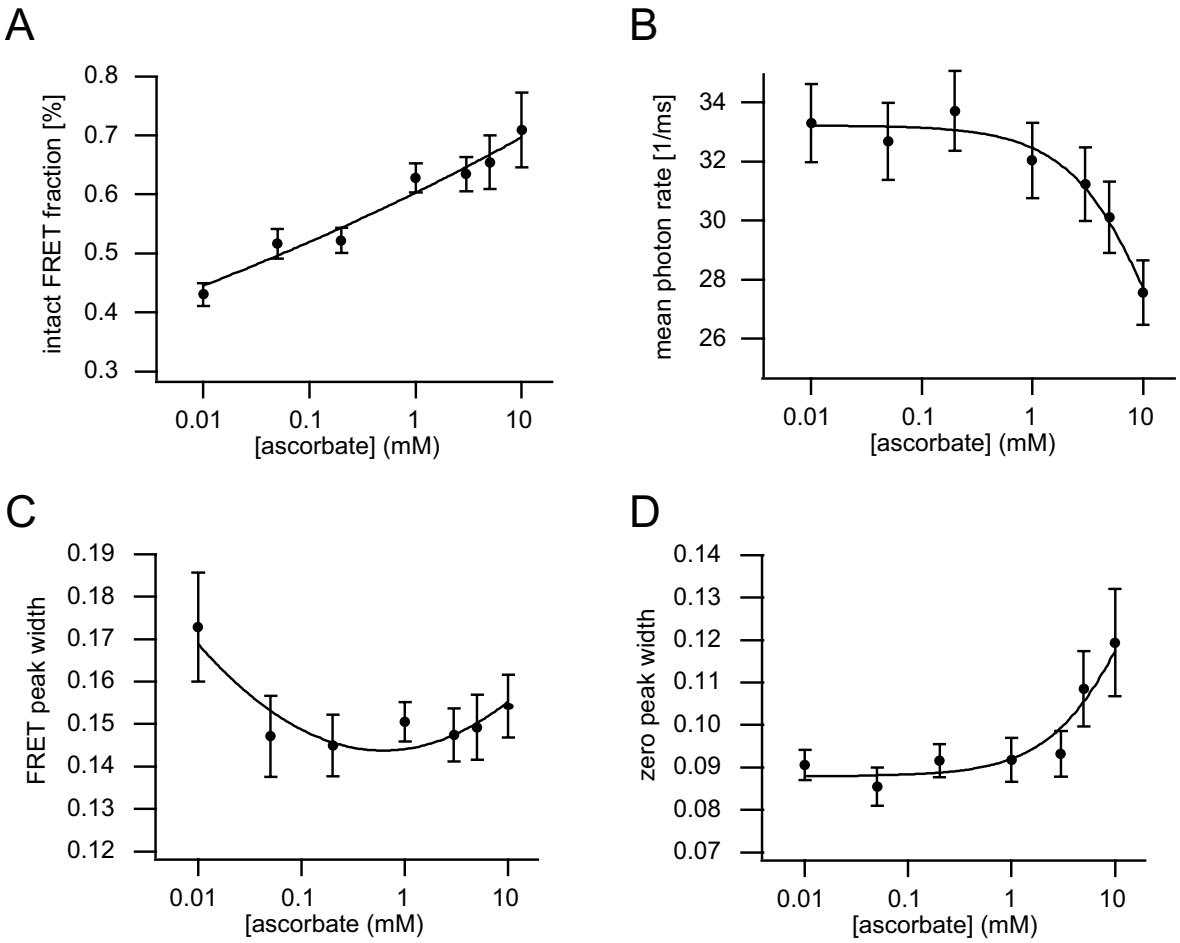

Figure 4.4: Dependence of various descriptive burst parameters on the concentration of sodium ascorbate added to the buffer solution. **A**: fraction of intact molecules, **B**: mean in-burst photon rate, **C**: FRET population width, **D**: zero-FRET population width.

Additive concentration

The results from bulk experiments suggest that concentrations up to $5\,mM$ ascorbate or $2\,mM$ ascorbic acid are suited to stabilize the molecules without causing significant quenching of the fluorophores. Experiments on the single molecule level, however, might require a further restriction of the additve concentrations applied. To check this, the characteristic burst parameters from the SMD experiment were analysed at different concentrations of the additives. Exemplary data for sodium ascorbate is shown in Figure 4.4.

An optimum stabilisation was achieved between 0.5 and $2\,mM$ ascorbate. Higher concentrations slightly enhanced the FRET population (panel A), but lead to a $15-20\,\%$ reduction in the in-burst photon rate (panel B). At the same time the width of the intact FRET population (panel C) and the zero-FRET peak (panel D) were increased, if higher ascorbate concentrations were added. Notably, the broadening of the zero-FRET peak was significantly larger than that observed for the intact FRET species. This increase in distribution width is unfavorable for SMD experiments, since it limits

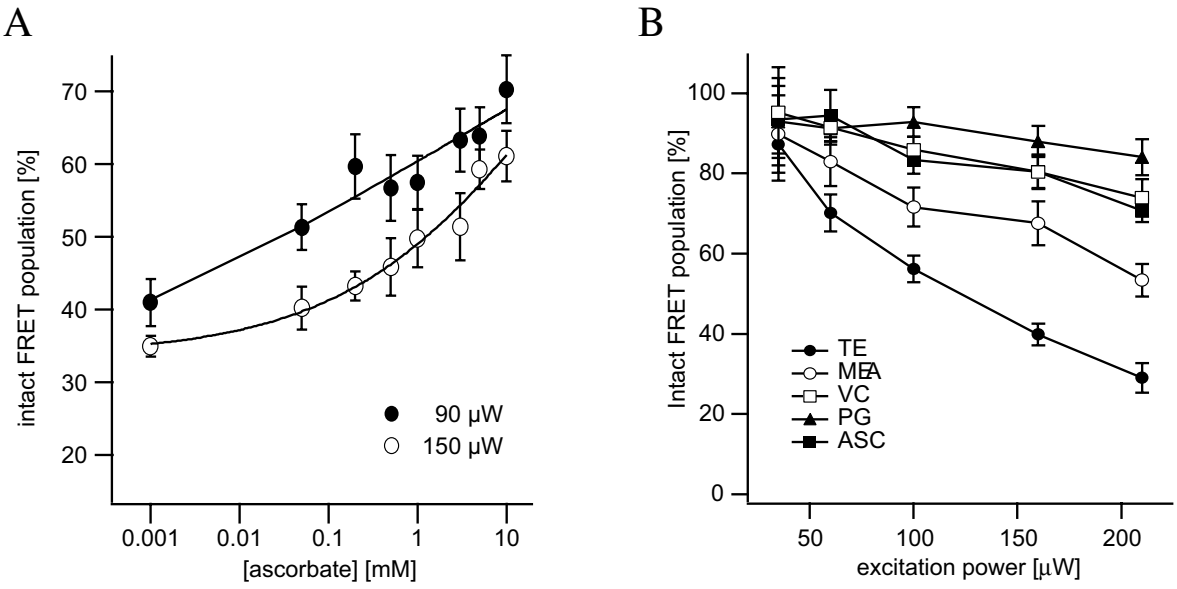

Figure 4.5: (**A**) Stabilisation achieved at various ascorbate concentrations for a laser power of 90 and 150 μW. Exemplary data is shown for a FRET standard labeled with Alexa488 and Alexa568. (**B**) Intact FRET population as a function of laser power for various additives present at a concentration of $1\,mM$.

the resolution of subpopulations in the ensemble. Similar results were obtained for ascorbic acid, although no further increase in stability was observed at concentrations above $1\,mM$ ascorbic acid.

Dependence of stabilisation on laser intensity

Higher irradiances require larger concentrations of ascorbate or ascorbic acid to compensate the increased accumulation of the triplet state, from which photodestruction can occur. Figure 4.5A compares the efficiency of different ascorbate concentrations at an applied laser intensity of 90 and $150\,\mu W$. At the higher laser intensity the relative photostabilisation is reduced and larger ascorbate concentrations were required to achieve the same effect.

Figure 4.5B compares the stabilisation as a function of laser power for various additives present at $1\,mM$. As shown before, all protective agents showed a beneficial effect on the intact FRET population compared to pure buffer. The least stabilisation was observed for MEA. For ascorbic acid and sodium ascorbate a reasonable stability was achieved, where even at higher laser intensities more than 85 % of the molecules remained intact. Besides, no significant quenching was observed. The best stabilisation was observed for propyl gallate, unfortunately accompanied with a reduced emission of the donor fluorophore. Other reseach groups reported on a PG-induced destabilisation of the conformation of single proteins (Prof. Schuler, Uni Zürich, personal communication), which might affect the histone proteins. It was therefore decided not to work with propyl gallate.

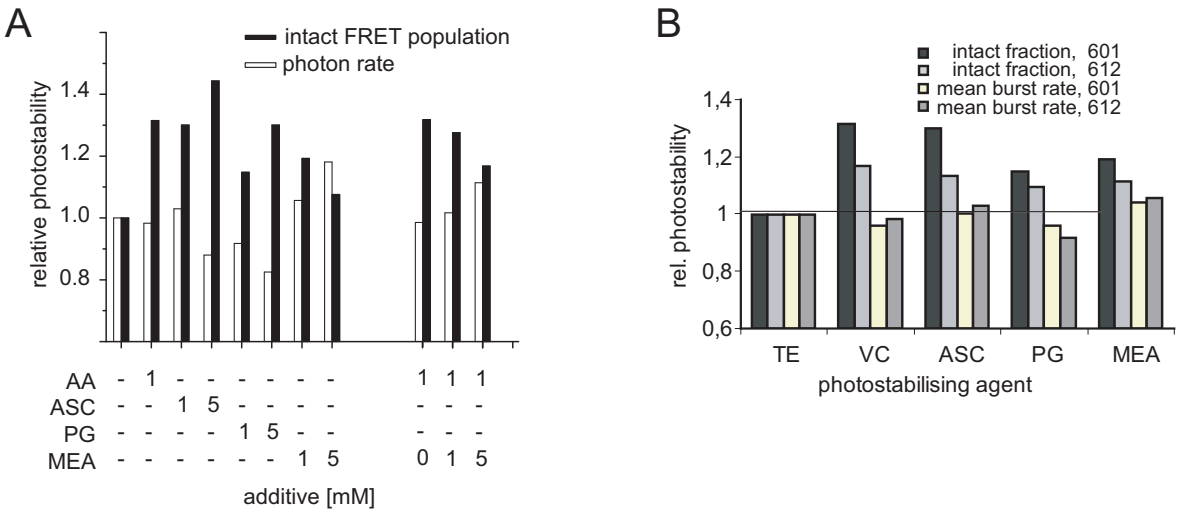

Figure 4.6: Summary of the photostabilisation observed for internally labeled nucleosomes. **A**: Comparison of different additive concentrations. Shown are the relative change in the FRET fraction (black bars) and apparent photon rate per burst (white bars). **B**: Photostabilisation observed for internally labeled nucleosomes of different DNA sequences. Additive concentration was $1\,mM$ each.

Photostabilisation of labeled nucleosomes

Oligonucleotides provide an easy-to-prepare model system for SMD experiments. They can be used to optimise a variety of different experimental factors. It has to be checked, however, that the results obtained do not differ from those observed for nucleosome samples. Figure 4.6 summarizes the response of internally labeled nucleosomes to the different additives used for this study.

The overall behavior was similar to that observed for the oligonucleotides. Panel A compares the fraction of intact molecules and the in-burst photon rate for different additive concentrations at a laser intensity of approximately $70\,\mu W$. Again, the best stabilisation was observed for $1\,mM$ ascorbate or ascorbic acid at minimal reduced photon rate. The increase in the intact nucleosome population and the simultaneous decrease of the photon rate at higher ascorbate concentration is comparable to the data observed for the oligonucleotides, compare to Figure 4.5.

With the nucleosome sample also the combined effect of MEA and ascorbic acid was tested. The addition of MEA to $1\,mM$ ascorbic acid already present in the buffer led to a successive reduction of the intact FRET population and an increase in the emissivity. Figure 4.6B demonstrates that the sequence itself does not influence the photostabilisation. The fraction of intact FRET standards and the mean photon rate are affected in the same way regardless of the sequence used.

Taken together the experiments on photostabilisation yielded comparable results regardless whether the fluorophores were attached to free DNA or to DNA assembled into nucleosomes. This suggests that the presence of the histones did not noticably influence the photophysics of the fluorophores. For nucleosomes samples neither the

fluorophore position nor the DNA sequence did affect the efficiency of the protective agents. Best results were obtained upon addition of $1\,mM$ ascorbic acid or ascorbate. Further addition of a few mM MEA caused a slightly reduced FRET population but led to an increase in emissivity. This, in turn, will enhance the detection probability and increase the sample throughput. If very low particle concentrations are analysed, the combination of MEA and VC/ASC might prove useful.

4.3 Optimisation of the detection efficiencies

The proper choice of the excitation intensity and the photostability of the fluorophores guarantee an optimum fluorescence flow from the molecule. For an efficient identification of the particle a maximum fraction of these emitted photons has to be detected. Consequently, the efficiency with which the fluorescence is collected in its corresponding channel has to be optimised. At the same time, the crosstalk into the other detection channel(s) has to be minimised.

4.3.1 Calculation of detection efficiencies

The efficiency with which fluorophore i is detected in channel j, η_{ij} (i,j: donor, acceptor), can be factorized into a spectral component, η_{ij}^{spec}, and a wavelength-independent part η_{ij}^{geom}:

$$\eta_{ij} = \eta_{ij}^{geom} \cdot \eta_{ij}^{spec}. \tag{4.3}$$

The spectral term depends on the transmission function of all optical elements, the sensitivity of the avalanche photodiode and the emission spectrum of the fluorophore. η_{ij}^{geom} includes the collection efficiency of the objective lens (≈ 0.25) and is particularly sensitive to the alignment of the lenses L3 and L4 in front of the detectors. Ideally, a change of the optical filter leaves η_{ij}^{geom} unaffected and only influences the spectral component. The detection efficienciers for different filter sets can then be directly compared by their η_{ij}^{spec} values.
For the different filters used in this work, η_{ij}^{spec} was calculated as the product of the transmission curves $T_k(\lambda)$ of all optical parts, the spectral sensitivity of the avalanche photodiode, $D(\lambda)$, and the normalised emission spectrum of the fluorophore, $f_i(\lambda)$. The product was integrated over all wavelengths:

$$\eta_{i,j}^{spec} = \int f_i(\lambda) \cdot \left(\prod_k T_k(\lambda) D(\lambda) \right)_j d\lambda \tag{4.4}$$

The index k denotes the various filters and dichroic mirrors of the detection channel. Figure 4.7 shows the spectral detection efficiency for two representative filter sets, denoted as Q and N (table 3.2). Panel A shows the transmission profiles of the individual parts in the acceptor detection channel. In panel B the net transmission profiles of donor and acceptor channel are plotted with a rescaled emission spectrum of DNA-conjugated Alexa488 and Alexa594. The overlap of the net transmission profiles with

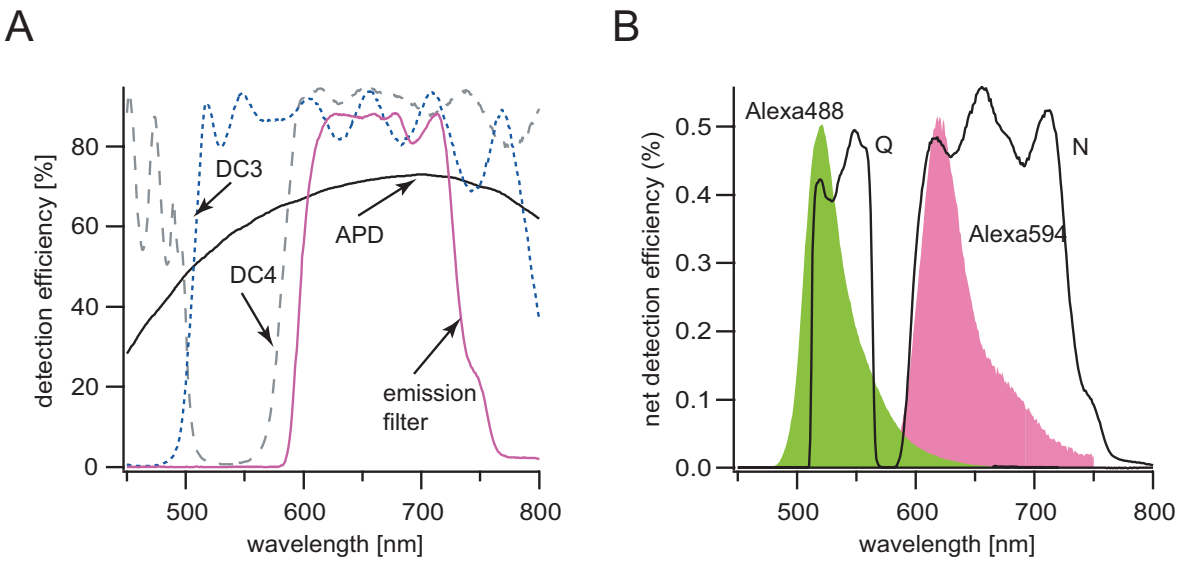

Figure 4.7: **A**: Spectral profiles of the optical elements, which determine the spectral detection efficiency η_A^{spec} of the acceptor channel. The notation is identical to that used in Figure 3.7. **B**: Overlap of the fluorophore emission spectra with the calculated profiles for both detection channels. The emission spectra were re-scaled for better visualisation.

the emission spectra yields the values for η_{ij}^{spec}. A list of calculated η_{ij}^{spec} for different combinations of filter sets and fluorophores is given in table 4.3 . To simplify the notation, we denote the detection efficiency of the donor fluorophore in the donor channel with $\eta_{dd} \equiv \eta_D$. Correspondingly, we use $\eta_{aa} \equiv \eta_A$.

filter	**Alexa488**	**Rhodamine X**		**Alexa594**	
	oligos	**oligos**	**nucleosomes**	**oligos**	**nucleosomes**
N	0.0196	0.2976	0.4068	0.4490	0.4388
G	0.0077	0.1284	0.1956	0.2611	0.2442
E	0.1792	0.0006	0.0012	0.0004	0.0007
Q	0.2858	0.0029	0.0017	0.0003	0.0009
XF3081	0.0103	0.1728	0.2684	0.3453	0.3268
XF3094/IRB	0.0096		0.2662	0.3423	0.3424

Table 4.3: Calculated spectral detection efficiencies η_{ij}^{spec} for various combinations of filters and fluorophores. Values were compared for the dyes attached to short DNA fragments and to fluorophores attached to longer DNA fragments used for nucleosome reconstitution. The last two entries were test filters for the acceptor channel which lower the crosstalk but showed a lower detection efficiency than N.

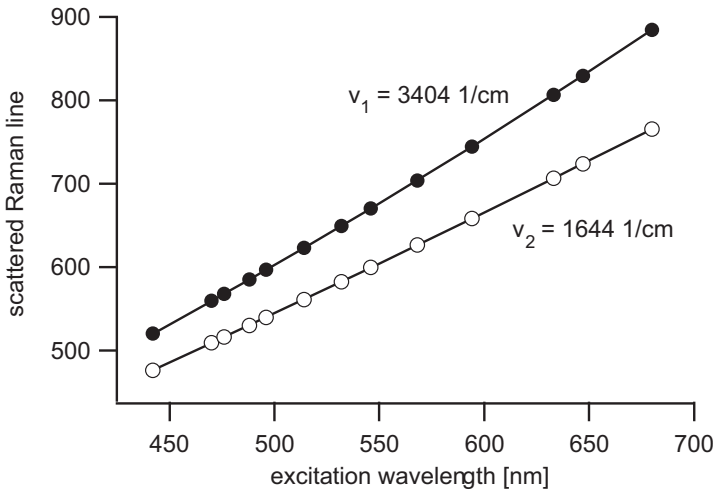

λ^{ex}	λ_1^{Raman}	λ_2^{Raman}
470	559	509
476	568	516
488	585	531
496	597	540
514	623	562
532	650	583
568	704	627
633	807	707
647	830	724

Figure 4.8: Wavelength of Raman-scattered photons from an aqueous medium at laser excitation with λ^{ex}. Values are given for different laser sources, which can be implemented into the current spectrometer setup.

4.3.2 Influence of Raman scattering

According to equation 4.4 the filter with the largest value of η_{ij}^{spec} should be used for detection. This *maximises* the total detection efficiency, however, it does not necessarily *optimise* it. Under conditions of high laser intensity and low total fluorescence signal, which are typical encountered in single molecule experiments, the effect of Raman scattering has to be considered.
In aqueous solution two vibration modes of water become excited at wavenumbers of $\nu_1 = 3400\,cm^{-1}$ and $\nu_2 = 1640\,cm^{-1}$. The latter is about 5 times less intense than the first band. An incident laser wavelength λ^{ex} generates scattered photons with a wavelength $\lambda_{1,2}^{Raman}$ where $2\pi(1/\lambda_{1,2}^{Raman} - 1/\lambda^{ex}) = \nu_{1,2}$. These Raman lines are listed in Figure 4.8 for various excitation wavelengths. The cross section for Raman scattering is only $10^{-29} - 10^{-30}\,\mathrm{cm}^2$ per water molecule and thus considerably lower than the absorption cross section of the fluorophore $\sigma_{01} \approx 3 \cdot 10^{-16}\,cm^2$. The large excess of water molecules present in the focus (about $2 \cdot 10^{10}$), renders Raman scattering a non-negligible contribution to the total signal. While the Raman band at $\nu_1 = 3400\,cm^{-1}$ is easily blocked by appropriate filters, the lower band usually coincides with the emission spectrum.
The optical filters have to be chosen such that as many fluorescence photons are detected as possible while efficiently suppressing the Raman scattering at λ_1^{Raman}.
For example the spectral detection efficiency for Alexa488 is higher for filter Q ($\eta_D^{spec} = 0,286$)than for filter R (520DF40), where $\eta_D^{spec} = 0.233$. At excitation with 488 nm this would be the filter of choice. If the fluorophore was excited with $470\,nm$, however, the Raman band would be partially included in the transmission band of filter Q. In this case, filter R has to be chosen instead.

4.3.3 Estimation of the crosstalk and the detection factor

If we assume identical geometric efficiencies of the donor and acceptor channel[1], the relative donor crosstalk into the acceptor channel can be computed as

$$\alpha_{DA} = \frac{\eta_{DA}^{spec}}{\eta_{D}^{spec}} \tag{4.5}$$

According to table 4.3 for Alexa488 we have $\alpha_{DA} = 0.0193/0.2858 = 0.067$ for the filter set (Q,N).
Similarly a rough estimate for the detection factor γ, which is essential to transform the measured intensity ratio into a FRET efficiency, can be derived from equation 4.4. Provided that the geometric terms are identical, we have

$$\gamma = \frac{\Phi_A}{\Phi_D} \cdot \frac{\eta_{A}^{spec}}{\eta_{D}^{spec}}. \tag{4.6}$$

where Φ_A and Φ_D are the quantum yields of acceptor and donor fluorophore, which can determined in bulk fluorimetry.
It is noted that equations 4.5 and 4.6 only provide an estimate and assist in choosing an appropriate filter combination. The assumption of identical geometric contributions might not be adequate, e.g. due to non-perfect alignment or damage of the optical surface of the filters and mirrors. Consequently, the crosstalk and γ-factor in the actual experiment might significantly deviate from the calculated values.
It is advisable to perform an independent measure for this quantities in each experimental session, as described in section 3.4.1.

4.4 Optimisation of the burst selection process

A crucial step in the analysis of single molecule experiments is the discrimination of individual particles from the background. Even if the excitation of the fluorophore, its photostability and the detection of its emitted photons are optimised, an improper burst selection still results in suboptimal single molecule identification.
An insufficient threshold setting will accept too many false positive events or even multiparticle transits, while too stringent selection conditions discard many valuable true single molecule events. In particular the majority of events diffusing in the peripheral focus region will hardly be registered. The degree of raw data filtering, which is controlled by the LEE filter size M_L, also affects the qualitiy of the subsequent data analysis.
In this section, a typical SMD experiment was performed on double labeled, 26 bp FRET standards. Distributions of various burst parameters were analysed for different threshold settings (N_{min} and IPT_{max}) and LEE window sizes M_L to find optimum selection criteria.

[1]This assumption is reasonable, if both lenses L3 and L4 are aligned for maximum detection. The two detection pathways then differ by an additional mirror in the acceptor channel only.

4.4.1 Burst selection thresholds

The effect of the selection parameters IPT_{max} and N_{min} was analysed for a given LEE window size of $M_L = 8$. Figure 4.9 shows several burst parameters as a function of IPT_{max} and N_{min}. For a given value of IPT_{max} an increase of N_{min} reduces the number of events being detected (panel A) and the width of the FRET distribution (panel E). At the same time, the burst size (panel B)and the in-burst photon rate (panel C) were slightly increased. The burst duration (panel D) slightly increased with N_{min}. Events which stay longer in the focus are more likely to emit enough photons to overcome N_{min}. The reduction in detected bursts at larger N_{min} resulted from the decreased probability that a molecule emits enough photons during its passage through the focus. Only those molecules were selected which predominantly reside in the center of the focus, the region of highest intensity. This in turn resulted in an increase in effective photon rate and mean burst size. The smaller width observed at larger N_{min} was a consequence of the reduced shot noise. The observed change, however, did not scale with $1/\sqrt{N}$, as expected. This discrepancy presumably arised from the excess broadening introduced by the correction procedure for background and crosstalk (section 3.4.2).

The variation of IPT_{max} had a larger impact on the burst properties. For a given N_{min} the number of detected events almost doubled as IPT_{max} was increased upto $200\,\mu s$. This was accompanied by a strong decrease in mean photon rate per burst, while burst size and distribution width only showed a minute increase. Small IPT_{max} only selected those events that crossed the center of the focus and emitted photons at a sufficiently high rate. As IPT_{max} was increased more events from the outer rims of the focus were accepted, which showed a lower emission rate. This also resulted in an increase in burst duration, which compensated the reduced emission rate and led to only minor changes in the burst size.

For $IPT_{max} > 200\,\mu s$, all parameters but the burst duration showed a sudden change in their behavior. Most notably, a strong increase in burst size and in-burst photon rate were observed. IPT_{max} is now comparable to the background level and multiple particle events start to contribute to the selected subensemble. The reduced number of registered events might be a consequence of more events being discarded by the upper threshold of allowed burst durations. This quantity was set to 10 during the whole analysis. Under conditions, where multiparticle events start to intrude the subensemble, more and more events showed an increased burst duration. Consequently, the mean value increases (panel E).
The influence of multiparticle events is further evident from the fact that at $IPT_{max} > 200\,\mu s$ the mean burst duration exceeds the meaningful time introduced in equation 2.31. To give a rough estimate fot T_m, an average of $N = 1/30$ particles in the focus is assumed. With a diffusion time of $\approx 250\,\mu s$. we obtain a value of $T_m \approx 5.9\,ms$. A mean burst duration above 6 ms was found for all values $IPT_{max} > 200\,\mu s$. This regime is obviously no longer suitable for single molecule experiments.

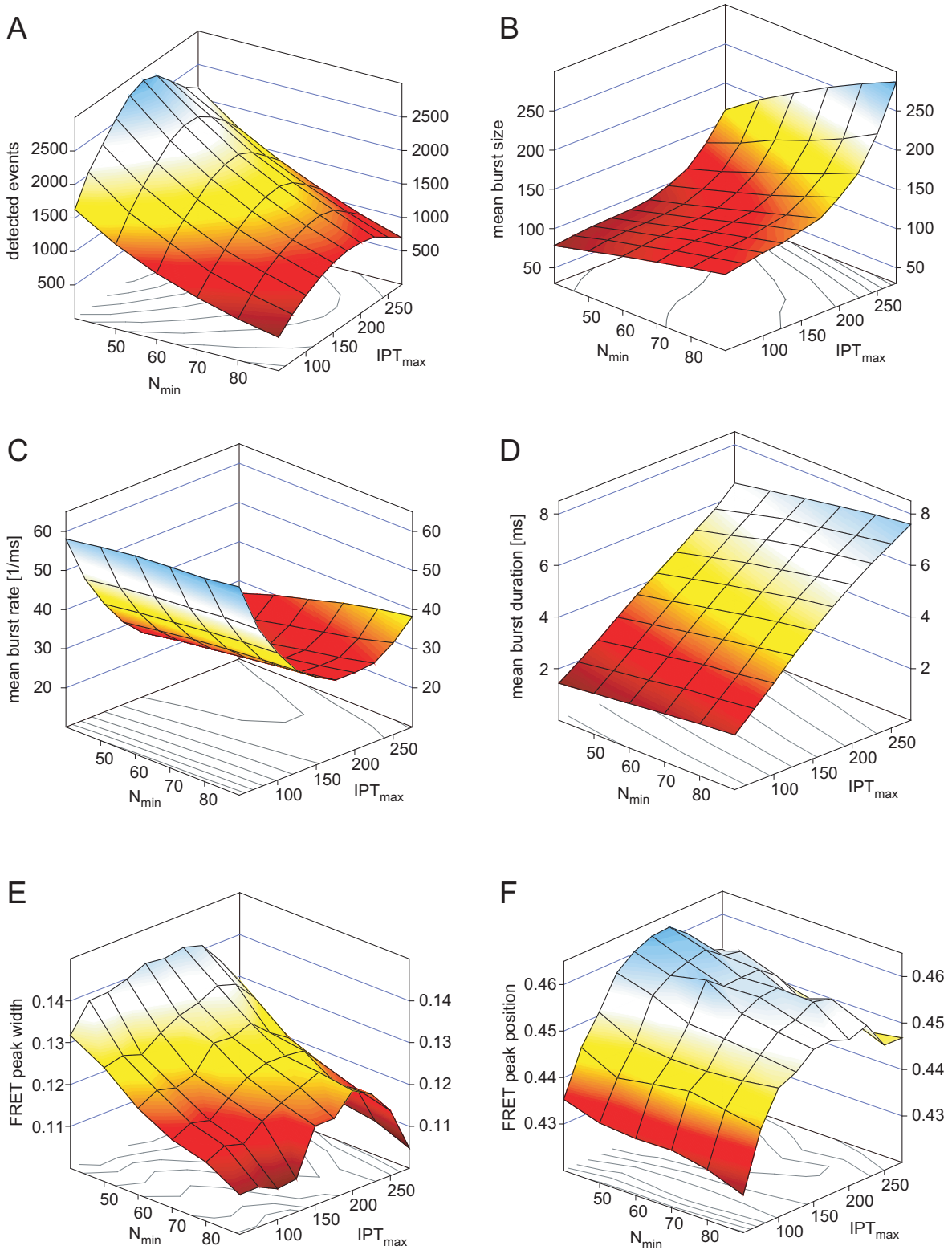

Figure 4.9: Dependence of the average value of different burst parameters on the threshold settings (N_{min}, IPT_{max}). The parameters were calculated as the average over the selected subensemble. A detailed discussion is presented in the text.

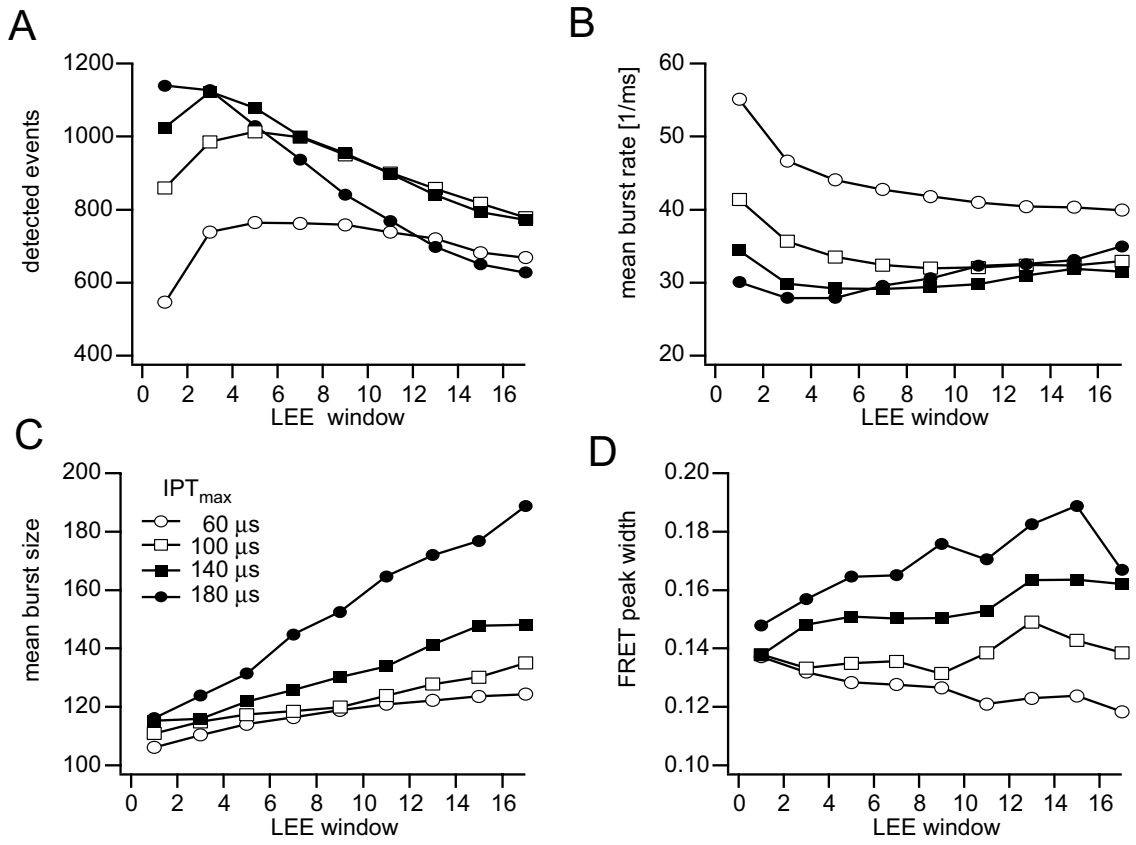

Figure 4.10: Variation of different mean burst parameters as a function of applied LEE window M_L for several threshold settings IPT_{max}. A detailed discussion is presented in the text.

4.4.2 LEE filter window

The size of the LEE filter defines over how many successive photons a given interphoton time will be averaged. In general, if the filter size is chosen too large, the fluorescence burst will be contaminated with too many adjacent background photons. The photon rate per burst will be reduced and the distribution width will be increased. To understand the effect of M_L on the outcome of the analysis, the single molecule data from a $26\,bp$ FRET atandard was analysed under various combinations of M_L and IPT_{max}. A few representative curves are shown in Figure 4.10.

The effect is rather small for stringent selection conditions, where $IPT_{max} << 100\,\mu s$. The interphoton time between successive background photons is by far larger than IPT_{max} and even if they are averaged with a few fluorescence photons from the adjacent burst, their averaged interphoton time is still likely to exceed IPT_{max}. As a consequence, neither the distribution width (panel D) nor the number of detected events (panle A) change significantly at values $M_L > 3$. The in-burst photon rate (panel B) is slightly more sensitive to the averaging over adjacent background photons.

The effect of filtering becomes more pronounced at increasing values of IPT_{max}. The probability that the smoothed interphoton time between background photons adja-

cent to the burst is smaller than IPT_{max} increases significantly. As a result, more background photons were included and the burst size increased (panel C). Also the distribution width was found to be enlarged. This is, at first glance, contradictory to the increase in mean burst size, however, the effect of additional broadening due to the correction of crosstalk and background has to be considered as well.
Noteworthy, at the highest IPT_{max} value analysed all parameters show the largest dependence on M_L. The accepted interphoton times are quite large and the inclusion of background photons is now accompanied by the generation of multiparticle events. These significantly increase the mean burst size, in-burst photon rate and distribution width. The reduced number of detected events is a consequence of more events now exceeding the upper threshold on the burst duration. The regime of larger values of M_L and IPT_{max} is not suited for single molecule conditions.

4.5 Measures to increase the photon yield

The previous sections were concerned with finding optimum conditions for the factors that affect the number of photons being detected from a diffusing molecule. These included parameters of the optical setup and the intrinsic photophysical dynamics of the fluorophore. They did not address the diffusion process *per se*.
The diffusion time of the molecule defines how long the molecule will reside in the focus, i.e. the time span during which photons can be observed from the particle (compare to equation 2.12). An increase in diffusion time will produce a larger number of emitted photons, which in turn might improve the resolution of potential subconformations in the ensemble. The diffusion time depends on the spatial extent of the laser focus, w_0 and the translational diffusion coefficient of the particle, $\tau_0 = w_0^2/4D$. The diffusion coefficient D is a function of the shape and size of the molecule, quantified in the hydrodynamic radius R_h, the viscosity of the medium, η, and its temperature T. For a spherical particle we have $D = kT/(6\pi\eta R_h)$ and

$$\tau_0^{sp} = \frac{3\pi\eta R_h w^2}{2kT}. \tag{4.7}$$

All parameters in equation 4.7 can be changed to slow down the diffusion process. In this section we focus on the variation of the viscosity by appropriate substances and the increase of the effective hydrodynamic radius.

4.5.1 Increasing the viscosity

The viscosity of the solvent was increased by addition of glycerol or sucrose into the buffer. Changes in diffusion time and molecular brightness F/N were monitored by fluorescence correlation spectroscopy to assess their potential to increase the photon yield from the molecule.

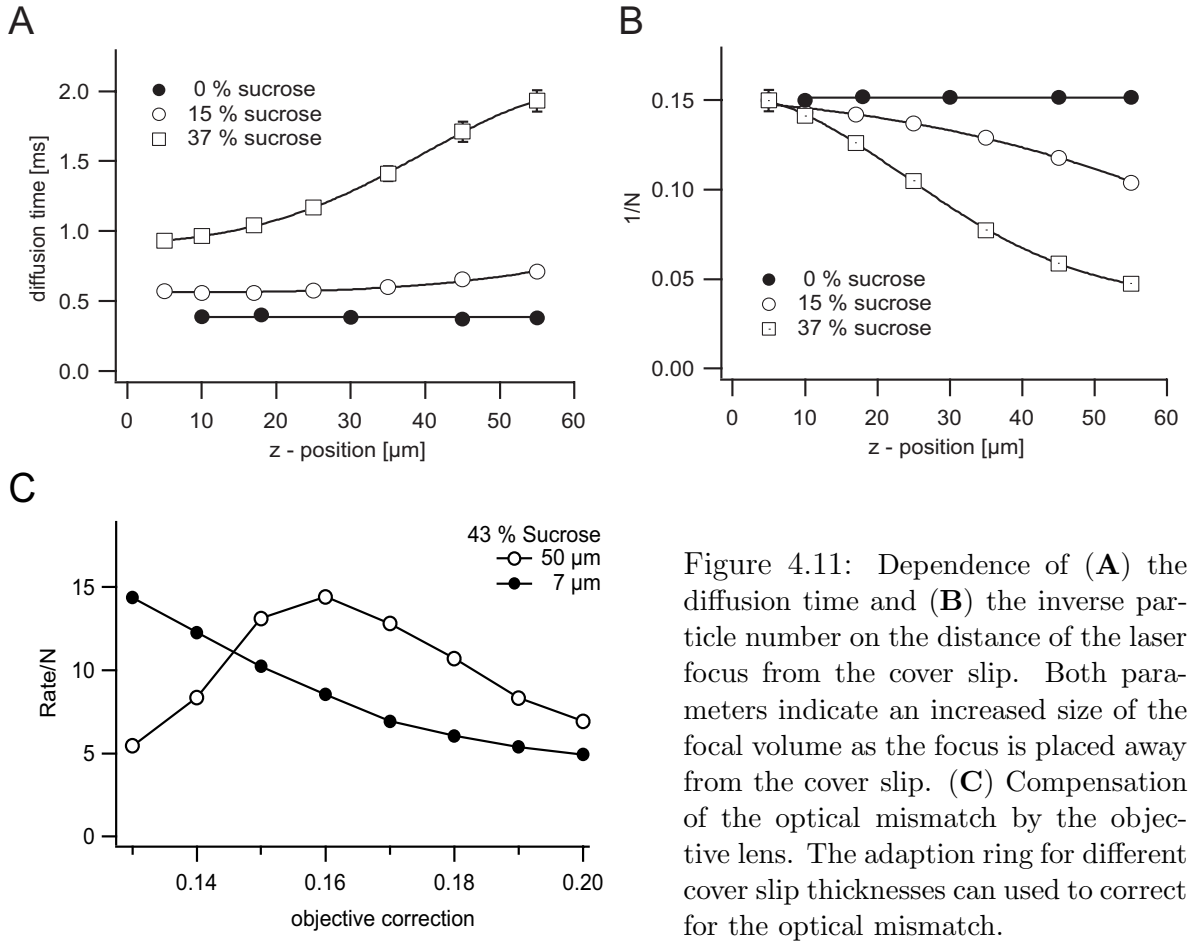

Figure 4.11: Dependence of (**A**) the diffusion time and (**B**) the inverse particle number on the distance of the laser focus from the cover slip. Both parameters indicate an increased size of the focal volume as the focus is placed away from the cover slip. (**C**) Compensation of the optical mismatch by the objective lens. The adaption ring for different cover slip thicknesses can used to correct for the optical mismatch.

Optical effects of glycerol and sucrose

Apart from a change in viscosity these substances altered the refractive index of the buffer. This generated an optical mismatch between the immersion fluid (water, $n = 1.33$) and the buffer medium (e.g. 50 % sucrose in water, $n = 1.35$) and severely influenced the correlation analysis as shown in Figure 4.5.1. The optical mismatch caused a distortion of the laser focus which resulted in an increase of the effective volume. As a result, a position-dependent diffusion time and ACF amplitude were observed. Both τ_0 and N increased as the focus was moved away from the surface (decreasing $1/N$), while only minor deviations were observed if the focus was placed near the chamber walls. This is not surprising, since the extent of distortion depends on the optical path length through the medium. A laser spot within the bulk solution is more affected than a laser spot located near the cover slip. Most objective lenses offer a correction mechanism to adapt the optical system to different cover slip thickness or solvent conditions. This can be used to compensate for the optical mismatch as demonstrated in Figure 4.5.1C . No correction was required if the laser was focused near the cover slip, while a larger compensation was necessary at a position away from the surface.

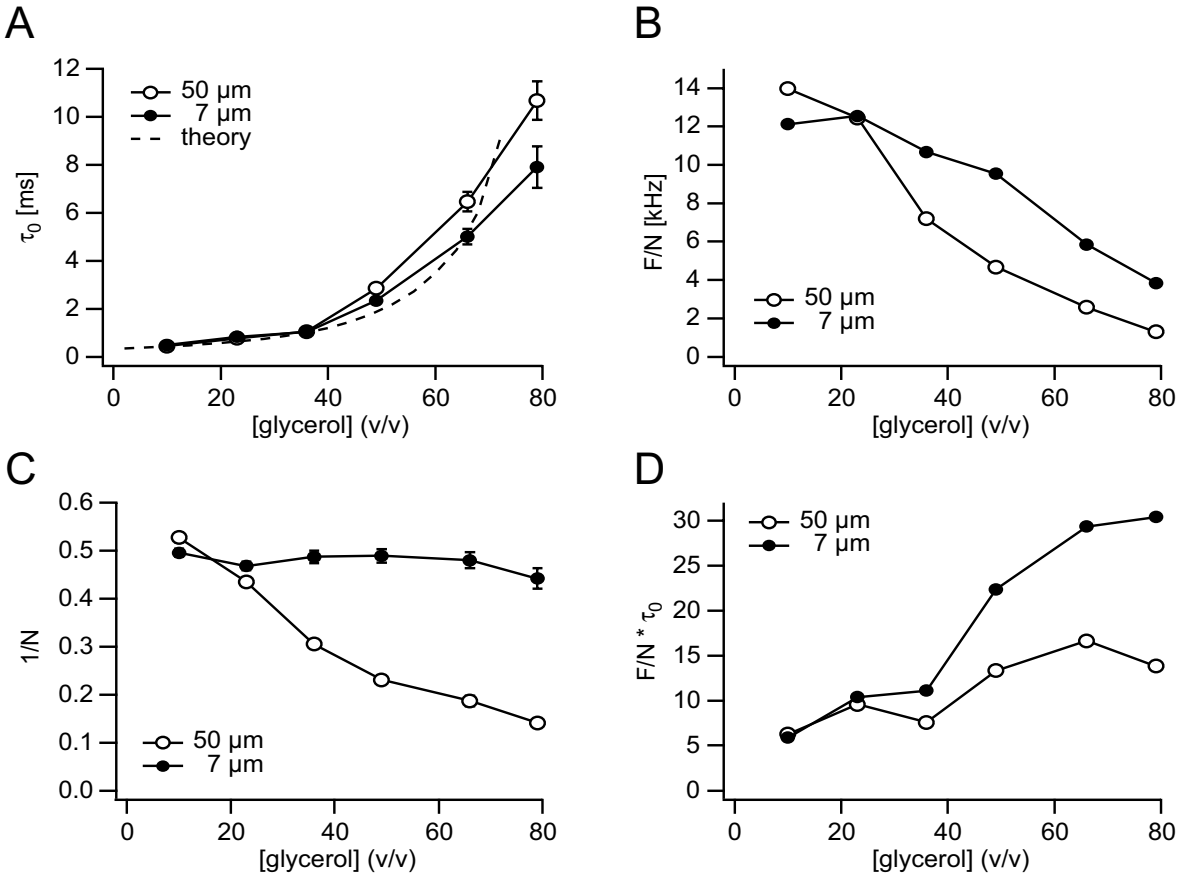

Figure 4.12: Effect of glycerol on the mobility and emissivity of Alexa488 conjugated to a short DNA. **A**: diffusion time, **B**: inverse particel number in the focus, **C**: molecular brightness and **D**: the product of the diffusion time and the molecular brightness as a measure of total photon yield. Data were taken $50\,\mu m$ (open circles)and 7 mum (filled circles) away from the cover slip.

The data presented is equally valid for glycerol. In fact this substance was found to be more suited for further experiments, since is showed a considerably lower background level than sucrose. The rest of this section thus deals with glycerol only.

Comparison of different glycerol concentrations

Figure 4.12 summarizes the effect of various glycerol concentrations measured close to the cover slip and $50\,\mu m$ inside the chamber. Near the cover slip the increase in diffusion time matched the change in viscosity (panel A), while the $1/N$ value remained constant. At $50\,\mu m$ height the optical mismatch caused an excess increase in diffusion time and a reduction in apparent $1/N$ as noted before. The molecular brightness F/N significantly decreased at higher glycerol concentration. At $50\,\mu m$ height, the same incident power was distributed over a larger focal area and the effective light flux was reduced. Near the cover slip a less strong yet notable decrease in brightness was observed, which cannot be attributed to the optical mismatch. Apparently, higher glycerol concentrations induced a quenching of fluorescence, which could not be compensated by the addition of various

photostabilising agents, such as ascorbic acid or cysteamine. Neither the quantum yield of the fluorophores nor the shape of the absorption and emission spectrum did change significantly to account for a reduced detection efficiency. Similar observations were made in the Seidel lab, where a loss of polarisation was observed at larger glycerol concentrations (Prof. Seidel, University of Düsseldorf, personal communication).
The product $F/N \cdot \tau_0$ was taken as a measure of an effective photon yield. As shown in panel D a six-fold increase was obtained at 60 % glycerol, which is to be compared to an almost ten-fold increase in diffusion time. This points to a dynamic quenching of the fluorophore at higher glycerol concentrations and restricts the useful range to [glycerol] $< 40\,\%$.

Single molecule experiments

Changes of the properties of individual FRET standards were monitored under single molecule conditions. Figure 4.13 shows the distributions of the burst duration (panel A), burst size (panel B) and burst rate (panel C) for 10 % (solid line) and 40 % (dotted line) v/w glycerol. The inlay sketches show the corresponding mean values for three separate experiments. Burst size and duration increased as glycerol was added to the buffer but deviate from the linear behavior at concentrations above 40 % glycerol. At these conditions a drop in burst rate was observed, which agrees with the data from FCS experiments. The overall gain in burst duration was considerably smaller than expected from the FCS data though (Figure 4.12). The interfluorophore distributions in Figure 4.13D were insensitive to the glycerol concentration. Only above 60 % v/w glycerol the reduced number of detected molecules increased the noise on the overall histogram and caused a broadening of the subpopulations.
In summary, the addition of a moderate glycerol concentration (less than 50 %) enhanced the number of detected molecules and preserved the ratiometric information within the histogram. At larger glycerol concentrations a strong quenching of the fluorescence is to be expected. A residual optical mismatch can be easily compensated by the objective lens.

4.5.2 Changing the hydrodynamic radius

A different strategy to improve the photon yield is to increase the effective hydrodynamic radius of the molecule. The size of a nucleosome is predefined and cannot be altered *per se*, without interfering with its structure. Its effective hydrodynamic radius can be increased by coupling to a larger carrier molecule though, e.g. to a bead or a plasmid. This, however, requires tethering of the nucleosome to a surface and might impede its rotational mobility or introduce unwanted interactions. Thus a different strategy was tested.

Vesicle encapsulation

The problem of confining the rotational mobility of tethered particles is overcome if the molecule is encapsulated into larger vesicles. Within the liposome the molecule is free to move, while the effective hydrodynamic radius is determined by the size of the

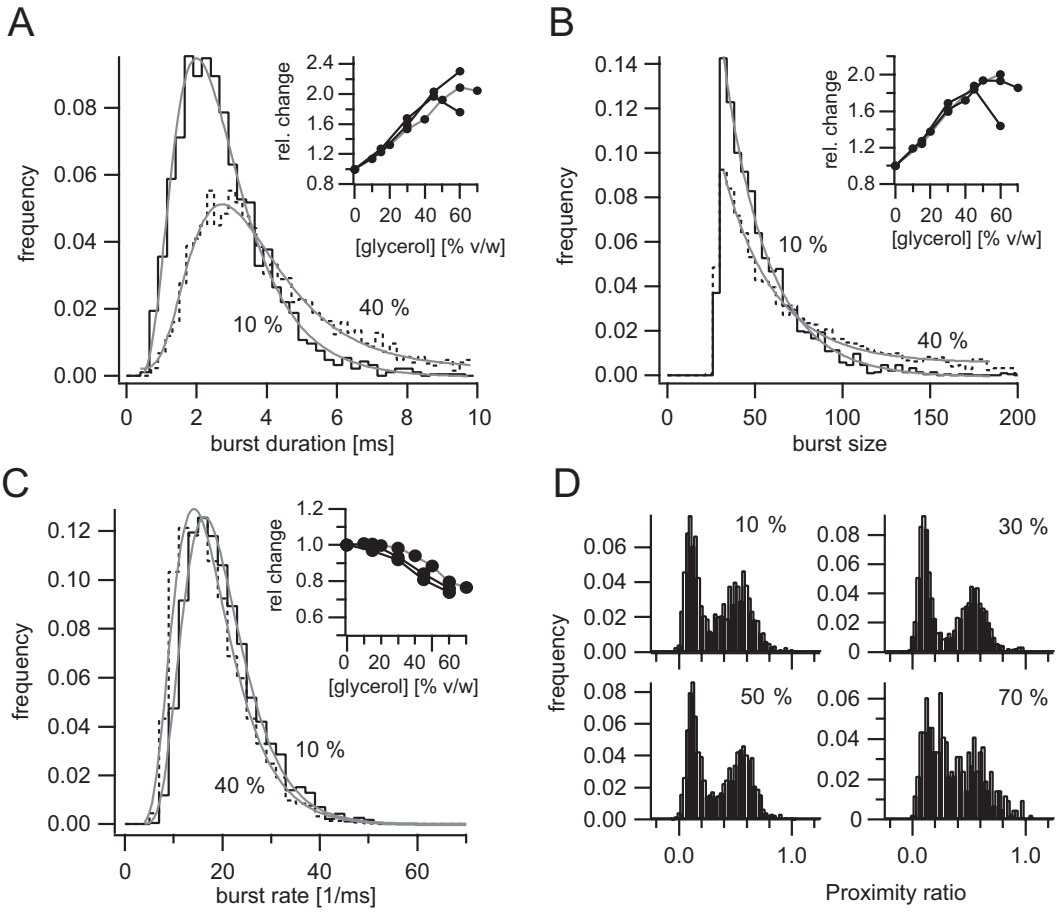

Figure 4.13: Single molecule distributions of (**A**) the burst duration, (**B**) the burst size, (**C**) the burst rate, measured in $1 \times TE$ buffer containing 10 % and 40 % glycerol. The inlay sketches depict the variation of the average values as a function of applied glycerol concentration. A few representative proximity ratio histograms are shown in (**D**). Glycerol concentrations were as denoted.

lipid container. Initial experiments on small 26 *bp* oligonucleotides were performed to test this approach. The molecules were encapsulated in neutral lipid vesicles following the protocol outlined in section 3.1.5 and [115]. Preliminary single molecule histograms are presented in Figure 4.14.

The proximity ratio distribution of the nonencapsulated FRET standards showed a narrow population at $P = 0.8$ and only 27 % of the molecules resided in the zero-FRET peak. On the contrary, about 45 % zero-FRET events were observed for the encapsulated sample and the FRET distribution was considerably broadened. The center peak position was not altered, which indicates that no dramatic change in the detection parameters or quantum efficiencies occured. A minor fraction of events was observed at intermediate P values and at $P = 1$. Whether these relate to an overall broadening of the FRET population, or arise from additional conformations triggered by the encapsulation should be subject of further investigations.

The twofold increase in mean burst duration of the liposomes (4.9 *ms*) compared to

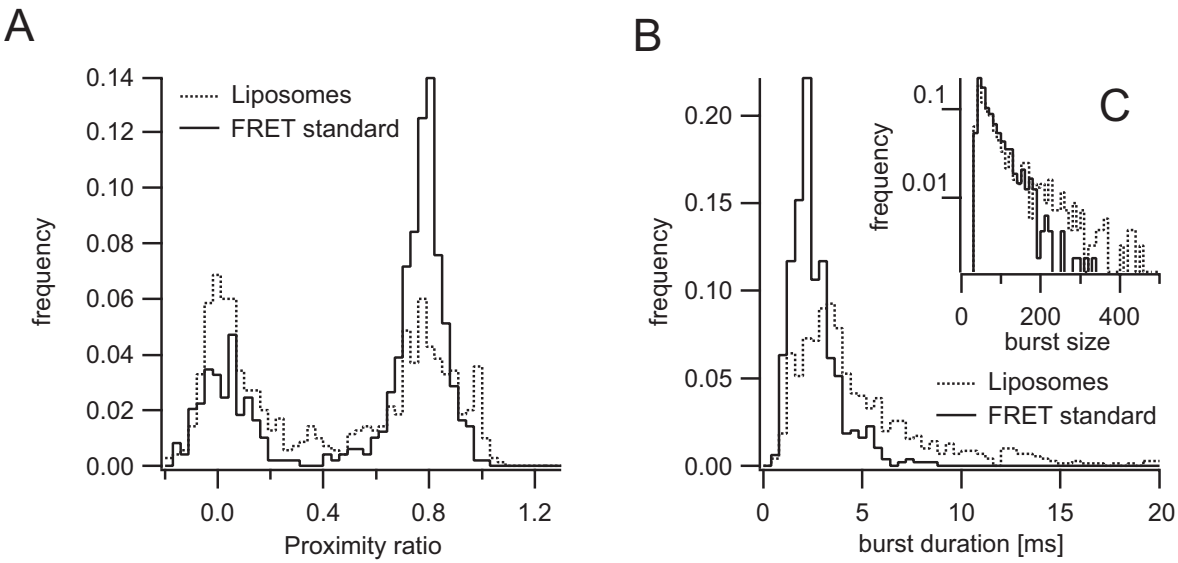

Figure 4.14: Preliminary single molecule results comparing small FRET standards in free solution (solid lines) with those encapsulated into 100 nm sized lipid vesicles (dotted lines). Shown are distributions of (**A**) the proximity ratio, (**B**) the burst duration and (**C**) the burst size (in a semi-logarithmic plot).

the small oligonucleotides (2.6 ms) reflects the enlarged hydrodynamic radius of the vesicles (panel B). A somewhat lower increase of only 50 % was observed for the mean burst size (liposomes: 123.6, nonencapsulated FRET standards: 81.7). This discrepancy points towards a potential quenching of the fluorophores, which is further evident from the mean photon rate per burst. The emissivity of encapsulated molecules was found to be reduced by 25 %, where a rate of 25.6 photons/ms was observed, compared to free oligonucleotides emitting at a rate of 33.6 photons/ms.
While the diffusion process of the molecules was successfully slowed down, the emissivity was severely reduced. A net gain in photon emission was achieved, however, and the overall proximity ratio distribution remained similar. These results render the encapsulation approach promising for further experiments, which will show whether the combination of the vesicle approach with glycerol and different photostabilising agents leads to better results.

4.6 Control experiments on FRET standards

This chapter concludes with a few test experiments that were performed to ensure, that the setup is capable to correctly reproduce the properties of known FRET standards. As a test system 26 bp FRET standards were labeled with Alexa488 and Alexa568 to either yield no FRET (donor-only), low FRET (21 bp separation) or high FRET (15 bp separation), compare to section 3.1.2. Special attention was paid to

- an accurate determination of subspecies stoichiometry within a mixture.
- a consistent reproduction of FRET efficiencies under different filter settings.

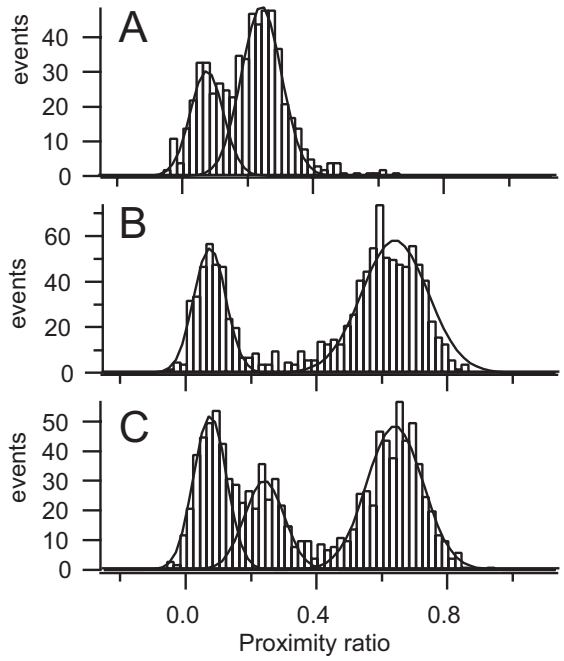

ratio	events	peak area
1:0	596	zero : 33.8 ± 2.2 peak1: 66.2 ± 2.2 peak2: ———
0:1	1118	zero : 31.3 ± 2.6 peak1: ———- peak2: 68.7 ± 2.6
1:1	1089	zero : 30.5 ± 1.5 peak1: 21.2 ± 1.8 peak2: 48.4 ± 2.3

Figure 4.15: Test mix of two differently labeled FRET standards. **A**: low-FRET standards, **B**: high-FRET standards, **C**: 1:1 v/v mixture of the isolated samples. The table shows the number of detected events and peak areas of the model Gaussian distributions. Further details are given in the text.

These requirements should be met by the setup to allow for a quantitative analysis on more complex structures like the nucleosome.

A mixture of low- and high-FRET standards was analysed under nominal filter conditions of $\gamma = 0.85$. Figure 4.15A and B show histograms of isolated samples, while a 1:1 v/v mixture of the oligonucleotides is depicted in panel C . The fractional occupancy of the populations and the number of detected molecules are listed in the table. For each histogram data was collected for a time period of 10 minutes.

For all samples the same fraction of about 30 % carried an inactive acceptor fluorophore. The remaining 70 % formed well defined subpopulations at proximity ratios $P_{low} = 0.20$ and $P_{high} = 0.61$. Their corresponding FRET efficiency was calculated from equation 2.48 to be 0.22 and 0.65. The high-FRET value agrees well with the energy transfer determined from the interfluorophore distance of 51$\mathring{A}$ and an estimated Förster radius of $R_0 = 56\mathring{A}$. The low-FRET efficiency significantly overestimates the interfluorophore distance of 75.2 $\mathring{A}$, for which an energy transfer of only 0.15 was calculated.

This discrepancy might be partially due to a non-negligible contribution from direct acceptor excitation. Under low-FRET conditions and detection factors $\gamma < 1$, only

peak	P	$\mathbf{P_{corr}}$	E	$\mathbf{E_{corr}}$	E(56Å)
low	0.196	0.136	0.223	0.156	0.146
high	0.612	0.586	0.649	0.625	0.637

Table 4.4: Peak center positions of the two non-zero FRET populations in Figure 4.15. P and E denote the proximity ratio and calculated FREt efficiency without additional corredtion for direct excitation. The corrected quantities are P_{corr} and E_{corr}. For comparison, a FRET efficiency was estimated from the helical model of DNA, section 3.1.2, and a Förster radius of 56 $\mathring{A}$.

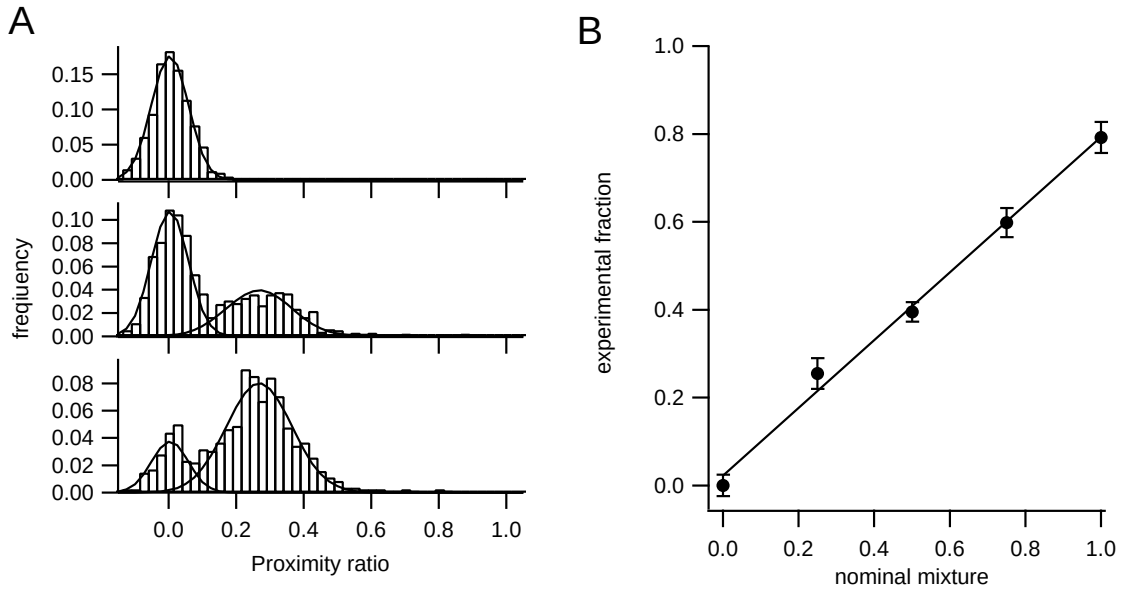

Figure 4.16: Single molecule analysis of a mixture of zero-FRET and low-FRET standards. **A**: Three representative histograms for mixing ratios of 1:0, 1:1 and 0:1 (zero-FRET:low-FRET). **B**: Fraction of low-FRET species as a function of nominal mixing ratio.

few photons in the acceptor channel result from energy transfer and any excess due to direct excitation will overestimate the FRET efficiency. The effect should be largest for the low-FRET sample and somewhat lower for high-FRET states. To check this, the data was corrected with an estimated rate of direct excitation $f_{dir} = 2\,kHz$. For the low-FRET standard the proximity ratio was reduced by 30 %, while the effect on the high-FRET sample was only 5 %. The corrected proximity ratios and FRET efficiencies are given in table 4.4. After the correction, the FRET efficiencies estimated from the helical DNA model were better reproduced.
The number of detected events in the isolated samples indicated a two-fold higher concentration of the high-FRET sample (1118/598 = 1.9). In the 1:1 v/v mixture we therefore expect to observe the same ratio between the peak areas of the two FRET subpopulations. From the measured distributions a ratio of 2.27 ± 2.2 was calculated, which is in good agreement with the expected value.

Various mixtures were prepared from donor-only and low-FRET standards to check, if the system can correctly reproduce different substate stoichiometries. The relative peak fraction was determined from the proximity ratio histogram and plotted vs. the nominal mixing ratio as shown in Figure 4.16. Panel A shows three representative histograms for the pure donor-only sample, a 1:1 mixture of both standards and the pure low-FRET species. 80 % of intact low-FRET molecules were observed, where the remaining 20 % carried an inactive acceptor dye and showed up as a donor-only species. In the 1:1 mixture the fraction of intact FRET standards is thus reduced to about 0.4, which agrees well with the expectations, if each fifth low-FRET molecule is inactive. For the pure donor-only species no molecules with non-zero FRET characteristics were

observed. As shown in Panel B the fraction of observed low-FRET states follows the linear dependence expected from the relative mixing ratios.

These two examples demonstrate that a mixture of FRET species can be recovered with correct stoichiometry and that different mixing ratios are satisfyingly reproduced. This is essential to investigate kinetic processes by a redistribution between different subpopulations. We are now in a position to investigate the dynamics and structural changes occuring on individual nucleosomes.

4.7 Discussion

Richard Keller, one of the pioneers of single molecule spectroscopy, once said, that it's not difficult to detect the signal from a single molecule but not to detect anything else [9]. This is particularly true for diffusion-based techniques, which profit from the properties of modern fluorophores. These provide a large absorption cross-section and a sufficiently high quantum yield to emit enough fluorescence photons during their passage through the laser focus. Fluorescence, however, is not the only source of photons from the medium. Additional photons arise from impurities and scattering in the buffer solution, which result in a laser-dependent background level, against which the valuable fluorescence signal has to be discriminated. A successful single molecule detection was achieved by optimisation of the flux of fluorescence photons, which are detected from the molecule. The individual steps, which are involved in the formation of the detetion signal, were gradually optimised.

Fluorophore excitation

A large excitation rate $k_{01} \propto I_0$ is essential to generate a large fluorescence flux from the fluorophore. From an analysis of the molecular brightness of the donor fluorophore an optimum laser intensity was found to be slightly below the saturation intensity, at which the rate of absorption equals the rate of de-excitation. Higher intensities led to useless accumulation of the triplet state and did not provide a net gain in fluorescence. The saturation intensity for free Alexa488 was found to be around $50\,kW/cm^2$, which was in good agreement with calculations from photokinetic parameters which were taken from the literature [42, 38]. The choice of the saturation intensity as an optimum excitation irradiance was also suggested by Tsien and Weggener [136]. An optimum signal-to-background level (SBR) was achieved at intensities $I < I_{sat}$, i.e. for free Alexa488 at $\approx 30\,kW/cm^2$. This value agrees with a theoretical calculation by Enderlein [42], who considered the contribution of Raman scattering and eletronic noise to the background. With the same set of photokinetic constants a value around $I_{opt} = 25\,kW/cm^2$ was calculated. Actual experiments used an intermediate intensity $I_{opt} < I < I_{sat}$.
I_{sat} and I_{opt} varied significantly between free Alexa488 and the dye conjugated to DNA. For end-labeled DNA fragments that were used for nucleosome assembly the saturation intensity and the maximum emission were reduced by almost a factor of 2. This is rather unpleasant, since fewer photons will be detected. It remained to be checked whether this is also observed for internally labeled DNA fragments.

Photostability of fluorophores

Once the excitation was optimised it has to be ensured that the fluorophore efficiently coverts the absorbed energy into fluorescence photons. Prior saturation and photobleaching reduce or terminate the fluorescence flux and thus impede the identification of single molecule events. A significant body of research is devoted to the photokinetic of individual molecules [41, 136, 142, 40, 40] but detailed information on stabilisation of specific fluorophores is rare.
In this thesis the photostability of the reporter dyes was optimised in an extensive test series of various photostabilising agents. Data was acquired on the bulk level, as well as under true single molecule sconditions. The results agree with findings from other research groups [Dietrich2002c] in such that the effect of ascorbic acid and cysteamine on Alexa488 were qualitatively reproduced. Ascorbic acid (and sodium ascorbate) caused a significant increase in triplet population which was attributed to their antioxidant effect. Lowering the oxygen concentration reduces the quenching rate of the triplet state. Cysteamine, on the contrary, efficiently quenched the triplet state and caused an increase in emissivity. The effects were larger for Alexa488 than for the acceptor fluorophores. The data presented in this thesis extends the discussion by e considerable treatment of the photostabilising potential in single molecule FRET experiments. Rhodamine X was identified as the most sensitive fluorophore w.r.t photostabilisation, while the spectrally similar Alexa dyes were less affected. A comparison with labeled nucleosomes indicated that the presence of the octamer did not influence the photostability of the fluorophores. At the same time this data validate the use of easy-to-handle oligonucleotides as a photophysical model system for the nucleosome samples. The nucleosome preparation is quite time-consuming and costly, whereas the oligonucleotides are less expensive and readily available in larger quantities.
From our studies the use of $\leq 1\,\mathrm{mM}$ ascorbic acid and $3-5\,\mathrm{mM}$ cysteamine proved to be most useful for further experiments. This agrees well with concentrations used by other research groups (Prof. Seidel, personal communication).

Optimisation of the detection efficiency

The detection efficiency deserved attention in the process of system optimisation, since the highest photon flux from the molecule is useless if the fluorescence is not adequately detected. The overall detection efficiency was calculated as the product of a geometric term and a spectral factor. The latter strongly depends on the transmission properties of the filters and can be used to compare different filter sets. In doing so the maximum detection in the donor and acceptor channel was achieved by filter sets Q and N.
Depending on the excitation wavelength it was found that optimising the detection efficiency does not always mean to maximise it. Under single molecule conditions (high irradiance, low total fluorescence signal) the contribution from Raman scattering cannot be neglected. For excitation with the 470 nm laser diode the filter set Q overlaps with a Raman band from the aqueous solvent and produced an intolerable background signal. For this excitation wavelength a different filter set is more appropriate (e.g. filter set R).

A second Raman band of water coincides with the emission region of the fluorophores and cannot be discarded by appropriate filter settings. In this case the unwanted background can be reduced by applying a time-gated detection [87]. This uses the fact that fluorescence is delayed w.r.t. prompt scattering of excitation light by a few nanoseconds, i.e. its natural lifetime. A properly set time gate on the arrival time will discard most scattered photons and greatly reduce the background level. This will be incorporated into future experiments with pulsed excitation.

Burst selection

The imfluence of the burst selection process on the outcome of the single molecule experiment was analysed to define a useful set of threshold parameters. Low IPT_{max} settings favored those events which predominantly reside in the central region of the laser focus. The intensity is highest and the photons are emitted fast enough to meet the burst selection criteria. In combination with a larger value of N_{min} only few molecules will be detected, but these will produce a smaller distribution width in the histogram and enhance the separability of subconformations. At the same time, however, a larger acquisition time is required to obtain a reasonable statistics. Less stringent selection conditions increased the number of events, since more particles were detected from the peripheral focus regions. The improved sample throughput was accompanied by an increased distribution width, though.
Almost all parameters deviated from the expected behavior as the burst duration exceeded the meaningful time introduced by Foldes-Papp [55]. The threshold settings are then no longer adequate, and the probability that multiparticle events become included in the analysis is considerably increased. T_m depends on the diffusion time of the molecule and the mean number of particles in the focus. The results from the FRET standards, for which T_m was estimated between 5.5 and 6 ms, cannot be generalized to nucleosomes which showed a three-fold increased diffusion time. Moreover, the particle concentration might be chosen differently in each experiment. For each sample, the corresponding value of T_m should be estimated by equation 2.31.

Additional measures to increase the photon yield

In the absence of photobleaching fluoresence photons are emitted as long as the molecule resides in the focus. Slowing down the diffusion process therefore produced an increased overall photon signal. To reduce the mobility of the molecule either the viscosity of the medium or the effective hydrodynamic radius of the particle were increased.
An increase in viscosity was achieved by adding glycerol into the buffer medium. Care had to be taken to minimise the effect of optical mismatch introduced by the change in refractive index. A titration series of glycerol showed most convincing results near the cover slip where the optical path through the medium was minimal. The change in diffusion time matched the increase in viscosity, and an alomost six-fold increase in the photon yield was observed in the presence of 50 % v/w glycerol were added. In

subsequent single molecule studies this emerged as an upper limit of useful concentrations. If more glycerol was added a significant reduction in emissivity was observed. An overall increase in burst size and burst duration of a factor 2 was by far lower than the changes observed in the FCS experiments. This is probably caused by the preference of the burst selection process for long lasting events, which consequently emit more photons. Molecules, which transit the focus too fast, might not emit enough photons to be registered.
A different approach to slow down the molecule is to encapsulate it into a larger lipid container [10]. Within the liposome, the sample is free to rotate and the effective hydrodynamic radius is defined by the size of the liposome. Preliminary test results from small oligonucleotides showed that the interfluorophore distance was correctly reproduced after encapsulation. A substantial increase in the average burst size and duration were observed but quenching effects were not negligible either. It remains to test, whether this is a consequence of residual interactions with the lipid membrane or a result of the encapsulation procedure. The statistical character of the encapsulation process leads to a non-vanishing probability that more than one molecule is contained in a vesicle. These events are difficult to be separated from those events which show a single vesicle occupancy. Such events might be a problem for future experiments, and the encapsulation process will have to be optimised in order to minimise the probability of have more than one molecule inside a vesicle.

Both methods produced a similar change in burst size, while the proximity ratio distribution changed significantly in the vesicle-based approach. The increase in detected zero-FRET events is of substantial concern. Further experiments will be required to optimise the encapsualtion process. A different use for the vesicle containers is to tether them onto lipid-coated surface[10, 115, 21]. By this the molecule of interest can be immobilized on the surface while retaining free mobility inside the vesicle.

Chapter 5

Stability and dynamics of nucleosomes

The previous chapter was devoted to finding the optimum conditions for the detection of single molecules in our diffusion-based system. Various technical factors were optimised to enable an accurate analysis of the conformational heterogeneity in an ensemble of nucleosomes. This chapter now focusses on the structural properties of nucleosomes under single molecule conditions and the constrains their structure might impose on the single molecule experiment.
To set a framework for future experiments, a thorough analysis of the stability of individual nucleosomes is presented as a function of various environmental factors: ionic strength, nucleosome concentration and addition of inert protein. The delicate balance between the attractive DNA-octamer interactions and the energy required to bend the DNA around the histone core is easily shifted towards a destabilisation of the complex, which prevents the successful performance of SMD experiments. On the other hand the dissociation behavior provides useful information on the stability of nucleosomes. Preliminary results are presented in which the intrinsic dynamics of individual nucleosomes was analysed under highly destabilising conditions.
The inevitable presence of free DNA caused by dissociation of the nucleosome and imperfect sample purification complicated the analysis of linker DNA dynamics. Since this is an integral part of its structure a refinement of the detection sensitivity for this low-FRET regime had to be improved. This is outlined at the end of the chapter.

5.1 Nucleosome stability

Test experiments on small FRET standards suggested that in the current setup single molecule experiments could be performed at concentration between 5 and 100 pM. At higher concentrations the impact of multiparticle transits is no longer negligible. At lower concentrations the sample throughput is considerably reduced, and larger acquisition times are required to detect enough molecules for a good statistics. Moreover, experiments on macromolecular complexes such as the nucleosome have to consider the intrinsic dissociation behavior of the complex. This is particularly relevant under

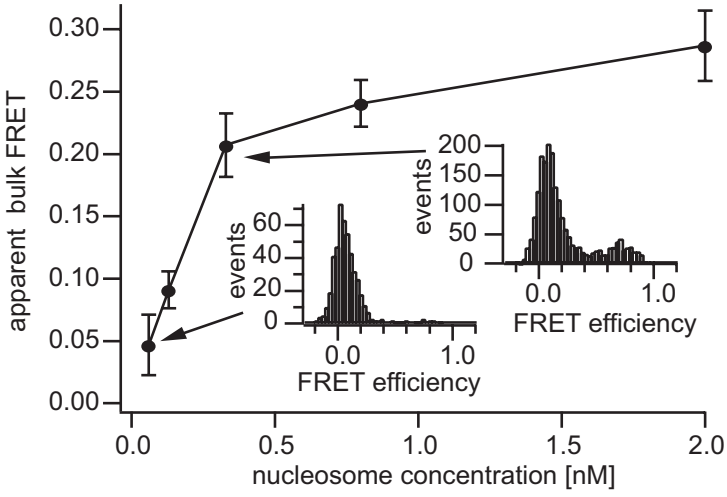

Figure 5.1: Dilution-driven dissociation of nucleosomes. From the count rates in both detection channels, a bulk proximity ratio was calculated according to equation 2.46. The two inlay sketches show proximity ratio histograms, which were obtained under single molecule concentrations. The disappearance of the high-FRET population is caused by the loss of intact nucleosome complexes.

sub-nM concentrations as has been shown by Gottesfeld and Luger [61]. The authors determined apparent dissociation constants between 30 and 60 pM for weaker binding positioning sequences at physiological ionic strength. Only at larger concentrations than this, a sufficient nucleosome stability is achieved. Unfortunately, these values coincide with the concentrations used in single molecule experiments.
Consequently, fluorescently labeled nucleosomes showed a significant decrease in the mean energy transfer, if they were successively diluted to sub-nM concentrations. This is demonstrated in Figure 5.1, where the bulk proximity ratio of 601^{170}_{high} nucleosomes was determined as a function of nucleosome concentration.
The decrease of the bulk proximity ratio at sub-nM concentrations indicated the loss of intact nucleosomes, where DNA has dissociated from the octamer. As a result the interfluorophore distance was increased above values at which energy transfer can occur. The inlay histograms were taken for two different nucleosome concentrations and prove that the reduced proximity ratio was indeed due to the loss of intact molecules and not caused by a shift of the total population to smaller P values.
Apparently, the stability of nucleosomes has to be improved significantly, before their conformation can be analysed on the single molecule level. This was achieved by two means: passivation of the sample container with inert protein and addition of an excess of unlabeled nucleosomes.

5.1.1 Stabilisation by inert protein

One way to stabilise nucleosomes was the addition of an excess of inert protein into the solution. For this purpose we chose bovine serum albumin (BSA), which is a standard reagent in protein biochemistry. This protein is often used to passivate charged surfaces to prevent unspecific interactions with biomolecules and subsequent sample degradation. The stabilising potential was monitored at nucleosome concentrations around $60\,pM$. The fraction of intact 601^{170}_{med} nucleosomes was monitored at different BSA concentrations and ionic strength. Figure 5.2A shows time traces of proximity ratios obtained at $100\,mM$ NaCl with and without addition of $0.1\,g/l$ BSA. Panel B

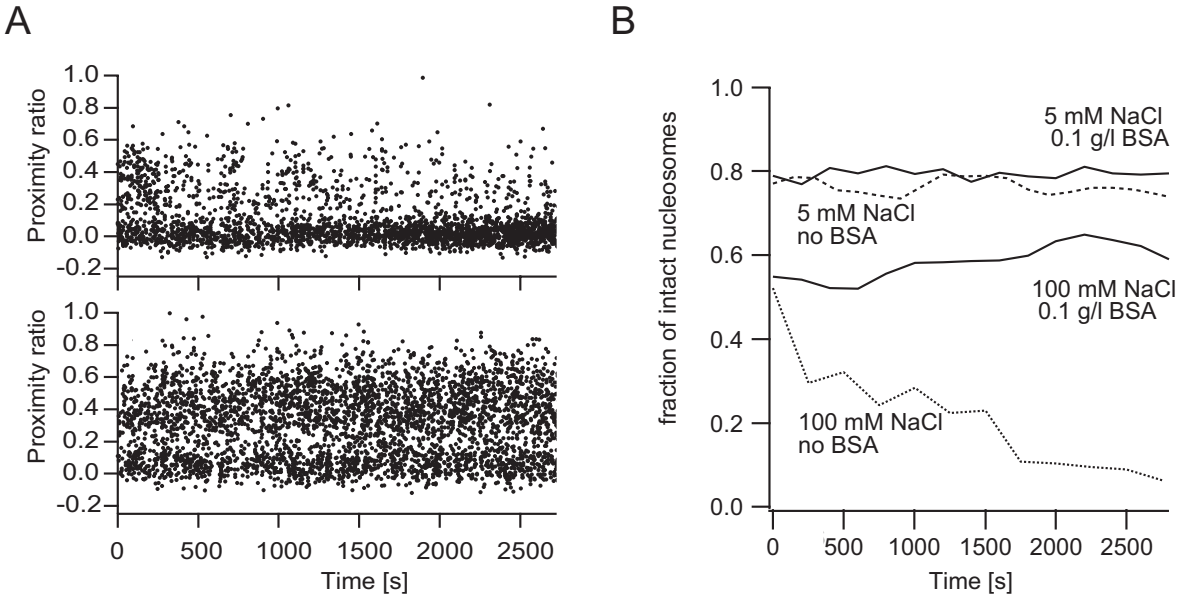

Figure 5.2: **A**: Time trace of the proximity ratio of $60\,pM$ 601^{170}_{med} nucleosomes diluted in $1x\,TE$, $1\,mM$ ascorbic acid, $100\,mM$ NaCl with (lower panel) and without(upper panel) additional $0.1\,g/l$ BSA. **B**: Comparison of the nucleosome stability over time for different concentrations of salt and BSA. Low salt conditions ($5\,mM$ NaCl) apparently do not require additional stabilisation of the nucleosome.

compares the fraction of intact nucleosomes as a function of time for different concentrations of BSA and NaCl. At $100\,mM$ NaCl a significant decrease in the intact nucleosome population was observed during the first 30 minutes after incubation in BSA-free buffer. In BSA-containing buffer the fraction of intact nucleosomes remained constant over the whole period of one hour. At low ionic conditions ($5\,mM$ NaCl) nucleosomes were stable even in the absence of BSA.
To further investigate the salt dependence the nucleosome stability was monitored at different BSA concentrations as shown in Figure 5.3A . Again, at $5\,mM$ NaCl no difference was observed whether or not BSA was added. Salt concentrations above $50\,mM$ NaCl caused a significant destabilisation in the absence of protein. A progressive increase in BSA concentration improved the nucleosome integrity, and dissociation occured at successively larger ionic strength. At $0.1\,g/l$ BSA the dissociation was observed above $300\,mM$ NaCl only. BSA concentrations above $0.2\,g/l$ did not further improve the stability. The amount of BSA that has to be added to stabilise the nucleosomes obviously depends on the ionic strength. This is not surprising since nucleosomes tend to destabilise at higher salt concentrations due to a screening of the electrostatic attraction between octamer and DNA. Various control experiments were performed to ensure that the presence of BSA did not alter the properties of the nucleosome.

- The influence of BSA on the dye properties was assessed by comparing nucleosomes compacted with linker histone H1 to non-compacted nucleosomes. The data were taken at low BSA concentrations. The binding of linker histone H1 to the ends of the DNA should not affect the fluorophore properties at internal

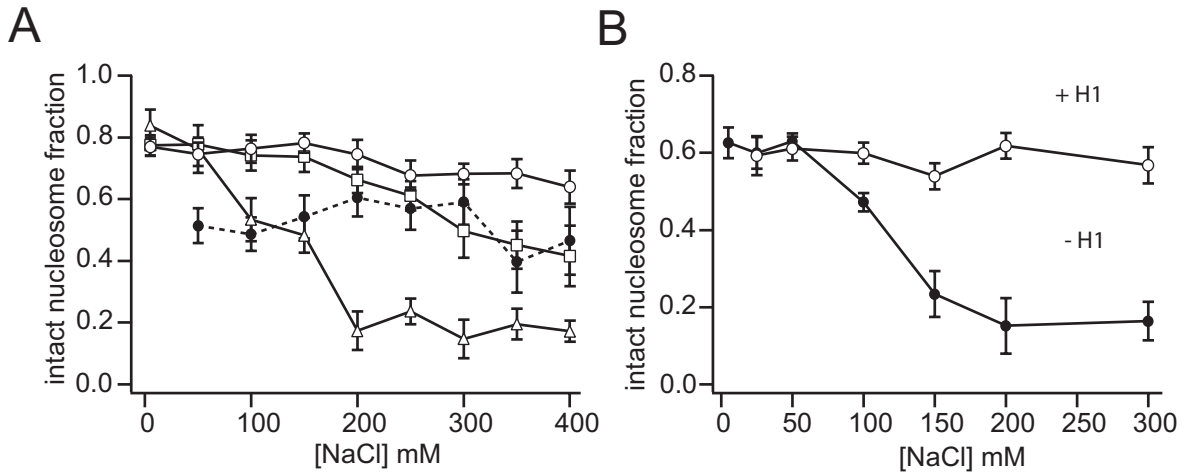

Figure 5.3: **A**: Salt-dependent stabilisation of 601^{170}_{med} nucleosomes. Shown is the fraction of intact nucleosomes for different salt concentrations and amounts of BSA added to the buffer. **B**: Control experiment with nucleosomes compacted with linker histone H1.

DNA sites so any dye-related effect should show up in both experiments. As shown in Figure 5.3B , a constant fraction of intact nucleosomes was maintained if the nucleosomes were compacted by H1. In the absence of H1 dissociation of nucleosomes took place in the usual way. This suggests that the reduction in the FRET population was indeed due to the dissociation of the nucleosome and not caused by any dye related artefacts.

- Ion conductance measurements probed for potential changes in the effective ionic strength, which might result from the presence of the protein. The stock solution of BSA ($10\,g/l$) showed an ionic strength of approximately $70\,mM$ monovalent ions. Under typical dilution conditions ($0.1\,g/l$ BSA, corresponding to a 100-fold dilution) an excess of only $0.7\,mM$ monovalent salt was added. This is negligible under higher salt concentrations.

At highly diluted nucleosome concentrations, the use of BSA alone did not prevent the dissociation of the complexes as demonstrated in Figure 5.4. Panel A shows the time trace of the fraction of intact nucleosomes at three different nucleosome concentrations of $60\,pM$, $20\,pM$ and $5\,pM$. Each experiment was performed at $100\,mM$ NaCl and $0.1\,g/l$ BSA. Panel B depicts subhistograms collected for the first and second half of the experiment.

At larger nucleosome concentrations no significant dissociation was observed. The two subhistograms did neither indicate a dissociation of intact nucleosomes nor a slow redistribution between different conformations. On the contrary, a significant loss of intact nucleosomes was observed at a concentration of $5\,pM$. The corresponding time course of the total intact nucleosome fraction was described by an apparent dissociation rate of $k_{off} = (1.1 \pm 0.1) \cdot 10^{-4}\,s^{-1}$. The intact nucleosome population did not vanish uniformly but showed an interconversion dynamics as can be seen in the lower panel of Figure 5.4B . A redistribution between at least two substates might be anticipated.

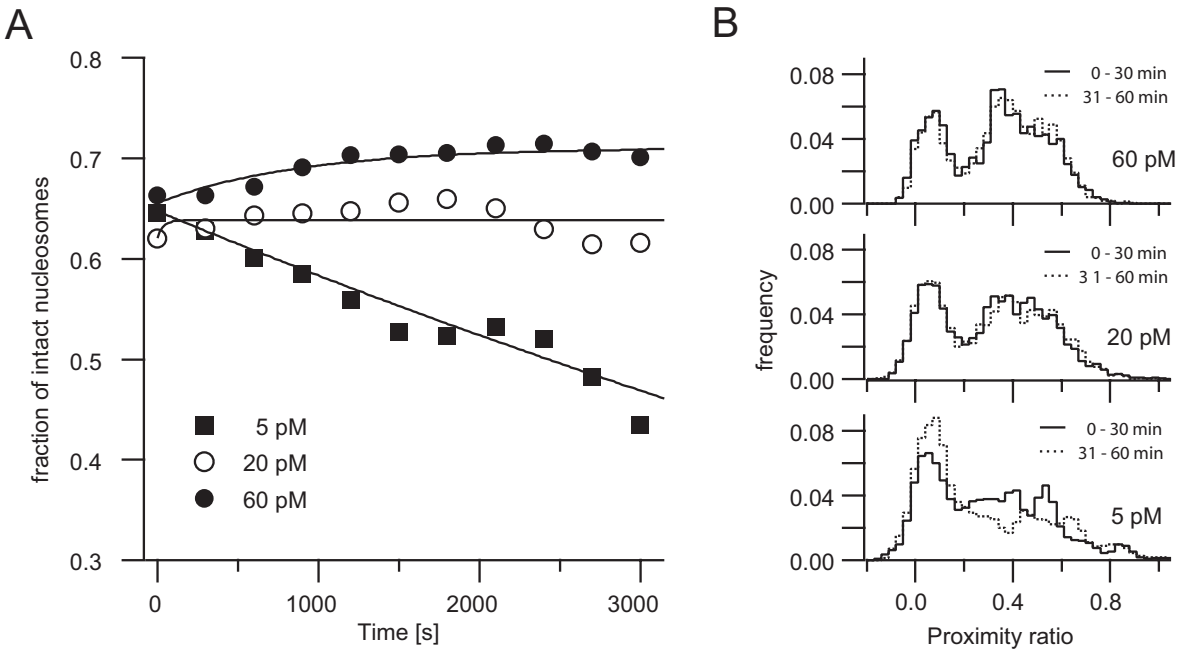

Figure 5.4: Failure of BSA to stabilise nucleosomes at higher dilutions and elevated salt concentrations. **A**: Time trace of the intact nucleosome fraction at three different nucleosome concentrations ($60\,pM$, $20\,pM$ and $5\,pM$). **B**: Subhistograms for the first half (solid line) and second half (dotted line) of each measurement. Data was taken for a total of one hour.

Unfortunately, the low sample throughput prevented a detailed analysis, since too few molecules were detected to offer a reasonable statistics. This aspect will be discussed in more detail in the forthcoming section. First, however, a second method to improve the nucleosome stability is introduced, namely the increase of the effective nucleosome concentration.

5.1.2 Stabilisation by unlabeled nucleosomes

Dissociated DNA can no longer report on structural properties of the nucleosome, and a thorough analysis of conformational changes, e.g. upon acetylation, is severely hindered. The failure of BSA to prevent dissociation of highly diluted nucleosomes made it thus necessary to further consider the impact of nucleosome concentration on their stability. The constrains of SMD conditions prohibit the use of more than $100\,pM$ fluorescent nucleosomes. Taken on its own, this is not sufficient to prevent dissociation of less stable complexes. By adding unlabeled nucleosomes into the solution, however, the total nucleosome concentration can be raised to bulk values while true SMD conditions still hold, since only $50\,pM$ of them are labeled.
Nucleosomes that were diluted into a buffer containing an excess of $10\,nM$ unlabeled nucleosomes were significantly stabilised, as shown in Figure 5.5. At $100\,mM$ NaCl an increased fraction of intact nucleosomes was observed for both linker DNA labeled (panel A) and internally labeled 601^{170} nucleosomes (panel B). In the absence of unlabeled complexes, the fraction of intact nucleosomes was considerably reduced. Only

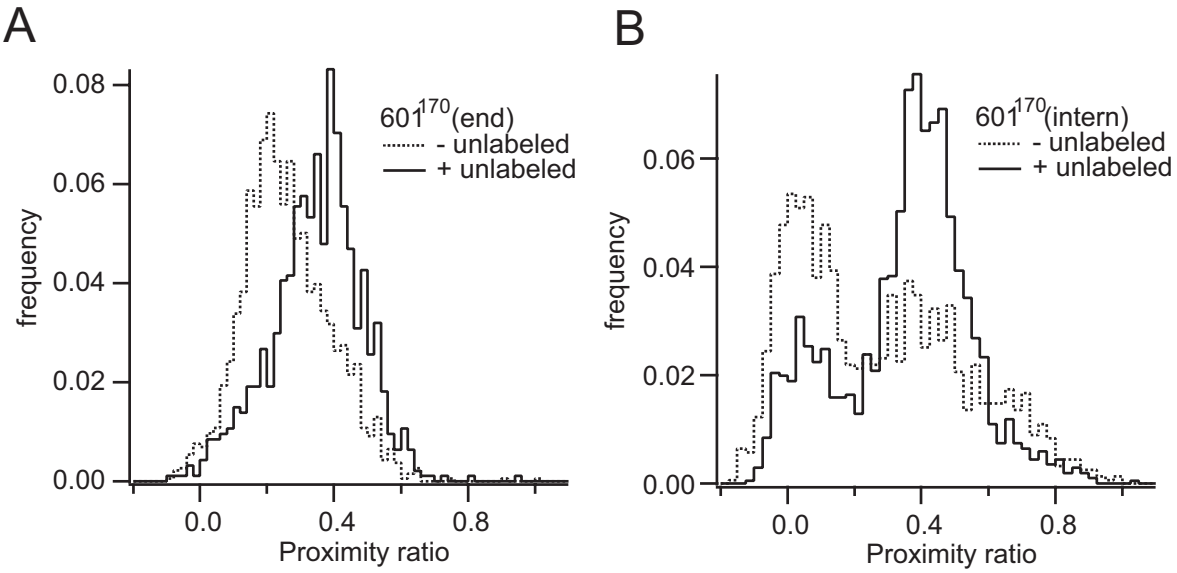

Figure 5.5: Stabilisation of nucleosomes by addition of an excess of unlabeled complexes. **A**: linker DNA labeled 601^{170} nucleosomes, **B**: internally labeled constructs. Experiments are compared, where $50\,pM$ labeled nucleosomes were added into the buffer, which contains $0\,nM$ (dotted lines) or $10\,nM$ (solid lines) unlabeled nucleosomes. Data were taken under different filter settings where $\gamma \approx 1.9$ in panel A and $\gamma \approx 0.8$ in panel B .

51.2 % of the nucleosomes remained intact, while 76.4 % intact nucleosomes were observed, if $10\,nM$ unlabeled complexes were present in the buffer. Moreover, in the absence of unlabeled nucleosomes the intact FRET population appeared to contain another subpopulation at higher proximity ratio (around $P = 0.7$), which increased in relative strength as the unlabeled nucleosomes were omitted.

As in Figure 5.4, this might indicate the presence of intermediate nucleosome conformations at low sample concentrations. It it therefore worthwhile to take a closer look on the behavior of nucleosomes at highly destabilising conditions.

5.2 Nucleosome dynamics

A multiparameter analysis was performed in collaboration with the group of Prof. Seidel in Düsseldorf to learn more about the nucleosome dynamics under destabilising conditions. 601^{170}_{med} nuclesomes were exposed to increased salt concentrations at high dilution, i.e. in the absence of unlabeled nucleosomes. Owing to their low concentration a substantial dissociation of nucleosomes was observed above $50\,mM$ NaCl. Figure 5.6 compares single molecule distributions for 5 and $50\,mM$ NaCl. Panels A and C show two-dimensional distributions of the donor lifetime in the presence of the acceptor, $\tau_{D(A)}$, versus measured intensity ratio S_G/S_R. The time course of the intensity ratio is plotted in panels B and D .

At $5\,mM$ NaCl the nucleosome population remained stable over the whole time period of more than 1 hour. This agrees with the data presented in the previous section where

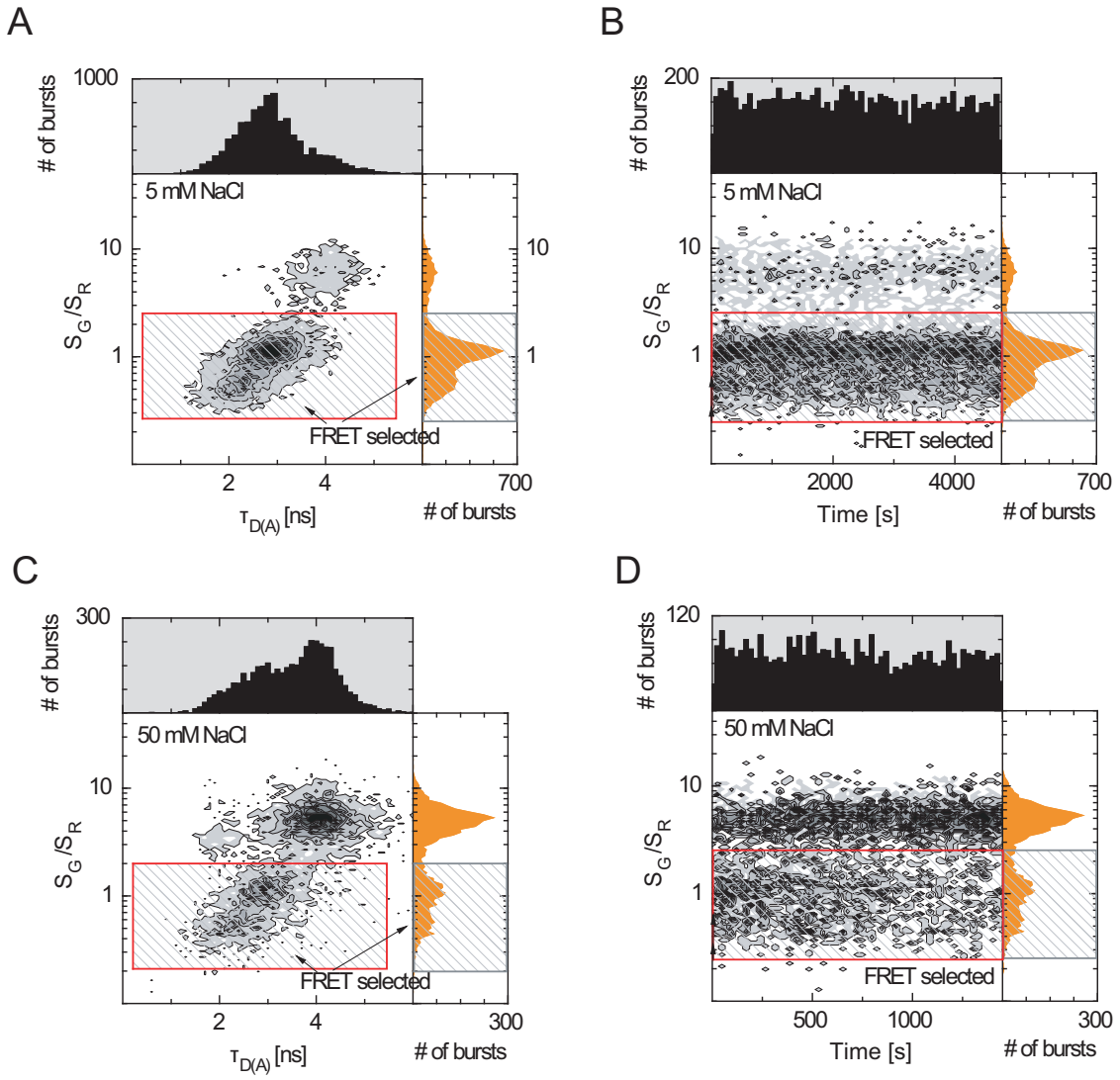

Figure 5.6: Multidimensional analysis of single nucleosomes **A**: Two-dimensional distribution of donor lifetime versus the measured intensity ratio S_G/S_R at $5\,mM$ NaCl **B**: Time trace of the intensity ratio at $5\,mM$ NaCl, **C**: and **D**: Respective data for $50\,mM$ NaCl. The top histogram in the time traces show the total number of detected events per time bin and indicate that no significant adsorption of the sample to the cover slip took place.

dissociation occured at larger ionic strength only. At $50\,mM$ NaCl a significant dissociation was observed and only few nucleosomes remained intact after 20 minutes. At higher salt concentrations, the dissociation proceeded too fast to collect enough intact nucleosomes for a reasonable analysis. Apparent dissociation rates were determined by an approximation with a monoexponential function. For $50\,mM$ NaCl we obtained an off-rate of $k_{off} = 8.6 \cdot 10^{-4}\,s^{-1}$ which increased to $k_{off} = 1.6 \cdot 10^{-3}\,s^{-1}$ at $100\,mM$ NaCl.

To analyse the composition of the intact nucleosome distribution we performed a PDA analysis for different salt concentrations between $5\,mM$ and $50\,mM$ NaCl. In all experi-

ments a minimum of three Gaussian populations was required to describe the measured intensity ratio distribution. From these model states a theoretical intensity ratio histogram was calculated and compared to the experimental data, as shown in Figure 5.8A and B . The corresponding model populations are displayed in the lower part. Two sharp populations reflect conformations with only minor intrinsic dynamics which are referred to as HF (high-FRET) and MF (medium-FRET) bound states. A third, broadly distributed component was always required to match the data which is termed a "loose" state.

Notably, the relative fraction of the individual states changed considerably as a function of ionic strength. The medium-FRET component decreased in favor of the high-FRET state and the mobile component. The center position of the bound states remained stable and a slight increase in width was observed at $50\,mM$ NaCl only. The bound states probably arise from compact conformations whose inherent structure is rather insensitive to higher ionic strength. The change in their relative occupancy points towards significant differences in the binding affinity of DNA to the octamer between both conformations. The medium-FRET state dissociated at lower ionic strength already, while the high-FRET state appeared more stable. This static analysis cannot exclude an interconversion between both states though.

A PDA analysis was performed for different time windows of $0.5\,ms$, $1\,ms$ and $3\,ms$ to investigate this aspect in more detail. Any dynamic process faster than the diffusion time results in significant differences between the intensity ratio distributions observed for different binning times. As can be seen from Figure 5.8A and B , under low salt conditions the model histograms were quite similar, except for an excess broadening at $3\,ms$ bining time. If nucleosomes were diluted into higher salt, however, significant changes were observed for smaller time windows already. Obviously, a structural dynamics occurs on the millisecond time scale, which becomes faster as the salt level is increased.

This dynamics correlates with the dissociation of the nucleosome as demonstrated by a sequential PDA analysis that is shown in Figure 5.8C and D . Events from the beginning and the end of the experiment were analysed with a binning time of $0.5\,ms$.

At $5\,mM$ NaCl (panel C) both model histograms showed similar features which indicates the absense of any significant changes in the dynamics. The change between the histograms is highly significant at $50\,mM$ NaCl (panel C). Compared to the distributions obtained from the first ten minutes, additional states were required to describe the data at a later atage.

One might speculate that additional conformations are induced as a consequence of dilution-driven destabilisation. The DNA might be partially dissociated from the octamer and show a faster dynamics and higher flexibility. At higher salt concentration the increase in subpopulation dynamics correlates with an larger dissociation of complexes indicating the close relationship between both observations.

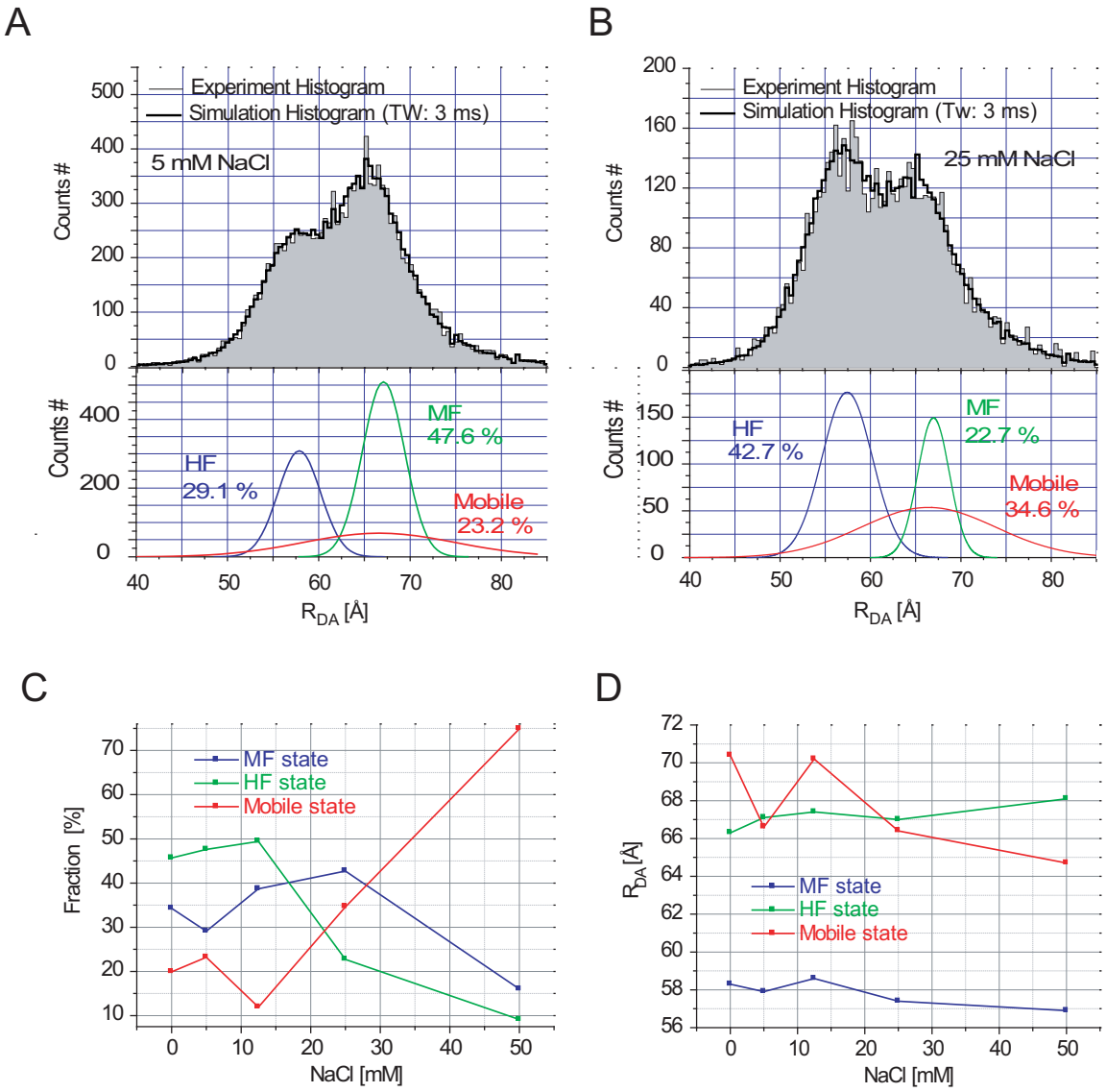

Figure 5.7: Photon distribution analysis for the measured histogram at (**A**) $5\,mM$ and (**B**) $25\,mM$ NaCl. The three model populations required to fit the histogram are depicted in the lower part. **C**: Variation of the relative occupancy of the model states as a function of salt concentration. Notably, the MF and HF states show a different dissociation behavior with HF being more stable at larger ionic strength. **D**: Salt dependence of the respective center position. The peak center position is not affected by the elevated salt concentrations.

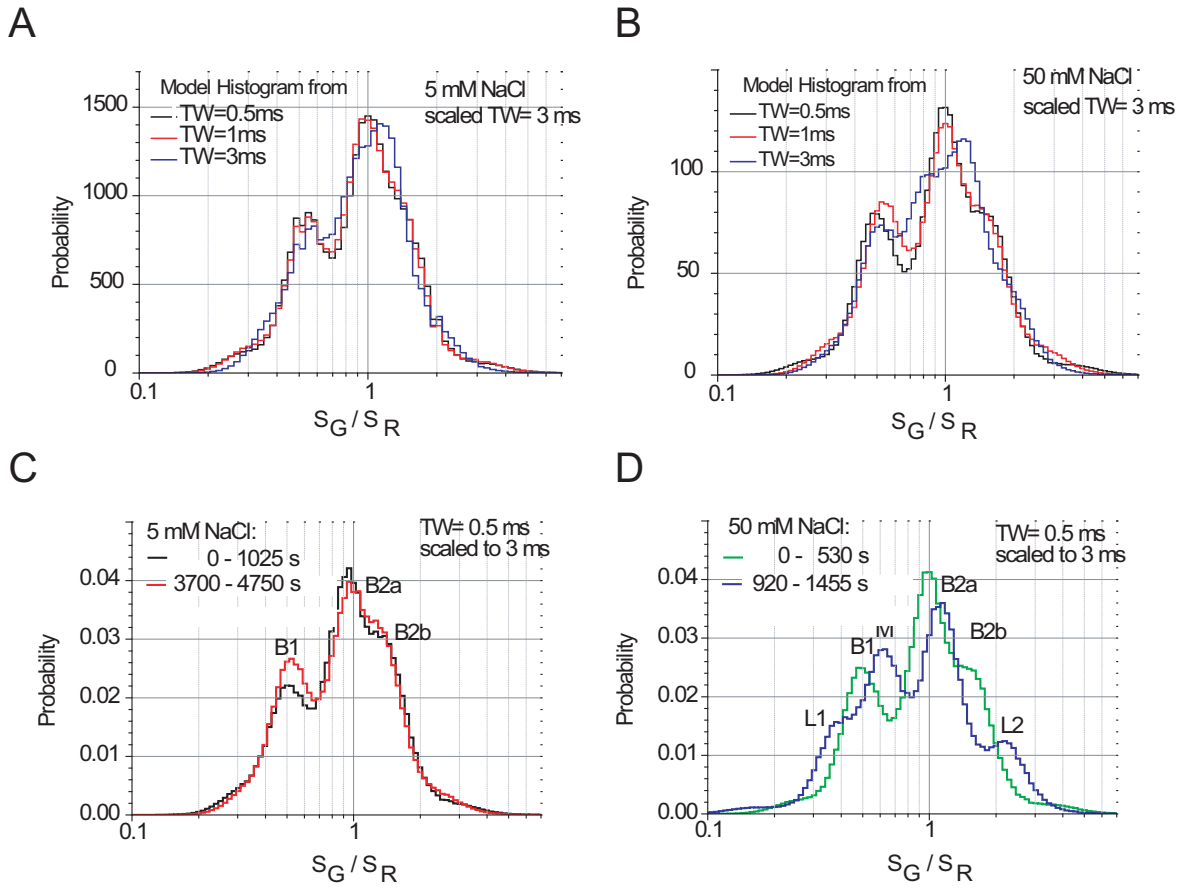

Figure 5.8: Time-window analysis of the histograms obtained at different salt concentrations **A**: 5 mM NaCl, **B**: 50 mM NaCl. Shown are three histograms corresponding to time windows of 0.5 ms, 1 ms and 3 ms. Significant changes in the histograms at 50 mM NaCl indicate the presence of dynamics occuring on the ms-time scale. **C** and **D**: Sequential time window analysis for 5 and 50 mM NaCl indicating anchange in nucleosome dynamics over time at higher salt concentrations. The potential substates are denoted as B1, B2a, B2b : bound states, M: mixing peak, L1, L2: loose states.

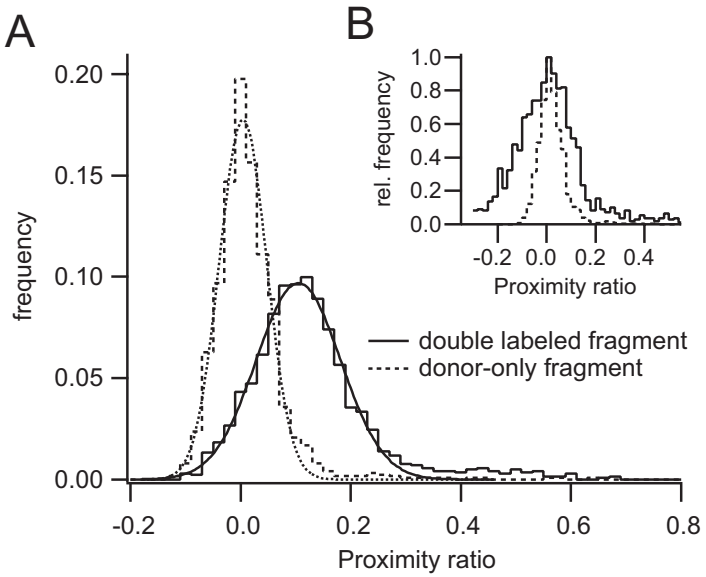

Figure 5.9: (**A**) Proximity ratio histograms of a donor-only labeled DNA (dotted line) and a double labeled DNA-fragment (solid line). The width of the double labeled DNA is considerably increased (0.109 ± 0.003 compared to 0.061 ± 0.002 for the donor-only sample. (**B**) Comparison of both distributions after the correction for direct excitation. The width of the double labeled DNA is enlarged by another 25 % (0.136 ± 0.006).

5.3 Detection scheme for low-FRET nucleosomes

The complete analysis of nucleosome dynamics under different conditions requires data to be obtained from both linker DNA and octamer-bound DNA sites. Internal labeling of DNA fragments generates constructs with upto 80 % FRET efficiency [57, 133, 94], whereas attachment of fluorophores to the linker DNA ends limits the average FRET efficiency to approximately 30 % [135].

The resolution of nucleosome subconformations in the low FRET regime is hindered by two factors: the omnipresent zero-FRET peak due to inactive or missing acceptor fluorophores and the presence of free DNA. Being a result of nucleosome dissociation, the amount of free DNA is non-negligible under single molecule conditions. The fluorophore separation on nucleosomal DNA fragments is long enough to show no FRET and should therefore coincide with the zero-FRET peak. Due to the acceptor presence, however, the DNA population is centered around a non-vanishing proximity ratio, if the direct excitation is not corrected for. As demonstrated in Figure 5.3A , the distribution for double labeled DNA is considerably broadened compared to the distribution of an equivalent donor-only labeled DNA. In panel B , the direct acceptor excitation was corrected for, which caused a further increase in distribution width, which exceeded the width of the donor-only sample by more than a factor of two.

This might complicate experiments on linker DNA labeled nucleosomes, which have to be discriminated against the free DNA. It is thus essential to increase the dynamic range, in which low-FRET subpopulations can be analysed. This section discusses an approach which is based on the controlled dealignment of the detection efficiency in the donor channel (**d**eliberately **d**etuned **d**etection, D^3).

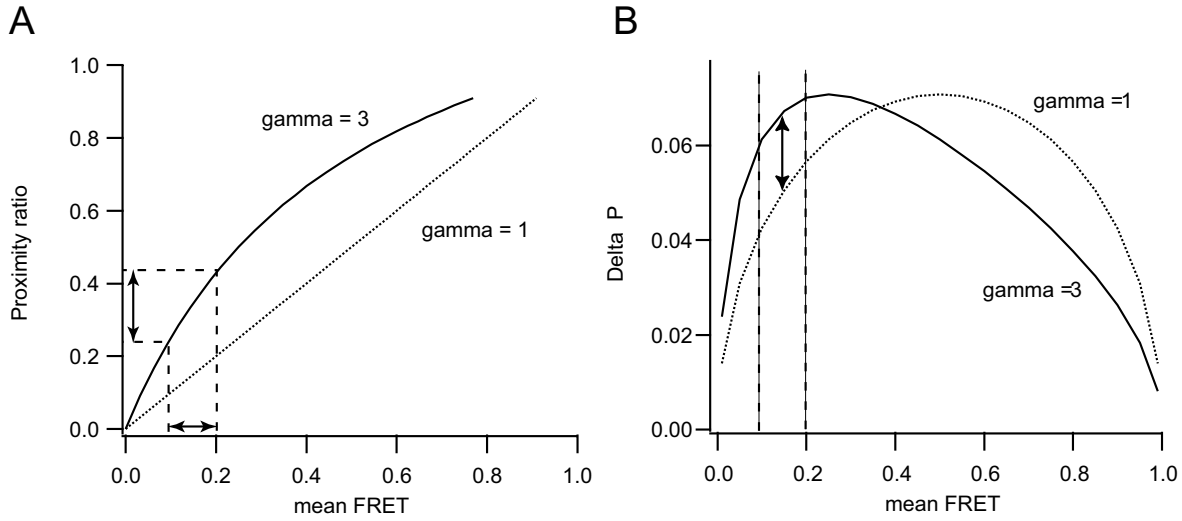

Figure 5.10: Effect of changing the detection factor on (**A**) the separability of two low-FRET substates and (**B**) on the shot noise of the corresponding populations. Both contradictory effects will balance off, where a compromise has to be found to yield best results.

5.3.1 The idea behind D^3

The distribution of interfluorophore distances can be analysed either as the FRET efficiency, E, or in terms of the proximity ratio P (section 2.3.2). P is calculated from the detected photon counts and does not require an explicite knowledge of the detection factor γ. Both quantities are related to each other by equation 2.48 and generally contain the same information on the interfluorophore distribution. In many experiments only relative changes within the histogram are of interest, so both quantities should yield comparable results.
The optical system can be tuned more sensitive either towards the low-FRET or high-FRET regime, as pointed out in section 2.3.2. A large $\gamma-$factor was shown to increase the separation of low-FRET states in their respective proximity ratio (compare to Figure 2.3.2). At the same time, however, the shot noise limit ΔP will increase as well (equation 2.55). These two contradictory aspects are illustrated in Figure 5.10.

As a rough estimate, the analysis of the proximity ratio is beneficial as long as the increased separation is not compensated by the increase in shot noise width, i.e. $P_2 - P_1 > \Delta P_1 + \Delta P_2$. Values of P and ΔP, which correspond to $E_1 = 0.1$ and $E_2 = 0.2$, are listed in table 5.1 for various values of γ and selection thresholds S. The simple estimate shows that at conditions of larger $\gamma-$factors and higher thresholds S the separability still exceeds the shot noise broadening.
It is noted that the model of point-like distributions is far too simple to describe real data. Every distribution is broadened beyond the shot noise limit due to conformational or dynamic heterogeneity and the effect of background and crosstalk (section 3.4.2). Thus it was tested experimentally how far a controlled manipulation of the detection factor can improve the analysis of low-FRET subconformations.

5.3.2 Experimental realisation of D^3

The detection factor γ is determined by the quantum yields of donor and acceptor and the efficiencies of both detection channels, $\gamma = \eta_A \Phi_A / \eta_D \Phi_D$. The overall detection efficiency of each channel is composed of a geometric term and a spectral factor, equation 4.3. Both factors can be selectively altered to generate different detection conditions. η^{spec} is manipulated by replacing the optical filters, while η^{geom} can be conveniently altered by detuning the lenses L3 and L4 in front of the photodiodes. Both strategies were compared in Figure 5.11, where a mix of donor-only and high-FRET standards was analysed at different $\gamma-$factors. The upper part shows histograms, which were obtained by a change of η^{geom}, while the lower histograms were acquired with different spectral filters.
Both methods produced a similar shift in the center position of the high-FRET population. As γ is increased, the width of the zero-FRET distribution increased, which is in agreement with the expectations from the theory. A similar change in the distribution width of the high-FRET standard is less obvious and probably skewed by the additional sources of broadening as outlined above. Table 5.2 lists the estimated $\gamma-$factor, the center position of the proximity ratio and the calculated energy transfer efficiency for the high-FRET distribution. Q' and N' denote filter conditions where η^{geom} was detuned. Unprimed quantities were aligned for maximum detection efficiency. A larger discrepancy between the estimated FRET efficiencies was noted, if different spectral filters were used. Replacing the emission filters might cause additional uncertainties in the estimation of γ, since the geometric term in the detection efficiency might be affected as well. Filter quality changes over time due to abrasion or dirt on the optical interfaces, These are effects, which were not accounted for in the estimation of the filter profiles.
On the contrary, the FRET efficiencies calculated under dealigned filter conditions agreed much better within their errors. The determination of γ was more robust, since the spectral properties were not influenced. The slight increase in transfer efficiencies calculated for small detection factors might reflect the residual effect of direct excitation, which was not adequately corrected for.

		$\mathbf{\Delta P(E_2) + \Delta P(E_1)}$			
γ	$\mathbf{P(E_2) - P(E_1)}$	$\mathbf{S = 25}$	$\mathbf{S = 50}$	$\mathbf{S = 75}$	$\mathbf{S = 100}$
1.0	0.100	0.140	0.099	**0.081**	**0.071**
1.5	0.130	0.159	**0.113**	**0.092**	**0.080**
2.0	0.152	0.171	**0.121**	**0.099**	**0.086**
2.5	0.167	0.180	**0.127**	**0.104**	**0.090**
3.0	0.175	0.186	**0.131**	**0.107**	**0.093**

Table 5.1: Separability of two point-like distributions at $E_1 = 0.1$ and $E_2 = 0.2$ under different detection factors γ and minimum burst sizes S. For the bold numbers, the sum of the distribution widths $\Delta P(E_2) + \Delta P(E_1)$ is smaller than the separation of the respective proximity values $P(E_2) - P(E_1)$. The effect of additional broadening was not considered.

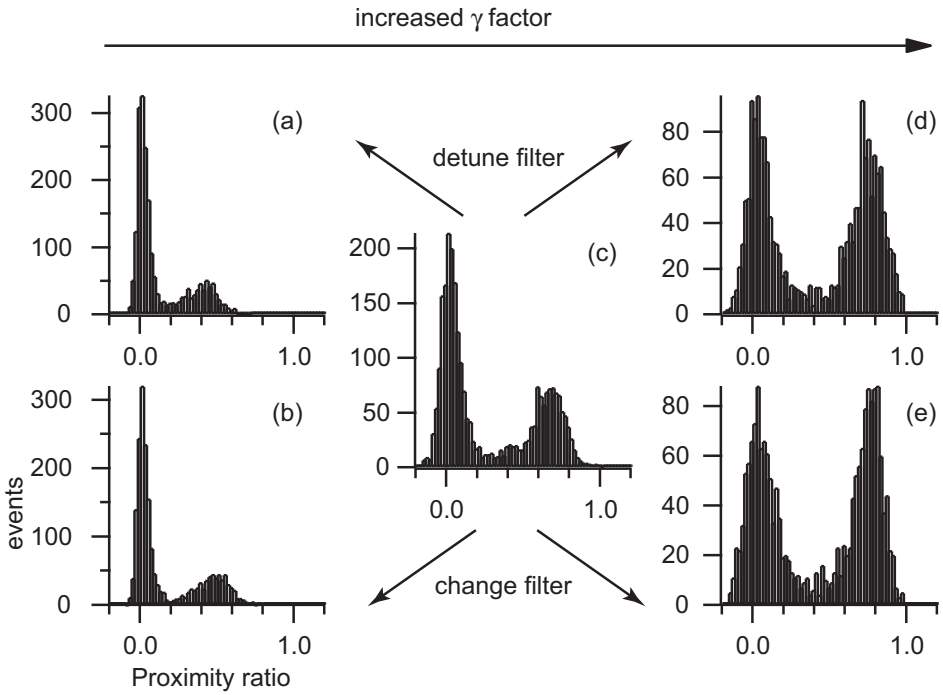

Figure 5.11: Comparison of two different methods to manipulate the detection factor γ. Starting from the filter combination QN the detection factor was lowered by (**A**) detuning the acceptor channel or (**B**) replacing filter N by filter G. Correspondingly, γ was increased by (**C**) detuning the donor detection channel or (**D**) replacing filter Q by filter E. The filter notation resembles that used in table 3.2.

filter	γ	$\mathbf{P_{exp}}$	$\mathbf{E_{calc}}$
QG	0.41	0.460 ± 0.007	0.676 ± 0.027
QN'	0.35	0.384 ± 0.005	0.654 ± 0.021
EG	0.56	0.543 ± 0.011	0.686 ± 0.023
$Q'N'$	0.64	0.504 ± 0.008	0.614 ± 0.020
QN	1.2	0.653 ± 0.005	0.631 ± 0.022
EN	1.82	0.745 ± 0.009	0.619 ± 0.025
$Q'N$	1.66	0.738 ± 0.006	0.629 ± 0.022

Table 5.2: Detection factors, proximity ratios and calculated transfer efficiencies of the high-FRET standard for different filter conditions. Filter notations are identical to those used in table 3.2.

The variation of the geometric detection efficiency seems to be a better way to manipulate the detection factor γ. The lens L3 is easily dealigned and provides a convenient mean to reduce the detection efficiency of the donor channel. Replacing the spectral filters requires a re-optimisation of the alignment, which potentially alters the geometric term in an unexpected fashion. From a practical aspect the change of the spectral filters is also not preferable, since too frequent replacement might cause a degradation of their sensitive surface. Improper handling might result in tiny scratches or abrasions, which lowers the quality of the optical filter.

Biasing of distributions at larger γ

Closer inspection of Figure 5.11 points towards a potential drawback of the approach. Large $\gamma-$factors result in a successive decrease in the fraction of registered donor-only events. This is due to the reduced probability of green photons being detected, so the transit of donor-only molecules will not result in a photon signal high enough to be registered. Molecules that undergo FRET, on the contrary, have a significant emission in the acceptor channel, and their probability of being detected is less affected. This restricts the range of useful values for γ. From the experience during this work a factor less than $\gamma = 3$ still yielded reasonable results.

5.4 Discussion

FRET-based assays that are able to monitor structural changes within nucleosomes gained substantial interest in recent years. Most of these operated on the ensemble level and provided valuable information for example about the activity of remodeling factors [146] or histone dynamics [71]. Other studies analysed salt-induced conformational changes in the linker DNA trajectory [134] or the increase in nucleosome stability after replacing the canonical histone H2A by the natural variant histone H2A.Z [110]. Only few experiments reported on single molecule experiments yet. These studies unraveled spontaneous unwrapping events in the nucleosome where the DNA partially unwrapped from the octamer for a time period 50-120 ms [133, 80] and then remained in an closed state for about 250 ms. This spontaneous breathing could facilitate access to the buried DNA sites as was recently demonstrated with the DNA binding protein *LexA* in a related study [91]. In order to study these kinetics with single nucleosomes the complex has to be fixed to a surface. Residual interactions of the complex with the surface might introduce significant alterations in their intrinsic dynamics. Minimal perturbative conditions are generated in a system that analyses nucleosomes in free diffusion.

Nucleosome stability under single molecule conditions

A diffusion-based single molecule experiment requires sample concentrations of a few $10\,pM$ or less to minimise the probability to simultaneously observe more than one particle. Unfortunately the stability of the nucleosome complex is considerably reduced at such low concentrations. Gottesfeld et al. reported on dissociation constants of $30 - 60\,pM$ for weaker binding sequences and higher salt concentrations [61]. Their work was based on a successive dilution of nucleosomes and subsequent quantification of the dissociated complexes in a gel. In a follow-up publication they put the reliability of the analysis in question though [131]. Recent AFM studies further reported on the loss of integrity at true single molecule conditions [22]. Since the interaction between DNA and histone octamer is largely electrostatic increased salt concentration is a major source for nucleosome degradation. As the nucleosome concentration is lowered the complexes were found to dissociate at lower salt concentrations already. This interplay between salt and sample concentration agrees with predictions from previous

biochemical studies on nucleosome stability by Cotton and Hamkalo [25].
During this thesis the passivation of the container walls was found to prevent instantaneous dissociation of the nucleosomes. After adding bovine serum albumine into the solution, experiments could be performed at concentrations as low as $10\,pM$ before dissociation set in. This worked fine for the particular nucleosome constructs used in this set of experiments. Results obtained from differently preparad 601^{170} nucleosomes, however, showed that addition of BSA alone was insufficient to prevent dissociation at higher salt concentrations. Thus a different strategy was used to maintain nucleosome stability. Unlabeled nucleosomes were added into the buffer to raise the total nucleosome concentration well above the dissociation constant. An excess of $10 - 15\,nM$ provided enough stabilisation of nucleosomes under physiological conditions.

Dilution-driven dissociation assay

On the one hand the maintenance of nucleosome integrity is important for the correct interpretation of data on subensemble heterogeneities. On the other hand the destabilising conditions (low nucleosome concentrations and high ionic strength) trigger conformational changes from which additional information on DNA-histone interactions can be retrieved. Electrophoretic assays, which aim to investigate such dilution effects usually require radioactive labeling of the DNA to be sensitive to such low concentrations. Potential interactions of the host matrix with the low number of molecules are difficult to exclude.
A control of the total nucleosome concentration through the addition of unlabeled complexes provides an intriguing opportunity to study concentration-dependent effects on the single molecule level. The occurence of transient intermediates in the proximity ratio histogram can be analysed as a function of overall nucleosome concentration. This could provide information on the nature of the conformational changes which is not accessible in the conventional assays. The use of the same amount of labeled nucleosomes ($50\,pM$ or less) also guarantees a better comparability of the results. Such experiments require a considerable amount of unlabeled nucleosomes to be prepared. A typical stock preparation ($100\,\mu l$ of $300\,nM$ concentration) provides enough material to perform about 30-50 experiments in sample volumes of $30 - 40\,\mu l$. Larger quantities of unlabeled nucleosomes could be obtained by isolation of native nucleosomes from HeLa cells. These are not defined w.r.t. their state of histone modification and may interfere with the defined structure of the recombinant model system. Under low salt concentrations an exchange between the different octamer components in solution is unlikely to occur [132] and a "contamination" with native components should not occur. It will bew interesting to test whether the use of native complexes alters the local structure of the labeled nucleosomes.

Bridging between bulk and SMD

Beside the stabilisation of nucleosomes the use of unlabeled complexes is favorable for a different reason: To compare the results obtained from a single molecule experiment with data from an ensemble method the conditions have to be as similar as possible. Accurate bulk fluorimetry experiments can be performed at concentrations around $10\,nM$

or slightly less and SMD experiments should be performed at comparable concentrations. The use of unlabeled nucleosomes allows to generate these quasi-bulk conditions, while the constrains for single molecule detection are still met, since only $50\,pM$ or less are labeled constructs. This requires that labeled and unlabeled nucleosomes behave identical, which can be checked in conventional biochemical assays.

Nucleosome dynamics on the ms-time scale

The dynamics of nucleosomes under highly destabilising conditions was investigated by a multiparameter analysis. The recently developed method of Probability Distribution Anaylsis (PDA) allows to extract the most probably distribution of conformational states from shot noise broadened experimental data [4, 75]. This technique was applied to 601^{170}_{med} nucleosomes at different ionic strength and nucleosome concentrations around $1\,pM$.
A significant dissociation was observed at lower salt concentrations than observed in provious experiments with our setup. This is not surprising since for the multiparameter analysis lower nucleosome concentrations were used. The observed dissociation rate k_{off} increased with higher ionic strength and experiments at $100\,mM$ NaCl did not yield enough intact complexes for a thorough analysis of the underlying dynamics. The distribution of FRET states was best described by three Gaussian distributions, two of which showed only low intrinsic dynamics. These were assigned to conformations where the DNA is tightly attached to the octamer. This two-state behavior was also observed in the experiments performed on out setup where they contributed to the overall broadening of the FRET peak. It is tempting to identify the two bound substates with the symmetric and asymmetric positioning states observed in the electrophoretic analysis of 601^{170} nucleosomes (Figure 3.4). This, however, needs further validation by a FRET analysis of the individual positioning states, either extracted from the gel or measured in the gel directly.
The ratio between the occupancy of these states reversed at lager ionic strength. While at $5\,mM$ NaCl the medium-FRET state predominated, the opposite was observed at higher salt concentrations. This sugests that the two states have a different binding strength between DNA and octamer. The medium-FRET population appeared to be less stable and dissociated at lower ionic strength. The high-FRET state is more stable and dissociated and higher salt concentrations. The distribution of apparent FRET states changed over time at higher ionic strength which points towards a potential rearrangement of the DNA-histone interactions. During the dissociation process additional subconformations could be introduced, where one or both H2A/H2B dimers already dissociated from the octamer. Such hexasomes and tetrasomes are expected to form intermediate states in nucleosome assembly and are likely to exist in the reverse process [148]. To our knowledge, this is the first time, where such a heterogeneous dissociation behavior was observed on the single molecule level.

Deliberately detuned detection - D^3

The analysis of nucleosome dynamics is considerably improved if both internal DNA sites and the linker DNA region are monitored. The dissociation of nucleosomes produces an additional fraction of free DNA around zero-FRET which limits the resolution of subconformations in the low-FRET region. While internally labeled nucleosomes provide enough FRET to be easily resolved in the proximity ratio histogram linker DNA labeled constructs offer less than 30 % average energy transfer [134] and are difficult to discriminate against the free DNA.
In this work an approach was developed to investigate low-FRET species in a comparably simple one-color excitation scheme. The method is based on a controlled alteration of the optical pathway to enhance the relative detection efficiency of the acceptor fluorophore. The increased detection factor γ improves the separability of substates in the low-FRET regime if the data were analysed in their proximity ratio. At the same time the shot noise increases and restricts the range of useful γ values to less than 3. A convenient way to alter the detection factor is the de-alignment of the lens L3 in the donor detection channel. This minimises abrasion of the filter surfaces and is faster than replacing the emission filters, which generally requires re-optimisation of the alignment.
D^3 is an easy-to-implement and simple way to qualitatively screen for relative changes in the low FRET regime. The approach is comparable to previous work which utilized different threshold criteria for selective detection of either medium-FRET or high- and low-FRET species [147]. As has been pointed out in the literature this introduced a bias on the whole dataset [32]. By reducing the detection efficiency to the necessary amount we can restrict the bias set on the analysis to a tolerable level.
Alternating excitation schemes [76, 104] which rapidly switch between donor and acceptor excitation during the particle transit are not able to remove the contribution from free DNA if the acceptor is still intact. They cannot discriminate between a DNA dissociated from the octamer and an intact nucleosome conformation, where the fluorohores happen to be too far apart to undergo FRET.

Chapter 6

Nucleosome remodeling

The previous chapter focussed on the nucleosome stability and spontaneous conformational changes under single molecule conditions. With the expertise obtained in how to handle nucleosomes under these destabilising conditions we are now in the position to investigate how structural changes are induced by enzymes and histone modifications. Both factors are key aspects in nucleosome remodeling which is the basis for organisation of the local chromatin morphology as described in chapter 1.
Recent experiments unraveled a close linkage between the modifications of the histone proteins and the ability to remodel these specific DNA regions. Neutralisation of the positive charges by acetylation of the histone tails alter the DNA-octamer interaction. This will have a considerable impact on the nucleosome stability which to a great extent determines its response to remodeling complexes. At the same time the attachment of various chemical groups provides a target site for the recruitment of various enzymatic factors.
The first part of this chapter is devoted to monitor structural changes within the nucleosome that are induced by the ATP-hydrolysing activity of remodeling factors. The second part investigates the effect of different DNA sequences and histone acetylation on the nucleosome conformation and stability.

6.1 Nucleosome repositioning

One major aspect of nucleosome remodeling is the rearrangment of the DNA on the octamer core. This controls the accessibility of gene loci to nuclear factors which are responsible for replication, transcription and DNA repair. Remodeling is performed by a group of ATP-dependent enzymes like ISWI or SWI/SNF. The question of the exact mechanism that leads to a repositioning of the DNA along the octamer is still unresolved. Different models are currently discussed which vary in the type of intermediate states that are induced upon remodeling. These intermediate nucleosome conformations can, in principle, be resolved in single molecule experiments and help to differentiate between different models.
This section aims to analyse the underlying processes of nucleosome remodeling on the single molecule level. Once a suitable nucleosome model system was selected, conformational changes were induced by either thermal treatment or by the activity of

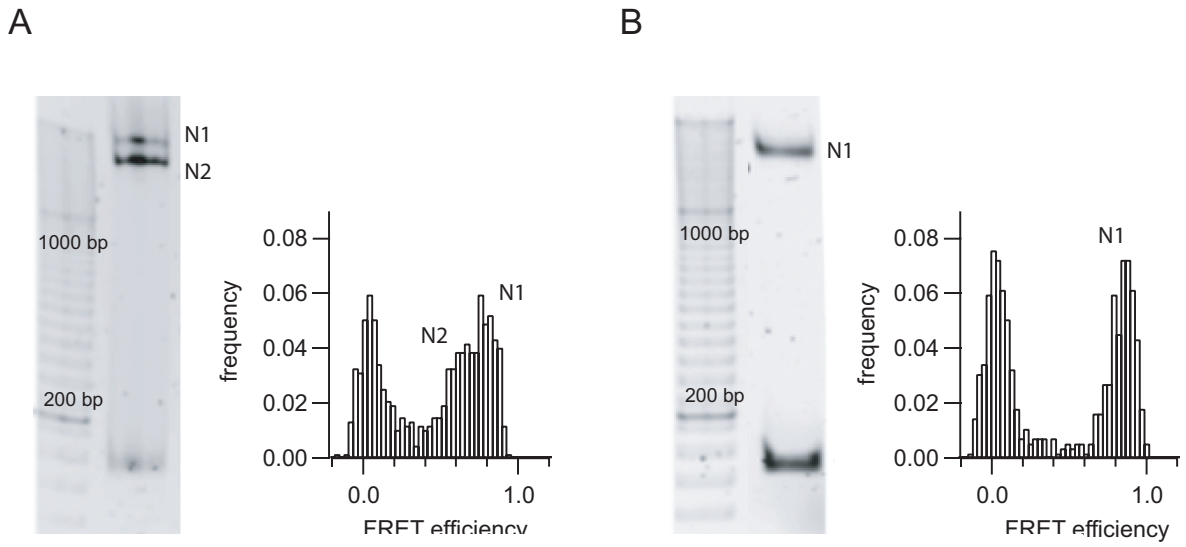

Figure 6.1: Comparison of PAGE analysis and proximity ratio histogram for two different internally labeled nucleosome sequences. **A**: 601^{170} nucleosomes, **B**: 612^{160} nucleosomes. Both single molecule histograms were obtained from high-FREET labeled constructs. The band structure in the gel analysis resembles the peak distribution in the corresponding proximity ratio histogram. The assignment of the two nucleosome substates is N1: symmetric positioning state, N2: asymmetric state.

remodeling factors. Data is presented for two different ATP-dependent enzymes, ISWI and BRG1, as well as the ATP-independent nucleosome assembly factor NAP1.

6.1.1 Model system to detect a loop based repositioning

First, a suitable reporter construct had to be found to perform successful experiments on nucleosome repositioning, This concerned the position of the fluorophore as well as the DNA sequence. End-labeled nucleosomes are indicators for a net change in conformation upon remodeling, any intermediate population will hardly be resolvable though. On the contrary, internally labeled nucleosomes show enough energy transfer to potentially distinguish intermediates from the initial conformation.

Various sequences were tested for their usefulness as remodeling substrates. This work is described in detail in the thesis by F. Hauger and in [57]. We focused on the 601 and 612 positioning sequences introduced by J. Widom that formed well positioned nucleosomes. Octamers reconstituted on the 601^{170} template usually formed three bands in an 8 % polyacrylamide gel: one for symmetrically positioned nucleosomes, a second nucleosome population with asymmetric positioning and one band corresponding to free DNA (Figure 6.1A). 612^{160} nucleosomes, on the contrary, were found to produce only a symmetric nucleosome conformation (Figure 6.1B). The positions were verified by a restriction analysis as described in [66].

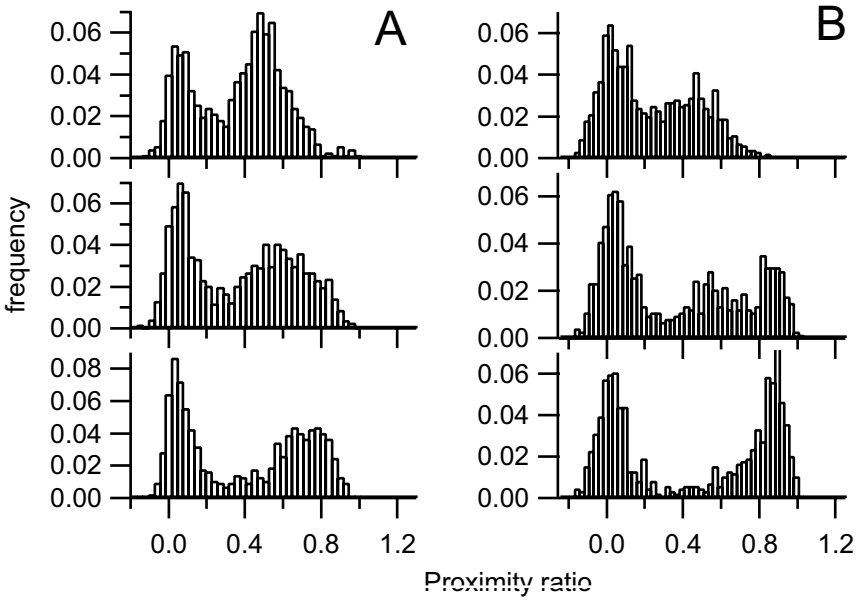

Figure 6.2: Single moelcule histograms of mixtures of medium- and high-FRET labeled nucleosomes of (**A**) 601^{170} nucleosomes and (**B**) 612^{160} nucleosomes. From top to bottom: isolated medium-FRET nucleosomes, 1:1 mixture of both saqmples, isolated high-FRET constructs

The proximity ratio histograms of both nucleosome constructs resemble the different positioning properties observed in the gel analysis. For both sequences the intact nucleosome population seperated well from the zero-FRET peak. An additional subpopulation with lower energy transfer was observed for the 601^{170}_{high} sequence. 612^{160}_{high} nucleosomes only showed one sharp population around $P = 0.8$. From a comparison with the band pattern observed in the gel we assign the lower FRET population to the asymmetric nucleosome conformation.
The static heterogeneity observed for the 601^{170} constructs raised the question in how far this sequence provides a suitable model system to detect conformational changes upon remodeling. To answer this we compared a mixture of differently labeled nucleosomes of both sequences. Mixing ratios of 1:0, 1:3, 1:1, 3:1 and 0:1 were analysed under single molecule conditions. Figure 6.2 shows three representative histograms for each sequence. Differently labeled 601^{170} nucleosomes were more difficult to resolve in the histogram. The additional positioning heterogeneity caused a significant broadening of the overall histogram where essentially 4 subconformations contributed. On the contrary, the 612^{160} nucleosomes showed a good separation of medium- and high-FRET complexes. Owing to their sharp positioning properties the conformational heterogeneity was much lower.
The experiment favors the 612^{160} constructs as a remodeling substrate. On the other hand the positioning heterogeneity of 601^{170} nucleosomes allows to directly monitor the symmetric and the asymmetric conformation. A change in their respective occupancy, e.g. induced by enzymatic or thermal remodeling, should cause a selective increase of one of these substates. Even if the individual subconformations are barely resolvable a

net redistribution should still be detectable in the overall FRET distribution. For this reason the majority of remodeling experiments was performed on 610^{170} constructs. Depending on the amount of enzyme provided, both 601^{170}_{med} and 601^{170}_{high} nucleosomes were used as a remodeling substrate.
A combination of experiments on medium- and high-FRET nucleosomes is essential to unambigously prove the existence of potential loop intermediates. In the case of medium-FRET labeled complexes the fluorophores are expected to transiently approach each other during loop migration. This would result in the appearance of an additional subpopulation at higher proximity ratios that correspond to an intermediate state. For high-FRET labeled constructs the loop formation is expected to cause a transient increase in the interfluorophore distance. These loop intermediates would then form an additional population at lower energy transfer.

6.1.2 Thermally induced repositioning

Nucleosomes have been shown to be spontaneously mobilised by elevated temperatures [111, 53]. In this way conformational changes can be induced in a controlled way. The corresponding repositioning pattern was found to be similar to that produced by many ATP-driven remodeling factors [50].
We monitored the repositioning potential of 601^{170} nucleosomes by exposing them to 55°C for about 2 hours. The distribution of FRET conformations was subsequently analysed under low salt conditions to prevent any spontaneous dissociation. Experiments were performed on linker DNA labeled and internally labeled nucleosomes as summarized in Figure 6.1.2.
For both nucleosome constructs the fraction of intact nucleosomes remained constant for the treated and untreated sample. This indicates that neither the mobilisation under bulk conditions nor the dilution to $50\,pM$ caused any substantial dissociation. Linker DNA labeled complexes showed a shift towards lower proximity ratios which indicates a net mobilisation of the sample (panel A). The center position of the nucleosome distribution changed from $P_i = 0.41$ to $P_f = 0.32$, that correspond to energy transfer values of $E_i \approx 0.23$ and $E_f \approx 0.18$. We note that this is an overestimate of the FRET efficiencies since the direct excitation was not corrected for. It could not be unambigously resolved whether the redistribution arised from a global shift of all nucleosomes or a redistribution between different FRET substates.
Thermally treated 601^{170}_{high} nucleosomes showed no significant population with intermediate FRET values (panel B). They did, however, show an inversion of the asymmetry in the high-FRET populationas becomes apparent from the zoom-in of the high-FRET region (bottom panels). While for the untreated sample the subconformation around $P = 0.8$ dominated over the population at $P \approx 0.65$, the thermal treatment caused a selective increase of the subpopulation with lower FRET. The net effect was considerably smaller than for the linker DNA labeled constructs.
Both nucleosome constructs showed the same response to the thermal treatment, namely an increased population of the asymmetric positioning state. The experiment agrees with ensemble data which showed that nucleosomes assembled centrally

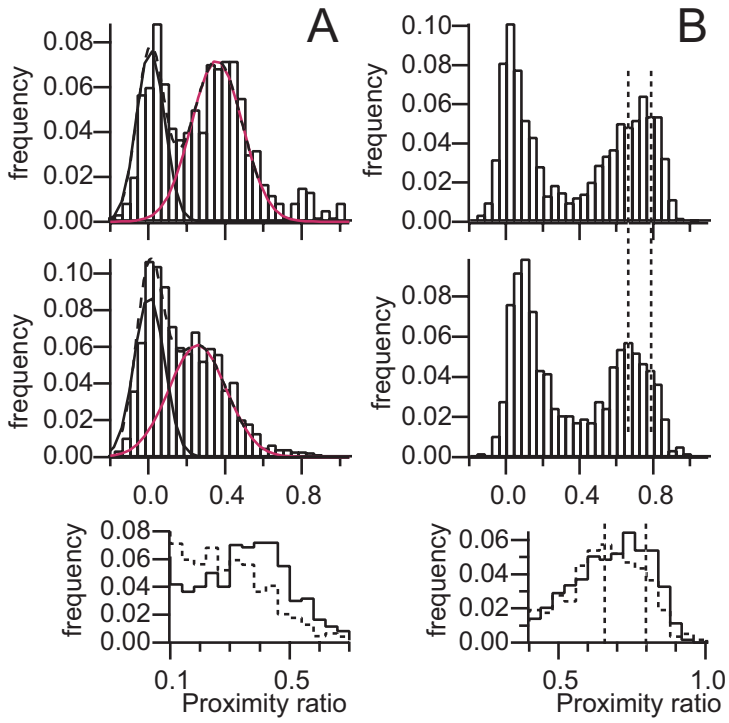

Figure 6.3: Thermal mobilisation of **A**: 601^{170}_{end} nucleosomes and **B**: 601^{170}_{high} nucleosomes. The observed changes in the proximity ratio histogram suggest a redistribution of some nucleosomes into the asymmetric conformation. Both subpeaks in panel B were too close together for a proper two-Gaussian fit. The vertical lines show the estimated center positions of the two substates.

on short DNA fragments preferentially migrate towards the end upon thermal repositioning [101, 66]. Being aware that the observed changes were rather small, yet still detectable, the 601^{170} model system was then used for the analysis of various remodeling enzymes.

6.1.3 ATP-independent remodeling - NAP1

Internally labeled 601^{170}_{high} nucleosomes were used to probe the activity of the nucleosome assembly factor NAP1 on the single nucleosome level. This chaperone promotes the correct folding of the histone octamer and was shown to have numerous effects in the context of chromatin organsation [148]. Various recent reports indicate that NAP1 may even have the capability to reposition the octamer along the DNA template presumably in an ATP-independent manner [1, 105]. To test this hypothesis bulk experiments were performed by F. Hauger. An exemplary PAGE analysis of 601^{170} nucleosomes before and after incubation with NAP1 is shown in Figure 6.4A . The ratio of free DNA to nucleosomes was strongly reduced ndicating a stabilisation or reassembly of nucleosomes by NAP1. The symmetric conformation N1 only showed a small decrease in relative size (less than 10 %). The asymmetric state N2 increased by more than 65 % compared to its initial fraction.

Apparently, the activity of NAP1 lead to the (re-)formation of intact complexes, which predominantly resulted in asymmetrically positioned nucleosomes. From the PAGE analysis the details of the assembly process could not be resolved. Whether asymmetric nucleosomes were formed *per se* or whether symmetric conformations were assembled first which were then remodeled into the asymmteric state remained unclear.

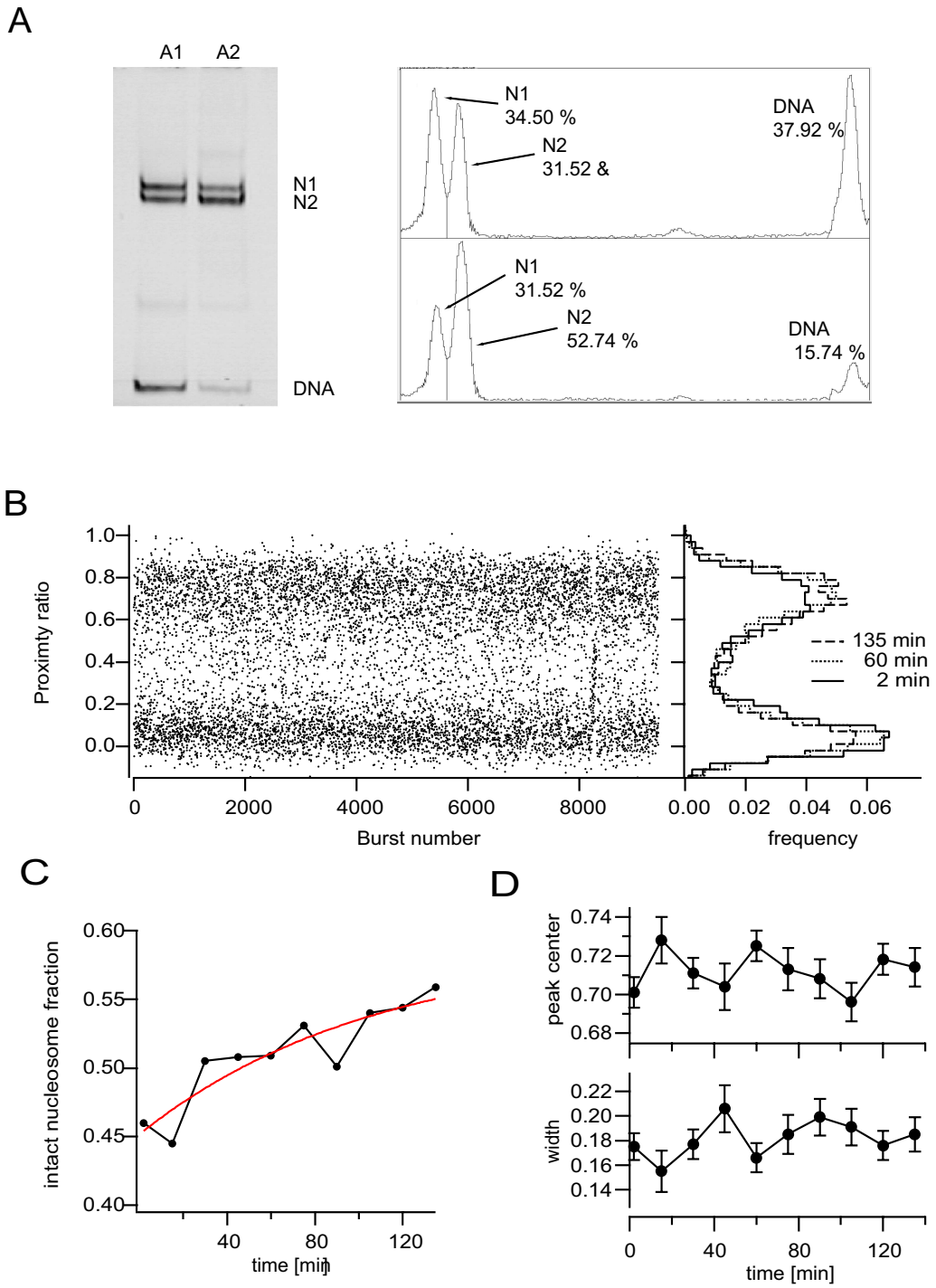

Figure 6.4: Remodeling activity of NAP1 observed with 601^{170} mononucleosomes. **A**: PAGE gel analysis of nucleosome positioning before and after incubation with NAP1. N1: symmetrically positioned nucleosomes, N2: asymmetrically positioned nucleosomes. The respective grey scale scans of both lanes show the fraction of signal observed for each subpopulation. **B**: Time trace of the observed proximity ratio with three subhistograms, which show the gradual increase in the intact FRET population. **C**: Calculated fraction of intact nucleosomes as a function of time after incubation with NAP1. **D**: Center position and width of a model Gaussian approximated to the intact nucleosome distribution.

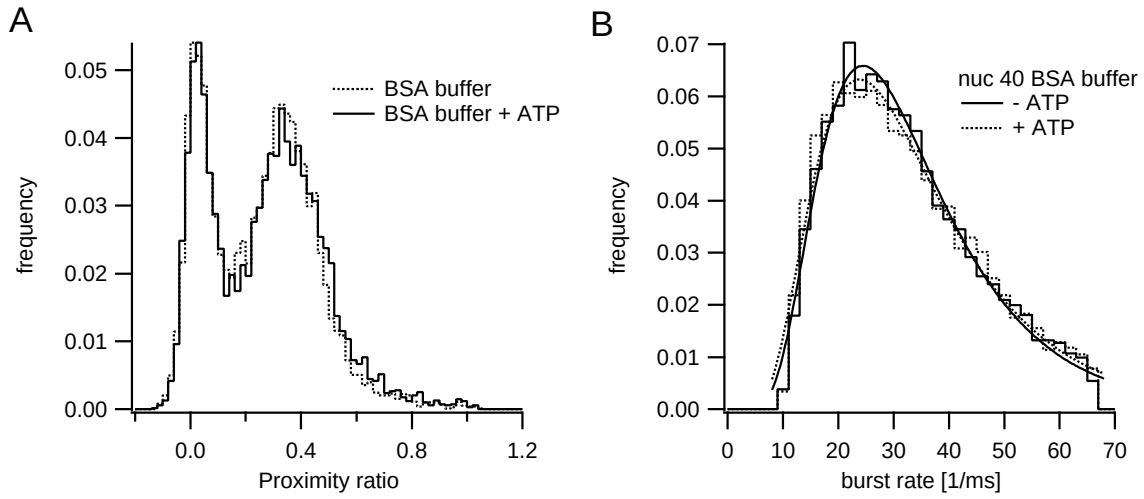

Figure 6.5: **A**: proximity ratio histogram and **B**: in-burst photon rate distribution for 601^{170}_{med} nucleosomes. Data was acquired in standard buffer ($1 \times TE$, $5\,mM$ NaCl, $1\,mM$ ascorbic acid and $0.1\,g/l$ BSA) with (solid line) and without (dotted line) addition of $1\,mM$ ATP. The in-burst photon rate distributions were approximated by a LogNormal function. With ATP: peak value: 23.8, width 0.70, without ATP: peak value: 24.5, width: 0.66).

To address this question single molecule experiments were performed with $6.7\,nM$ enzyme added to $50\,pM$ of 601^{170}_{high} nucleosomes. Data was taken every 15 minutes to monitor changes in the distribution of the proximity ratio. Addition of NAP1 increased the fraction of intact nucleosomes over time (Figure 6.4B). This observation agrees with the findings from the PAGE analysis that NAP1 is capable to reduce the amount for free DNA present in solution. An apparent first-order rate constant of $k_{on} = 9.4 \cdot 10^{-3}\,min^{-1}$ was determined, which corresponds to a two-fold increase in nucleosome population every 74 minutes (panel C). The intact nucleosome population was approximated by a Gaussian function whose center position and width are shown in Figure 6.4D as a function of time. Both parameters did not change significantly over time and a redistribution between the symmetric and asymmetric conformation was not observed.
Taken together, bulk and single molecule experiments verified the *in vitro* nucleosome assembling activity of NAP1. Even at diluted nucleosome concentrations the effect of NAP1 is detectable. The proposed remodeling activity could not be detected though.

6.1.4 ATP-dependent remodeling - ISWI and BRG1

ATP-dependent remodeling factors require the presence of ATP to exert their function. A control experiment ensured that the additional presence of ATP did not produce any unwanted side effects on nucleosome conformation or emissivity. As shown in Figure 6.5, 601^{170}_{med} nucleosomes were analysed under standard buffer conditions with and without addition of $1\,mM$ ATP. Addition of $1\,mM$ ATP caused a minor ($< 3\,\%$) reduction of the mean photon rate per burst and a slight increase in the number of events detected at larger proximity ratios. The overall differences were rather small

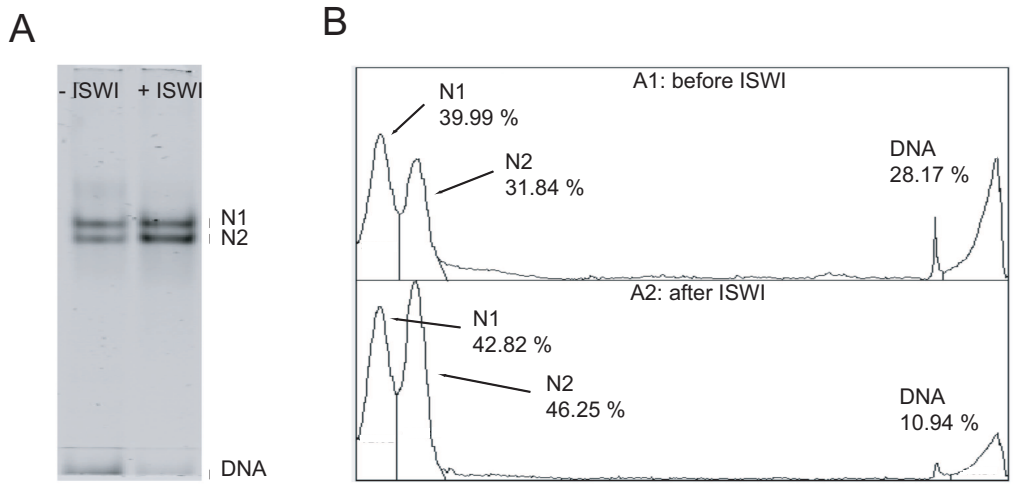

Figure 6.6: **A**: PAGE gel analysis of 601^{170} nucleosomes before and after incubation with ISWI. N1: symmetrically positioned nucleosomes, N2: asymmetrically positioned nucleosomes. **B**: grey scale profile of the respective lanes in the gel. The fractional intensity of the different bands is given in percent.

though. The background level did not increase substantially and a change of only 0.8 % (2.6 %) was observed in the green (red) detection channel. Apparently the addition of 1 mM ATP did not influence the nucleosome conformation or its emissivity.

ISWI

The ISWI protein used for this study was a generous gift from the group of Peter Becker in munich. It shows remodeling activity in an uncomplexed form as demonstrated in various biochemical assays [6, 24] and validated in the thesis of F. Hauger. Owing to the limited amount of enzyme present, single molecule experiments were performed on medium-FRET labeled nucleosomes only.

Figure 6.6A shows a gel electrophoretic analysis of 601^{170} nucleosomes before and after incubation with the enzyme. The details of this experiment can be found in [66]. The strong decrease of free DNA correlates with a predominant increase of the asymmetric positioning state (by ≈ 35 %). The fraction of symmetrically positioned nucleosomes remained almost unchanged. This is somewhat surprising, since no chaperone activity has been reported for ISWI so far. The reduced amount of free DNA suggests that the presence of ISWI caused a stabilisation of the nucleosome, e.g. through binding. Complexed nucleosomes are then less prone to potential degradation in the gel matrix. To learn more about the activity of ISWI single molecule experiments were performed with enzyme concentrations of $5nM$ and $50nM$. After careful mixing data was taken for 1 hour. The results for different ISWI concentrations and buffer conditions are summarized in Figure 6.7. In the absence of the enzyme the nucleosome population separated well from the zero FRET peak with a proximty ratio around $P \approx 0.38$ which corresponds to an estimated FRET efficiency of $E \approx 0.45$. Addition of ISWI lead to a significant change into a broad and less defined distribution (Panel A). The

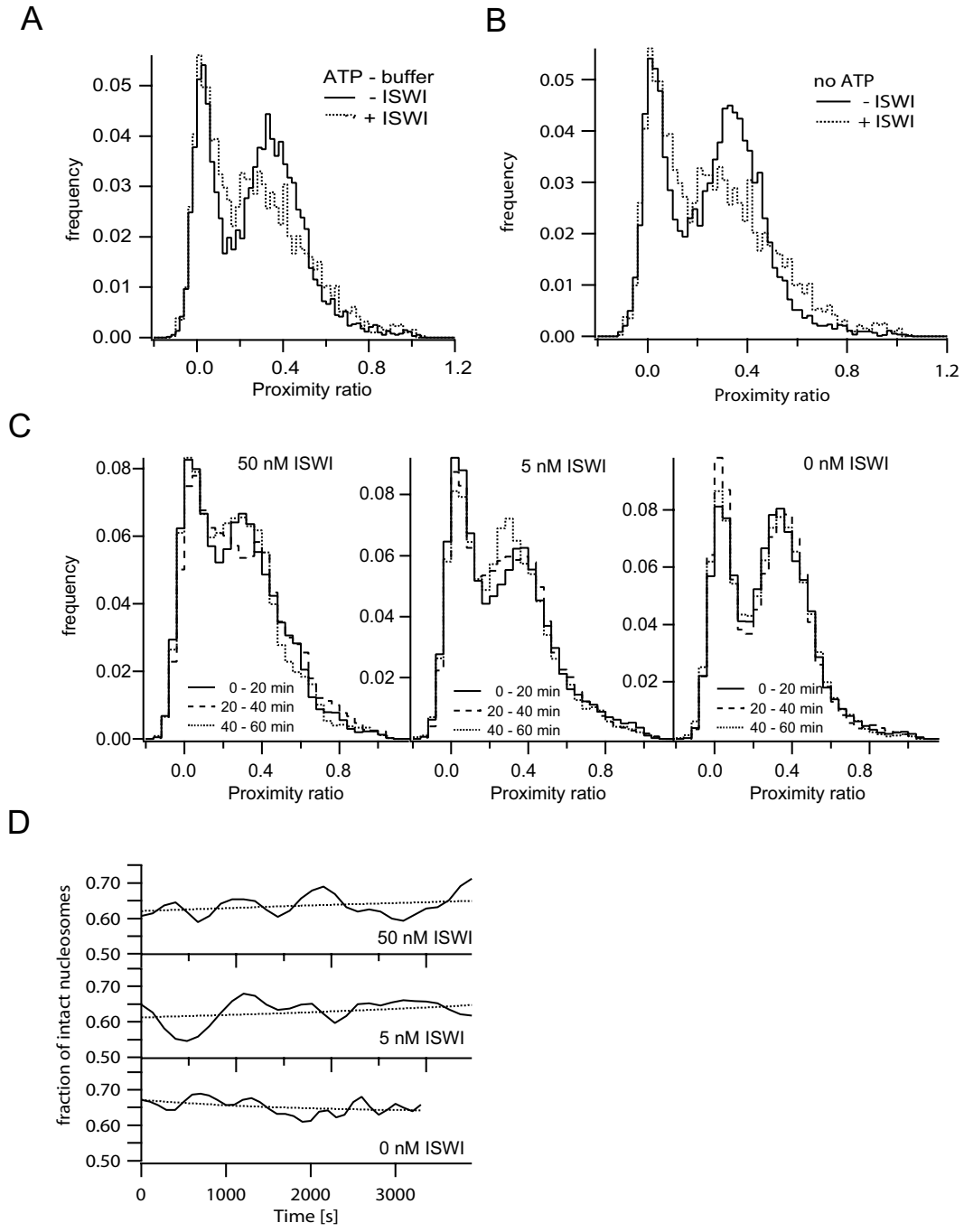

Figure 6.7: Summary of single molecule experiments with ISWI. **A**: Proximity ratio histogram of nucleosomes in the presence (dotted line) and absence (solid line) of $50\,nM$ ISWI. Data was acquired in ATP-containing buffer. **B**: Same as (A) but without ATP. **C**: Proximity ratio subhistograms for 20 minute intervals, measured at three different ISWI concentrations. **D**: Corresponding time trace of the fraction of intact nucleosomes. The data was fit by a first-order model function. The corresponding time constants were: $50\,nM$ ISWI: $t_0 = 9524 \pm 126644\,s$, $5\,nM$: $t_0 = 4728 \pm 29298\,s$, $0\,nM$ ISWI: $t_0 = 1774 \pm 2989\,s$. The immense error on those parameters indicate the uselessness of the parameters obtained from a forced fit. It is assumed that the fraction of nucleosomes is constant over time.

proximity ratio distribution shifted towards lower values which indicates an increase in interfluorophore distance. Notably, ISWI caused a similar change in the proximity ratio distribution in the absence of (panel B). ISWI binding itself obviously caused a significant change in nucleosome conformation already. Although ATP is expected to be required for the remodeling activity the binding of ISWI to the nucleosome might not depend on ATP.
As can be seen in panel C a ten-fold dilution of the enzyme led to a slower change in histogram shape where a gradual shift of the FRET population to lower values was observed. At $50\,nM$ ISWI a significant shift was noticed after 20 minutes already. On the contrary, the shape of the proximity ratio distribution remained unchanged if no ISWI was added. This indicates that the effect which caused the redistribution of the nucleosomes is most probably due to the presense of the enzyme. The time evolution of the nucleosome fraction indicated a rapid (< 10 minutes) conformational change induced by the presence of $50\,nM$ ISWI (panel D). The time trace showed a considerable noise owing to the limited number of molecules being detected. For all ISWI concentrations the total fraction of intact nucleosomes remained stable over time which indicates that ISWI did not assemble new nucleosome complexes.
With the findings from the PAGE analysis, this further supports the idea that ISWI forms a complex with the nucleosome which leads to stabilisation of the complex but not to a repositioning of the octamer.

BRG1

BRG1 is the catalytic subunit of human SWI/SNF remodeling complexes. Like ISWI, it is able to reposition octamers along the DNA without being embedded into the larger SWI/SNF complex. This is demonstrated in Figure 6.1.4, which shows a PAGE analysis, where $200\,nM$ 601^{170} nucleosomes were exposed to $100\,nM$ BRG1 enzyme.
As in the case of the other enzymes the amount of free DNA was considerably reduced if the enzyme was present (by almost a factor of 3). Nucleosomes appeared to be preferentially positioned in the asymmetric conformation. Unlike ISWI, BRG1 also caused a 50 % increase of the symmetric conformation. Subsequent single molecule experiments were performed with $50 - 75\,pM$ nucleosomes and BRG1 concentrations between 1.5 and $15\,nM$. Since the enzyme was available in larger quantities, experiments could be done with internally labeled as well as linker DNA labeled nucleosomes.

Linker DNA labeled nucleosomes

The ability of BRG1 to remodel short nucleosomes such as our 601^{170} model system was probed with 601^{170}_{end} nucleosomes. The nucleosomes were incubated with BRG1 and subsequently analysed under single molecule conditions as shown in Figure 6.9A . A considerable fraction of intact nucleosomes shifted to lower P values that presumably arise from an increase in the interfluorophore distance. To get a rough idea of the relative effect the histograms were approximated by a sum of two Gaussian functions, one for the zero-FRET peak and one for the nucleosome population. Mean values of $P_{-BRG1} = 0.41 \pm 0.01$ and $P_{+BRG1} = 0.35 \pm 0.02$ for the untreated and BRG1-mobilised sample were retrieved. For an estimated $\gamma-$factor of 2.3 this corresponds to

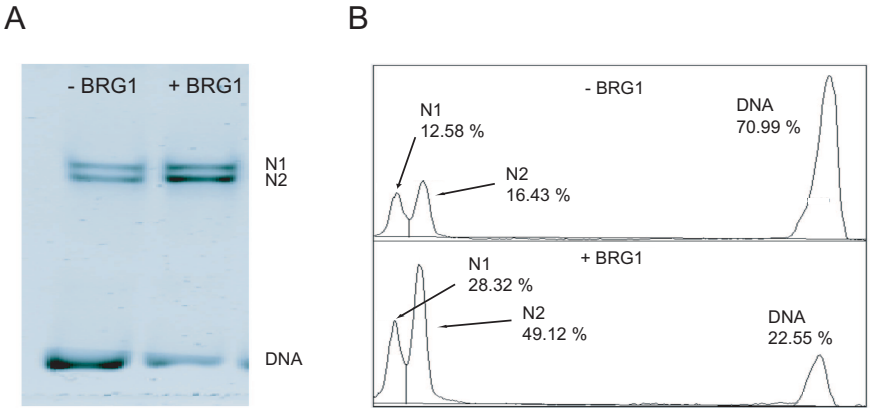

Figure 6.8: **A**: PAGE analysis of 601^{170} nucleosomes before and after incubation with BRG1. $200\,nM$ nucleosomes were incubated with $100\,nM$ BRG1 at $1 \times TE + 5\,mM$ NaCl $+ 1\,mM$ ATP at 37°C for 1 hour. N1: symmetrically positioned nucleosomes, N2: asymmetrically positioned nucleosomes. **B**: Grey scale scan of the respective lanes. The fractional intensity of the different bands is given in percent.

$E_{-BRG1} = 0.23 \pm 0.01$ and $E_{+BRG1} = 0.19 \pm 0.01$.
Unlike this simple model the broad nucleosome distribution is likely to be composed of at least two substates, e.g. the symmetric and the asymmteric positioning state. The apparent shift in the overall nucleosome distribution might then result from a redistribution between those substates. Nevertheless the simple estimate already indicates that a small but notable change in conformation occured. The enzyme seemed to be able to remodel nucleosomes.

Internally labeled nucleosomes
To probe for a possible redistribution further experiments were performed on internally labeled 601^{170}_{med} nucleosomes and are summarized in panels B to F of Figure 6.9. Compared to nucleosomes under BRG1-free conditions, addition of BRG1 caused a constant increase in the population of intact nucleosomes over time (panels B and C). This indicates a potential nucleosome assembly capability but could as well reflect the stabilisation of partially unwrapped nucleosomes. The increase agrees with the PAGE data shown in Figure and was dependent on the enzyme concentration as shown in panel D . For $15\,nM$ BRG1 a steady increase in the nucleosome population was found with an apparent first-order time constant of $t_0 = 1358 \pm 374\,s$. If a ten-fold lower enzyme concentration was used, the change in the nucleosome fraction apparently stagnated after 30 minutes and an apparent time constant of $t_0 = 699 \pm 416\,s$ was obtained.
The variation of the center position and the distribution width of the intact nucleosome fraction is shown in panel E and F . The peak center position appeared to be slightly enlarged which suggests a potential change in nucleosome conformation. Promoting the model of two conformational substates for 601^{170} nucleosomes the change in peak center position might arise from a redistribution into the higher FRET conformation. The distribution width did not vary significantly with time and does not provide further

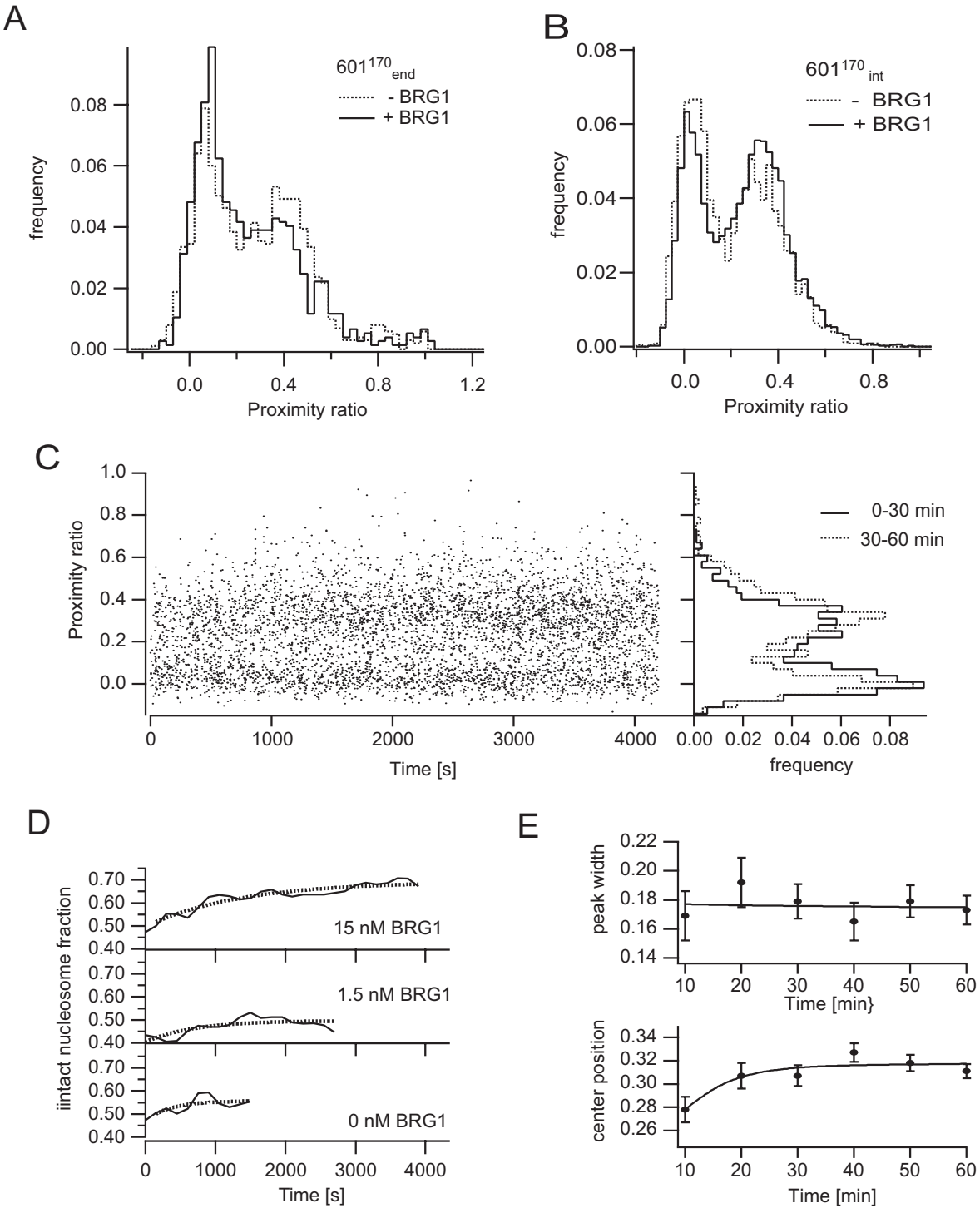

Figure 6.9: Summary of single molecule experiments performed with BRG1. **A**: Linker DNA labeled 601^{170}_{end} nucleosomes before (dotted line) and after (solid line) incubation with BRG1 at 37 °C. **B**: Corresponding experiment performed on 601^{170}_{med} nucleosomes. **C**: time trace and subhistograms for 20 minute intervals of the proximity ratio in the presence of $15\,nM$ enzyme. **D**: Comparison of different enzyme concentrations. The characteristic times were: $15\,nM$ BRG1: $1358 \pm 374\,s$, $1.5\,nM$ BRG1: $699 \pm 416\,s$. **E**: Center peak position and width of a model Gaussian approximated to the intact nucleosome population as a function ot time. Data is shown for $15\,nM$ BRG1.

information on the nature of the observed change. As in the case of the other enzymes no additional population was observed at high-FRET values, which could reflect a loop intermediate during BRG1 activity.

6.2 Effect of DNA sequence and histone acetylation

Beside the active process of ATP-dependent remodeling, changes in nucleosome conformation also result from modification of the DNA sequence or the octamer protein. In particular, the posttranslational modification of histones is now widely accepted to be an important mechanism involved in nucleosome remodeling. The attachment of acetyl or methyl groups to residues of the N-terminal histone tails emerged as a key player in chromatin organisation. This reduces the positive charge of the histone tails and potentially alters DNA-octamer interactions. Apparently, acetylation of histone tails opens the local chromatin density *in vivo* [60] which generally correlates with an enlarged remodeling activity. To understand the molecular basis of the changes, which acetylation causes in the chromatin morphology, it is essential to understand its impact on the local nucleosome structure. Recent FRET experiments found a significant modulation of the linker DNA conformation, as different histone tails were selectively acetylated [135]. Details on potential heterogeneity within the nucleosome conformation were not accessible in this experiment.
This section is devoted to the analysis of conformational changes in nucleosomes due to histone tail acetylation. Two different DNA sequences were reconstituted onto completely acetylated recombinant octamers. The conformation of the linker DNA as well as internal DNA sites were analysed. This structural information was then compared with the stability of the nucleosomes by exposing them to elevated salt concentrations.

6.2.1 Prerequisites

The 601^{170} DNA used in previous experiments and the ribosomal $5S^{170}$ DNA were chosen as model systems. They are well studied test sequences which are frequently used in the literature.Compared to the previous experiments on the remodeling enzymes, the nucleosome model system has been redesigned in several aspects.

Change of the acceptor fluorophore

The experiments on the remodeling enzymes were performed with Alexa488 and Rhodamine X. The rather low quantum yield of this acceptor (≈ 0.25) did not hinder the analysis of medium- or high-FRET constructs. In fact referring to Figure 2.3.2 the low quantum yield produced a reduced detection factor γ that was found to be adequate for the analysis of high-FRET samples.
The effect of acetylation is to be monitored for both linker DNA sites *and* octamer-bound DNA. The analysis of conformational changes in the linker DNA region requires a large detection factor and thus a rather strong emitting fluorophore. The acceptor fluorophore was replaced by Alexa594 which showed an over two-fold increased quantum yield (≈ 0.60). Besides, this fluorophore was less sensitive to the addition of

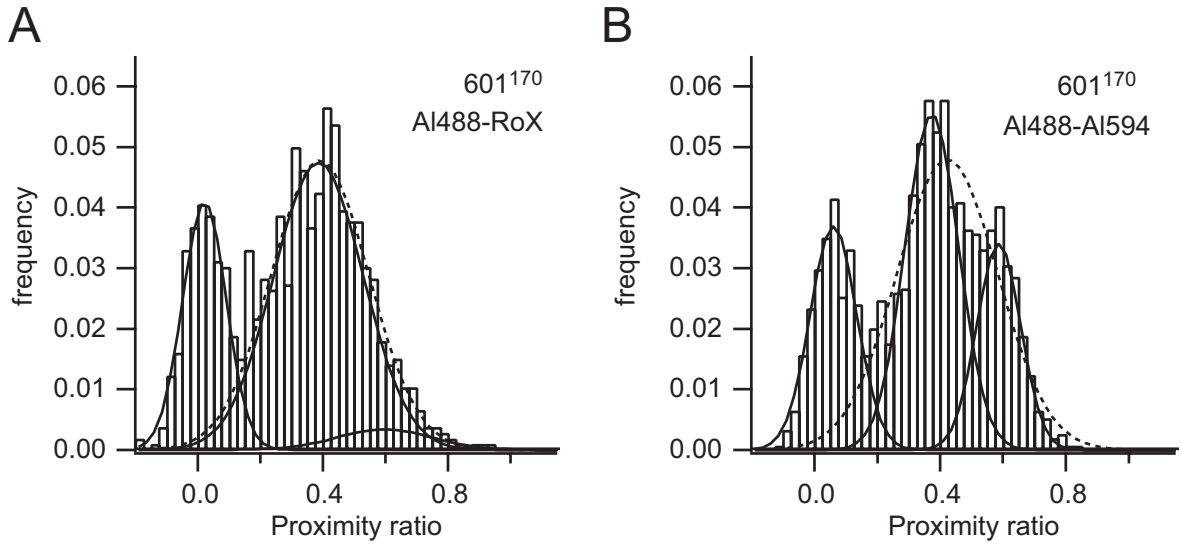

Figure 6.10: Comparison of 601^{170}_{med} nucleosomes labeled with different fluorophore pairs. **A**: Alexa488 and Rhodamine X, **B**: Alexa488 and Alexa594. The improved separation of the two subpopulations in the intact nucleosome distribution is clearly visible. The corresponding one- and two-component fits yielded: Rhodamine X: $(\chi^2)_{2\,comp} = 0.00094$, $(\chi^2)_1\ comp = 0.00057$; Alexa594: $(\chi^2)_{2\,comp} = 0.00017$, $(\chi^2)_{1\,comp} = 0.00099$. In the case of Rhodamine X, the two populations also showed a significantly enhanced width.

photostabilizers (section 4.2) and showed a slight increase in detection efficiency due to the red-shifted emission spectrum (about +8 % in filter N and almost +25 % in filter G) as compared to Rhodamine X.

Notably even internally labeled 601^{170}_{med} nucleosomes profit from the change in acceptor. Figure 6.10 compares histograms for 601^{170}_{med} nucleosomes, labeled with Rhodamine X or Alexa594, measured under identical buffer conditions ($1x\,TE$, $100\,mM$ NaCl, $0.1\,g/l$ BSA and $1\,mM$ ascorbic acid). The total fraction of intact complexes remained unchanged (72.2 % (Alexa594 labeled) versus 71.9 % (Rhodamine X labeled)) and Alexa594 readily provided an increased separation of the subpopulations in the intact nucleosome distribution. This is reflected in the χ^2 values for a one- and two-component fit on the intact nucleosome population, which are given in the Figure caption.

Change in preparation protocol

For the experiments in the following section nucleosomes were analysed that were prepared using a different protocol than that used for the experiments on the remodeling factors. It was found that nucleosomes which were composed of the same DNA and histones but reconstituted in an altered protocol differed substantially in their stability. Figure 6.11 compares nonacetylated nucleosomes, which were assembled onto 601^{170}_{med} DNA fragments under different conditions and DNA:octamer mixing ratios. Samples denoted by "nucA" were prepared at a molar ratio of 1:1.3 DNA:octamer with the salt-step dialysis method [66]. Nucleosomes denoted as "nucB" were prepared with the

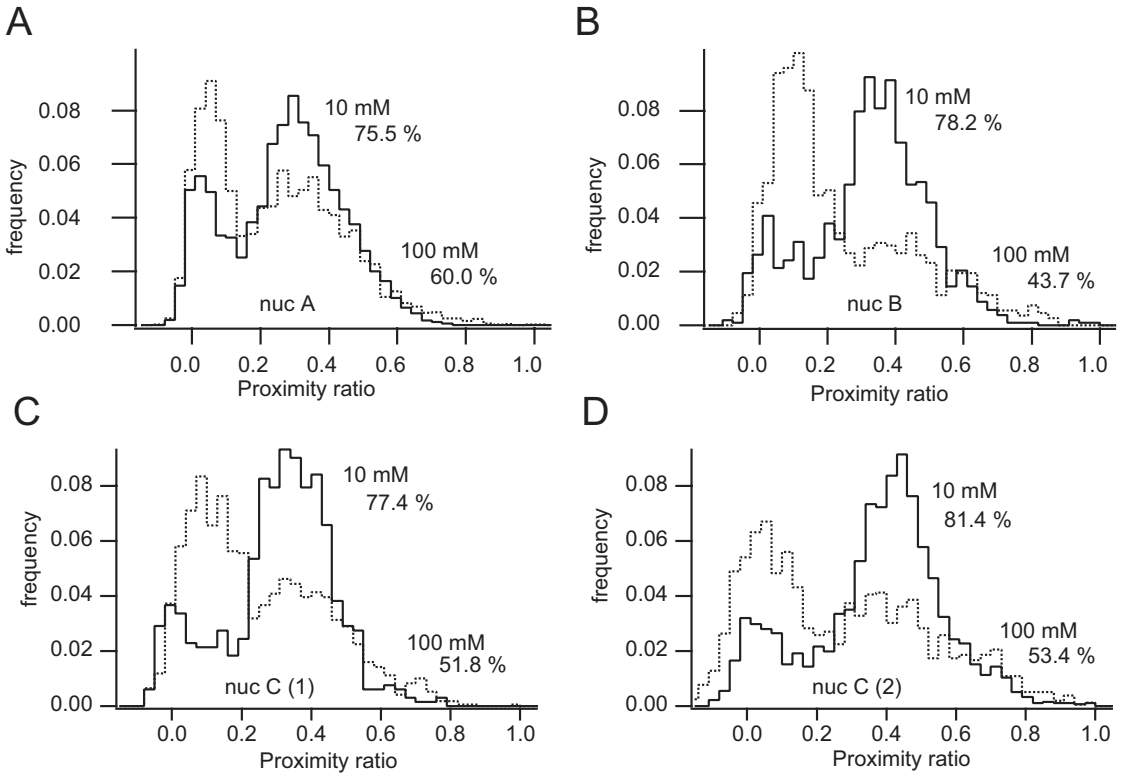

Figure 6.11: Heterogeneity in nucleosome stability under single molecule conditions. The same DNA was reconstituted onto octamers with different preparation protocols and DNA:octamer ratios. Details on the respective samples are given in the text. The fraction of intact nucleosomes was estimated from the number of events with $P > 0.2$.

same components but at a different molar ratio (1:1.8 DNA:octamer) and a gradual change of ionic strength during assembly. For "nucC" nucleosomes a different histone preparation was assembled on the DNA at a ratio of 1:1.8 (DNA:octamer), again with the gradual change of salt concentration. Histograms were compared for 10 and $100\,mM$ NaCl.At nucleosomes were measured at identical buffer conditions ($1 \times TE$, $1\,mM$ VC, $0.1\,g/l$ BSA and salt as denoted).

In general, "nucA" nucleosomes produced a larger fraction of free DNA. The intact nucleosome population was broadened and showed a slight asymmetry which reflecte the double positioning character of this particular sequence, compare to Figure 6.1. "nucB" and "nucC" complexes showed slightly less free DNA and a sharp, almost monomodal FRET population with only a small fraction of nucleosomes at higher proximity ratio. Despite this minor differences the overall histograms for all three preparations were rather similar at low salt concentration.

Significant differences were observed at higher salt. All preparations suffered from nucleosome dissociation which was strongest for the "nucB" nucleosomes (almost two-fold reduction of intact complexes). On the contrary, only 1 out of 5 "nucA" nucleosomes dissciated at $100\,mM$ NaCl. Apparently these nucleosomes are more resistent against dissociation than those assembled with the other protocol. Nucleosomes that were prepared in different reconstitutions with the same protocol showed more consistent

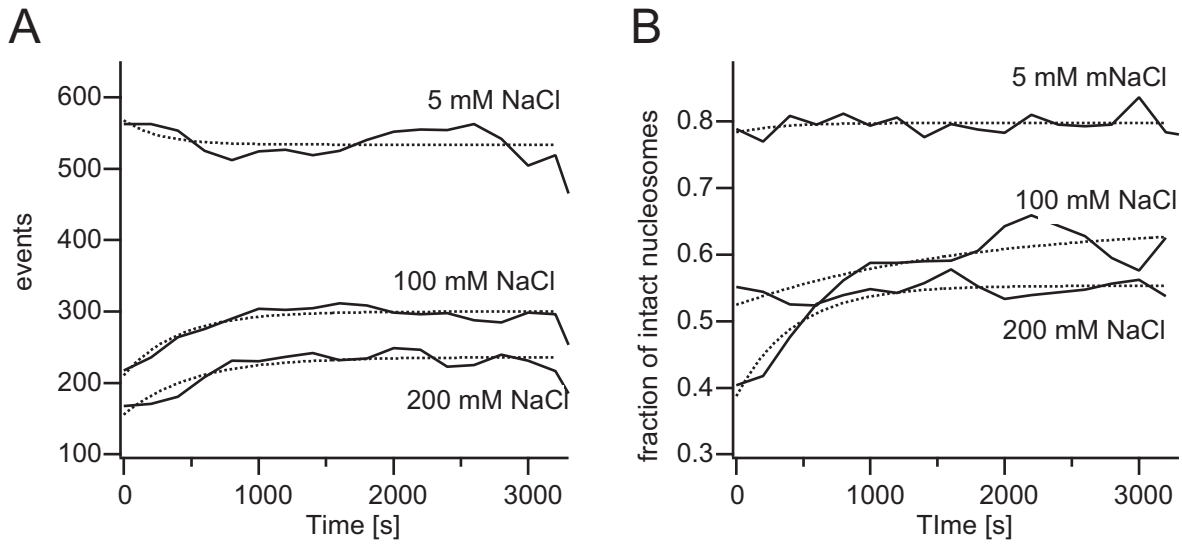

Figure 6.12: Equilibration of nucleosomes at different salt concentrations. Significant changes in **A**: the number of detected events and **B**: the fraction of intact nucleosomes were observed within the first 15 minutes of the experiment.

results. Two different "nucC" preparations ("nucC(1)" and "nucC(2)"), which only differed in their date of preparation, showed a similar dissociation behavior (panel C and panel D).
In summary, a comparability of nucleosomes is feasible as long as the same protocol is used. Then different preparations yield similar results, provided that the detection properties are identical. Nucleosomes prepared with diferent protocols were less compatible to each other. The data appeared similar at low ionic strength, but significant differences were oberved at higher salt concentrations and higher dilutions.

Temporal equilibration of nucleosomes

Another aspect, which had to be considered is that nucleosomes generally require some time to equilibrate if they are diluted from stock solution and placed into the sample container. Only gentle mixing should be applied and steep salt gradients should be avoided, when buffers at higher salt concentrations are used.

When the nucleosomes were placed into the sample container, the number of detected molecules and the fraction of intact nucleosomes varied with time as shown in Figure 6.12. No significant effect was observed at low ionic strength, whereas both parameters showed an initial increase if higher salt concentrations were used. After a certain time the burst parameters remained stable if no additional source of dissociation was present. An apparent time constant of 400-500 seconds (table 6.1) suggests that the nucleosomes required about 15 minutes to equilibrate.

[NaCl] (mM)	time constant derived from number of bursts	time constant derived from intact FRET fraction
5	268 ± 309	325 ± 755
100	405 ± 79	1063 ± 647
200	508 ± 149	431 ± 83

Table 6.1: Apparent first-order time constants for the nucleosome equilibration within the sample container. A monoexponential function was approximated to both, the time course of the fraction of intact nucleosomes and the number of detected events.

6.2.2 Influence of the DNA sequence

Static heterogeneity under quasi-bulk conditions

Figure 6.13 shows representative proximity ratio histograms for linker DNA labeled (panel A) and internally labeled nucleosomes (panel B) of both sequences measured in the presence of $10\,nM$ unlabeled nucleosomes. The linker DNA distribution of the $5S^{170}$ nucleosomes showed a significant fraction of events with proximity ratios as high as 0.7. This value corresponded to an estimated energy transfer E around 0.55, and the interfluorophore distance was of the order to the R_0. This estimation is based on a detection factor of $\gamma = 1.8$. The exact distribution of linker DNA conformations cannot be resolved yet, but it likely that it is composed of at least 2 substates, excluding the free DNA. 601^{170}_{end} nucleosomes formed a narrower distribution with proximity ratios barely exceeding 0.5 ($E \approx 0.35$ respectively). This indicates a more rigid linker DNA conformation of 601^{170} nucleosomes.
Differences were also observed for internal DNA sites. $5S^{170}$ nucleosomes formed a broader distribution of proximity ratios than the respective 601^{170} constructs. The center peak position was not changed and both sequences could be approximated by three Gaussian functions, one for the free DNA and two nucleosome populations. While this is justified for 601^{170} nucleosomes it is less obvious for the other sequence. Applying this model, we found a relative occupancy between the low- and high-FRET subpopulations of 7.5:1 for 601^{170} nucleosomes and 6.2:1 for $5S^{170}$ constructs. This indicates that under our conditions 601^{170} DNA predominantly forms nucleosomes with an increased interfluorophore distance, presumably where the octamer is positioned symmetrically on the DNA. $5S^{170}$ nucleosomes showed an enhanced contribution of states with reduced interdye distance, potentially a more asymmetric conformation, but this is rather speculative. In general both distributions were found to be rather similar.

Taken together this indicates that the nucleosome conformation in the octamer-bound region is only partially influenced by the details of the DNA sequence. Larger differences are to be expected in the linker DNA region.

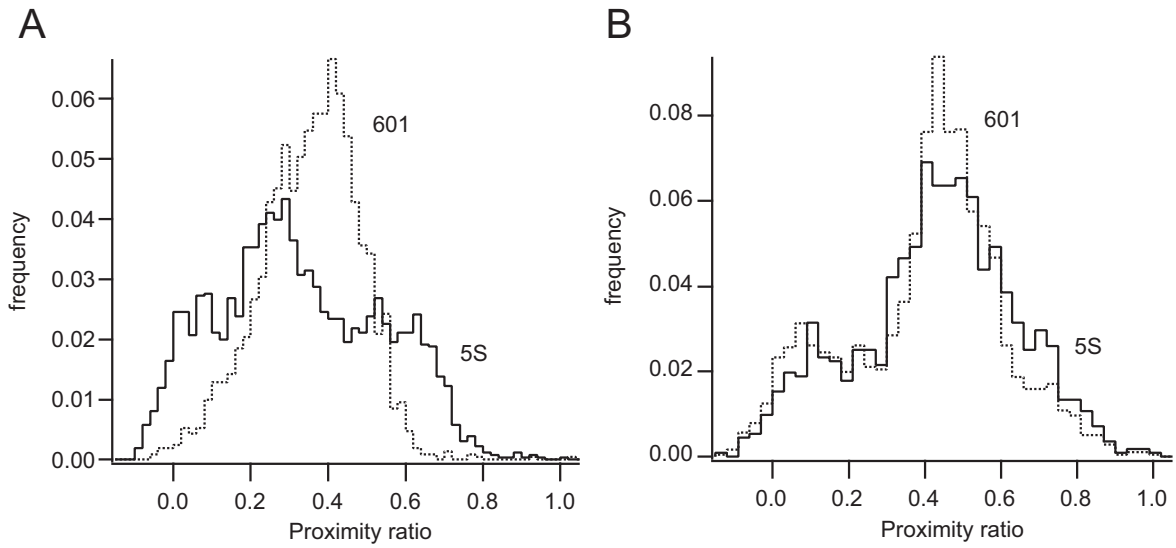

Figure 6.13: Structural heterogeneity observed for nucleosomes assembled with different DNA sequences. **A**: Linker DNA distribution for 5S (solid line) and 601 nucleosomes (dotted line). **B**: Respective proximity ratio for internally labeled complexes. All data was acquired in the presence of $10\,nM$ unlabeled nucleosomes. Estimated detection factors were $\gamma = 1.8$ for panel A and $\gamma = 0.9$ for panel B .

Salt-induced destabilisation

Further differences between both sequences were observed in their response to elevated salt concentrations. Figure 6.14 summarizes the change in the intact nucleosome fraction as a function of ionic strength. Data was taken either under quasi-bulk conditions ($+15\,nM$ unlabeled HeLa nucleosomes, denoted as "+ul") or true single molecule concentrations ($50\,pM$, denoted as "-ul"). For comparison, the intact nucleosome fraction is normalised to the value observed at low ionic strength (panel A). Panel B depicts a few representative histograms at low and high ionic strength for $5S^{170}$ nucleosomes (left column) and 601^{170} complexes (right column). Salt and nucleosome concentration are given in the Figure caption.

$5S^{170}$ nucleosomes were more affected by higher ionic strengths than 601^{170} nucleosomes at both quasi-bulk and true SMD concentrations. The broadening of the distributions in Figure 6.13 is directly linked to the intrinsic stability of the complex. Being less strong binding, the $5S^{170}$ DNA showed larger dynamics in all parts of the nucleosome and dissociation was found at lower salt concentrations. For the highly affine 601 sequence the more rigid nucleosome conformation provided an enhanced resistance against salt-induced dissociation. The shape of the histograms in panel B reflects the structural properties of both sequences. Interestingly at $150\,mM$ NaCl in the absence of unlabeled complexes the 601^{170} nucleosomes show a remarkable redistribution in the intact FRET population ehich is not observed for $5S^{170}$ complexes.

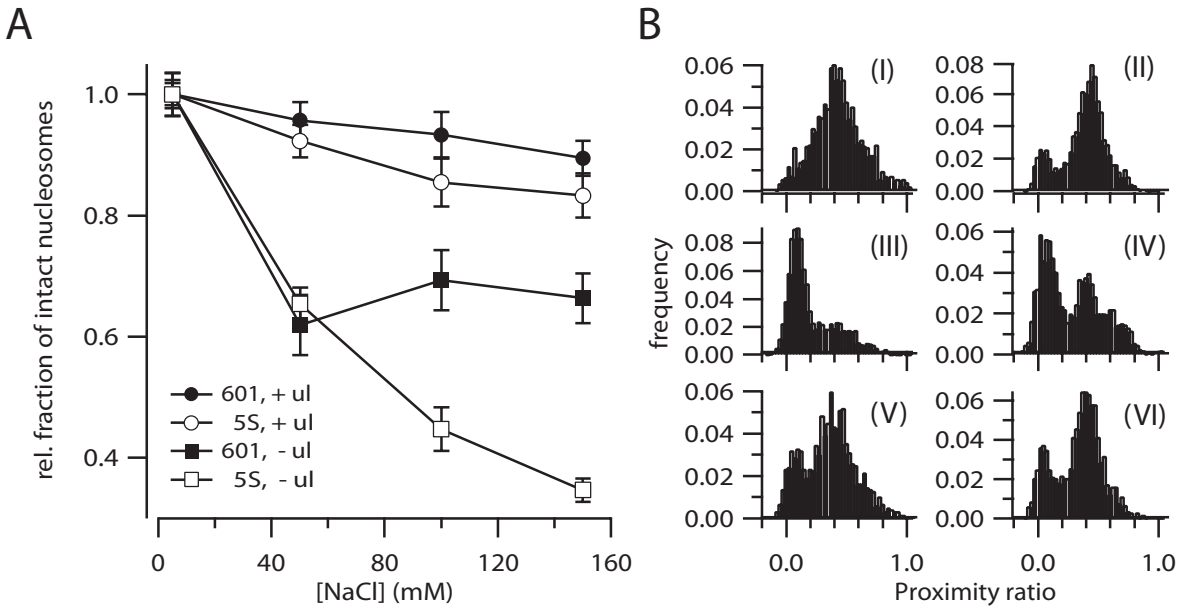

Figure 6.14: Stability of nucleosomes reconstituted with the different DNA sequences. **A**: salt sependence of the fraction of intact nucleosomes. "+ul": addition of $10\,nM$ unlabeled nucleosomes, "-ul": no unlabeled nucleosomes added. **B**: Representative proximity ratio histograms for (I) 5S, $5\,mM$ NaCl +ul, (II) 601 $5\,mM$ NaCl + ul, (III) 5S, $150\,mM$ NaCl -ul, (IV) 601, $150\,mM$ NaCl, -ul, (V) 5S, $150\,mM$ NaCl, +ul, (VI) 601, $150\,mM$ NaCl, +ul.

6.2.3 Effect of histone acetylation

After we characterised the structure and stability of the two reporter sequences, we now discuss the effect of histone acetylation on the structure of the nucleosomes. The individual histones were chemically acetylated prior to octamer formation by acetyl phosphate as detailed in [135]. Both linker DNA labeled and internally labeled constructs were used to monitor different regions of the nucleosome. All experiments were performed after equilibration of the nucleosomes for 30 minutes. The ionic strength and the total nucleosome concentration were varied to correlate changes in nucleosome conformation with their corresponding stability.

Alteration of nucleosome structure

The effect of histone acetylation was analysed for both DNA sequences in the presence of $15\,nM$ unlabeled HeLa nucleosomes. Conformational changes were monitored for the linker DNA portion as well as internal DNA sites. Figure 6.15 compares the effect of acetylation of all histone proteins to unmodified histones at $100\,mM$ NaCl. For internal DNA sites acetylation caused a small excess broadening of the nucleosome population (panels A and B). The effect is similar for both sequences which indicates that the underlying DNA sequence has only minor impact on the interaction of the histone tails with nucleosomal DNA.
A considerably larger effect was observed for the linker DNA portion. As shown in panel C and D , a conformational change is induced for both DNA sequences. 601^{170}_{end}

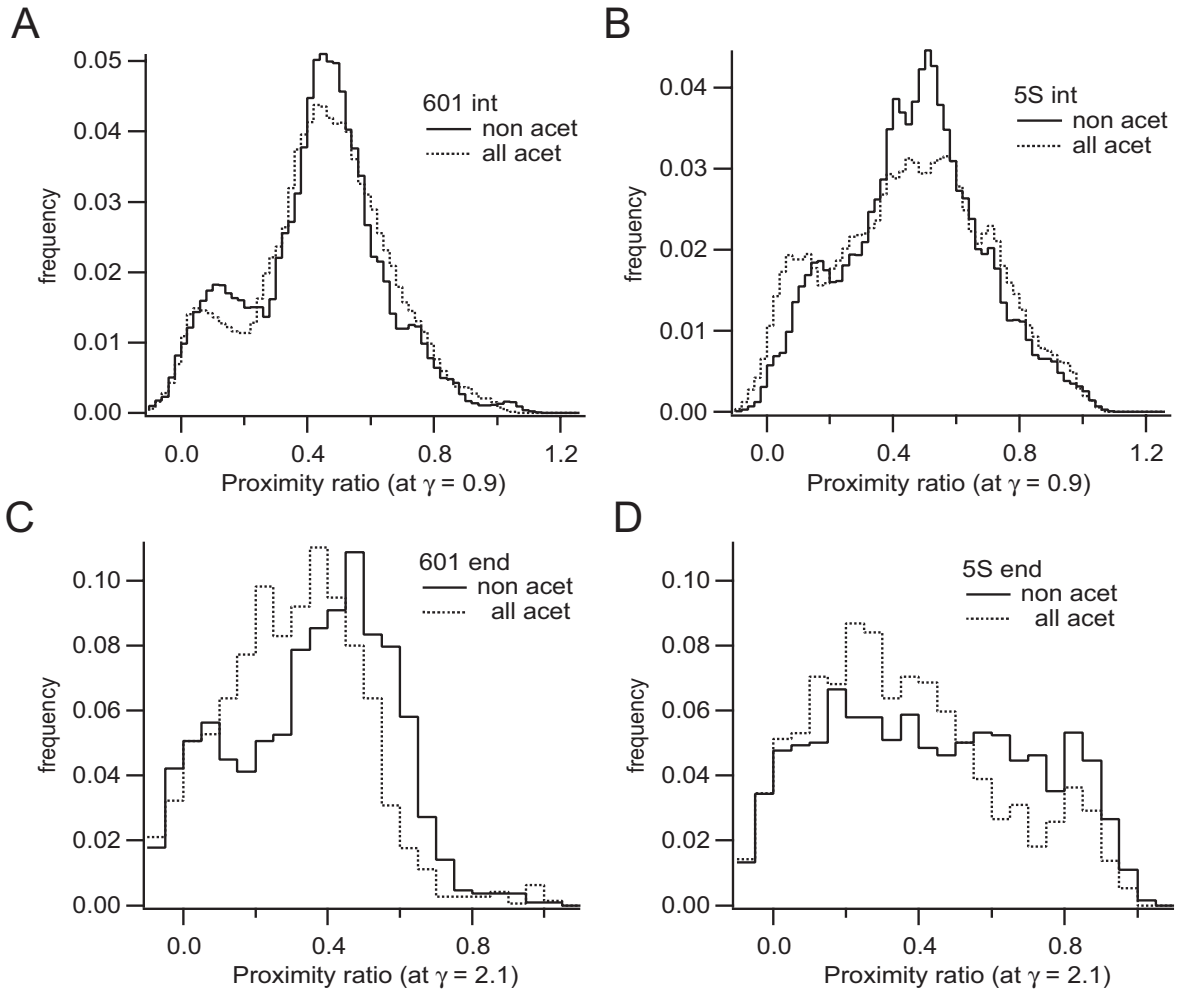

Figure 6.15: Proximity ratio distributions of acetylated (dotted lines) vs. non-acetylated (solid lines) nucleosomes assembled on either the $5S^{1}70$ DNA or the 601^{170} fragment. Linker DNA labeled and internally labeled nucleosomes are compared at $100\,mM$ NaCl. Details are given in the Figure and in the text.

nucleosomes positioned with an increased linker DNA distance, resulting in a shift towards lower proximity ratios. The overall distribution remained well defined and no additional conformations were induced. Completely acetylated $5S^{170}_{end}$ nucleosomes showed a broader distribution of linker arm distances, again extending upto values of $P = 0.7$ as in the case of non-acetylated nucleosomes. The relative fraction of high-FRET conformations, however, is reduced and more nucleosomes were observed with increased linker arm distances. This is in agreement with observations from ensemble fluorimetry, which reported on an increase of the average linker arm distance upon acetylation [135].

The single molecule data suggests that acetylation of all histones causes a redistribution between multiple linker DNA conformations present in the ensemble, which, at the time scale of the experiment (few ms), appear as quasi-static conformations. Notably, the major effect occurred on the linker DNA portion, where the reduced charge of the

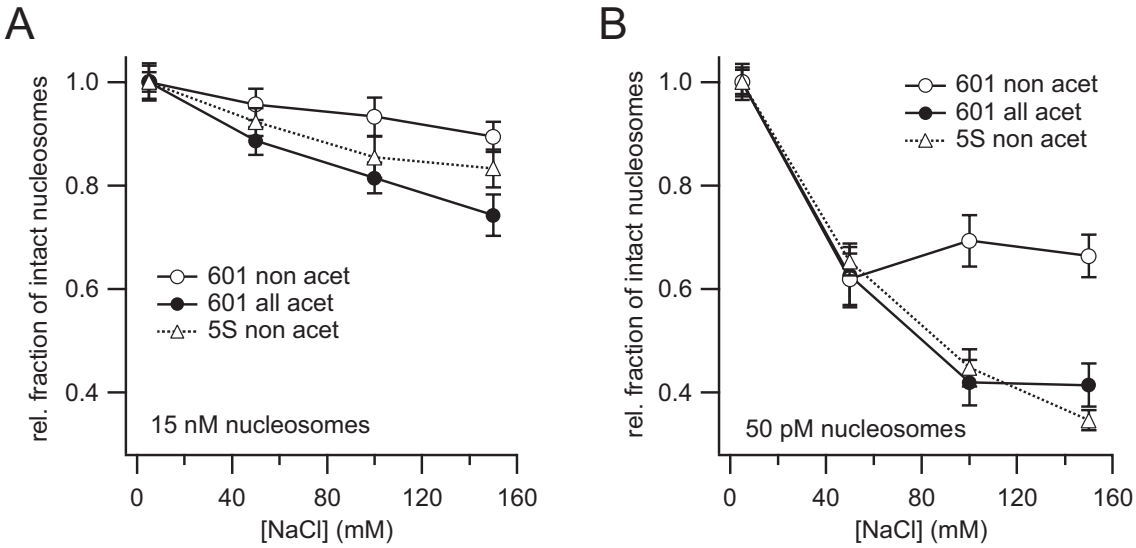

Figure 6.16: Alteration of nucleosome stability by histone acetylation. **A**: Intact nucleosome fraction measured under quasi-bulk conditions (addition of 10 nM unlabeled nucleosomes). **B**: same experiment under single molecule concentrations (no additional unalbeled nucleosomes present). In both cases, histone acetlyation lowers the stability of nucleosomes at elevated salt concentrations.

tails led to an opening of the nucleosome structure for both sequences. DNA wrapped around the central part of the octamer was less affected by histone tail acetylation, which suggests that the tails significantly interact with the linker DNA region. The details of the DNA sequence itself seem to have only minor impact in determining the effect of histone acetylation.

Alteration of nucleosome stability

Finally, it was analysed how far complete acetylation of histones alters the intrinsic stability of the nucleosomes. Non-acetylated 601^{170}_{med} nucleosomes were compared with all-acetylated 601^{170}_{med} nucleosomes at increasing salt concentrations. The experiments were performed under quasi-bulk conditions (addition of $15\,nM$ unlabeled nucleosomes: "+ul") and true single molecule concentrations ("-ul"). The concentration of labeled nucleosomes was set to $50\,pM$ in all cases. Figure 6.16 shows the fraction of intact nucleosomes at NaCl concentrations between 5 and $150\,mM$ normalised to the value at low ionic strength. Data obtained from non-acetylated $5S^{170}_{med}$ nucleosomes are shown for comparison.

The difference in structure correlated with the stability of the nucleosome complex at higher ionic strength. Histone acetylation reduced the stability of 601^{170}_{med} nucleosomes at elevated salt concentrations. The destabilisation at quasi-bulk conditions exceeded that observed for non-acetylated $5S^{170}_{med}$ nucleosomes. At $50\,pM$ a similar tendency was observed for all constructs, though all nucleosomes suffered from dissociation at higher salt levels. Again, the non-acetylated 601 nucleosomes were far more stable than the constructs.

The increased conformational dynamics observed of acetylated nucleosomes is directly linked to their larger tendency to dissociate. Neutralisation of the positive lysine residues decreases the interaction of the tails with the negative DNA backbone and the complex is rendered less stable. Additional screening of the electrostatic interactions by salt ions will further promote the disruption of the complex. Closer inspection of the proximity ratio distributions revealed a potential redistribution within the intact nucleosome population. As in the case of high nucleosome dilution discussed in section 5.2 a considerable heterogeneity is induced upon histone acetylation and elevated ionic strength. At low salt concentration this was not observed in the histograms. The loosening of the nucleosome structure could facilitate a spontaneous rearrangement of the DNA on the octamer that results in a different nucleosome conformation. However, further experiments will be required to unambigously clarify this aspect.

6.3 Discussion

Enzymatic remodeling

While in recent years a lot has been learned about the interplay of different factors which are involved in nucleosome remodeling this field still offers many unanswered questions. In particular the exact mechanism by which the remodeling process is mediated is still a matter of debate. Different models are proposed that lead to characteristic changes in nucleosome conformation. One prominant model is based on the formation and migration of a DNA bulge along the octamer which results in a displacement of multiples of ten base pair of DNA towards the linker DNA region. Another model proclaims the generation of twist defects that can travel along the DNA and exit at the ends of the nucleosome. This causes an exposure of DNA in the linker region to a different extent of 1 bp per step. An experimental system that can quantify the amount of DNA displaced per remodeling step allows to distinguish between those models.
We analysed the activity of different remodeling factors on the single nucleosome level. First the potential of different reporter sequences to resolve conformational substates was tested. The double positioning properties of the 601^{170} sequence produced less separable distributions than an equivalent mixture of differently labeled 612^{160} nucleosomes. In gel electrophoretic studies this sequence mainly formed one band corresponding to a symmetric nucleosome conformation. In the case of 601^{170} nucleosomes apparently the symmetric and asymmetric positioning resulted in slightly different FRET efficiencies. Changes between these subpopulations could be induced by a thermal mobilisation of 601^{170} nucleosomes. Linker DNA labeled nucleosomes showed an increase in interfluorophore distance which indicated a repositioning of a fraction of nucleosomes into the asymmetric conformation. This observation was further supported from an experiment on internally labeled nucleosomes which showed a redistribution between different FRET subpopulations. This property rendered the 601^{170} nucleosomes the model system of choice for the experiments on nucleosomal repositioning. A series of

experiments then analysed the changes in nucleosome conformation that were induced by the ATP-dependent remodeling factors ISWI and BRG1. Moreover, the activity of the ATP-independent nucleosome chaperone NAP1 was monitored. Single molecule FRET experiments were compared with PAGE gel analysis.

ATP-independent remodeling - NAP1
A reduction in free DNA was observed by both methods and suggests a stabilisation or reassembly of partially unwrapped nucleosomes. For the formation of new complexes an apparent time constant of $k_{on} = 9.4 \cdot 10^{-3}\, min^{-1}$ was determined, where the fraction of intact nucleosomes doubled every 74 minutes. While NAP1 caused a considerable increase in the asymmetric positioning state in the gel such a change could not be unambigously detected in the SMD experiments. The overall histogram shape did not change significantly. neither did the peak position or distribution width of a model Gaussian function. It is quite likely that the small differences between the two substates were not resolvable due to the low number of detected events.

ATP-dependent remodeling - BRG1 and ISWI
Two prominent examples for ATP dependent remodeling factors were analysed: BRG1, which is the subunit of the human SWI/SNF complex and ISWI, the catalytic subunit of another class of remodeling enzymes. Biochemical assays reported on potential differences in their mechanistic function [45] and differences between both enzymes were found in the PAGE gel analysis.In the gel electrophoretic analysis the incubation with ISWI led to an almost exclusive conversion of nucleosomes into the asymmetric state. BRG1 addition resulted in more nucleosomes being symmetrically positioned.
On the single molecule level ISWI induced a change in nucleosome conformation which was observed in the absence of ATP as well. This suggests that it originates from binding of the protein to the nucleosome rather than from an ATP hydrolysing activity. For all ISWI concentrations analysed no increase of intact nucleosomes was observed. The time trace of the proximity ratio revealed that at the highest enzyme concentration any changes occurred within the first ten minutes. A ten-fold lower ISWI concentration appeared to slow down the conformational change induced by the binding to the enzyme to the nucleosome. Similar time scales for comnformational changes were observed in recent bulk-FRET experiments which analysed the activity of an ISWI-related enzyme complex [146].
On the contrary, BRG1 did not result in such a dominant change in nucleosome conformation itself but caused an increase in intact nucleosomes over time. The increase in the intact nucleosome fraction was found to depend on the actual enzyme concentration. A ten-fold reduced BRG1 concentration lead to a stagnation of the increase in the nucleosome fraction. As in the case of the other enzymes any repositioning was not detected in the single molecule histograms. The only indication for an interconversion dynamics was a slightly enlarged center position for a hypothetical Gaussian fit to the nucleosome fraction.
Though being still preliminary in character, these experiments are among the first that monitored the activity of remodeling factors on single nucleosomes in free diffusion.

The occurence of a loop migration along the octamer was expected to generate intermediate conformations where a transient high-FRET state is formed. The SMD experiments failed to unravel such intermediates. Given the low concentration of nucleosome substrate the fraction of such conformations simultaneously present might be too small to be detectable against a major population of initial and final states. Alternatively, this raises the question whether these loops occured at all. Under SMD conditions the enzyme-substrate ratio does not reflect the optimal conditions determined in bulk experiments. This could cause some unpredictable outcomes. All bulk experiments that provided mobilisation data used a smaller enzyme:substrate ratio. For further experiments it is thus recommended to apply an excess of unlabeled nucleosomes of the same type of constructs. Optimum concentration conditions determined in bulk experiments can then be directly used for the SMD experiment.

It is finally noted that the PAGE analysis of 601^{170} nucleosomes also failed to reveal intermediate states upon remodeling. It should be subject of further investigations whether longer linker DNA is required to yield a significant formation of looping intermediates. Such looping states were recently observed on long DNA plasmids [13]. PAGE analysis of 601^{220} nucleosomes also indicated the presence of intermediate band structures upon enzymatic activity [66].
An experimental obstacle of using longer DNA fragments is the strong decrease of labeling quality if larger internally labeled primers are used for the PCR amplification. More single labeled species will be present that pile up in the donor-only peak. By using multiparameter detection and dual color excitation schemes [76], [90], [104] this unwanted contribution can be efficiently removed. It might be worthwhile to include such constructs for future experiments.

Dependence of nucleosome structure on DNA sequence and histone acetylation

The local porperties of the nucleosome are influenced by modification of its individual components, i.e. DNA and histone proteins. For example the DNA sequence itself was found to influence the reconstitution affinity to the octamer [95], the nucleosome stability [59] and to produce different response to nucleosome repositioning [84]. A recent single molecule approach similar to our system reported on sequence-specific salt-induced nucleosome destabilisation [79]. This was linked to the loss of the H2A/H2B dimer which is expected to form an intermediates state upon nucleosome dissociation as previously reported by other groups [22]. In this thesis the stability of individual complexes was assessed as a function of DNA sequence, histone acetylation, ionic strength and nucleosome concentration. Unlike other single molecule reports this approach made use of the controlled variation of the total nucleosome concentration by addition of unlabeled nucleosomes to the buffer. This assists to control the amount of dilution-driven dissociation by using different amounts of unlabeled complexes. By this the sample can be exposed to a titration series and the dissociation behavior can be monitored on the single nucleosome level.

In doing so we found that 5S nucleosomes were more destabilised by salt and dilution than nucleosomes of the 601 sequence. Moreover, significant differences were observed in the distribution of linker DNA conformations between both sequences. 5S nucleosomes showed a large portion of complexes with a reduced linker arm distance that was not observed for 601 nucleosomes. Together with an increased heterogeneity of octamer-bound DNA sites this indicates that the 5S sequence forms more dynamic nucleosomes. This appeared to be linked with the stability of the complex. Lowary and Widom showed that different DNA sequences strongly vary in their affinity towards the histone octamer [95]. Its therefore not surprising that less affine sequences like the 5S sequence are easier destabilised by salt concentration and sample dilution than the 601 complexes. An interesting feature that was produced under low nucleosome concentration was a redistribution within the intact nucleosome population. As already pointed out in the previous chapter the highly destabilising conditions might trigger the formation of new conformations. Noteworthy this redistribution was not observed for 5S nucleosomes though. It should be subject to further studies to improve the resolution of these changes in histogram shape to further elucidate the dynamics of nucleosomes under these conditions.

A second aspect, which is often found to correlate with repositioning of nucleosomes *in vivo* is a posttranslational modifications of histones. In this work we investigated the effect of linker histone acetylation on nucleosome structure and stability. Bulk-FRET experiments on reconstituted, linker DNA labeled mononucleosomes indicated a systematic change in average linker length, but the details on conformational heterogeneity were not resolvable [135]. In this project, for the first time experiments were performed under true single molecule conditions, which monitored different sites of the nucleosome. Acetylation of all histones led to an increase of linker DNA distance. While 601 nucleosomes showed a rather uniform redistribution at lower proximity ratios the histogram of 5S nucleosomes indicated a selective redistribution between different conformations. A significant portion of the high-FRET conformations vanished in favor of an increased population at lower proximity ratios. The increase of average interfluorophore distance is compatible with the observations from ensemble fluorimetry. Unfortunately, the existing data cannot resolve the exact distribution of subconformations yet. We then analysed the effect of acetylation on the stability and also found a significant destabilisation and premature dissociation compared to nonacetylated complexes. In all cases the increaseed tendency to dissociate correlated with the appearance of a loosened DNA conformation on the nucleosome. The proximity ratio distribution for acetylated internally labeled 601 nucleosomes also showed an increased heterogeneity of the FRET population both at quasi-bulk as well as true single molecule concentrations.
We suggest that acetylation of the positive lysine residues in the N-terminal tails reduced the interactions of the tails with the negatively charged DNA backbone. The attractive interactions between octamer and DNA are weakened and the mutual repulsion between the two DNA windings has a larger destabilising effect. This resulted both in an opening of the global nucleosome conformation and an increased destabilisation at higher salt concentrations.

Chapter 7

Concluding remarks

7.1 Conclusion

The last decade witnessed an enormous increase in the understanding of chromatin structure and its relation to gene regulation. It became clear that the local structure of nucleosomes and their mutual interactions considerably influence the folding into higher-order chromatin structures such as the 30 nm fiber. A rearrangement of DNA within the nucleosome can generate access to formerly occluded DNA regions but it can also prevent nuclear factors from binding to previously accessible sites. By now many factors have been reported to participate in the modulation of nucleosome structure. The details on how they interact with the nucleosome are still a matter of debate but the induced conformational changes occur on dimensions of the size of the nucleosome itself. Experimentally, this range is accessible by methods such as Fluorescence Resonance Energy Transfer which proved to be a suitable ruler for intermolecular distances. During this thesis an experimental platform was established that allows to analyse conformational changes within freely diffusing nucleosomes. By using a confocal setup and fluorescently labeled nucleosomes in the pM concentration range it was possible to extract information on conformational heterogeneity from individual members of the nucleosome ensemble. This information cannot be obtained from conventional ensemble-based experiments owing to the inherent averaging over all molecules that are observed simultaneously. If, on the other hand, the individual molecules are analysed one-by-one the heterogeneity in the system can be directly resolved. This ability is important to discriminate between different models that attempt to explain the mechanism by which DNA is made accessible to protein factors.

The experimental setup is based on an inverted microscope which was equipped with a multipurpose excitation beam path and a modular detection unit. Either pulsed or continuous-wave excitation was provided by coupling various external laser sources to the optical setup. The variation of the beam diameter allowed to extend the observation volume and to enhance the single molecule detection probability. The fluorescence of individual molecules travelling through the confocal laser spot was detected on the single photon level and analysed by a software which was written during this work.
In a first set of experiments optimum conditions were established under which consis-

tent single molecule results can be obtained. Optimum settings were defined for the laser intensity, the choice of detection filters and the use of additional photostabilising agents to prevent photoinactivation of the fluorophores. Consideration of the threshold settings used for single molecule identification led to a restriction of useful values. Generally, a compromise had to be found between a large number of detected events which provides a good statistice for subsequent analysis and an increased width of the proximity ratio distribution. Control experiments on small double labeled oligonucleotides ensured that mixing stoichoimetries and energy transfer values are correctly reproduced in the single molecule analysis.

The second part of this thesis was devoted to the analysis of structural heterogeneity within freely diffusing nucleosomes. By specific labeling of different DNA sites in the nucleosome it was possible to obtain an improved picture of local dynamics in the complex. A major problem that is encountered when working with individual nucleosomes is the spontaneous dissociation at pM concentrations which are typical for single molecule experiments. Complex dissociation was found to be further enhanced in the presence of higher ionic strength and elevated temperatures. While the disruption of nucleosmes could be partially prevented by passivation of the sample container walls with inert protein this method alone was not sufficient to maintain the integrity of weaker bound DNA-octamer complexes. An elegant way to maintain sample intactness was the addition of unlabeled nucleosomes. In combination with $0.1\,g/l$ BSA a total concentration of $10\,nM$ nucleosomes provided sufficient stability for all nucleosome constructs under study.
Moreover, the controlled change of nucleosome concentration allowed to study the stability of the nucleosome complex as a function of overall sample concentration. By progressively lowering the total nucleosome concentration a conformational change was induced which indicated a redistribution between different nucleosome conformations. This observation was further validated by a detailed analysis of the conformational heterogeneity. The results from the multiparameter analysis showed a coexistence of at lesst two bound nucleosome substates with an interfluorophore distance of approximately $62\,\mathring{A}$ and $78\,\mathring{A}$. Their relative occupancy changed with increasing salt concentration which led to the identification of the high-FRET state as the more stable conformation. Moreover, an increased intranucleosome dynamics seemed to correlate with an increased tendency to desintegrate at higher ionic strength. The increase in structural heterogeneity might reflect the transient appearance of intermediate states during the dissociation process. One might speculate that new conformations are induced as the result of H2A/H2B dimer loss but this needs further validation.

Finally, the effect of DNA sequence and histone acetylation on the structure and stability of nucleosomes was investigated. Structural information was obtained from the linker DNA region as well as from an octamer-bound DNA site. All modifications had only minor effects on internal DNA sites while significant differences could be observed in the linker DNA conformation. Replacing the 601 sequence by the less affine 5S sequence led to a considerably increased heterogeneity in the distribution of linker DNA end-to-end distances. This was accompanied by a broadening of the proximity ratio

distribution observed for octamer-attached DNA sites. Moreover, exposure to elevated salt concentrations caused an increased dissociation of 5S nucleosomes as compared to 601 nucleosomes which formed an overall more rigid structure.
The effect of histone acetylation caused an overall opening of the nucleosome structure. Again, the largest effects were observed in the linker DNA region while only a minor broadening was noticed for internal DNA sites. The effect was similar for both sequences which suggests that the DNA sequence itself does not play an important role in the DNA-histone tail interaction. For both sequences an increase in linker DNA distance agreed with previous ensemble data. For 601 nucleosomes a rather uniform change in end-to-end distance was observed while 5S nucleosomes behaved more in a two-state fashion. These differences are not resolvable in ensemble-based assays and demonstrate the benefits of our single-molecule approach. Subsequent analysis of nucleosome stability verified that the acetylation-mediated opening of the nucleosome structure caused an increased dissociation of the complex at higher ionic strength.
This thesis presented a thorough discussion of nucleosome stability and conformation under various conditions. Detailed information on the nucleosome structure under native conditions is still rare. Experiments like those presented in this thesis will help to further understand the complex nature of DNA-octamer interactions that provides the basis of the dynamic chromatin organisation in the eukaryotic cell.

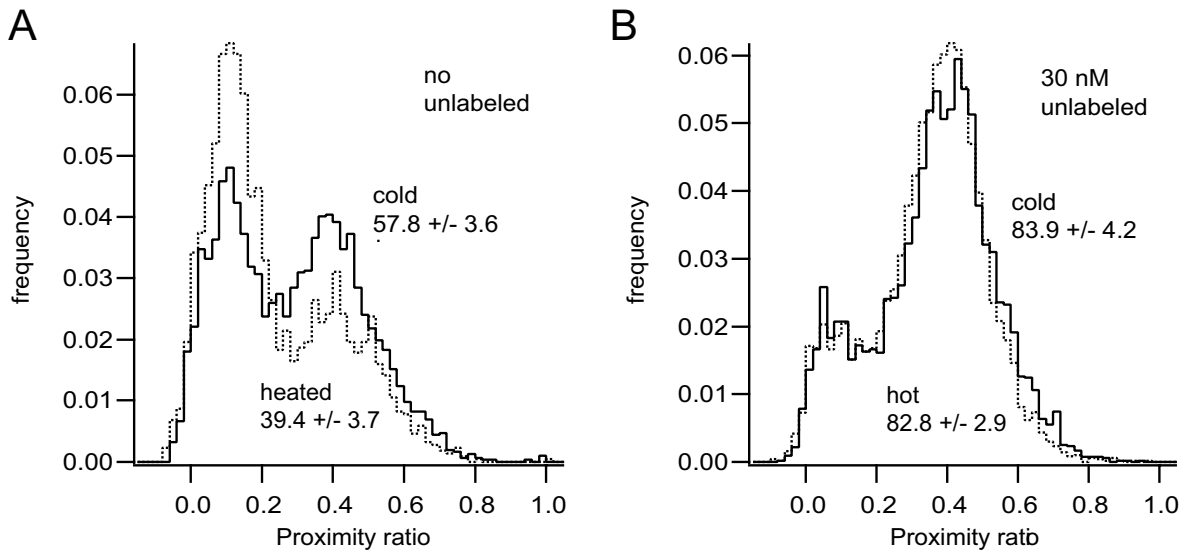

Figure 7.1: Stabilisation of nucleosomes against thermally induced dissociation. **A**: $50\,pM$ 601^{170} nucleosomes before (solid line) and after (dotted line) exposure to 55 °C for 2 hours. **B**: Same experiment, where $30\,nM$ unlabeled nucleosomes were added prior to the heating process. Under quasi-bulk conditions, the proximity ratio distribution did not change, indicating that the loss of intact nucleosomes observed in panel A is caused by degradation, rather than repositioning.

7.2 Future perspectives

7.2.1 Improved protocol for mobilisation assays

The exposure of nucleosomes to elevated temperatures provided a convenient way to induce conformational changes on individual nucleosomes [101, 53]. During this thesis it has been used on the single molecule level to test the potential of different sequences as a remodeling substrate. To implement this method as a standard diagnostic tool in our single molecule experiments a few improvements are suggested in the following.

mobilisation under quasi-bulk conditions

Under highly diluted nucleosome concentrations the increased temperature was found to further destabilise the complexes. An increase in the effective nucleosome concentration improved the stability against thermal degradation as shown in Figure 7.1. Upon exposure to elevated temperatures (55°C for 2 hours) a $50\,pM$ solution of 601^{170}_{med} nucleosomes showed a significant dissociation at low ionic strength already. On the contrary, if the labeled nucleosomes were diluted into a buffer containing unlabeled nucleosomes prior to heating, no thermal degradation was observed. The dissociation of nucleosomes during the heating process is an unwanted side effect and might be falsely interpreted as a redistribution into a conformation where the interfluorophore distance is increased beyond the FRET limit. The mobilisation of nucleosomes should thus not be performed under highly diluted conditions.

Thermal mobilisation online

Experiments which were performed so far analysed the histograms before and after exposure to elevated temperatures. By this a net difference between the nucleosomal states was detected. Far more interesting is a continuous monitoring of the processes underlying the mobilisation. To perform such experiments single molecule histograms have to be acquired during the heating process itself. This requires the sample being heated on the microscope. While such thermostages are available in our group a few aspects have to be considered:

1. Elevated temperatures lead to the heating of the optical elements, mostly the objective lens which couples to the sample container by means of the immersion water. The immersion water will evaporate faster and care has to be taken to avoid loss of the immersion film.

2. The increased temperature will cause a more rapid solvent evaporation. This will increase the net sample concentration which might result in a loss of single molecule conditions.

3. A rise in temperature will enlarge the diffusion coefficient. Particles will diffuse faster through the volume and emit less photons (equation 4.7). As a result less events with on average fewer photons will be registered. This will cause a further broadening of the distributions.
   In the simplest case of a spherical molecule the diffusion coefficient is determined by the viscosity, the temperature and the (generally temperature dependent) refractive index. For $\eta_{H_2O} = 0.89$ at bei 20°C and $\eta_{H_2O} = 0.54$ at 50°C respectively, we face a reduction in diffusion time of almost 50 %. This drawback could be overcome by adding additional $25 - 30$ % glycerol into the buffer solution.

Improved remodeling szbstrates

Another factor that potentially improves the mobilisation assay is to use nucleosome constructs which consist of larger DNA fragments. It was shown that various remodeling complexes require a minimum number of base pairs available in the linker region to exert their function. An improved mobility of nucleosome with longer DNA was also observed in gel electrophoretic studies, where 220 *bp* long fragments showed a significantly increase in their mobility upon thermal mobilisation and enzymatic remodeling [66]. Their preparation required longer DNA primers to be used and it was noticed that the labeling quality of internally labeled nucleosomes was reduced. While this produced a larger donor-only fraction in one-color FRET experiments the implementation of alternating dual-color excitation will be able to remove this unwanted contribution from the subsequent analysis.
It might also be beneficial to change the DNA sequence itself. Rippe et al. observed that the DNA sequence itself determines to some extent the remodeling activity of various factors [118]. A less affine binding sequence such as the 5S DNA might prove to be a suitable alternative to the 601 sequence used so far.

7.2.2 Analysis of immobilised nucleosomes

The discussion based assay is limited to observation times of a few ms which is the typical burst duration that can be obtained. Fast dynamical processes that occur on this time scale require sophisticated analysis tools such as the combined time window - PDA analysis presented in section 5.2. The transient changes in nucleosome conformation caused by the activity of remodeling factors such as ISWI are expected to occur on timescales of the order of minutes [146]. A great deal of information can be obtained if one is able to monitor an individual nucleosome for such long a time. This requires to immobilise the nucleosome on a surface as has been recently reported in [80, 133]. The presence of the surface might cause unwanted side effects on nucleosome dynamics and it might be advantageous to provide a more native condition for immobilisation.
The encapsulation of nucleosomes into lipid vesicles might be one way to indirectly fix the nucleosomes to the surface. It remains to be seen in how far the encapsulation process which involves the extrusion of the sample through a polycarbonate filter can be applied to nucleosomes without disrupting them. Once the sample is embedded in the vesicle these can be coupled to a pre-coated surface via standard biotin-streptavidin anchoring [115].
A different way to immobilize single nucleosomes was initiated in collaboration with Prof. Chirico from Milano. Single molecules are embedded in a porous silia nanogel. A thin gel matrix provides an optically transparent medium to investigate the dynamics of the samples contained within [18]. As the gel matrix is porous in nature it allows for an easy exchange of buffer conditions. In conjunction with a piezo-scanning device this approach would allow to detect local nucleosome dynamics for a prolonged time period. Similar to the vesicle approach, the molecules are free to move within the small nanocompartments formed in the gel. This avoids the need for tethering the nucleosome to the surface.

Acknowledgements

Ich danke Prof. Dr. Jörg Langowski für die Möglichkeit diese multidisziplinäre Arbeit anzufertigen und für seine wissenschaftliche Betreuung. Seine fachlichen und persönlichen Ratschläge waren jederzeit hilfreich, in allen Bereichen dieser Arbeit.

Bei Herrn Prof. Cremer möchte ich mich für seine Bereitschaft bedanken, mich seitens der Fakultät für Physik und Astronomie zu betreuen. und für sein Verständnis, besonders während der letzten Tage des Zusammenschreibens dieser Arbeit.

Besonderer Dank gilt Florian Hauger für die jederzeit freundliche und hilfsbereite Zusammenarbeit, fachliche Diskussionen und die Bereitstellung zahlreicher Nukleosomenproben. Im gleichen Atemzug danke ich Nathalie Brun für die Bereitstellung weiterer Nukleosomenproben.
Katalin Toth danke ich für den regen fachlichen Austausch, ohne den manche Messungen nicht geklappt hätten.

Herrn Prof. Dr. Claus Seidel, Dr. Suren Felakyan und Alessandro Valeri gilt mein Dank für die perfekte Zusammenarbeit im Rahmen der Kooperation im DFG Programm SPP1128 und die Möglichkeit, weit mehr über die Struktur der Nukleosomen zu erfahren.

Für das Durchlesen meiner Arbeit bedanke ich mich besonders bei Annika Wedemeier, Tomasz Wocjan, Karine Voltz, Tabea Elbel und Katalin Toth. Malte Renz und Carina Reble danke ich für zahlreiche ermunternde Gespräche, die einen den Alltag für kurze Zeit vergessen ließen. Dank auch an meine Zimmerkollegen Nicolas Dross und Aaron Hieb für ein stets offenes Ohr und die angenehme Zimmeratmosphäre and an Maria für ihre stets aufmunternde Art .
Ein abschliessender Dank an alle anderen, bisher nicht genannten Mitglieder des Arbeitskreises, welche mir ein paar angenehme Jahre im DKFZ bescherten.

Bibliography

[1] C. W. Akey and K. Luger. Histone chaperones and nucleosome assembly. *Curr Opin Struct Biol*, 13(1):6–14, Feb 2003.

[2] B. Albrecht, A. V. Failla, R. Heintzmann, and C. Cremer. Spatially modulated illumination microscopy: online visualization of intensity distribution and prediction of nanometer precision of axial distance measurements by computer simulations. *J Biomed Opt*, 6(3):292–299, Jul 2001.

[3] J. D. Anderson and J. Widom. Sequence and position-dependence of the equilibrium accessibility of nucleosomal DNA target sites. *J Mol Biol*, 296(4):979–987, Mar 2000.

[4] M. Antonik, S. Felekyan, A. Gaiduk, and C. A. M. Seidel. Separating structural heterogeneities from stochastic variations in fluorescence resonance energy transfer distributions via photon distribution analysis. *J Phys Chem B*, 110(13):6970–6978, Apr 2006.

[5] S. Aoyagi and J. J. Hayes. hSWI/SNF-catalyzed nucleosome sliding does not occur solely via a twist-diffusion mechanism. *Mol Cell Biol*, 22(21):7484–7490, Nov 2002.

[6] P. B. Becker. Nucleosome remodelers on track. *Nat Struct Mol Biol*, 12(9):732–733, Sep 2005.

[7] P. B. Becker and W. Hörz. ATP-dependent nucleosome remodeling. *Annu Rev Biochem*, 71:247–273, 2002.

[8] J. Bednar, R. A. Horowitz, S. A. Grigoryev, L. M. Carruthers, J. C. Hansen, A. J. Koster, and C. L. Woodcock. Nucleosomes, linker DNA, and linker histone form a unique structural motif that directs the higher-order folding and compaction of chromatin. *Proc Natl Acad Sci U S A*, 95(24):14173–14178, Nov 1998.

[9] M. Böhmer and J. Enderlein. Fluorescence spectroscopy of single molecules under ambient conditions: methodology and technology. *Chemphyschem*, 4(8):793–808, Aug 2003.

[10] E. Boukobza, A. Siommerfeld, and G. Haran. Immobilisation in surface-tethered lipid vesicles as a new tool for single biomolecule spectroscopy. *J Phys Chem B*, 105(48):12165 – 12170, Dec 2001.

[11] B. D. Brower-Toland, C. L. Smith, R. C. Yeh, J. T. Lis, C. L. Peterson, and M. D. Wang. Mechanical disruption of individual nucleosomes reveals a reversible multistage release of DNA. *Proc Natl Acad Sci U S A*, 99(4):1960–1965, Feb 2002.

[12] M. Bruno, A. Flaus, C. Stockdale, C. Rencurel, H. Ferreira, and T. Owen-Hughes. Histone H2A/H2B dimer exchange by ATP-dependent chromatin remodeling activities. *Mol Cell*, 12(6):1599–1606, Dec 2003.

[13] M. Bussiek, K. Toth, N. Brun, and J. Langowski. DNA-loop formation on nucleosomes shown by in situ scanning force microscopy of supercoiled DNA. *J Mol Biol*, 345(4):695–706, Jan 2005.

[14] M. Bussiek, K. Toth, N. Schwarz, and J. Langowski. Trinucleosome compaction studied by fluorescence energy transfer and scanning force microscopy. *Biochemistry*, 45(36):10838–10846, Sep 2006.

[15] e. a. C. Eggeling. Photobleaching of Fluorescent Dyes under Conditions used for Single-Molecule Detection. *Anal. Chem.*, 70:2651 – 2659, 1998.

[16] B. R. Cairns. Emerging roles for chromatin remodeling in cancer biology. *Trends Cell Biol*, 11(11):S15–S21, Nov 2001.

[17] B. R. Cairns. Chromatin remodeling: insights and intrigue from single-molecule studies. *Nat Struct Mol Biol*, 14(11):989–996, Nov 2007.

[18] F. Cannone, S. Bologna, B. Campanini, A. Diaspro, S. Bettati, A. Mozzarelli, and G. Chirico. Tracking unfolding and refolding of single GFPmut2 molecules. *Biophys J*, 89(3):2033–2045, Sep 2005.

[19] Y. Chen, J. D. Müller, K. M. Berland, and E. Gratton. Fluorescence fluctuation spectroscopy. *Methods*, 19(2):234–252, Oct 1999.

[20] Y. Chen, J. D. Müller, P. T. So, and E. Gratton. The photon counting histogram in fluorescence fluctuation spectroscopy. *Biophys J*, 77(1):553–567, Jul 1999.

[21] I. Cisse, B. Okumus, C. Joo, and T. Ha. Fueling protein DNA interactions inside porous nanocontainers. *Proc Natl Acad Sci U S A*, 104(31):12646–12650, Jul 2007.

[22] C. Claudet, D. Angelov, P. Bouvet, S. Dimitrov, and J. Bednar. Histone octamer instability under single molecule experiment conditions. *J Biol Chem*, 280(20):19958–19965, May 2005.

[23] R. M. Clegg. Fluorescence resonance energy transfer and nucleic acids. *Methods Enzymol*, 211:353–388, 1992.

[24] D. F. Corona, G. Längst, C. R. Clapier, E. J. Bonte, S. Ferrari, J. W. Tamkun, and P. B. Becker. ISWI is an ATP-dependent nucleosome remodeling factor. *Mol Cell*, 3(2):239–245, Feb 1999.

[25] R. W. Cotton and B. A. Hamkalo. Nucleosome dissociation at physiological ionic strengths. *Nucleic Acids Res*, 9(2):445–457, Jan 1981.

[26] C. Cremer and T. Cremer. Considerations on a laser-scanning-microscope with high resolution and depth of field. *Microsc Acta*, 81(1):31–44, Sep 1978.

[27] T. Cremer and C. Cremer. Chromosome territories, nuclear architecture and gene regulation in mammalian cells. *Nat Rev Genet*, 2(4):292–301, Apr 2001.

[28] T. Cremer, G. Kreth, H. Koester, R. H. Fink, R. Heintzmann, M. Cremer, I. Solovei, D. Zink, and C. Cremer. Chromosome territories, interchromatin domain compartment, and nuclear matrix: an integrated view of the functional nuclear architecture. *Crit Rev Eukaryot Gene Expr*, 10(2):179–212, 2000.

[29] C. A. Davey, D. F. Sargent, K. Luger, A. W. Maeder, and T. J. Richmond. Solvent mediated interactions in the structure of the nucleosome core particle at 1.9 $\AA$ resolution. *J Mol Biol*, 319(5):1097–1113, Jun 2002.

[30] A. A. Deniz, M. Dahan, J. R. Grunwell, T. Ha, A. E. Faulhaber, D. S. Chemla, S. Weiss, and P. G. Schultz. Single-pair fluorescence resonance energy transfer on freely diffusing molecules: observation of Förster distance dependence and subpopulations. *Proc Natl Acad Sci U S A*, 96(7):3670–3675, Mar 1999.

[31] A. A. Deniz, T. A. Laurence, G. S. Beligere, M. Dahan, A. B. Martin, D. S. Chemla, P. E. Dawson, P. G. Schultz, and S. Weiss. Single-molecule protein folding: diffusion fluorescence resonance energy transfer studies of the denaturation of chymotrypsin inhibitor 2. *Proc Natl Acad Sci U S A*, 97(10):5179–5184, May 2000.

[32] A. A. Deniz, T. A. Laurence, M. Dahan, D. S. Chemla, P. G. Schultz, and S. Weiss. Ratiometric single-molecule studies of freely diffusing biomolecules. *Annu Rev Phys Chem*, 52:233–253, 2001.

[33] A. Dietrich, V. Buschmann, C. Müller, and M. Sauer. Fluorescence resonance energy transfer (FRET) and competing processes in donor-acceptor substituted DNA strands: a comparative study of ensemble and single-molecule data. *J Biotechnol*, 82(3):211–231, Jan 2002.

[34] M. Diez, B. Zimmermann, M. Börsch, M. König, E. Schweinberger, S. Steigmiller, R. Reuter, S. Felekyan, V. Kudryavtsev, C. A. M. Seidel, and P. Gräber. Proton-powered subunit rotation in single membrane-bound $F_0F_1 -$ ATP synthase. *Nat Struct Mol Biol*, 11(2):135–141, Feb 2004.

[35] P. S. Dittrich and P. Schwille. Photobleaching and stabilisation of fluorophores used for single-molecule analysis with one- and two-photon excitation. *Appl Phys B - Lasers and optics*, 73(8):829 – 837, Dec 2001.

[36] S. Doose, H. Neuweiler, H. Barsch, and M. Sauer. Probing polyproline structure and dynamics by photoinduced electron transfer provides evidence for deviations from a regular polyproline type II helix. *Proc Natl Acad Sci U S A*, 104(44):17400–17405, Oct 2007.

[37] A. Eberharter and P. B. Becker. ATP-dependent nucleosome remodelling: factors and functions. *J Cell Sci*, 117(Pt 17):3707–3711, Aug 2004.

[38] C. Eggeling. *Analyse von photochemischer Kinetik und Molekül̈dynamik durch mehrdimensionale Einzelmolekül-Fluoreszenzspektroskopie*. PhD thesis, Georg-August-Universität Göttingen, 1999.

[39] C. Eggeling, S. Berger, L. Brand, J. R. Fries, J. Schaffer, A. Volkmer, and C. A. M. Seidel. Data registration and selective single-molecule analysis using multi-parameter fluorescence detection. *J Biotechnol*, 86(3):163–180, Apr 2001.

[40] C. Eggeling, J. Widengren, L. Brand, J. Schaffer, S. Felekyan, and C. A. M. Seidel. Analysis of photobleaching in single-molecule multicolor excitation and Förster resonance energy transfer measurements. *J Phys Chem A*, 110(9):2979–2995, Mar 2006.

[41] C. Eggeling, J. Widengren, R. Rigler, and C. Seidel. *Photostability of Fluorescent Dyes for Single-Molecule Spectroscopy*, chapter 10, pages 193 – 240. Springer Verlag, 1999.

[42] J. Enderlein. *Single Molecule Detection in Solution - Methods and Applications*, chapter 2, pages 21 – 67. Wiley-VCH, 2002.

[43] J. Enderlein, D. L. Robbins, W. P. Ambrose, P. W. Goodwin, and R. A. Keller. Statistics of single-molecule detection. *J. Phys. Chem. B*, 101(18):3626 – 3632, March 1997.

[44] H. Eshaghpour, A. E. Dieterich, C. R. Cantor, and D. M. Crothers. Singlet-singlet energy transfer studies of the internal organization of nucleosomes. *Biochemistry*, 19(9):1797–1805, Apr 1980.

[45] H.-Y. Fan, X. He, R. E. Kingston, and G. J. Narlikar. Distinct strategies to make nucleosomal DNA accessible. *Mol Cell*, 11(5):1311–1322, May 2003.

[46] T. G. Fazzio and T. Tsukiyama. Chromatin remodeling in vivo: evidence for a nucleosome sliding mechanism. *Mol Cell*, 12(5):1333–1340, Nov 2003.

[47] J. T. Finch and A. Klug. Solenoidal model for superstructure in chromatin. *Proc Natl Acad Sci U S A*, 73(6):1897–1901, Jun 1976.

[48] J. T. Finch, L. C. Lutter, D. Rhodes, R. S. Brown, B. Rushton, M. Levitt, and A. Klug. Structure of nucleosome core particles of chromatin. *Nature*, 269(5623):29–36, Sep 1977.

[49] A. Flaus and T. Owen-Hughes. Mechanisms for ATP-dependent chromatin remodelling. *Curr Opin Genet Dev*, 11(2):148–154, Apr 2001.

[50] A. Flaus and T. Owen-Hughes. Dynamic properties of nucleosomes during thermal and ATP-driven mobilization. *Mol Cell Biol*, 23(21):7767–7779, Nov 2003.

[51] A. Flaus and T. Owen-Hughes. Mechanisms for nucleosome mobilization. *Biopolymers*, 68(4):563–578, Apr 2003.

[52] A. Flaus and T. Owen-Hughes. Mechanisms for ATP-dependent chromatin remodelling: farewell to the tuna-can octamer? *Curr Opin Genet Dev*, 14(2):165–173, Apr 2004.

[53] A. Flaus and T. J. Richmond. Positioning and stability of nucleosomes on MMTV 3'LTR sequences. *J Mol Biol*, 275(3):427–441, Jan 1998.

[54] T. M. Fletcher and J. C. Hansen. Core histone tail domains mediate oligonucleosome folding and nucleosomal DNA organization through distinct molecular mechanisms. *J Biol Chem*, 270(43):25359–25362, Oct 1995.

[55] Z. Földes-Papp. What it means to measure a single molecule in a solution by fluorescence fluctuation spectroscopy. *Exp Mol Pathol*, 80(3):209–218, Jun 2006.

[56] J. R. Fries, L. Brand, C. Eggeling, M. Köllner, and C. A. M. Seidel. Quantitative identification of different single molecules by selective time-resolved confocal fluorescence spectroscopy. *J. Phys. Chem. A*, 102:6601 – 6613, 1998.

[57] A. Gansen, F. Hauger, K. Toth, and J. Langowski. Single-pair fluorescence resonance energy transfer of nucleosomes in free diffusion: optimizing stability and resolution of subpopulations. *Anal Biochem*, 368(2):193–204, Sep 2007.

[58] M. Garcia-Ramirez, F. Dong, and J. Ausio. Role of the histone "tails" in the folding of oligonucleosomes depleted of histone H1. *J Biol Chem*, 267(27):19587–19595, Sep 1992.

[59] G. J. Gemmen, R. Sim, K. A. Haushalter, P. C. Ke, J. T. Kadonaga, and D. E. Smith. Forced unraveling of nucleosomes assembled on heterogeneous DNA using core histones, NAP-1, and ACF. *J Mol Biol*, 351(1):89–99, Aug 2005.

[60] S. M. Görisch, M. Wachsmuth, K. F. Tth, P. Lichter, and K. Rippe. Histone acetylation increases chromatin accessibility. *J Cell Sci*, 118(Pt 24):5825–5834, Dec 2005.

[61] J. M. Gottesfeld and K. Luger. Energetics and affinity of the histone octamer for defined DNA sequences. *Biochemistry*, 40(37):10927–10933, Sep 2001.

[62] I. Gregor, D. Patra, and J. Enderlein. Optical saturation in fluorescence correlation spectroscopy under continuous-wave and pulsed excitation. *Chemphyschem*, 6(1):164–170, Jan 2005.

[63] T. Ha. Single-molecule fluorescence resonance energy transfer. *Methods*, 25(1):78–86, Sep 2001.

[64] T. Ha, T. Enderle, D. F. Ogletree, D. S. Chemla, P. R. Selvin, and S. Weiss. Probing the interaction between two single molecules: fluorescence resonance energy transfer between a single donor and a single acceptor. *Proc Natl Acad Sci U S A*, 93(13):6264–6268, Jun 1996.

[65] A. Hamiche, V. Carot, M. Alilat, F. D. Lucia, M. F. O'Donohue, B. Revet, and A. Prunell. Interaction of the histone (H3-H4)2 tetramer of the nucleosome with positively supercoiled DNA minicircles: Potential flipping of the protein from a left- to a right-handed superhelical form. *Proc Natl Acad Sci U S A*, 93(15):7588–7593, Jul 1996.

[66] F. Hauger. *Fluoreszenzspektroskopische Untersuchungen nukleosomaler Struktur und Dynamik*. PhD thesis, Ruprecht Karls - Universität Heidelberg, 2007.

[67] J. J. Hayes, D. J. Clark, and A. P. Wolffe. Histone contributions to the structure of DNA in the nucleosome. *Proc Natl Acad Sci U S A*, 88(15):6829–6833, Aug 1991.

[68] S. W. Hell. Far-field optical nanoscopy. *Science*, 316(5828):1153–1158, May 2007.

[69] S. W. Hell, M. Schrader, and H. T. van der Voort. Far-field fluorescence microscopy with three-dimensional resolution in the 100-nm range. *J Microsc*, 187(Pt 1):1–7, Jul 1997.

[70] T. Hirschfeld. Optical microscopic observation of small molecule. *Appl. Opt.*, 15(12):2965 – 2966, 1976.

[71] D. A. Hoch, J. J. Stratton, and L. M. Gloss. Protein-protein Förster resonance energy transfer analysis of nucleosome core particles containing H2A and H2A.Z. *J Mol Biol*, 371(4):971–988, Aug 2007.

[72] S. Hohng, C. Joo, and T. Ha. Single-molecule three-color FRET. *Biophys J*, 87(2):1328–1337, Aug 2004.

[73] T. Ito, M. Bulger, M. J. Pazin, R. Kobayashi, and J. T. Kadonaga. ACF, an ISWI-containing and ATP-utilizing chromatin assembly and remodeling factor. *Cell*, 90(1):145–155, Jul 1997.

[74] J. Jackson. *Classical Electrodynamics*. Academic Press, 1998.

[75] S. Kalinin, S. Felekyan, M. Antonik, and C. A. M. Seidel. Probability distribution analysis of single-molecule fluorescence anisotropy and resonance energy transfer. *J Phys Chem B*, 111(34):10253–10262, Aug 2007.

[76] A. N. Kapanidis, N. K. Lee, T. A. Laurence, S. Doose, E. Margeat, and S. Weiss. Fluorescence-aided molecule sorting: analysis of structure and interactions by alternating-laser excitation of single molecules. *Proc Natl Acad Sci U S A*, 101(24):8936–8941, Jun 2004.

[77] P. Kask, K. Palo, D. Ullmann, and K. Gall. Fluorescence-intensity distribution analysis and its application in biomolecular detection technology. *Proc Natl Acad Sci U S A*, 96(24):13756–13761, Nov 1999.

[78] S. R. Kassabov, B. Zhang, J. Persinger, and B. Bartholomew. SWI/SNF unwraps, slides, and rewraps the nucleosome. *Mol Cell*, 11(2):391–403, Feb 2003.

[79] L. Kelbauskas, N. Chan, R. Bash, P. Debartolo, J. Sun, N. Woodbury, and D. Lohr. Sequence-Dependent Variations Associated with H2A/H2B Depletion of Nucleosomes. *Biophys J*, Oct 2007.

[80] W. J. A. Koopmans, A. Brehm, C. Logie, T. Schmidt, and J. van Noort. Single-Pair FRET Microscopy Reveals Mononucleosome Dynamics. *J Fluoresc*, 17(6):785–795, Nov 2007.

[81] D. E. Koppel, D. Axelrod, J. Schlessinger, E. L. Elson, and W. W. Webb. Dynamics of fluorescence marker concentration as a probe of mobility. *Biophys J*, 16(11):1315–1329, Nov 1976.

[82] R. D. Kornberg. Chromatin structure: a repeating unit of histones and DNA. *Science*, 184(139):868–871, May 1974.

[83] R. D. Kornberg and J. O. Thomas. Chromatin structure; oligomers of the histones. *Science*, 184(139):865–868, May 1974.

[84] W. A. Krajewski. Histone acetylation status and DNA sequence modulate ATP-dependent nucleosome repositioning. *J Biol Chem*, 277(17):14509–14513, Apr 2002.

[85] I. M. Kulic and H. Schiessel. Chromatin dynamics: nucleosomes go mobile through twist defects. *Phys Rev Lett*, 91(14):148103, Oct 2003.

[86] I. M. Kulic and H. Schiessel. Nucleosome repositioning via loop formation. *Biophys J*, 84(5):3197–3211, May 2003.

[87] D. C. Lamb, A. Schenk, C. Röcker, C. Scalfi-Happ, and G. U. Nienhaus. Sensitivity enhancement in fluorescence correlation spectroscopy of multiple species using time-gated detection. *Biophys J*, 79(2):1129–1138, Aug 2000.

[88] G. Längst and P. B. Becker. ISWI induces nucleosome sliding on nicked DNA. *Mol Cell*, 8(5):1085–1092, Nov 2001.

[89] G. Längst and P. B. Becker. Nucleosome remodeling: one mechanism, many phenomena? *Biochim Biophys Acta*, 1677(1-3):58–63, Mar 2004.

[90] N. K. Lee, A. N. Kapanidis, Y. Wang, X. Michalet, J. Mukhopadhyay, R. H. Ebright, and S. Weiss. Accurate FRET measurements within single diffusing biomolecules using alternating-laser excitation. *Biophys J*, 88(4):2939–2953, Apr 2005.

[91] G. Li, M. Levitus, C. Bustamante, and J. Widom. Rapid spontaneous accessibility of nucleosomal DNA. *Nat Struct Mol Biol*, 12(1):46–53, Jan 2005.

[92] G. G. Lindsey, S. Orgeig, P. Thompson, N. Davies, and D. L. Maeder. Extended C-terminal tail of wheat histone H2A interacts with DNA of the "linker" region. *J Mol Biol*, 218(4):805–813, Apr 1991.

[93] H.-W. Liu, G. Cosa, C. F. Landes, Y. Zeng, B. J. Kovaleski, D. G. Mullen, G. Barany, K. Musier-Forsyth, and P. F. Barbara. Single-molecule FRET studies of important intermediates in the nucleocapsid-protein-chaperoned minus-strand transfer step in HIV-1 reverse transcription. *Biophys J*, 89(5):3470–3479, Nov 2005.

[94] D. Lovullo, D. Daniel, J. Yodh, D. Lohr, and N. W. Woodbury. A fluorescence resonance energy transfer-based probe to monitor nucleosome structure. *Anal Biochem*, 341(1):165–172, Jun 2005.

[95] P. T. Lowary and J. Widom. New DNA sequence rules for high affinity binding to histone octamer and sequence-directed nucleosome positioning. *J Mol Biol*, 276(1):19–42, Feb 1998.

[96] K. Luger, A. W. Mäder, R. K. Richmond, D. F. Sargent, and T. J. Richmond. Crystal structure of the nucleosome core particle at 2.8 $\AA$ resolution. *Nature*, 389(6648):251–260, Sep 1997.

[97] D. Magde, E. L. Elson, and W. W. Webb. Fluorescence correlation spectroscopy. II. An experimental realization. *Biopolymers*, 13(1):29–61, Jan 1974.

[98] S. Mangenot, A. Leforestier, P. Vachette, D. Durand, and F. Livolant. Salt-induced conformation and interaction changes of nucleosome core particles. *Biophys J*, 82(1 Pt 1):345–356, Jan 2002.

[99] M. Margittai, J. Widengren, E. Schweinberger, G. F. Schröder, S. Felekyan, E. Haustein, M. König, D. Fasshauer, H. Grubmüller, R. Jahn, and C. A. M. Seidel. Single-molecule fluorescence resonance energy transfer reveals a dynamic equilibrium between closed and open conformations of syntaxin 1. *Proc Natl Acad Sci U S A*, 100(26):15516–15521, Dec 2003.

[100] S. A. McKinney, E. Tan, T. J. Wilson, M. K. Nahas, A.-C. Dclais, R. M. Clegg, D. M. J. Lilley, and T. Ha. Single-molecule studies of DNA and RNA four-way junctions. *Biochem Soc Trans*, 32(Pt 1):41–45, Feb 2004.

[101] G. Meersseman, S. Pennings, and E. M. Bradbury. Mobile nucleosomes–a general behavior. *EMBO J*, 11(8):2951–2959, Aug 1992.

[102] J. Mertz. Molecular photodynamics involved in multi-photonexcitation fluorescence microscopy. *Eur Phys J D*, 3:53 – 66, 1998.

[103] Moerner and Kador. Optical detection and spectroscopy of single molecules in a solid. *Phys Rev Lett*, 62(21):2535–2538, May 1989.

[104] B. K. Müller, E. Zaychikov, C. Bräuchle, and D. C. Lamb. Pulsed interleaved excitation. *Biophys J*, 89(5):3508–3522, Nov 2005.

[105] K. Ohkuni, K. Shirahige, and A. Kikuchi. Genome-wide expression analysis of NAP1 in Saccharomyces cerevisiae. *Biochem Biophys Res Commun*, 306(1):5–9, Jun 2003.

[106] A. L. Olins and D. E. Olins. Spheroid chromatin units (v bodies). *Science*, 183(122):330–332, Jan 1974.

[107] A. V. Orden, N. P. Machera, P. M. Goodwin, and R. A. Keller. Single-molecule identification in flowing sample streams by fluorescence burst size and intraburst fluorescence decay rate. *Anal. Chem.*, 70:1444 – 1451, 1998.

[108] T. Owen-Hughes. Colworth memorial lecture. Pathways for remodelling chromatin. *Biochem Soc Trans*, 31(Pt 5):893–905, Oct 2003.

[109] K. Palo, U. Mets, S. Jäger, P. Kask, and K. Gall. Fluorescence intensity multiple distributions analysis: concurrent determination of diffusion times and molecular brightness. *Biophys J*, 79(6):2858–2866, Dec 2000.

[110] Y.-J. Park, P. N. Dyer, D. J. Tremethick, and K. Luger. A new fluorescence resonance energy transfer approach demonstrates that the histone variant H2AZ stabilizes the histone octamer within the nucleosome. *J Biol Chem*, 279(23):24274–24282, Jun 2004.

[111] S. Pennings, G. Meersseman, and E. M. Bradbury. Mobility of positioned nucleosomes on 5 S rDNA. *J Mol Biol*, 220(1):101–110, Jul 1991.

[112] S. Pennings, G. Meersseman, and E. M. Bradbury. Linker histones H1 and H5 prevent the mobility of positioned nucleosomes. *Proc Natl Acad Sci U S A*, 91(22):10275–10279, Oct 1994.

[113] T. D. Pollard and W. Earnshaw. *Cell biology*. Saunders, 2004.

[114] H. Qian and E. L. Elson. Analysis of confocal laser microscope optics for 3-D fluorescence correlation spectroscopy. *Appl. Opt.*, 30:1185, 1991.

[115] E. Rhoades, E. Gussakovsky, and G. Haran. Watching proteins fold one molecule at a time. *Proc Natl Acad Sci U S A*, 100(6):3197–3202, Mar 2003.

[116] T. J. Richmond and C. A. Davey. The structure of DNA in the nucleosome core. *Nature*, 423(6936):145–150, May 2003.

[117] T. J. Richmond, J. T. Finch, B. Rushton, D. Rhodes, and A. Klug. Structure of the nucleosome core particle at 7 Å resolution. *Nature*, 311(5986):532–537, 1984.

[118] K. Rippe, A. Schrader, P. Riede, R. Strohner, E. Lehmann, and G. Längst. DNA sequence- and conformation-directed positioning of nucleosomes by chromatin-remodeling complexes. *Proc Natl Acad Sci U S A*, 104(40):15635–15640, Oct 2007.

[119] A. Saha, J. Wittmeyer, and B. R. Cairns. Chromatin remodeling through directional DNA translocation from an internal nucleosomal site. *Nat Struct Mol Biol*, 12(9):747–755, Sep 2005.

[120] H. Schiessel. The physics of chromatin. *J Phys: Condens Matter*, 15:699 – 774, 2003.

[121] H. Schiessel. The nucleosome: a transparent, slippery, sticky and yet stable DNA-protein complex. *Eur Phys J E Soft Matter*, 19(3):251–262, Mar 2006.

[122] B. Schuler. Application of single molecule Förster resonance energy transfer to protein folding. *Methods Mol Biol*, 350:115–138, 2007.

[123] B. Schuler, E. A. Lipman, and W. A. Eaton. Probing the free-energy surface for protein folding with single-molecule fluorescence spectroscopy. *Nature*, 419(6908):743–747, Oct 2002.

[124] E. B. Shera, N. K. Seizinger, L. M. Davis, R. A. Keller, and S. A. Soper. Detection of single fluorescent molecule. *Chemical Physics Letters*, 174:553 – 557, 1990.

[125] R. T. Simpson. Structure of the chromatosome, a chromatin particle containing 160 base pairs of DNA and all the histones. *Biochemistry*, 17(25):5524–5531, Dec 1978.

[126] B. D. Strahl and C. D. Allis. The language of covalent histone modifications. *Nature*, 403(6765):41–45, Jan 2000.

[127] R. Strohner, M. Wachsmuth, K. Dachauer, J. Mazurkiewicz, J. Hochstatter, K. Rippe, and G. Längst. A 'loop recapture' mechanism for ACF-dependent nucleosome remodeling. *Nat Struct Mol Biol*, 12(8):683–690, Aug 2005.

[128] L. Stryer and R. P. Haugland. Energy transfer: a spectroscopic ruler. *Proc Natl Acad Sci U S A*, 58(2):719–726, Aug 1967.

[129] E. Tan, T. J. Wilson, M. K. Nahas, R. M. Clegg, D. M. J. Lilley, and T. Ha. A four-way junction accelerates hairpin ribozyme folding via a discrete intermediate. *Proc Natl Acad Sci U S A*, 100(16):9308–9313, Aug 2003.

[130] M. Tewes. *Aufbau eines Experiments zur Fluoreszenzkreuzkorrelationsspektroskopie, Erweiterungen der theoretischen grundlagen und biologische Anwendungen*. PhD thesis, Ruprecht-Karls Universität Heidelberg, 1998.

[131] A. Thaström, J. M. Gottesfeld, K. Luger, and J. Widom. Histone-DNA binding free energy cannot be measured in dilution-driven dissociation experiments. *Biochemistry*, 43(3):736–741, Jan 2004.

[132] A. Thaström, P. T. Lowary, and J. Widom. Measurement of histone-DNA interaction free energy in nucleosomes. *Methods*, 33(1):33–44, May 2004.

[133] M. Tomschik, H. Zheng, K. van Holde, J. Zlatanova, and S. H. Leuba. Fast, long-range, reversible conformational fluctuations in nucleosomes revealed by single-pair fluorescence resonance energy transfer. *Proc Natl Acad Sci U S A*, 102(9):3278–3283, Mar 2005.

[134] K. Toth, N. Brun, and J. Langowski. Trajectory of nucleosomal linker DNA studied by fluorescence resonance energy transfer. *Biochemistry*, 40(23):6921–6928, Jun 2001.

[135] K. Toth, N. Brun, and J. Langowski. Chromatin compaction at the mononucleosome level. *Biochemistry*, 45(6):1591–1598, Feb 2006.

[136] R. Tsien and A. Waggoner. *Handbook of Biological Confocal Microscopy*, chapter 16, pages 267 – 279. Plenum Press, 1995.

[137] P. Varga-Weisz. ATP-dependent chromatin remodeling factors: nucleosome shufflers with many missions. *Oncogene*, 20(24):3076–3085, May 2001.

[138] P. D. Varga-Weisz and P. B. Becker. Regulation of higher-order chromatin structures by nucleosome-remodelling factors. *Curr Opin Genet Dev*, 16(2):151–156, Apr 2006.

[139] M. Wachsmuth. *Fluoreszenzfluktuationsmikroskopie Entwicklung eines Prototyps, Theorie und Messung der Beweglichkeit von Biomolekülen im Zellkern.* PhD thesis, Ruprecht-Karls Universität Heidelberg, 2001.

[140] M. Wachsmuth, T. Weidemann, G. Müller, U. W. Hoffmann-Rohrer, T. A. Knoch, W. Waldeck, and J. Langowski. Analyzing intracellular binding and diffusion with continuous fluorescence photobleaching. *Biophys J*, 84(5):3353–3363, May 2003.

[141] S. Weiss. Measuring conformational dynamics of biomolecules by single molecule fluorescence spectroscopy. *Nat Struct Biol*, 7(9):724–729, Sep 2000.

[142] J. Widengren, A. Chmyrov, C. Eggeling, P.-A. Löfdahl, and C. A. M. Seidel. Strategies to improve photostabilities in ultrasensitive fluorescence spectroscopy. *J Phys Chem A*, 111(3):429–440, Jan 2007.

[143] M. U. Widengren J., Rigler R. Triplet-State Monitoring by Fluorescence Correlation Spectroscopy. *J. Fluoresc.*, 4:255 – 258, 1994.

[144] A. Wolffe. *Chromatin: Structure and Function.* Academic Press, 1995.

[145] J. L. Workman. Nucleosome displacement in transcription. *Genes Dev*, 20(15):2009–2017, Aug 2006.

[146] J. G. Yang, T. S. Madrid, E. Sevastopoulos, and G. J. Narlikar. The chromatin-remodeling enzyme ACF is an ATP-dependent DNA length sensor that regulates nucleosome spacing. *Nat Struct Mol Biol*, 13(12):1078–1083, Dec 2006.

[147] L. M. Ying, M. I. Wallace, S. Balasubramanian, and D. Klenerman. Ratiometric analysis of single-molecule fluorescence resonance energy transfer using logical combinations of threshold criteria: A study of 12-mer DNA. *J. Phys. Chem. B*, 104:5171 – 5178, 2000.

[148] J. Zlatanova, C. Seebart, and M. Tomschik. NAP1: taking a closer look at a juggler protein of extraordinary skills. *FASEB J*, 21(7):1294–1310, May 2007.